EARTHQUAKES IN THE CONTINENTAL CRUST

A Dissertation
Presented to the Faculty of the Graduate School
of Cornell University
in Partial Fulfillment of the Requirements for the Degree of
Doctor of Philosophy

by
Stephanie Devlin
August 2008

© 2008 Stephanie Devlin

EARTHQUAKES IN THE CONTINENTAL CRUST

Stephanie Devlin, Ph. D.

Cornell University 2008

Continental earthquakes are one of the most widely observable indicators of on-going continental lithospheric deformation. Accurate earthquake depth estimates are critical to tectonic interpretations, yet depths are not reliably provided by global earthquake catalogs and bulletins. Therefore, separate analyses are needed to determined accurate earthquake depths. In this thesis, I compile accurate estimates of continental earthquake depths and combine them with complementary datasets, such as topography, subsurface structural interpretations, and lithospheric thickness estimates, to investigate continental deformation.

I present results of focal mechanisms and accurate depth estimates for continental earthquakes throughout the Central Andes of South America. Through integration with high resolution topographic data and interpretations of subsurface structures, I find the following: (1) earthquakes in the foreland and Eastern Cordillera are consistently associated with basement-involved deformation, (2) earthquake focal mechanism P axis orientations indicate an east-west crustal shortening direction in the forelands, (3) local orientations of deformational structures influence earthquake focal mechanism orientation, and (4) normal and strike-slip focal mechanisms beneath southern Peru and northernmost Chile are consistent with the effects of the increase in vertical compressive stress, due to high topography and thick crustal root of the plateau, superimposed on the stress orientations seen in the foreland.

I also conduct a global study of the depth distributions of continental earthquakes by synthesizing previously reported accurate earthquake depth determinations to investigate in what tectonic settings lower crustal earthquakes occur in an attempt to understand their significance to lithospheric strength and deformation. I find that deep continental crustal earthquakes occur within stable lithosphere and within tectonically active lithosphere at a transitional state of lithospheric thickness and crustal deformation.

BIOGRAPHICAL SKETCH

Stephanie Devlin was born in 1978 in Philadelphia, Pennsylvania. She attended Bishop Eustace Preparatory High School in Pennsauken, New Jersey, where she was editor of the school newspaper her senior year, helped to start and lead the school's Environmental Club, and was awarded the Bishop Eustace Alumni Award at graduation in 1996. Stephanie attended Rutgers, The State University of New Jersey in Camden, New Jersey to pursue an undergraduate degree. She majored in Physics and minored in Computer Science before graduating in 2001.

During her undergraduate education, Stephanie participated in a number of research opportunities to explore how best to apply her physics education after graduation. She conducted research at the Cornell Center for Materials Research with Professor Rüdiger Dieckmann at Cornell University during the summer of 1999 and atmospheric science research on artic aerosols with Professor Glenn E. Shaw at the University of Alaska Fairbanks during the summer of 2000. These research opportunities were part of the National Science Foundation's Research Experiences for Undergraduates program. Stephanie was also a Rutgers Physics Undergraduate Research Fellow during the academic year from 1999 to 2000. That research was aided by the guidance of Professor E. Roger Cowley at Rutgers in Camden. In the year between Stephanie's undergraduate and graduate enrollment, she was employed as a Laboratory Assistant in the Geosciences Department at Princeton University in Professor Tullis C. Onstott's Geomicrobiology laboratory.

In order to combine her education in Physics and her love of nature, Stephanie entered the graduate student program in the Earth and Atmospheric Sciences Department at

Cornell University in 2002 to pursue a Ph.D. in Geophysics under the guidance of Professor Bryan L. Isacks. This dissertation represents the results of the research conducted during Stephanie's six years as a graduate student at Cornell University. After earning her Ph.D., Stephanie moved to the Washington D.C. area to work for the U.S. Nuclear Regulatory Commission in the Office of New Reactors.

This dissertation is dedicated to my family,

without whom this document would not have been possible.

ACKNOWLEDGMENTS

I need to thank many people who helped me fulfill my goals at Cornell. Advisors, faculty, fellow graduate students, friends, and family have provided inspiration, time, and most importantly their support during these past six years.

First and foremost, I thank Bryan Isacks, my principal advisor, for his scientific instruction, encouragement, and patience. Continuously, Bryan was generous with financial support, time, constructive feedback, and scientific ideas. Bryan has set a high, yet humble, standard of what it means to be a scientist. I have learned the benefits of free-flowing scientific ideas and transparency of reasoning. In addition to Bryan, the rest of my special committee, Richard Allmendinger, Matthew Pritchard, and Jim Bell, aided me by providing productive committee meetings and examinations and invaluable feedback. Under the guidance and expectations of my special committee, I strove, sometimes struggled, to create a Ph.D.-worthy dissertation. Without the challenges they set forth, I would not have conducted the global synthesis of lower crustal earthquakes described in Chapter 3. I can not thank them enough for providing me the appropriate encouragement and support to tour the world with that geophysical study.

Many other university faculty and staff members have also provided help during my time as a graduate student. Larry Brown and Teresa Jordan acted as mentors for me during my first year at Cornell. They kept me connected to the department until I found my footing in Bryan's research group. Larry Brown, Richard Allmendinger, and Kerry Cook helped by providing enjoyable and straightforward Teaching Assistant positions. Suzanne Kay was gracious to allow me to escape the Graphics Lab during

my third year by attending and acting as Teaching Assistant on her Argentine summer field course. Other faculty members have helped by continued interest in my research and by always leaving themselves open to scientific discussions and questions. Those faculty members include all the previously mentioned people, as well as, Christopher Andronicos, Muawia Barazangi, Robert Kay, and Rowena Lohman. In particular, I would like to thank Muawia Barazangi for his encouragement and guidance throughout my time at Cornell. Muawia allowed me to commandeer the position of seismograph ramrod, which allowed me to play a part in the inner workings of the department. Most importantly, I would like to thank Muawia for providing me the encouragement and information to pursue a career with the U.S. Nuclear Regulatory Commission. My future career path has benefited from his guidance and I am indebted to him for his help.

Developing this dissertation alongside fellow graduate students as they develop their own projects has been an honor. I thank them all for their camaraderie, scientific exchange, and support. Students that entered the Department of Earth and Atmospheric Sciences' (EAS) graduate program along with me include Adam Goss, Helen Jones, Jack Loveless, and Neil McGlashan. I am proud to be a part of such a successful group of scientists. Officemates have included Pat Carr, Danielle Glasgow, Meghan Herz, Melissa Morse, Steve Romaniello, and Tiffany Tchakirides. I thank them for providing such an enjoyable and friendly place to go to separate from the lab. Invaluable friendships developed of the years with Carrie Brindisi, Meghan Herz, Louise McGarry, and Julie Pett-Ridge. These friends set wonderful examples of what it takes to be a successful woman, successful in life, love, and your career. Katie Tamulonis and Peter Nester helped create an ideal lab environment full of science, socializing, and laughter. Other relationships with graduate students inside and outside

EAS have also been influential and I thank them for their support – Dan Baird, Bill Langin, Amy Kwiatkowski, Taryn Morrissey, Joey Rosario, Brian Ruskin, Herdis Schopka, Sarah Thébaud, and Tarka Wilcox.

I gratefully acknowledge the financial support I have received through the years. I deeply appreciate the three years of funding I received from the NSF Graduate Research Fellowship. Additional, much appreciated funding came from EAS who provided me with the McMullen Fellowship, the Cornell University Graduate School Travel Grant, S. Kaufman Travel Fund, the Harry and Lillian Dovovan Scholarship, and appointments as a Teaching Assistant.

My entire family, both immediate and extended, has been a constant source of enthusiasm and support. I acknowledge my parents, James and Sherry, for making education a priority, for putting me through high school and college, and for always encouraging me to pursue math and science. To my sisters Kelly and Elizabeth, thank you for your support and friendships. I am eternally grateful for the support and encouragement I have received from my family.

TABLE OF CONTENTS

LIST OF FIGURES

LIST OF TABLES

INTRODUCTION

Seismotectonics is the study of geologic structures and deformation associated with tectonic activity using earthquake and seismic wave data. Continental plates tend to be more structurally complex than oceanic plates, because continental rocks can be much older so they have experienced more deformation and plate composition is generally more heterogeneous. A fundamental type of earthquake data is location, but depths of earthquakes in continents, as reported in standard catalogues of locations such as the Bulletin of the International Seismological Center, are not sufficiently accurate to determine the role of earthquakes in crustal deformation [e.g., *Kagan*, 2003; *Maggi, et al.*, 2000]. Therefore, additional analyses are needed to constrain depths for continental earthquakes.

Studies of earthquakes that use local seismic networks provide the most reliable depths, but global coverage of local networks is sparse and deployment at any one location is sporadic when compared to the almost 50 years of recording by the combined operation of the World-Wide Standardized Seismograph Network (WWSSN) and Global Seismographic Network (GSN). Therefore, earthquake depth determinations in most places around the world is done using WWSSN and/or GSN data from stations located at regional and teleseismic distances from the event [e.g., *Chen and Molnar*, 1983; *Maggi, et al.*, 2000; *Nyblade and Langston*, 1995].

The relative time separation between an earthquake direct *P* and *SH* arrivals and surface reflected phases, such as *pP*, *sP*, and *sS*, can be used to obtain accurate earthquake depths. This is particularly useful because all earthquakes produce surface reflected phases. Time separation between phases for shallow events is short, so the

onsets of the reflected phases are often obscured by the direct phase coda. Modeling of *P* and *SH* waveforms recorded at teleseismic distances (approximately 30˚ to 90˚ between station and receiver) by long-period or broadband seismographs can retrieve the individual phases and is thus a powerful procedure for determining earthquake depth.

Earthquakes are one of the most widely observable indicators of on-going lithospheric deformation and so far, in continental regions, earthquakes mainly occur within the crust and not the mantle lid [*Maggi, et al.*, 2000]. A fundamental question in geology is how the strength and deformation of the lithosphere vary spatially and temporally [e.g., *Burov and Watts*, 2006; *Jackson*, 2002; *Thatcher and Pollitz*, 2008]. Investigating the depth distribution of earthquakes within continental lithosphere is one way we can understand where and how the lithosphere is deforming. Knowing the depths over which earthquakes occurs describes the thickness where stress relaxation in continents is accommodated in some part by seismic rupture.

To address how the earthquakes fit with deformational structure, earthquake hypocentral locations can be integrated with complimentary datasets, such as topography and subsurface structural interpretations. Integration of earthquake with topography data allows investigation of the topographic expression of the seismic activity, and subsurface imaging and geological interpretations allow earthquakes to be placed into context with hypothesized subsurface structures.

This dissertation is a seismotectonic study concentrating on obtaining accurate earthquake source parameters, in particular depths, and integrating them with interpretations of crustal structure and tectonic deformational histories. This document

is organized so that each chapter builds on knowledge described in detail in the preceding chapter. Chapter 1 describes the *P* and *SH* waveform modeling procedure used to obtain accurate earthquake depths. Teleseismic waveform modeling is an accurate procedure to use when analyzing earthquake source parameters for shallow ($\lesssim$ 70 km depth) seismic events. It is used in Chapter 2 to study continental seismicity of the Central Andes. In Chapter 3 results from this and similar procedures are gathered to conduct a global synthesis of continental seismicity.

Chapter 1 focuses on how well the *P* and *SH* waveform modeling technique constrains event depth. First, the general modeling algorithm is discussed. Second, the particular inversion procedure and modeling parameters are described. Third, the topic of procedural errors and sensitivity to solution parameters is presented. Lastly, solutions from waveform modeling are tested by comparing source parameters determined an independent analysis procedure based on InSAR-determined surface displacement analysis.

Chapter 2 uses new results obtained by *P* and *SH* waveform modeling to investigate Central Andean continental earthquakes. The Central Andes displays segmentation associated with continental seismicity and corresponding deformational structures. Relationships of segmentation have been known for some time now, but not since 1983 has there been an overview study of continental seismicity of the entire Central Andes. The purpose of the chapter is to do that by gathering the most recent accurate earthquake depth determinations and integrating the events with high resolution (90 m pixel size) topography from NASA's Shuttle Radar Topography Mission (SRTM) and previously published studies that describe surface and subsurface structures (e.g., seismic imaging, balanced cross-sections). SRTM data is the highest resolution,

spatially continuous topographic dataset available today, so integration of it with accurate earthquake locations allows the best investigation of the topographic expression of the seismic activity and related deformational structures. Compiling subsurface structural interpretations and integrating it with accurate earthquake depth allow us to identify possible seismically active subsurface structures.

Lastly, Chapter 3 investigates global patterns of earthquake depth distributions. A popular model of lithospheric strength proposes an aseismic, ductile lower crust between a seismic, brittle upper crust and mantle lid. In this chapter, a global dataset from previously published sources of accurately determined continental earthquake depths (± 5 km or better) are compiled to test that model. In many continental areas, crustal seismicity is restricted to the upper crust consistent with the crustal portion of the model, but in other localities lower crustal earthquakes have been documented, contrary to the model. Chapter 3 investigates in what tectonic settings lower crustal earthquakes occur in an attempt to understand their significance to lithospheric strength and deformation. This study includes data from the around the world and proposes a new lithospheric block model of variations in continental lithospheric thickness and strength, corresponding earthquake depth distribution, and dominant earthquake deformation mechanism.

REFERENCES

Burov, E. B., and A. B. Watts (2006), The long-term strength of continental lithosphere; "jelly sandwich" or "creme brulee"?, *GSA Today*, *16* (1), 4-10.

Chen, W.-P., and P. Molnar (1983), Focal depths of intracontinental and intraplate earthquakes and their implications for the thermal and mechanical properties of the lithosphere, *J. Geophys. Res.*, *88* (B5), 4183-4214.

Jackson, J. (2002), Strength of the continental lithosphere; time to abandon the jelly sandwich?, *GSA Today*, *12* (9), 4-10.

Kagan, Y. Y. (2003), Accuracy of modern global earthquake catalogs, *Phys. Earth Planet. In.*, *135* (2-3), 173-209, doi: 10.1016/s0031-9201(02)00214-5.

Maggi, A., et al. (2000), A re-assessment of focal depth distributions in southern Iran, the Tien Shan and northern India: do earthquakes occur in the continental mantle?, *Geophys. J. Int.*, *143* (3), 629–661.

Nyblade, A. A., and C. A. Langston (1995), East African earthquakes below 20 km depth and their implications for crustal structure, *Geophys. J. Int.*, *121* (1), 49-62.

Thatcher, W., and F. F. Pollitz (2008), Temporal evolution of continental lithospheric strength in actively deforming regions, *GSA Today*, *18* (4), 4-11, doi: 10.1130/GSAT01804-5A.1.

CHAPTER 1

P AND *SH* EARTHQUAKE WAVEFORM MODELING

This section describes the teleseismic waveform modeling procedure used to constrain earthquake source parameters, such as magnitude, focal mechanism orientation, and depth. Teleseismic waveform modeling is important throughout this dissertation, so this chapter is a thorough discussion of the procedure. The procedure is utilized throughout Chapter 2 to study continental seismicity of the Central Andes and in Chapter 3 results from this and similar procedures are gathered to conduct a global synthesis of continental seismicity. The focus of this dissertation is specifically concerned with the depth distribution of continental earthquakes, so this section mainly highlights how well the *P* and *SH* waveform modeling technique constrains event depth. First, the general modeling algorithm is discussed. Next, the particular inversion procedure and modeling parameters are described. Finally, the topic of procedural errors and sensitivity to solution parameters is presented. A solution verification test is conducted by comparing source parameters determined via waveform modeling to those determined by an independent analysis procedure based on InSAR-determined surface displacement analysis.

Modeling algorithm

Depths of earthquakes are particularly difficult to constrain, especially when the events are shallow (< 70 km) as they are in the continental crust [*Butler, et al.*, 2004]. Local network studies provide the most reliable depths, but the global coverage of local networks is sparse and deployment at any one location is sporadic when compared to the almost 50 years of recording by the combined operation of the World-

Wide Standardized Seismograph Network (WWSSN), Global Digital Seismographic Network (GDSN), and other continuously operated seismograph stations. Therefore, earthquake hypocenter determination in most places around the world is done using the globally distributed network of seismograph stations.

A number of global earthquake bulletins and catalogs exist that routinely report earthquake depths. However, technique limitations affecting parameter determination or the lack of teleseismic surface-reflected phase identification decreases these compilations' ability to resolve the differences in focal depth distribution within the continental crust that are important for tectonic interpretations [*Kagan*, 2003; *Maggi, et al.*, 2002]. Therefore, additional analyses are needed to constrain depths for continental earthquakes.

The relative time separation between direct *P* and *SH* arrivals and surface reflected phases, such as *pP*, *sP*, and *sS*, can be used to obtain accurate source depths. This is particularly useful because all earthquakes produce surface reflected phases. Time separation between phases for shallow events is short, so the onsets of the reflected phases are often obscured by the direct phase coda. Modeling of *P* and *SH* waveforms recorded at teleseismic distances (approximately 30˚ to 90˚ between station and receiver) by long-period or broadband seismographs can retrieve the individual phases and is thus a powerful procedure for determining earthquake depth. Because wave propagation through the Earth is assumed to be simple [*Helmberger*, 1974; *Langston and Helmberger*, 1975], the analysis is a standard technique in earthquake source studies. For earthquakes with Mw $\gtrsim$ 5.5 recorded by long-period or broadband seismographs, *P* and *SH* wave arrivals can be modeled by including the effects of focal mechanism orientation and moment release time function on the direct and

surface-reflected phases propagating without scattering or diffraction through a spherically symmetric earth model. The basic ideas behind the modeling algorithm are shown in Figure 1.1, which follows after Nabelek [1984]. First, source properties such as focal mechanism orientation and take-off angle (determined by the ray parameter) influence the relative amplitudes of the phases, while the depth of the earthquake determines the relative arrival times of the phases. The moment of the event sets the absolute phase amplitudes. Second, the effects of the velocity structure and attenuation response of the earth are convolved with the effects of the source properties to determine the incoming waveform properties at the receiving seismograph. Third, the estimated incoming waveform is convolved with the impulse response of the recording seismograph to produce a synthetic seismogram. Lastly, the synthetic seismogram is compared with the observed seismogram and the input parameters are iteratively changed until the synthetic seismogram reasonably matches the observed seismogram. Such analyses typically yield uncertainties of strike ± 10°, dip ± 5°, rake ± 10°, and depth ± 5 km [e.g., *Mitra, et al.*, 2005; *Stein and Kroeger*, 1980]. Synthetic waveforms are generated and compared to observed waveforms recorded at stations located at various azimuths from the event in order to best characterize focal mechanism orientation. Waveform comparisons are made visually or by a method of minimization of the difference between the observed and synthetic waveforms (this will be discussed in more detail later). To avoid upper mantle triplications and interference from core phases, *P* waveforms are used in the distance range between 30° to 90° and *SH* waves in the range from 30° to 75°.

In addition to *P* and *SH* waveform modeling, phase identification (*pP* and *sP*) on short-period records also produces accurate focal depths with uncertainties of around ± 5 km, if the phases are apparent by visual examination of the short-period

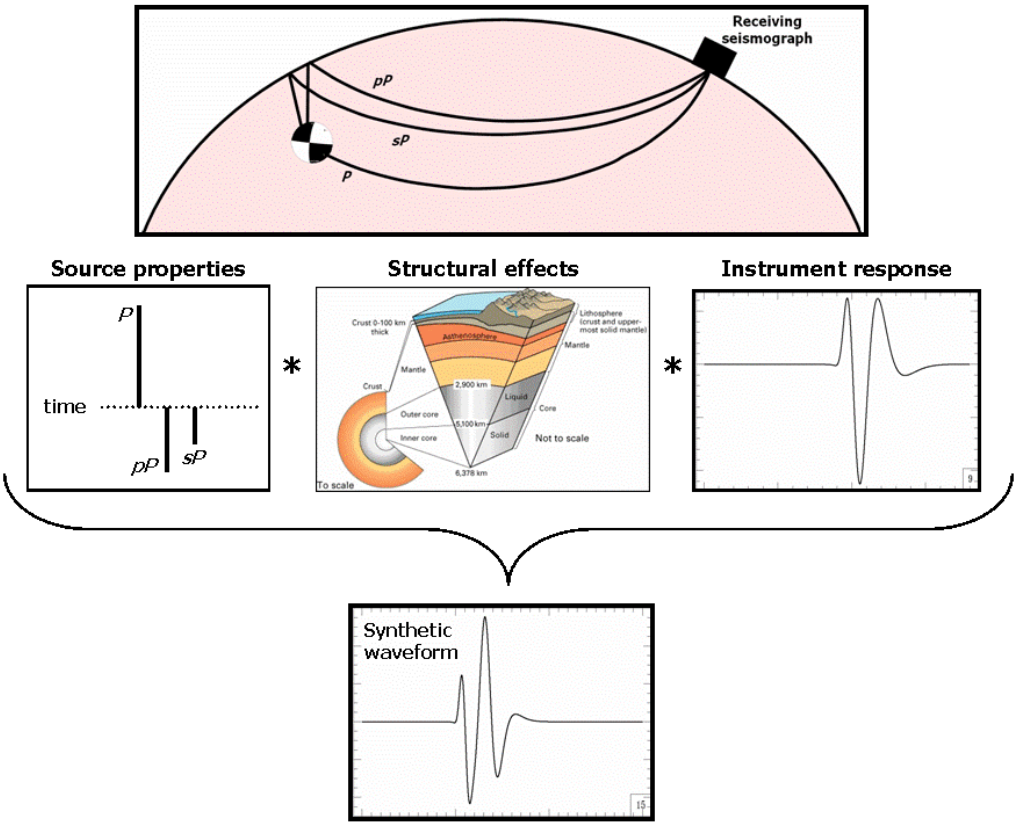

Figure 1.1: Synthetic seismogram algorithm. Schematic showing the basic input parameters of synthetic seismogram generation. The asterisk (*) represents the convolution operator.

seismograms. While surface reflected phase identification can be difficult without waveform modeling on broadband or long-period records, higher frequency short-period waveforms can sometimes reveal differential traveltimes of *pP-P* and *sP-P*, thereby allowing a depth estimate to be made. Waveform modeling provides a more complete determination of earthquake source parameters than short-period phase identification. However, where short-period and long-period records are both available, combining these two methods can provide additional robustness to depth determination. In cases of smaller magnitude events, where most of the teleseismic long-period signals are too small for modeling short-period depth phase identification may provide the only depth estimate available.

Inversion procedure and model parameters

Implementation of *P* and *SH* waveform modeling and the inversion analysis involves four basic steps – event identification, data acquisition, data preparation, and waveform analysis. This section describes how I accomplished each step.

Event identification is conducted by searching the Global Centroid Moment Tensor (CMT) Catalog (http://www.globalcmt.org/). The catalog reports estimates of earthquake source parameters for events of Mw $\gtrsim$ 5 for earthquakes that have occurred since 1976. The CMT catalog is the most complete and accurate catalog that routinely reports focal mechanism solutions [*Kagan*, 2003] and is used to identify events within the geographical area of interest. A starting focal mechanism solution needed to seed the waveform analysis is provided by the CMT catalog. Event data reported by other catalogs and bulletins is also compiled in order to gather all available source parameter estimates for each event. In particular, epicentral locations reported by the International Seismological Center (ISC) are used to plot earthquake

epicentral locations. The ISC bulletin and the CMT catalog report event locations determined from different analysis methods and therefore report different types of locations. CMT solutions are based on analysis of low-pass filtered data that is unable to resolve the depths of crustal earthquakes. The solutions give an estimate of the centroid, or average, location in time and space of the seismic energy release. ISC locations, determined from arrival times of mainly short-period body wave phases, estimate the point where the rupture began. Teleseismic waveform inversion is also based on body wave phase arrivals, so the ISC locations are more appropriate to use in conjunction with that procedure. Also, focal mechanism solutions reported by the US Geological Survey's National Earthquake Information Center (NEIC) are compiled. If either data quality or quantity is poor or if the CMT seed mechanism is too far from the correct solution, the inversion analysis may not converge to an accurate solution. As an alternative to the CMT solution, the NEIC focal mechanism solution is used as the seed mechanism and tested against the solution from the CMT seed. Whichever starting focal mechanism results in a more accurate inversion solution, that mechanism is used in the waveform analysis.

Data acquisition is done via the Incorporated Research Institutions for Seismology (IRIS) (http://www.iris.edu/) data distribution methods. Specifically, I requested data by email through the BreqFast request method (http://www.iris.edu/manuals/breq_fast.htm) or, if event data has been previously compiled by IRIS, a web request using the Wilbur II system (http://www.iris.edu/cgi-bin/wilberII_page1.pl). Data was downloaded in SEED (Standard for the Exchange of Earthquake Data) file format (http://www.iris.edu/manuals/SEED_chpt1.htm), an international standard format for digital seismological data.

Preparation of data for modeling was performed using Unix shell scripts, the TTIMES program [*Kennett, et al.*, 1995; *Montagner*, 1996], and the Seismic Analysis Code (SAC) program [*Goldstein and Snoke*, 2005]. The scripts were originally written by Alessia Maggi (alessia@sismo.u-strasbg.fr) and later modified by Brian Emmerson (emmerson@esc.cam.ac.uk) and myself. The script files are executed in the order they are discussed here. The run_rdseed.sh program unpacks the SEED data file and sorts the waveform and instrument response files into different folders. The waveform data is extracted in SAC file format. SEED_prep1.sh renames the waveform files and checks for duplicate station files. SEED_prep2.sh enters event parameters (date, origin time, and location) into the waveform header information by calling the SAC program. The script then uses the TTIMES program to obtain estimates of phase arrival times and inputs the information into the waveform header information. The MT5_prep.sh script file preprocesses the SAC waveform files so they can be reduced to a file format appropriate for the MT5 inversion program. MT5_prep.sh performs a deconvolution-convolution process on the waveforms. GDSN broadband waveforms contain high frequencies too difficult to model using this waveform modeling technique and their long-period data do not contain enough high frequencies. The deconvolution-convolution procedure takes the frequency responses of broadband data and removes some high frequency content, but leaves enough to enable earthquake property determination. Specifically, the MT5_prep.sh script deconvolves the GDSN station responses from the waveforms and the responses of the old WWSSN 15 to 100 s long-period instruments were reconvolved with the data. The WWSSN stations had a bandwidth well suited for the resolution of shallow, moderated-sized events [e.g., *McCaffrey and Nabelek*, 1987]. MT5_prep.sh then creates waveforms files that contain windowed *P* and *SH* waveform packages which include the integrated arrivals of the direct and surface reflected phases. The windowed waveforms are visually

reviewed using SAC plotting functions and waveforms containing the clearest direct phase arrivals are selected. The selected waveform files are converted from SAC file format to DSN, a format accepted by the MT5 inversion program, using the sac2mt5 program written by Maggi.

Waveform modeling and analysis is performed by the MT5 program [*Zwick, et al.*, 1994], a PC-based computer program that inverts teleseismic *P* and *SH* waveforms to obtain the best-fit earthquake strike, dip, rake, seismic moment, depth, and source time function. Predecessor programs to MT5 were the SYN3 and SYN4 programs [*McCaffrey and Abers*, 1988; *McCaffrey, et al.*, 1991] and inversion algorithms are similar between the programs. The MT5 version is available as a free download via the internet (http://ees2.geo.rpi.edu/rob/mt5/). As stated earlier, a starting solution is needed to seed the inversion program and the Global CMT focal mechanism solution and depth are most often used for that purpose. MT5 then iteratively modifies the seed solution to optimize synthetic-to-observed waveform fit. I always constrained the source to be a double couple, meaning the motions are modeled as resulting from two force couples that produce no net moment about an assumed point source. To find the simplest event solution that best fits the data, I limited the source time function (STF) to a prescribed single isosceles triangle. The STF of an earthquake describes seismic slip, or slip velocity, through time. So, the assumption of an isosceles triangle means slip velocity increased linearly to a maximum and slip slowed down (decreased velocity) at the same rate thereafter. The size of the triangle for each event is determined by a preliminary inversion in which the MT5 program is allowed to solve for the best fitting STF. The best-fit STF is then approximated using a single isosceles triangle of similar duration and the inversion was run again to solve for the best-fit solution using the simplified STF. This process is illustrated in Figure 1.2, where the

preliminary inversion and complicated STF solution are shown in (a) and the final solution with a simplified STF is shown in (b). When data of a limited azimuthal range is all that is available or when only data of poor quality is available, the seed focal mechanism orientation is held fixed to allow the inversion to solve only for depth. Events of about Mw5.5 to 5.0 are sometimes too small for analysis by teleseismic waveform modeling, because they produce such small waveform amplitudes. Low amplitude phases arrivals can also occur from strike-slip events due to the vertical null axis position. For a few events where direct phase arrival amplitudes were small but seismic energy packages were identifiable, a depth estimate from phase identification on short-period records was used to lock the depth parameter during waveform inversion and the quality of the waveform fit was assessed. MT5 corrects for wave amplitude decay through time from geometrical spreading and from anelastic attenuation using a Futterman Q operator with a value t^* of 1.0 s for P and 4.0 s for SH waves. A simple half-space source structure was used with velocities V_P = 6.5 km/s, V_S = 3.7 km/s and density ρ = 2800 kg/m^3. As stated above, P waveforms are used in the distance range between 30° and 90° and SH waves in the range from 30° to 75°. A sample inversion solution is shown in Figure 1.3.

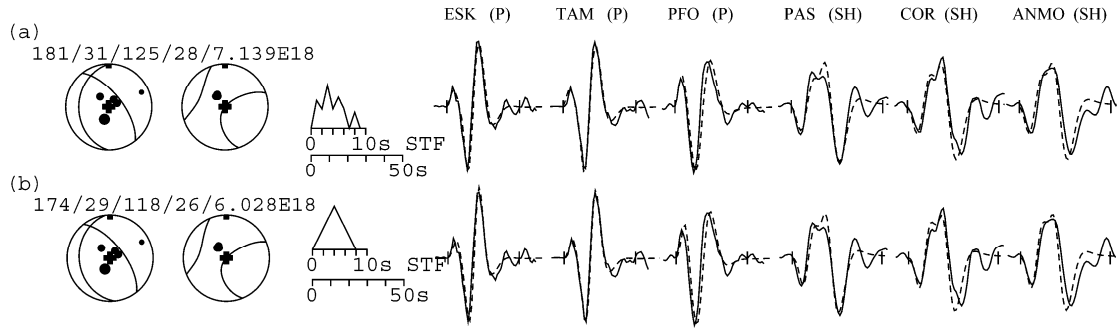

Figure 1.2: Sample source time function determination. Each row shows a different waveform inversion solution. *P* and *SH* focal spheres are shown in the first column. Strike, dip, rake, depth (km), and seismic moment (N-m) are labeled above the focal spheres. The source time function is shown above the waveform timescale in the second column followed by the observed and synthetic waveforms in the subsequent columns. Timescales are in seconds (s). The solid lines are the observed waveforms and the dashed lines are the synthetic waveforms. Station codes and phase type (shown in parentheses) are located above the waveforms. The inversion window is marked by the solid bars at either end of the waveforms. P and T axes within the spheres are represented by the small and large points, respectively, while stations used for the inversion are the middle-sized points. (a) is the preliminary MT5 inversion solution where the STF was allowed to vary. (b) shows the inversion solution using the simplified STF.

Inversion error and sensitivity analysis

The teleseismic waveform inversion has four main sources of error: velocity structure, synthetic-to-observed waveform fit, focal mechanism, and trade off between depth and source time function. Typical solution uncertainties are strike ± 10°, dip ± 5°, rake ± 10°, and depth ± 5 km [e.g., *Mitra, et al.*, 2005; *Stein and Kroeger*, 1980].

The velocity model used in this study is an average of models used in previous earthquake location and seismic imaging studies [e.g., *Alvarado, et al.*, 2005; *Chinn and Isacks*, 1983]. Chinn [1982] found that if model velocities are within ± 10% of the true bulk crustal velocity, then errors in depth are similarly ± 10%. In this case, for events at 20 and 40 km depth, the errors due to the velocity model is ± 2 km and ± 4 km or less, respectively. This means for V_P = 6.5 km/s, as is the case in the analyses reported in Chapter 2, the true bulk crustal velocity needs to be within ± 0.6 km/s (between 5.9 and 7.1 km/s) for depth errors to be on the order of ± 10%. Throughout the Andean margin, bulk crustal velocities used in local network seismic studies [e.g., *James and Snoke*, 1994; *Smalley and Isacks*, 1990] and other waveform modeling analysis studies [e.g., *Alvarado, et al.*, 2005; *Chinn and Isacks*, 1983] fall within the ± 0.6 km/s range. Similarly, previous studies are also consistent with bulk crustal *S*-wave velocities falling between 3.4 to 4.0 km/s, or V_S = 3.7 ± 0.3 km/s.

Waveform fit errors arise from such things as converting physical ground movement to digital representations, inaccurate picks of direct phase arrival times, and digital processing shifts. MT5 minimizes weighted squares of residuals between the relative amplitudes of the synthetic and observed seismograms summed over all the stations to obtain the best-fit solution. It adjusts the event source time function element, seismic

Figure 1.3: Sample waveform inversion solution plot from MT5 program. The header contains the date of the seismic event on the first line and the results of the inversion (strike, dip, rake, depth in km, and seismic moment in N-m) on the second. The letter 'f' is placed in front of the strike or depth solution parameter when the focal mechanism or depth, respectively, has been held fixed. The upper sphere shows the *P*-wave radiation pattern and the lower sphere that for *SH*. Both are lower hemisphere projections. The station code by each waveform is accompanied by a letter corresponding to its position in the focal sphere. These are ordered clockwise by azimuth. The solid lines are the observed waveforms and the dashed lines are the synthetic waveforms. The inversion window is marked by the solid bars at either end of the waveforms. P and T axes within the sphere are represented by solid and open circles, respectively. The source time function (STF) is shown below the *P* focal sphere, with the waveform timescale below it. Timescales are in seconds (s).

1991/04/04
157/24/90/29/2.414E19

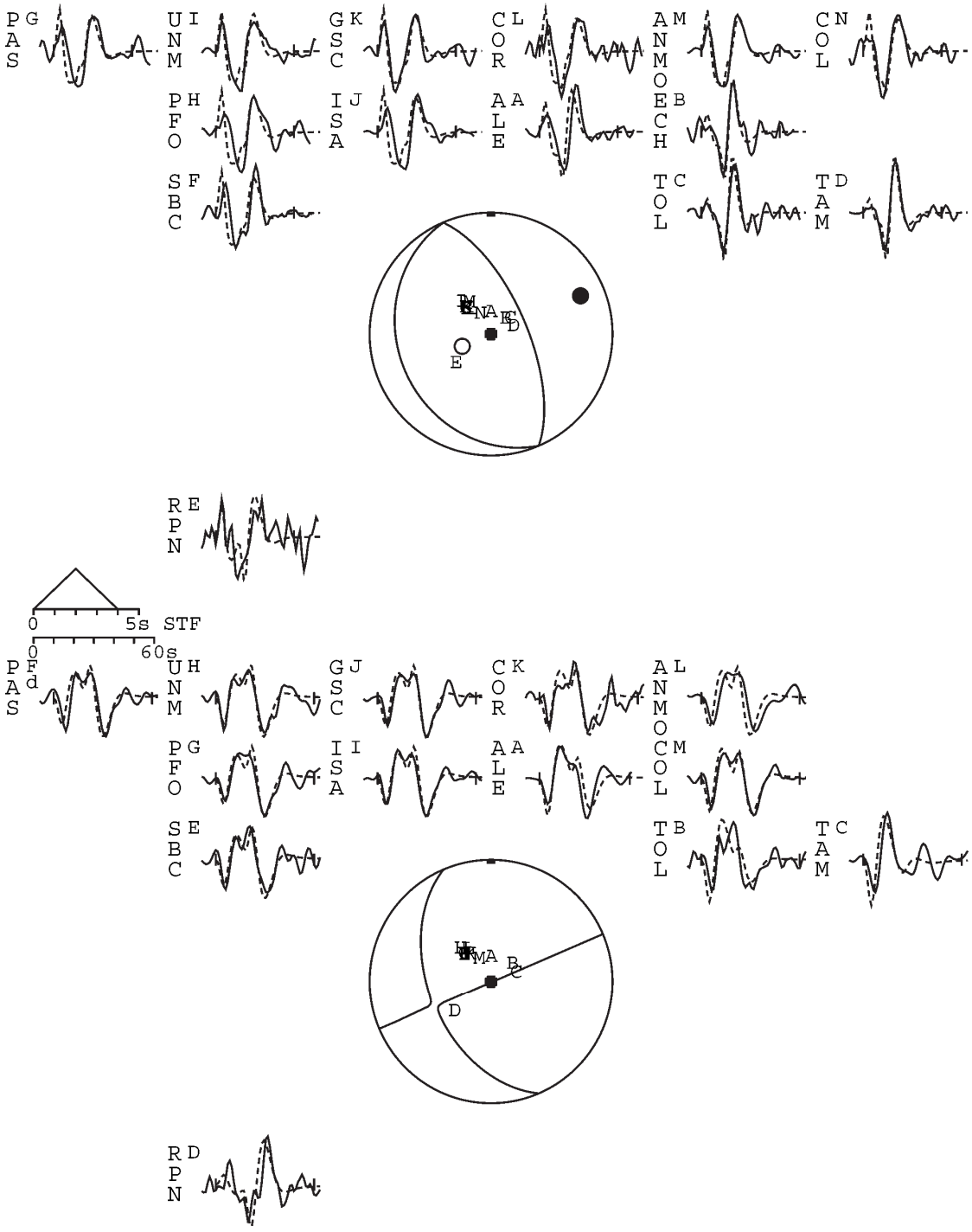

moment, focal mechanism orientation, and depth to minimize the misfit, although for certain events, as mentioned above, a few parameters were held fixed during inversion. For the same event inversion shown in Figure 1.3, Figure 1.4 is a plot of earthquake depth versus R/D% (a misfit parameter output by MT5 given by the ratio of the residual to data variance of all the modeled phases). The plot shows the inversion program's sensitivity to source depth and is an example of how the MT5 program employs error analysis and parameter constraint.

However, residual statistics of teleseismic waveform inversions have been shown to underestimate the true uncertainties associated with source parameters [*McCaffrey and Nabelek*, 1987]. Therefore, to appreciate waveform fit errors and their influence on source parameter uncertainty, visual sensitivity analysis is employed to validate waveform fit and to determine within what parameter window the synthetics fit the observed waveforms [e.g., *Emmerson, et al.*, 2006; *Maggi, et al.*, 2000; *McCaffrey and Nabelek*, 1987; *Molnar and Lyon-Caen*, 1989]. Figure 1.5 shows a sample sensitivity analysis for the same event featured in Figures 1.3 and 1.4. A sensitivity analysis plot accompanies each event waveform inversion solution plot (e.g., Figure 1.3). Sensitivity analysis plots illustrate the window of solution parameters, in particular the range of depths, which fit the observed waveforms. Figure 1.5 shows five of twenty-seven waveforms used in the inversion and five different event parameters to compare how the different parameters effect how synthetics match the observed waveforms. Line (a) is the best-fit inversion solution and lines (b) and (c) illustrate the depth range over which the synthetic waveforms match the data. For this particular event, the waveform fit is consistent for a depth range of ± 3 km, which is illustrated by the good, but

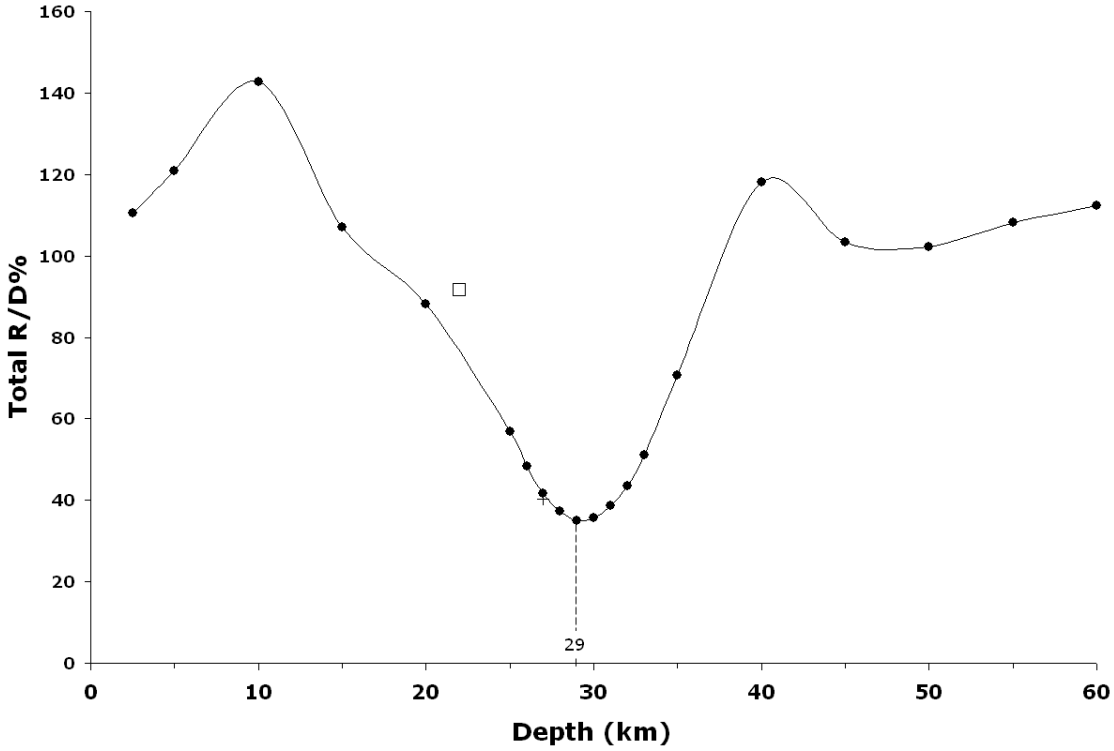

Figure 1.4: R/D% vs. depth plot for the inversion example shown in Figure 1.3. Each data point represents an inversion where the depth and source time function were held fixed. Filled circles (•) are inversions where focal mechanism orientation was permitted to vary The square (□) and cross (+) data points represent forward modeling solutions of *P* and *SH* waveforms where the focal mechanism and depth solutions were held fixed for the NEIC and CMT reported solutions, respectively.

Figure 1.5: Sample sensitivity analysis for the event shown in Figures 1.3 and 1.4. Each row shows a different waveform inversion solution. The title line shows the event date (yyyy/mm/dd), ISC reported origin time (hh:mm:ss.ss), ISC reported location (latitude, longitude), and CMT reported magnitude. When ISC origin time and location are unavailable, the CMT time and location are listed. *P* and *SH* focal spheres are shown in the first column. Strike, dip, rake, depth (km), and seismic moment (N-m) are labeled above the focal spheres. The source time function is shown above the waveform timescale in the second column followed by the observed and synthetic waveforms in the subsequent columns. Timescales are in seconds (s). Waveform display convention is the same as that in the waveform inversion solution plots (e.g., Figure 1.3) and here the station code and phase type (shown in parentheses) are located above the waveforms. (a) is the MT5 minimum misfit solution. (b) shows the shallow depth bound of the waveform inversion and (c) shows the deeper bound, such that the synthetic data fit the observe fairly well between 23 and 32 km depth and deteriorate thereafter, so according to waveform fit this event occurred at a depth of 29±3km. (d) shows how well the CMT solution (focal mechanism, depth, and moment) fit the observed data and (e) shows that for the NEIC solution (focal mechanism, depth, and moment). In contrast to lines (a), (b), and (c), (d) and (e) test how well catalog solutions fit the data and verify that deviations from catalog solutions are necessary to fit the waveforms.

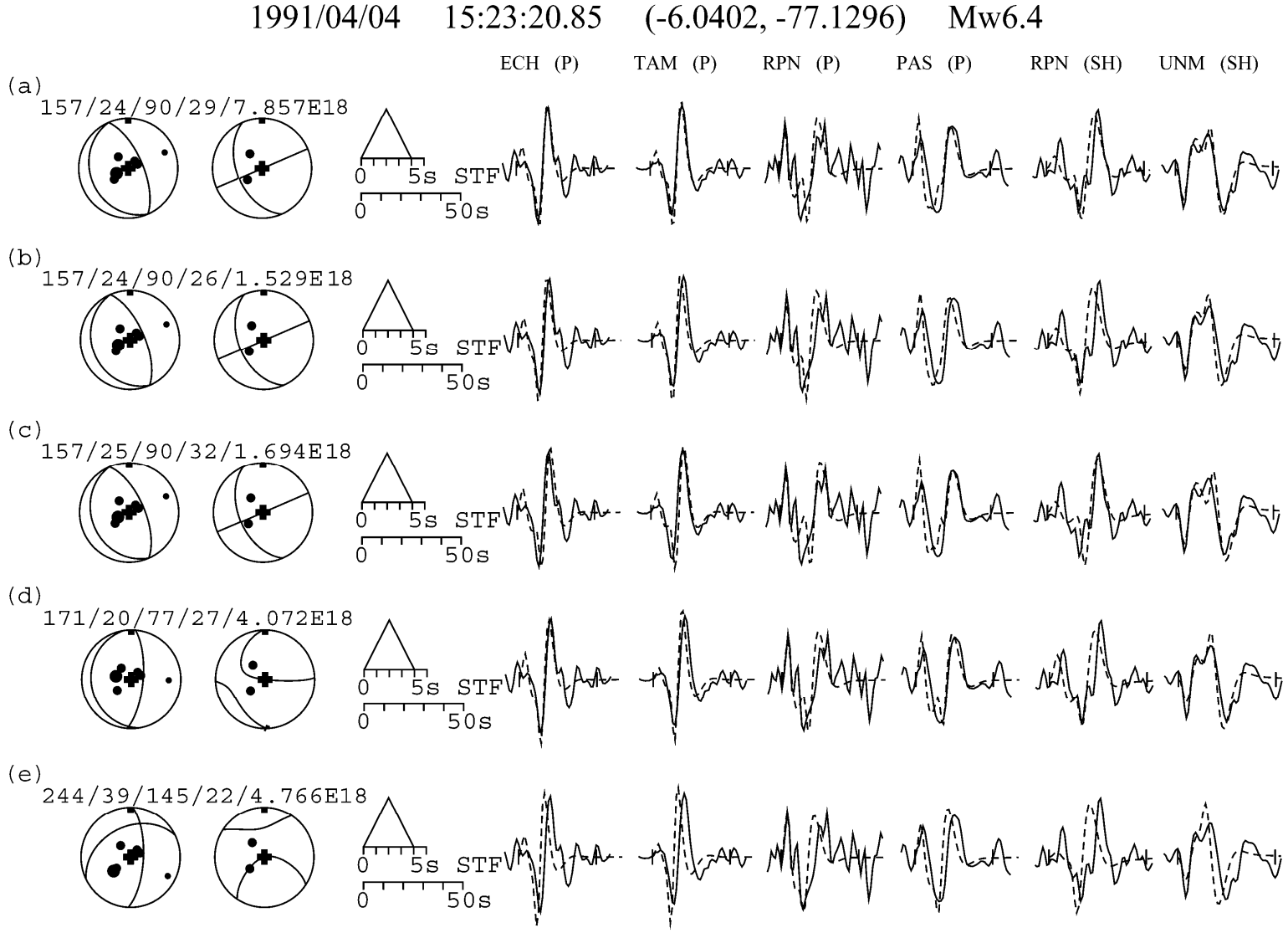
1991/04/04 15:23:20.85 (-6.0402, -77.1296) Mw6.4
ECH (P)
TAM (P)
RPN (P)
PAS (P)
RPN (SH)
UNM (SH)
(a)
157/24/90/29/7.857E18
(b)
157/24/90/26/1.529E18
(c)
157/25/90/32/1.694E18
(d)
171/20/77/27/4.072E18
(e)
244/39/145/22/4.766E18
0 5s STF
0 50s

deteriorating, synthetic-to-observed waveform fit of the solution for 26 km depth (b) and for 32 km depth (c). Such waveform errors are typical for teleseismic waveform modeling. Also shown in Figure 1.5 is how well the Global CMT (d) and the NEIC (e) focal mechanism solutions fit the observed waveforms.

Estimated focal mechanism orientation is known prior to inversion through the Global CMT catalog or the NEIC, and then MT5 inverts using iteration for its own focal mechanism solution that best fits the *P* and *SH* waveform data. Typically, CMT focal mechanism orientation errors vary from 5 to 20° depending on the quality of the solution [*Kagan*, 2003]. My inversion analyses found that often MT5 finds a solution that deviates from the seed mechanism by less than ± 10° and never did the MT5 solution change mechanism type from that of the CMT solution, e.g., from a thrust to a normal or strike-slip mechanism. However, in a few cases (Figure 1.6) the MT5 focal mechanism solution did deviate from the CMT solution by as much as 27°, as defined by the change in null axis orientation. Ambiguities in nodal plane position negligibly affect the depth if the relative amplitudes of phase arrivals remain relatively constant within orientation uncertainty. Figure 1.6 shows two contrasting cases to illustrate this point. For both event inversions, MT5 determined a greater than 20° shift in focal mechanism orientation. For the 1991/04/04 thrust event, the shift in focal mechanism orientation occurred mainly by rotating the mechanism about the near-vertical T axis, while depth and seismic moment remained equal. This shift did not result in significant changes in relative phase amplitudes because earthquake *P* and *SH* radiation patterns are symmetrical around the P and T axes. When all observed waveforms surround the T axis, like for event 1991/04/04, pivoting the focal mechanism about T does little to improve, or change, waveform fit. Therefore, the event mechanism has at least a 27° error window as modeled by teleseismic waveform

inversion. It is then most likely that the CMT focal mechanism is the best-fit focal sphere solution, because that mechanism fits the 15 to 100 s body waves of the teleseismic waveforms modeling, as well as, the CMT analyses of > 40 s body waves and > 135 s mantle waves. For the 2002/07/02 oblique slip event, rotating the focal sphere by 21° has a more significant effect on relative phase amplitudes, because stations are not clustered about the P or T axes. Since the focal sphere orientation does not rotate about a principal axis, amplitudes vary for any given station when the mechanism is rotated from the 2002/07/02 CMT solution orientation to that of MT5. Amplitude matching of synthetic and observed waveforms recorded at stations SJG, JCT, LBNH, and VNDA are noticeably improved by the MT5 focal mechanism determination given a fixed depth and seismic moment. Therefore, for the 2002/07/02 event, the MT5 focal mechanism solution better fits the observed waveform data and the 21° shift in the focal sphere orientation is necessary to best fit the synthetic waveforms to the observed.

On certain waveforms, the depth and source time function parameters can be coupled [*Christensen and Ruff*, 1985], which adds uncertainty to solution determination. An extreme example is when a waveform can be equally modeled using a relatively deep depth and short source function, or a relatively shallow depth and long source function. If observed waveforms recorded at stations varying in distance and azimuth are used for modeling, then the coupling effect will not occur on some seismograms and this effect will not add uncertainty to the solution. Therefore, recording stations used for modeling were chosen to optimize the range of distances and azimuths of observed data (e.g., Figure 1.3). Also, as mentioned above, a preliminary inversion is run for each event which allows the MT5 program to solve for the best-fit STF. Finding the best-fit STF and

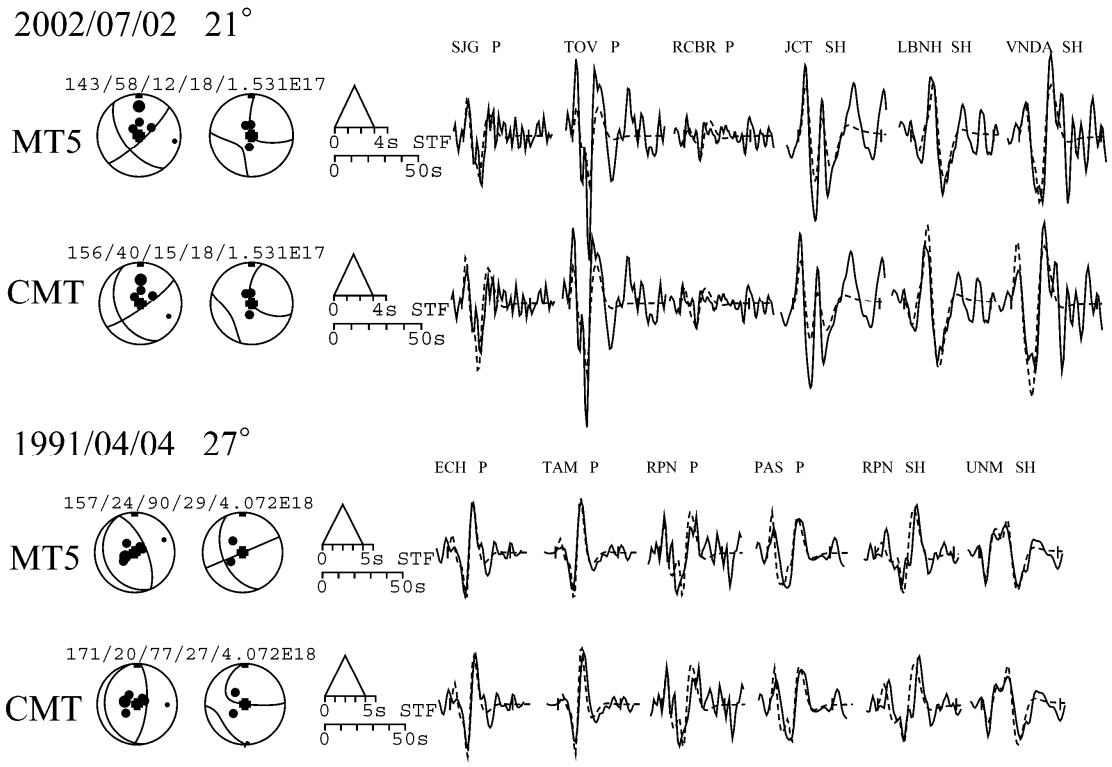

Figure 1.6: Example of MT5 best-fit solution focal mechanism orientation to that reported by the Global CMT catalog. Degree deviation between the mechanisms is reported next to the event date and is defined by the change in null axis orientation between the mechanisms. Plot convention is similar to that described in Figure 1.5.

optimizing azimuthal distribution of recording stations minimizes the effects of coupling between depth and STF. In practice, however, there remain some events where only a few observed seismograms were available for matching and azimuthal distribution of recording stations is poor. In these cases, I rely on the MT5 best-fit STF solution to minimize the depth-source time function coupling effect.

Since a simple half-space source structure was used, only the strongest initial phase arrivals (*P*, *pP*, *sP*, *S*, *sS*) are modeled. This is valid for the first ~ 25 sec of the seismogram. Possible later arrivals sometimes due to the structural effect of a surface water layer or the effect of crustal layering and conversions are not modeled in analyses of continental earthquakes (e.g., Chapter 2). After surface reflected phases, the next most significant effect is that of a surface water layer [*Stein and Kroeger*, 1980]. These effects are greatest in oceanic regions, so, since the Central Andean study (Chapter 2) is restricted to a continental region, a substantial surface water layer is not present and therefore its effects do not need to be modeled. Waveforms of subduction zone earthquakes are modeled and are used for procedural verification later in the next section of this chapter. When subduction zone sources have off-shore epicenters, a surface water layer is modeled during the waveform inversion. Crustal layering and conversions adds complexity to waveform after about 25 sec, but amplitudes are low and do not significantly interfere with direct and surface reflected phase arrivals. Not including these arrivals will inevitably leave some part of the coda unmatched, but modeling of the *P*, *pP*, *sP*, *S*, and *sS* arrivals routinely gives adequate results for depth estimation [*Helmberger and Burdick*, 1979]. Therefore, neglecting the effects of crustal layering should not greatly affect earthquake source depth estimates.

Comparing seismic waveform modeling solutions with InSAR analysis solutions

This section compares earthquake source parameters of six earthquakes determined by two independent data analysis methods – *P* and *SH* body waveform modeling and InSAR surface displacement analysis. This comparison illustrates that earthquake source parameters determined using teleseismic waveform inversion are comparable to those determined using an independent analysis method (i.e., InSAR).

Interferometric synthetic aperture radar (InSAR) is a radar technique that can be used to generate maps of surface deformation from the use of two or more synthetic aperture radar (SAR) images (e.g., Burgmann et al., 2000; Rosen et al., 2000). The technique can potentially measure millimeter-scale surface displacements over time spans of days to years. Here, InSAR analyses of earthquake surface displacements are used to constrain seismic event source parameters, which are then compared with teleseismic waveform modeling parameter solutions for the same seismic events. Six earthquakes located along the Chile subduction zone between 25°S and 30°S are analyzed using these two techniques. For each subduction zone earthquake, Table 1.1 lists earthquake solution parameters reported by the Global CMT catalog (labeled CMT), results from InSAR analysis (labeled Pritchard et al., 2006 and InSAR), and results from *P* and *SH* waveform inversion (labeled MT5). Figure 1.7 shows the MT5 solutions for the six earthquakes in map view.

Table 1.1 Chile subduction zone earthquakes studied using seismic waveform modeling and InSAR

	method	longitude (deg)	latitude (deg)	depth (km)	Mw	strike (deg)	dip (deg)	rake (deg)	length (km)	width (km)	Figures
1993/07/11 Mw 6.8	CMT	-70.56	-25.31	49.0	6.6	356	21	95	n/a	n/a	-
	Pritchard et al., 2006	-70.05	-25.23	53.0	6.8	5	30	104	28.0	35.0	1.8, 1.9
	MT5 (this study)	-70.05	-25.23	48	6.5	174	61	78	n/a	n/a	1.7, 1.10
1995 events near La Serena, Chile	CMT 1995/11/01	-71.68	-29.11	22.0	6.6	6	25	111	n/a	n/a	-
	InSAR (this study) 1995/11/01	-71.45	-28.92	27.0	6.6	1	13	112	24.0	11.0	1.12, 1.13
	MT5 (this study) 1995/11/01	-71.37	-28.88	28	6.6	22	32	28	n/a	n/a	1.7, 1.14
	MT5 (this study) 1995/10/31	-71.34	-28.98	24	5.5	55	29	149	n/a	n/a	1.7, 1.15
1996/04/19 Mw 6.7	CMT	-70.58	-23.95	50.0	6.6	11	19	109	n/a	n/a	-
	Pritchard et al., 2006	-70.09	-23.94	47.8	6.7	5	23	107	32.0	21.0	1.8, 1.9
	MT5 (this study)	-70.02	-23.96	46	6.4	13	23	111	n/a	n/a	1.7, 1.11
2006/04/30 seismic swarm on subduction zone near Copiapo, Chile	CMT 21:41:07	-71.55	-27.28	13.4	6.5	14	18	112	n/a	n/a	-
	CMT 19:17:25	-71.52	-27.17	15.4	6.6	11	14	106	n/a	n/a	-
	InSAR (this study)	-71.63	-26.90	39.4	7.6	211	39	128	18.9	24.8	1.16, 1.17
	MT5 (this study) 19:17:25	-71.23	-27.09	22	6.5	39	22	122	n/a	n/a	1.17, 1.18
	MT5 (this study) 21:41:07	-71.01	-27.23	22	6.4	15	20	104	n/a	n/a	1.7, 1.19

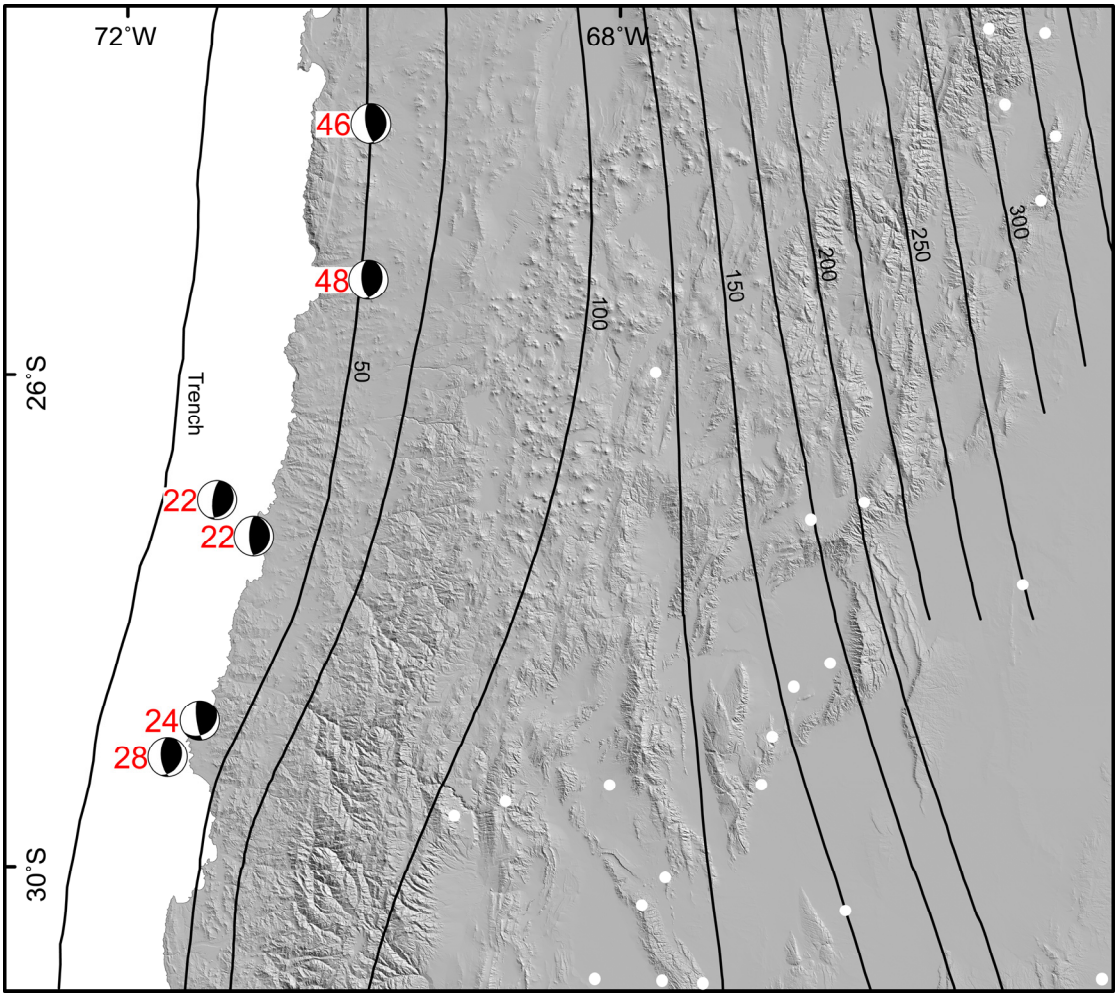

Figure 1.7: Earthquakes along the Chile subduction zone. Earthquake focal mechanism solutions are represented in lower hemispheric projections, where dark quadrants contain compressional motions. Events depths, determined by teleseismic waveform modeling (MT5), are labeled in red. Contours lines represent the depth (labeled in km) below sea-level of the subducting Nazca Oceanic plate. White points are earthquakes located in the continental crust of the South American plate.

InSAR Methodology

InSAR analysis was performed by Matthew Pritchard. Data is from the ERS-1, ERS-2 and Envisat satellites of the European Space Agency (with a C-band radar, ~ 5.6 cm wavelength). Different numbers of interferograms are available for each earthquake (see event discussions below for details). As found in previous studies of the central Andes [e.g., *Pritchard and Simons*, 2004], the quality of the interferograms along the Chilean Central Andes is excellent because of the generally arid climate. The InSAR data span different time intervals, and most includes several weeks to months of potential pre-seismic and post-seismic deformation.

The ROI_PAC software was used for InSAR processing [*Rosen, et al.*, 2004]. The number of data points in the interferograms was reduced from millions to thousands by subsampling a spatially compressed interferogram (~ 1 km/pixel) with a density of points determined by a data resolution matrix [*Lohman and Simons*, 2005]. Interferograms were power-spectrum filtered [*Goldstein and Werner*, 1998] and unwrapped using the conventional ROI_PAC software [*Goldstein, et al.*, 1988]. Unwrapping was done at different pixel resolutions, about 180 m/pixel for the Mw < 6 earthquakes and between 360 and 1440 m/pixel for the larger earthquakes. Digital elevation models from the Shuttle Radar Topography Mission with about 90 m pixel spacing are used to remove the topographic signature from the InSAR phase [*Farr and Kobrick*, 2000]. Noisy areas were masked out using a phase variance threshold and additional unwrapping errors were manually removed before modeling. Variations in the incidence angle across the radar scene are accounted for when calculating the InSAR forward models.

For the new models presented here, deformation modeling was done using finite fault dislocations in an elastic half-space [*Okada*, 1985]. Prior work is summarized from Pritchard et al. [2006], where deformation is modeled as a single or multiple point sources in either a layered- or homogeneous half-space. In comparison, *P* and *SH* waveform modeling analysis published in this dissertation assumes a homogeneous half-space. Inversion is done with the full covariance matrix using the method of Lohman and Simons [2005] which assumes the interferogram noise is isotropic and stationary (i.e., does not vary with space) and the Neighborhood Algorithm [*Sambridge*, 1998] to explore model parameter space.

The modeling solves for the absolute value (DC) and spatial variations in the InSAR phase (a.k.a. ramps). InSAR measurements are relative and not absolute, so that is why the DC term must be estimated. The ramp parameters are estimated to correct for errors in the satellite orbital parameters and long-wavelength deformation patterns (e.g., inter-seismic deformation from the subduction zone earthquake cycle). For most of the small earthquakes, linear ramps are used, but quadratic ramps were used for the earthquakes that we include here from Pritchard et al. [2006].
InSAR depths reported in Table 1.1 are the depth to the center of the fault slip surface and the subduction zone earthquakes' low angle, east-dipping nodal plane (the plane most consistent with the subduction zone plate interface) was assumed to be the fault plane.

Subduction zone earthquake source comparisons

1993/07/11 and 1996/04/19 events – These events were analyzed by Pritchard et al. [2006] who both jointly and separately inverted body wave and InSAR data to determine source parameters. Their results are shown in Figure 1.8 and 1.9. The MT5

teleseismic waveform analysis of the 1993/07/11 event is shown in Figure 1.10 and the solution for the 1996/04/19 event in Figure 1.11. The results presented in Figures 1.8 to 1.11 are also listed in Table 1.1. Magnitude, focal mechanism, and depth parameters are roughly consistent between all analyzes, such that the earthquakes likely occurred on the subduction zone interface. Specifically for depth, Pritchard et al. [2006] found the center of the 1993/07/11 earthquake fault surface at approximately 53 km depth, which is within the MT5 depth solution and error bounds (48 ± 5 km). Similarly, the three types of inversion shown in Figure 1.9 of the 1996/04/19 event constrain the center of its fault slip surface at about 48 km depth, which is also within the constraints determined by the MT5 waveform inversion (46 ± 5km).

1995/10/31 and 1995/11/01 events – These earthquakes are low-dip thrust events along the Chilean coast assumed to be on the subduction zone megathrust. With respect to InSAR, only the 1995/11/01 event is considered during analysis. Due to its larger magnitude (Mw5.8 on 1995/10/31 vs. Mw6.6 on 1995/11/01), it is most likely that displacements associated with the 1995/11/01 event dominate the observed geodetic data. Only a portion of the deformation field is imaged on land, primarily subsidence (Figure 1.12). InSAR analysis used the Neighborhood Algorithm [*Sambridge*, 1998] to explore a range of model parameters for a best fitting single fault plane (Figure 1.13). The InSAR analysis parameters are shown in Figure 1.12 and Table 1.1. Body waveform modeling results for the 1995/11/01 event and the 1995/10/31 event are in Figures 1.14 and 1.15, respectively. Regarding the depth of the 1995/11/01 event, InSAR analysis determined the depth to the center of the fault slip surface at ~ 27 km, while teleseismic waveform modeling found an event depth of 28 ± 5 km. Again, these depths are consistent with each other within the constraints

Figure 1.8: [Modified from *Pritchard, et al.*, 2006] InSAR solutions for the 1993/07/11 and 1996/04/19 earthquakes. (a) Five interferogram stack from track 96 for the 1996/04/19 earthquake (see Table 1 of Pritchard et al., (2006) for dates). For this and other stacks, the interferograms were combined, and then georeferenced. The NEIC location – why not ISC is shown as a white star and the focal mechanism is from the Global CMT catalog. (b) The predicted LOS (line of sight) displacement from this earthquake from teleseismic-only inversion. For all tracks, the 1993/07/11 and 1996/04/19 teleseismic-only model predictions of the LOS are visually similar to the geodetic-only and joint results. For track 96, the RMS difference between the data and models are as follows: geodetic, ~ 0.20 cm; joint, ~ 0.22 cm; teleseismic model ~ 0.22 cm (to make the comparison equivalent to the geodetic and joint results, we did not just difference the data and model, but also calculated the best-fit orbital ramp parameters). (c) Four interferogram stack from track 325 for the 1996/04/19 earthquake (see Table 1 of Pritchard et al., (2006) for dates). (d) The predicted surface LOS displacements from the teleseismic inversion for this track. For track 325, the RMS difference between the models and data are: geodetic, ~ 0.18 cm; teleseismic, ~ 0.20 cm; and joint, ~ 0.19 cm. (e) The only interferogram we have that spans only the 1993/07/11 earthquake (track 325). (f) Predicted LOS displacements from teleseismic slip inversion. The RMS difference between the data and the geodetic model is ~ 0.43 cm, while the RMS for both the teleseismic and joint models is about ~ 0.47 cm.

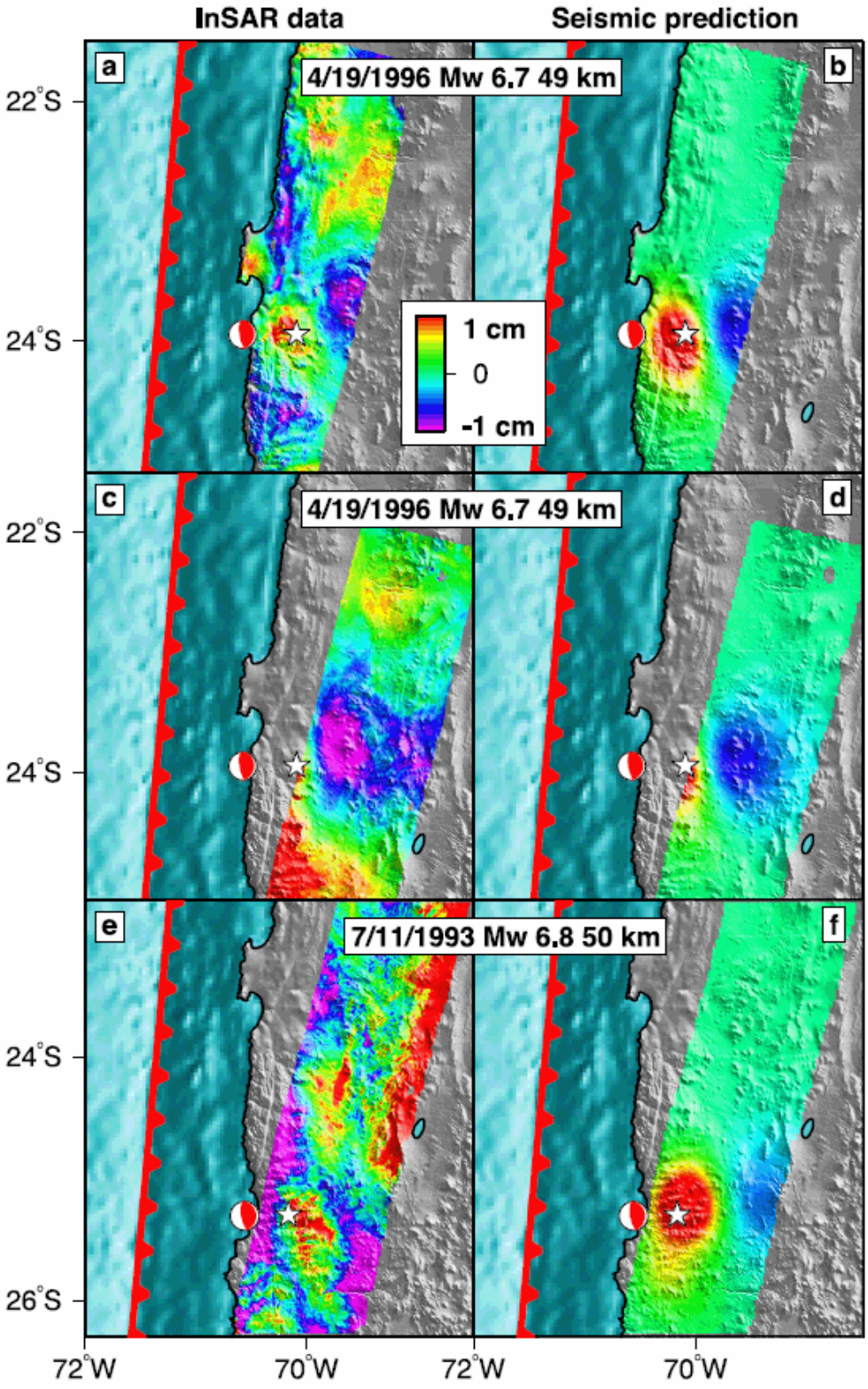
InSAR data
Seismic prediction
a
b
c
d
e
f
4/19/1996 Mw 6.7 49 km
4/19/1996 Mw 6.7 49 km
7/11/1993 Mw 6.8 50 km
1 cm
0
-1 cm
22°S
24°S
22°S
24°S
24°S
26°S
72°W
70°W
72°W
70°W

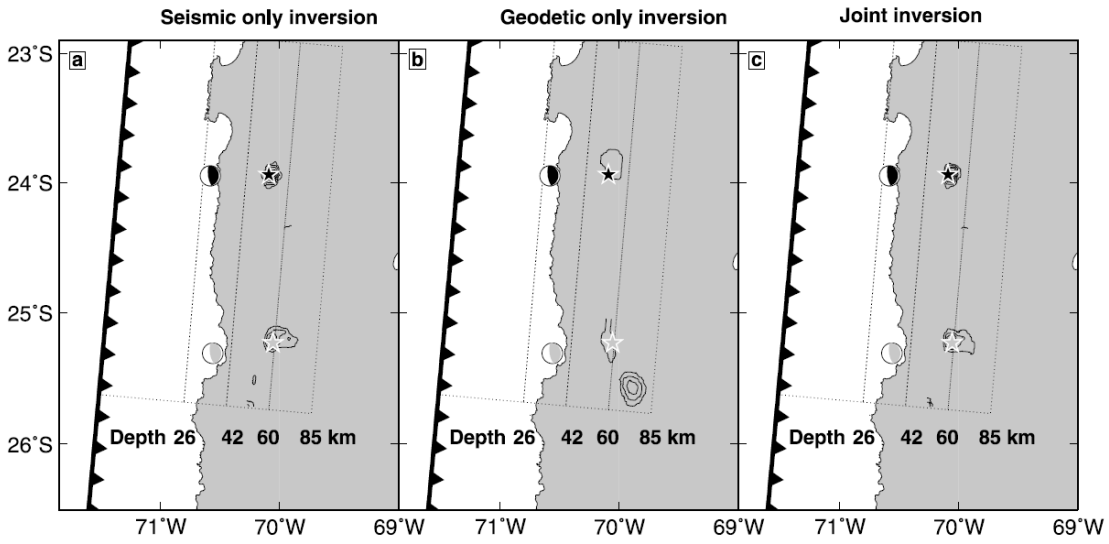

Figure 1.9: [Modified from *Pritchard, et al.*, 2006] Contours of slip from the 1993/07/11 and 1996/04/19 earthquakes from inversions using (a) only teleseismic data, (b) only InSAR data, and (c) both data sets. For both events, the maximum slip is about 1 m, and the contour interval is 0.2 m. The NEIC location is shown as the star, light gray for 1993/07/11 and black for 1996/04/19. The Global CMT location for both earthquakes (same colors as for the hypocenters) is located about 40 km from the actual centroid.

Figure 1.10: 1993/07/11 earthquake MT5 teleseismic waveform analysis solution. On the left is the waveform inversion solution plot with the same convention as Figure 1.3 and on the right is the sensitivity analysis plot with the same convention as Figure 1.5.

1993/07/11
174/61/78/48/5.569E18

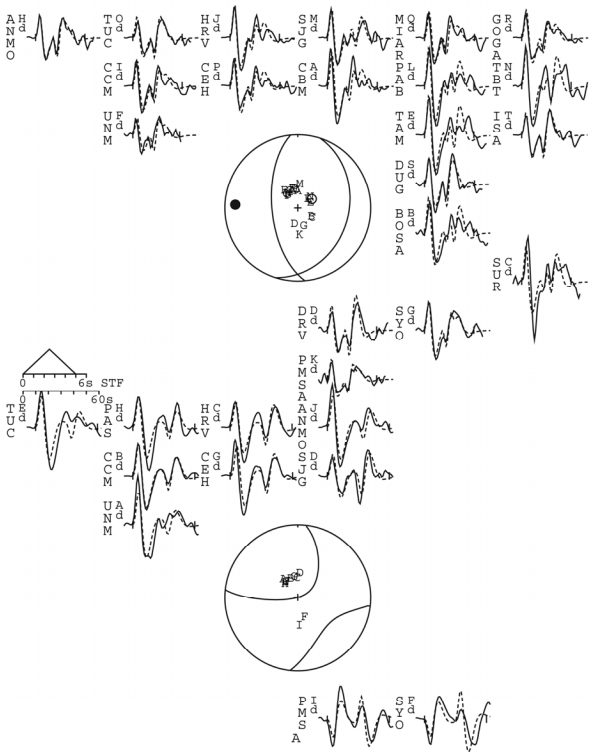

1993/07/11 13:36:22.21 (-25.2319, -70.0546) Mw6.6

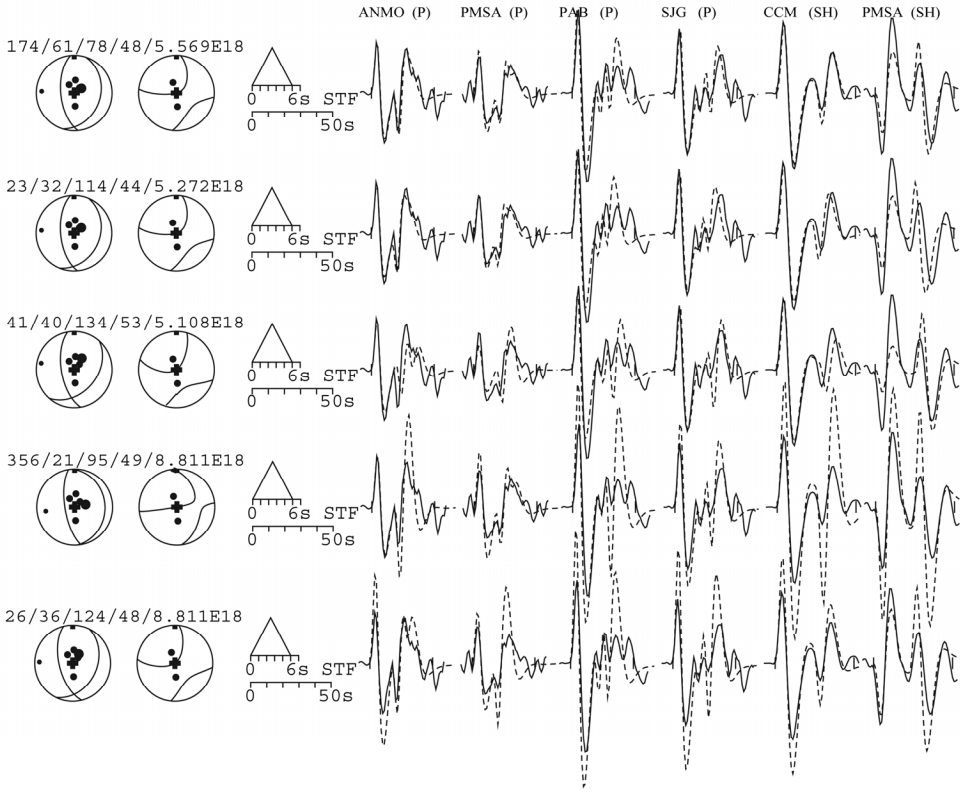

Figure 1.11: 1996/04/19 earthquake MT5 teleseismic waveform analysis solution. On the left is the waveform inversion solution plot with the same convention as Figure 1.3 and on the right is the sensitivity analysis plot with the same convention as Figure 1.5.

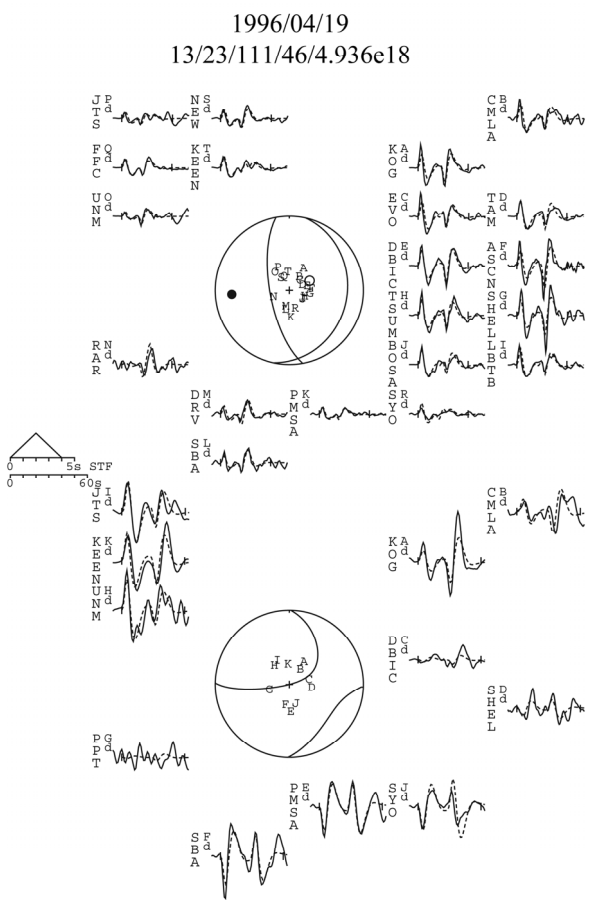
1996/04/19
13/23/111/46/4.936e18
0 5s STF
0 60s

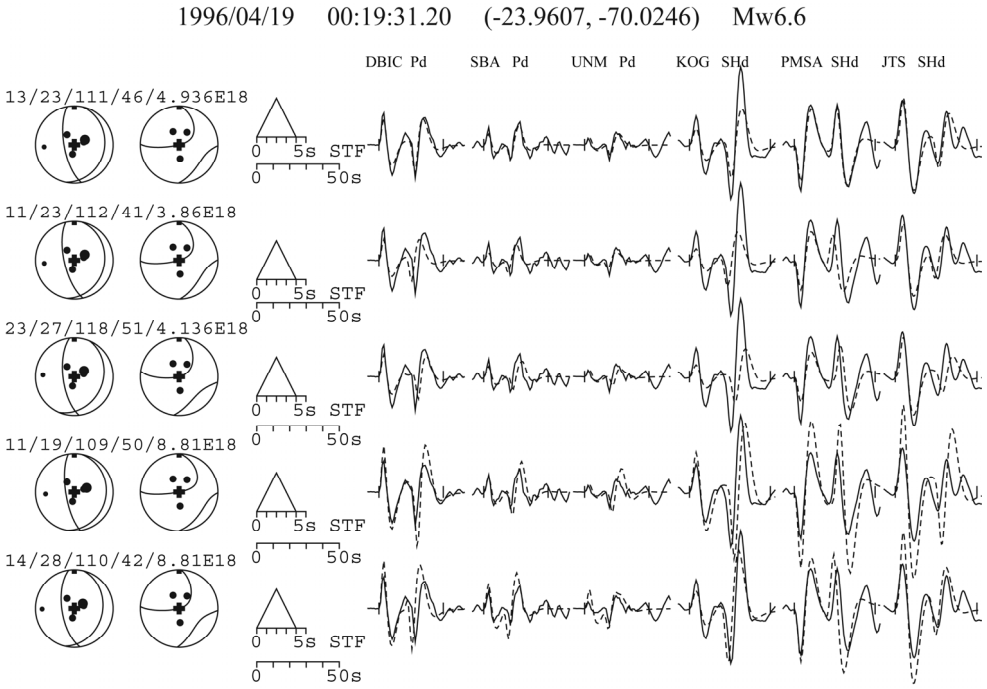
1996/04/19 00:19:31.20 (-23.9607, -70.0246) Mw6.6
DBIC Pd
SBA Pd
UNM Pd
KOG SHd
PMSA SHd
JTS SHd
13/23/111/46/4.936E18
11/23/112/41/3.86E18
23/27/118/51/4.136E18
11/19/109/50/8.81E18
14/28/110/42/8.81E18
0 5s STF
0 50s

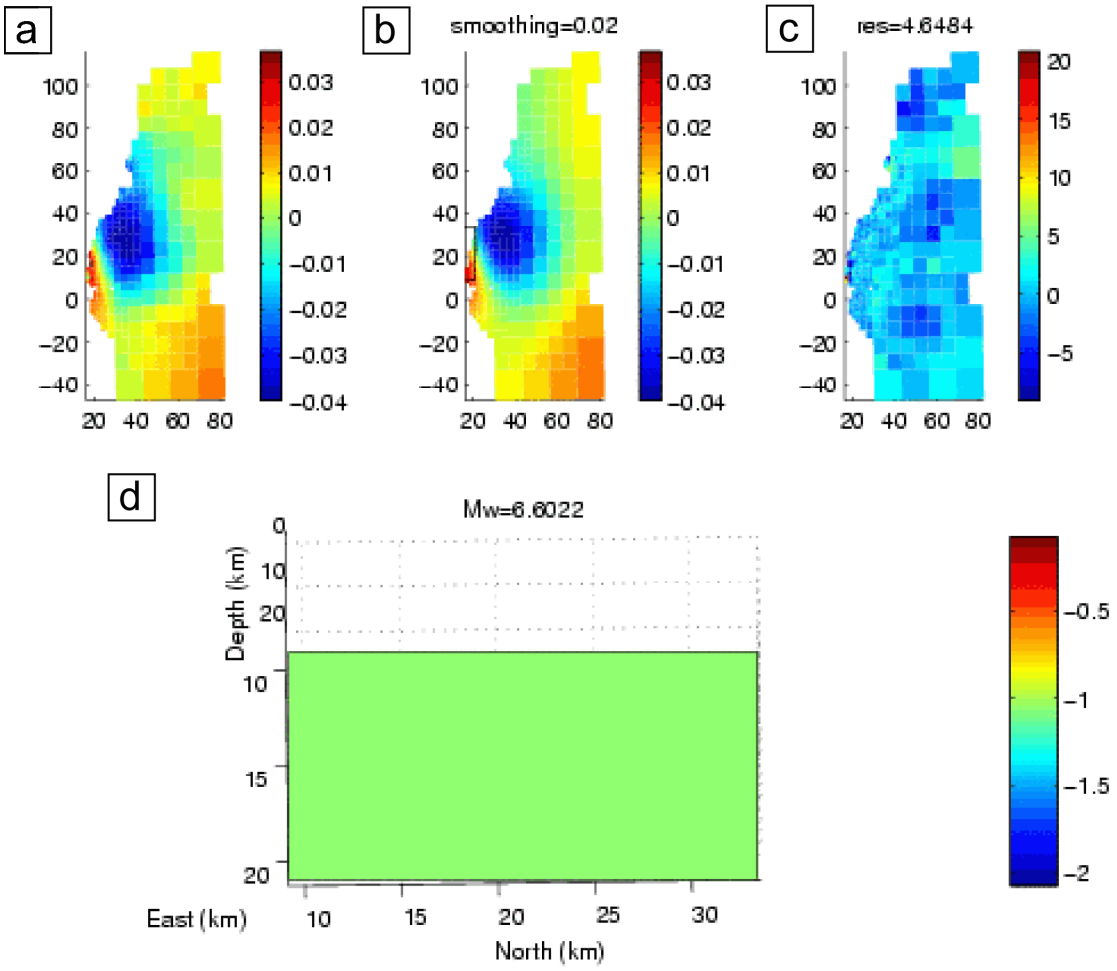

Figure 1.12: 1995/11/01 earthquake InSAR solution. (a) Resampled unwrapped interferogram where phase differences were converted to meters. The boxes outline the resampled points, and white areas show no data (either because the data did not successfully unwrap or was there was none to start with). (b) Predicted interferogram from our model. (c) The difference between the data and the model (residual) where the scale bar is cm. The residual value is shown above this figure value and has been weighted during the resampling procedure. (d) The fault model and predicted slip is shown.

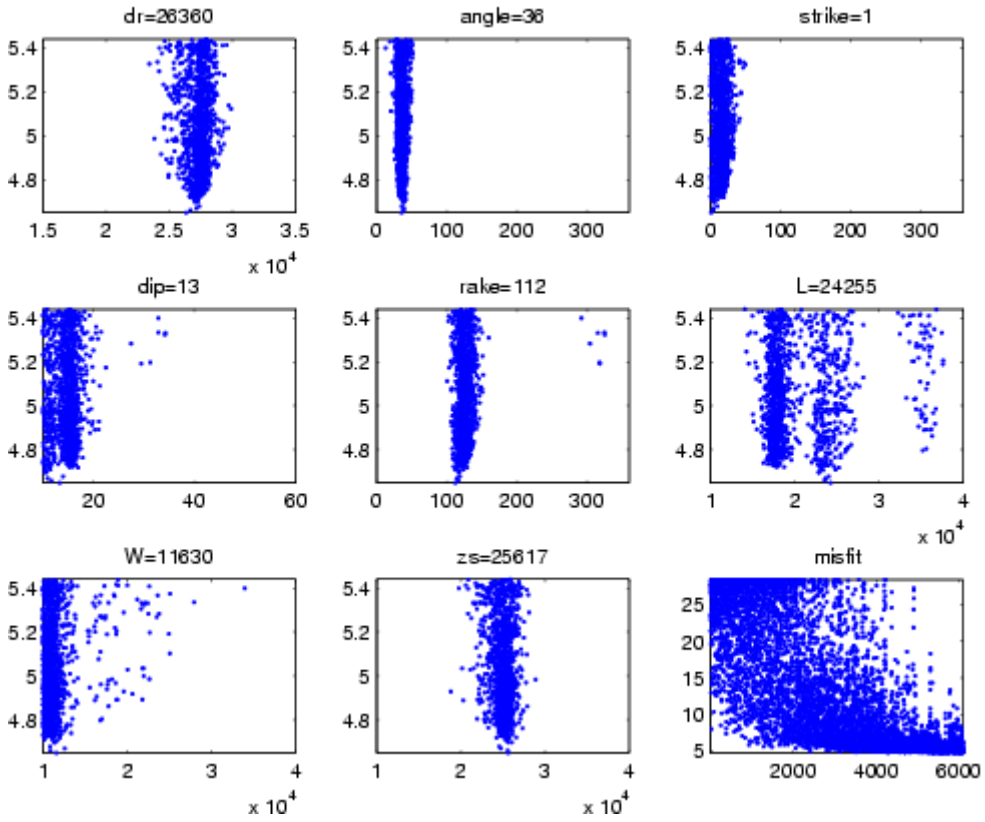

Figure 1.13: The output from the Neighborhood Algorithm showing the residual between the data and the model as a function of the different model parameters for the 1995/11/01 earthquake InSAR solution. From the upper left to the lower right the parameters are: the position of the best-fitting fault plane relative to the initial guess; the angle of the best-fitting fault relative to the starting position; the strike of the fault; the dip of the fault; the rake of the fault; the Length of the Fault, the width of the fault; the depth of the center of the fault; and the misfit as a function of the number of models tested.

Figure 1.14: 1995/11/01 earthquake MT5 teleseismic waveform analysis solution. On the left is the waveform inversion solution plot with the same convention as Figure 1.3 and on the right is the sensitivity analysis plot with the same convention as Figure 1.5.

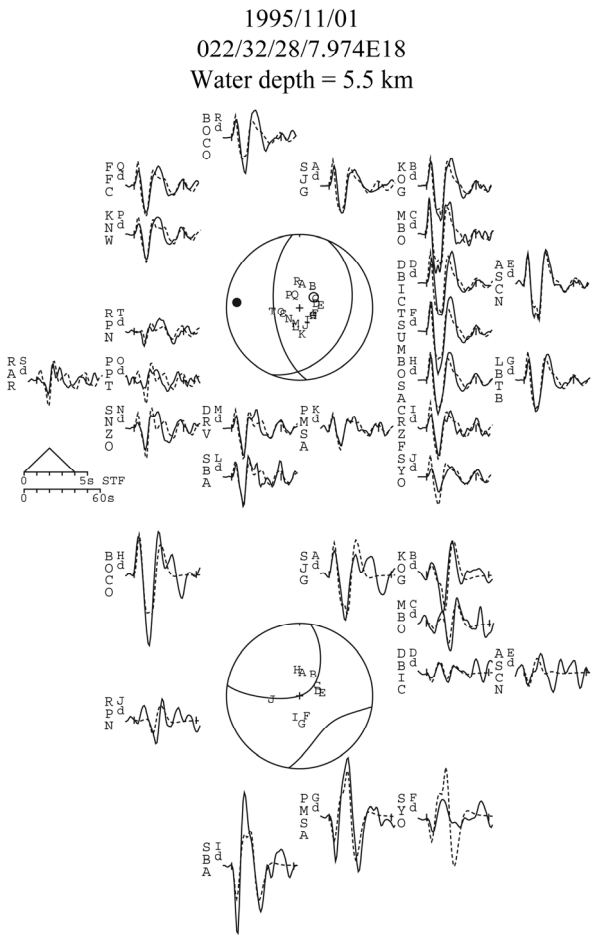
1995/11/01
022/32/28/7.974E18
Water depth = 5.5 km
0 5s STF
0 60s

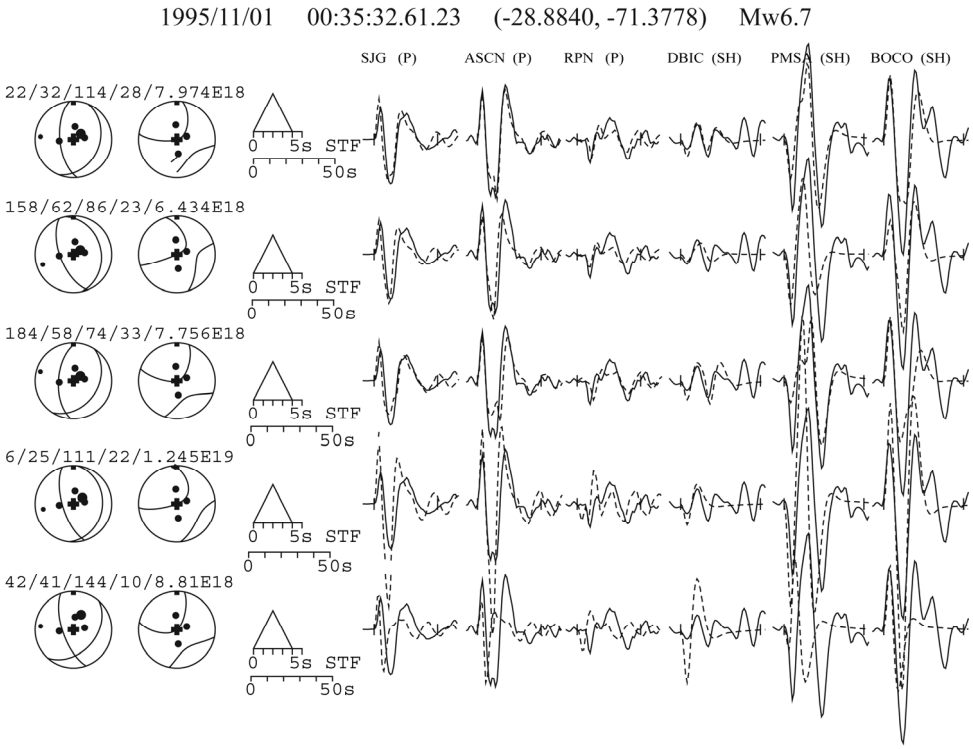
1995/11/01 00:35:32.61.23 (-28.8840, -71.3778) Mw6.7
SJG (P)
ASCN (P)
RPN (P)
DBIC (SH)
PMSA (SH)
BOCO (SH)
22/32/114/28/7.974E18
158/62/86/23/6.434E18
184/58/74/33/7.756E18
6/25/111/22/1.245E19
42/41/144/10/8.81E18
0 5s STF
0 50s

Figure 1.15: 1995/10/31 earthquake MT5 teleseismic waveform analysis solution. On the left is the waveform inversion solution plot with the same convention as Figure 1.3 and on the right is the sensitivity analysis plot with the same convention as Figure 1.5. One difference is that NEIC does not report a solution for this event, so its solution could not be included in the sensitivity analysis plot.

1995/10/31
055/29/149/24/2.326E17
Water depth = 4.5 km

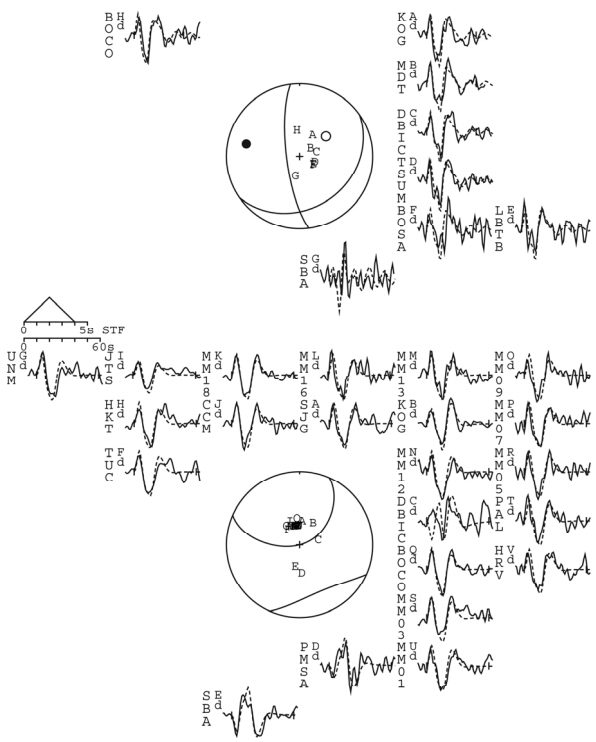

1995/10/31 03:55:48.23 (-28.9818, -71.3499) Mw5.8

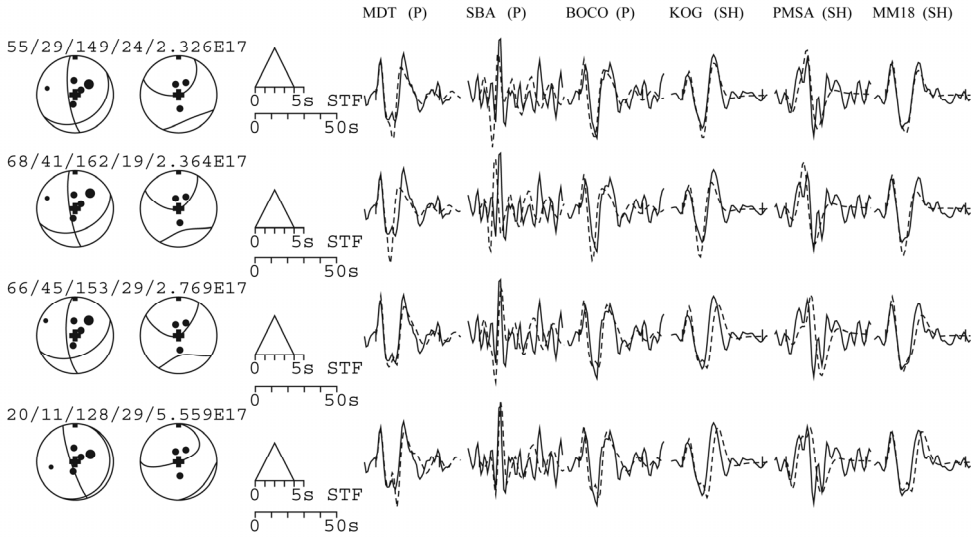

and errors of the analyses. The 1995/10/31 event was only analyzed by teleseismic waveform analysis and its depth was found to be approximately 24 km.

2006/04/30 seismic swarm – There was a seismic swarm on, or near, the subduction interface near Copiapo, Chile in late April to June, 2006 which included 18 earthquakes in the Global CMT catalog (Mw > 5). The largest two earthquakes in the sequence occurred on 2006/04/30 and were a Mw6.6 with an origin time of 19:17:25 and a Mw6.6 at with an origin time of 21:41:07. These earthquakes are thrust earthquakes with one low-angle, east-dipping nodal plane consistent with a subduction zone thrust event. Only a portion of the deformation field is imaged on land, primarily subsidence. It appears that all of the uplift is off-shore (Figure 1.16). InSAR analysis was conducted to model the displacement effects of both seismic events as one single event because of three factors – when the events occurred, where they occurred, and their relative magnitudes. The SAR data acquisitions span the time frame of 2004/09/06 to 2007/03/05 (from Envisat satellite images, mode beam 2, track 96, Bperp 170 m), which includes all of 2006/04/30. Therefore surface displacements from both events are likely contained within the InSAR analysis images. Additionally, the two events occurred off shore and close together, so that the displacement signals of the events are only partially visible on the InSAR data and it is likely that the proximal event locations allowed interference of the two events' displacement signals. Lastly, both events are of similar magnitude, therefore the displacements for each event could equally contribute to the observed signal captured in the InSAR data. The Neighborhood Algorithm [*Sambridge*, 1998] was used to explore a range of model parameters for a best fitting single fault plane (Figure 1.17). The parameters are shown in Figure 1.16 and are listed on Table 1.1. InSAR inversion found the subsidence surface displacements were consistent with a single off-shore, Mw7.6

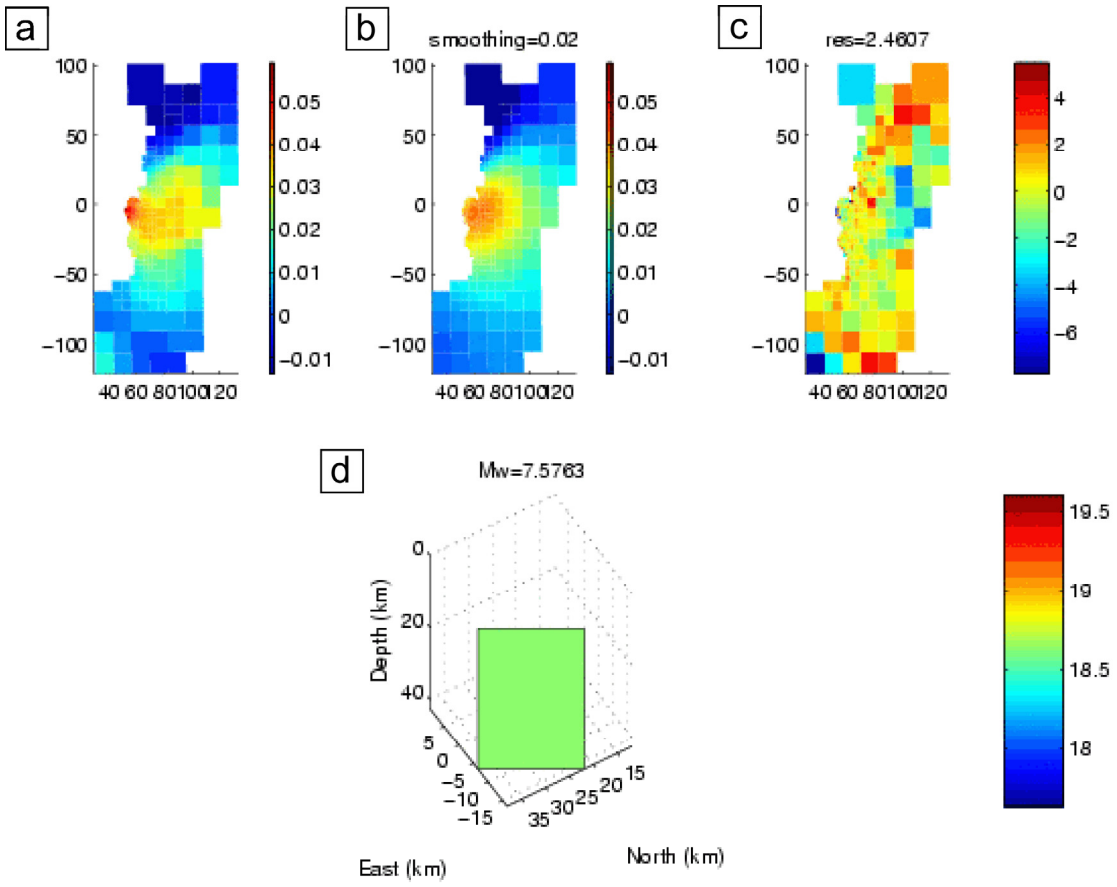

Figure 1.16: 2006/04/30 combined earthquake InSAR solution. (a) Resampled unwrapped interferogram where phase differences were converted to meters. The boxes outline the resampled points, and white areas show no data (either because the data did not successfully unwrap or was there was none to start with). (b) Predicted interferogram from our model. (c) The difference between the data and the model (residual) where the scale bar is cm. The residual value is shown above this figure value and has been weighted during the resampling procedure so it doesn't simply relate to the RMS. (d) The fault model and predicted slip is shown.

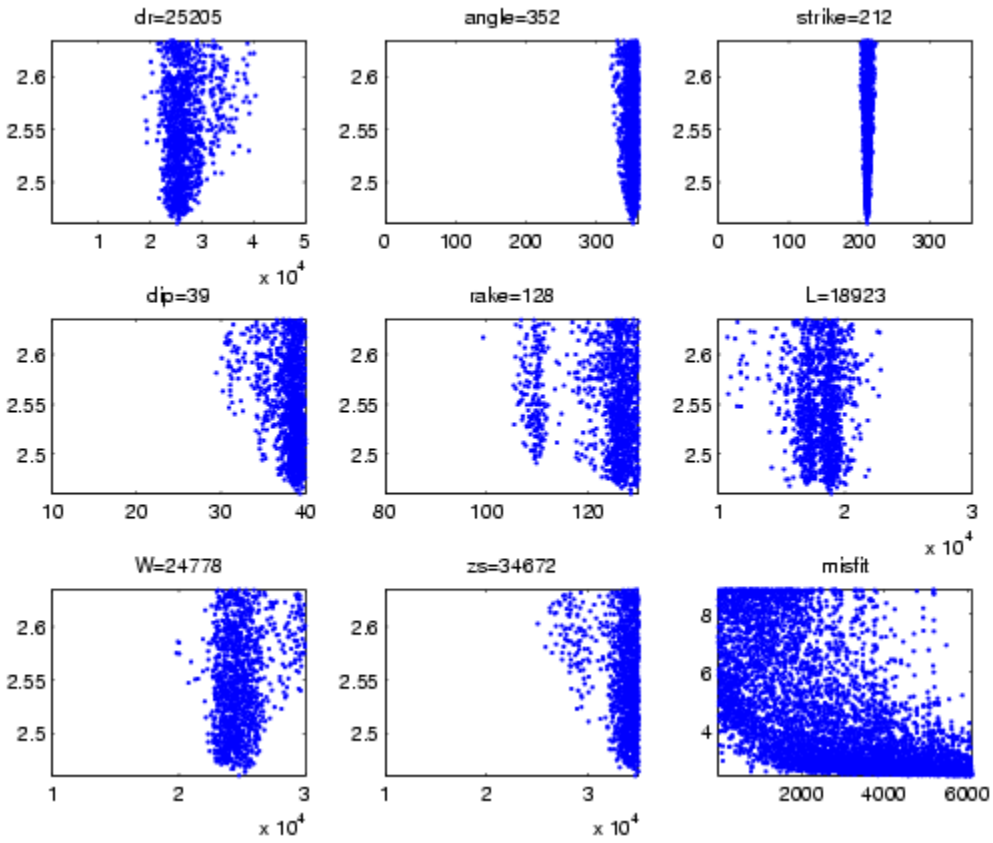

Figure 1.17: The output from the Neighborhood Algorithm showing the residual between the data and the model as a function of the different model parameters for the combined 2006/04/30 events. From the upper left to the lower right the parameters are: the position of the best-fitting fault plane relative to the initial guess; the angle of the best-fitting fault relative to the starting position; the strike of the fault; the dip of the fault; the rake of the fault; the Length of the Fault, the width of the fault; the depth of the center of the fault; and the misfit as a function of the number of models tested.

Figure 1.18: 2006/04/30 19:17:25 earthquake MT5 teleseismic waveform analysis solution. On the left is the waveform inversion solution plot with the same convention as Figure 1.3 and on the right is the sensitivity analysis plot with the same convention as Figure 1.5.

2006/04/30
039/22/122/22/5.354E18
Water depth = 4.5 km

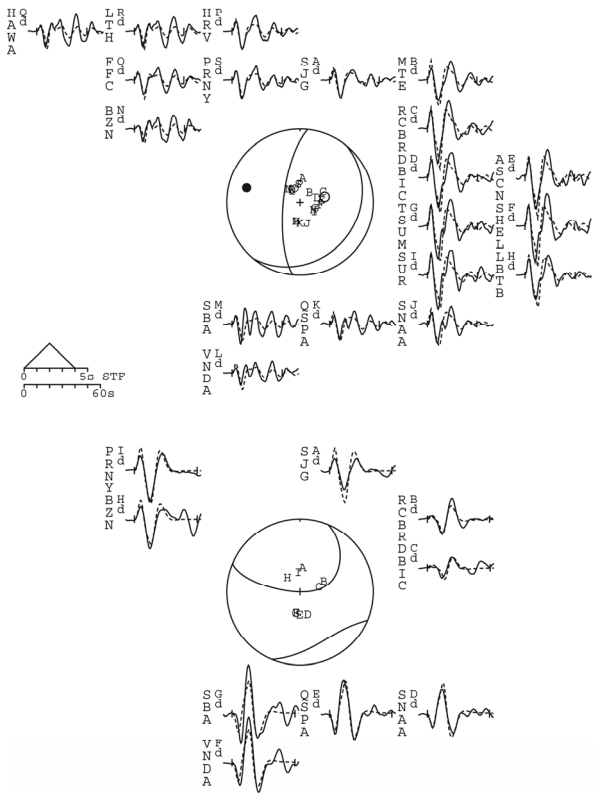

2006/04/30 19:17:15.70 (-27.0991, -71.2350) Mw6.6

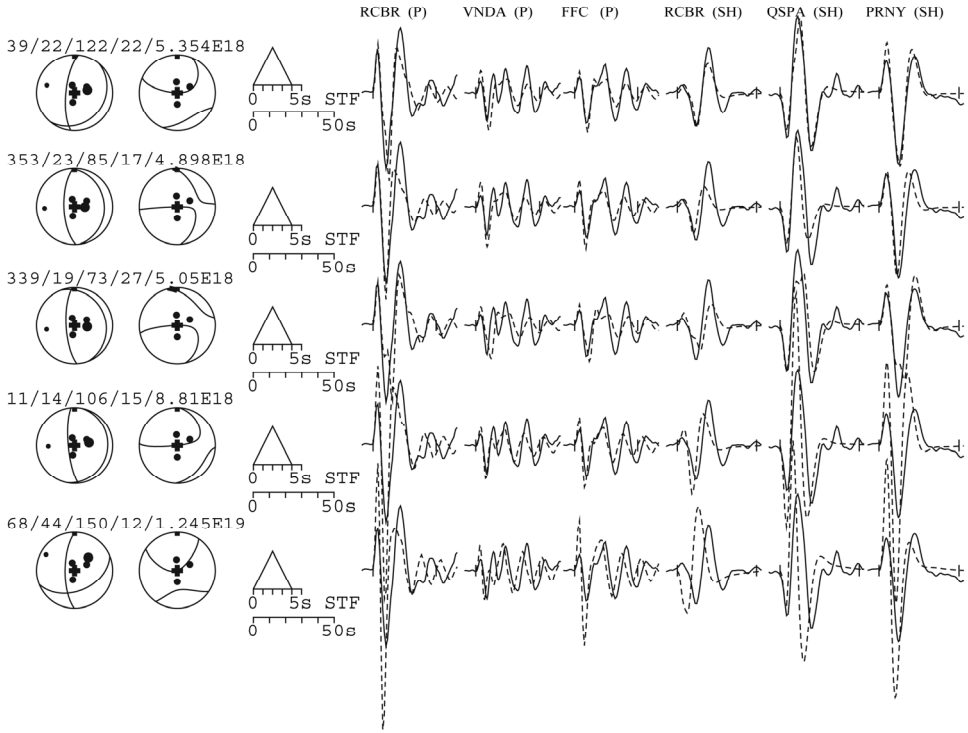

Figure 1.19: 2006/04/30 21:41:07 earthquake MT5 teleseismic waveform analysis solution. On the left is the waveform inversion solution plot with the same convention as Figure 1.3 and on the right is the sensitivity analysis plot with the same convention as Figure 1.5.

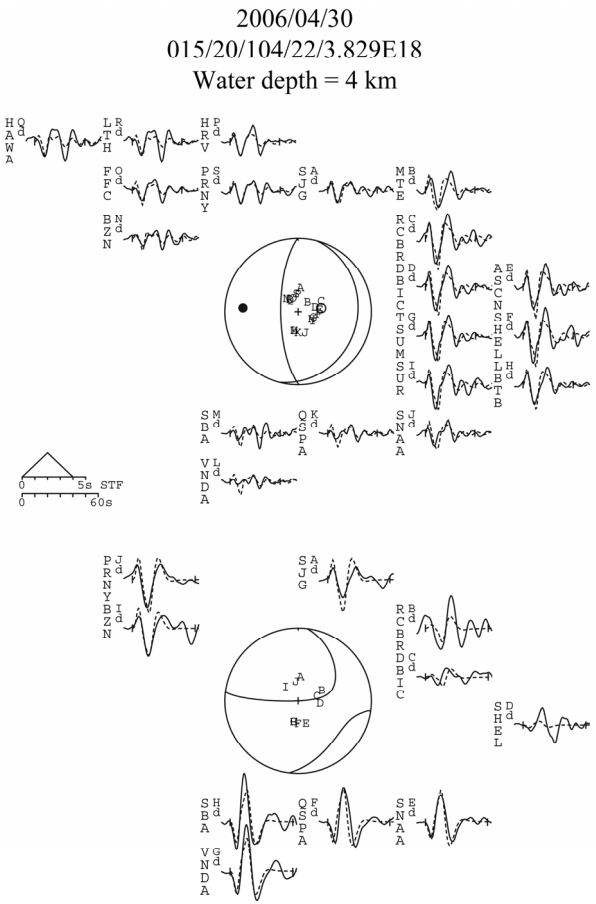
2006/04/30
015/20/104/22/3.829E18
Water depth = 4 km
0 5s STF
0 60s

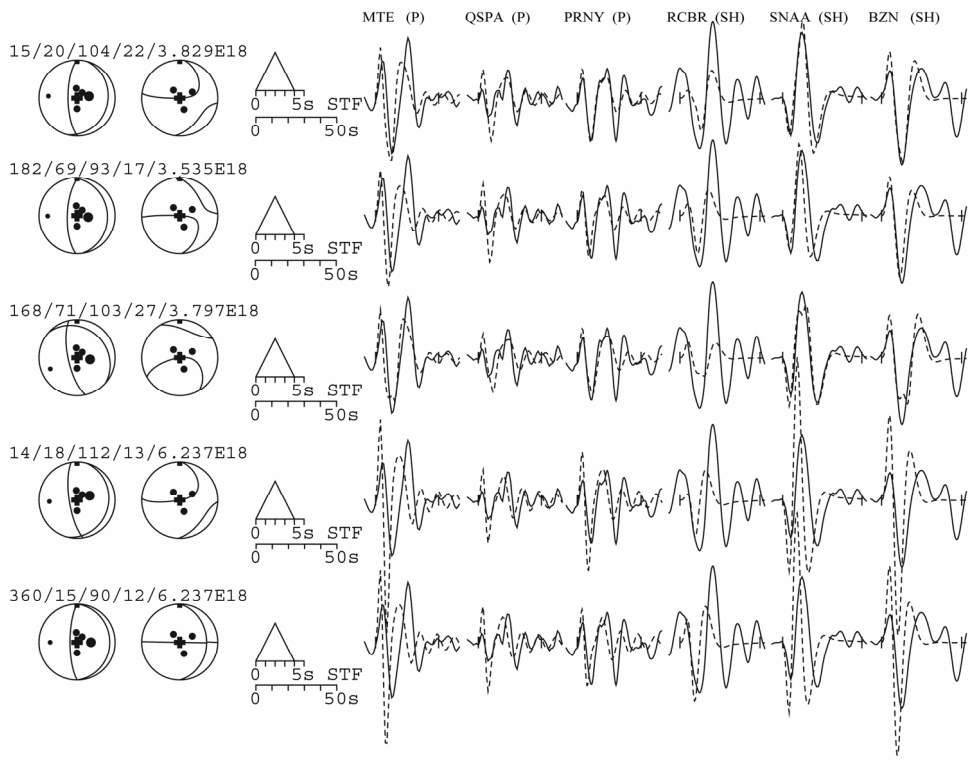
2006/04/30 21:41:01.27 (-27.2318, -71.0139) Mw6.5
MTE (P)
QSPA (P)
PRNY (P)
RCBR (SH)
SNAA (SH)
BZN (SH)
15/20/104/22/3.829E18
182/69/93/17/3.535E18
168/71/103/27/3.797E18
14/18/112/13/6.237E18
360/15/90/12/6.237E18
0 5s STF
0 50s

event at a depth of about 39 km. Due to the more precise time constraints on seismic data, teleseismic body waveform modeling is capable of separately analyzing the two large earthquakes that occurred on 2006/04/30. The results of the inversion are show in Figure 1.18 and 1.19 and are list on Table 1.1. Waveform modeling determined magnitudes (Mw), 6.5 and 6.4 for the 19:17:25 and 21:41:07, respectively, similar to those reported by CMT, as well as, focal mechanism orientation solutions were consistent with subduction zone thrust events. MT5 magnitude and depth (both events occurred at ~ 22 km depth) determinations did not, however, correlate well with the InSAR analysis solution. This could be due to the fact that it is not possible to distinguish the individual events within the InSAR images and that modeling their combined effects does not accurately estimate the source parameters of the individual events.

Conclusions

P and *SH* teleseismic waveform modeling is an accurate procedure to use when analyzing earthquake source parameters for shallow ($\lesssim$ 70 km depth) seismic events, which is most often the case with continental seismicity. Care has been taken to understand and minimize errors in the analysis and verification of the accuracy of the solutions has been shown through comparison with solutions from an independent analysis technique, InSAR.

REFERENCES

Alvarado, P., et al. (2005), Crustal deformation in the south-central Andes backarc terranes as viewed from regional broadband seismic waveform modeling, *Geophys. J. Int.*, *163* (2), 580–598, doi: 10.1111/j.1365-246X.2005.02759.x.

Butler, R., et al. (2004), The global seismographic network surpasses its design goal, *Eos Trans. AGU*, *85* (23), 225, 229.

Chinn, D. S. (1982), Accurate source depths and focal mechanisms of shallow earthquakes in western South America and in the New Hebrides island arc, Ph.D. thesis, 225 pp, Cornell University, Ithaca, NY.

Chinn, D. S., and B. L. Isacks (1983), Accurate source depths and focal mechanisms of shallow earthquakes in western South America and in the New Hebrides island arc, *Tectonics*, *2* (6), 529-563.

Christensen, D. H., and L. J. Ruff (1985), Analysis of the Trade-Off between Hypocentral Depth and Source Time Function, *B. Seismol. Soc. Am.*, *75* (6), 1637-1656.

Emmerson, B., et al. (2006), Seismicity, structure and rheology of the lithosphere in the Lake Baikal region, *Geophys. J. Int.*, *167* (3), 1233-1272, doi:10.1111/j.1365-246X.2006.03075.x.

Farr, T. G., and M. Kobrick (2000), Shuttle radar topography mission produces a wealth of data, *Eos Trans. AGU*, *81* (48), 583-585.

Goldstein, P., and A. Snoke (2005), SAC Availability for the IRIS Community, *IRIS DMS Newsletter*, *7* (1), http://www.iris.edu/news/newsletter/vol7no1/page1.htm.

Goldstein, R. M., and C. L. Werner (1998), Radar interferogram filtering for geophysical applications, *Geophys. Res. Lett.*, *25* (21), 4035-4038.

Goldstein, R. M., et al. (1988), Satellite Radar Interferometry : Two-Dimensional Phase Unwrapping, *Radio Sci.*, *23* (4), 713-720.

Helmberger, D. V. (1974), Generalized ray theory for shear dislocations, *Bulletin of the Seismological Society of America*, *64* (1), 45-64.

Helmberger, D. V., and L. J. Burdick (1979), Synthetic seismograms, *Annual Review of Earth and Planetary Sciences*, *7*, 417-442.

James, D. E., and J. A. Snoke (1994), Structure and tectonics in the region of flat subduction beneath central Peru; crust and uppermost mantle, *J. Geophys. Res.*, *99* (B4), 6899-6912.

Kagan, Y. Y. (2003), Accuracy of modern global earthquake catalogs, *Phys. Earth Planet. In.*, *135* (2-3), 173-209, doi: 10.1016/s0031-9201(02)00214-5.

Kennett, B. L. N., et al. (1995), Constraints on seismic velocities in the earth from travel times, *Geophys. J. Int.*, *122*, 108-124, doi:10.1111/j.1365-246X.1995.tb03540.x

Langston, C. A., and D. V. Helmberger (1975), A Procedure for Modelling Shallow Dislocation Sources, *Geophysical Journal of the Royal Astronomical Society*, *42* (1), 117-130, doi:10.1111/j.1365-246X.1975.tb05854.x.

Lohman, R. B., and M. Simons (2005), Locations of selected small earthquakes in the Zagros mountains, *Geochem. Geophys. Geosyst.*, *6* (1), Q03001, doi:10.1029/2004GC000849.

Maggi, A., et al. (2000), A re-assessment of focal depth distributions in southern Iran, the Tien Shan and northern India: do earthquakes occur in the continental mantle?, *Geophys. J. Int.*, *143* (3), 629–661.

Maggi, A., et al. (2002), Focal Depths of Moderate to Large Magnitude Earthquakes in Iran, *J. Seism. Earthq. Eng.*, *4* (2-3), 1-10.

McCaffrey, R., and G. A. Abers (1988), SYN3: A program for inversion of teleseismic body waveform on microcomputers., Air Force Geophysics Laboratory Technical Report, AFGL-TR-88-0099.

McCaffrey, R., et al. (1991), Inversion of teleseismic body waves in *Digital Seismogram Analysis and Waveform Inversion*, edited by W. H. K. Lee, pp. 81-166, Int. Assoc. Seismol. Phys. Earth Inter. Software Library.

McCaffrey, R., and J. L. Nabelek (1987), Earthquakes, gravity, and the origin of the Bali Basin; an example of a nascent continental fold-and-thrust belt, *J. Geophys. Res.*, *92* (B1), 441-460.

Mitra, S., et al. (2005), Crustal structure and earthquake focal depths beneath Northeastern India and southern Tibet, *Geophys. J. Int.*, *160* (1), 227-248.

Molnar, P., and H. Lyon-Caen (1989), Fault plane solutions of earthquakes and active tectonics of the Tibetan Plateau and its margins, *Geophys. J. Int.*, *99* (1), 123-153.

Montagner, J.-P. K., B.L.N. (1996), How to reconcile body-wave and normal-mode reference earth models, *Geophys. J. Int.*, *125* (1), 229-248, doi:10.1111/j.1365-246X.1996.tb06548.x

Nabelek, J. L. (1984), Determination of earthquake source parameters from inversion of body waves, Ph.d. thesis, Massachusetts Institute of Technology, Cambridge.

Okada, Y. (1985), Surface deformation due to shear and tensile faults in a half-space, *B. Seismol. Soc. Am.*, *75* (4), 1135-1154.

Pritchard, M. E., et al. (2006), Distribution of slip from 11 Mw > 6 earthquakes in the northern Chile subduction zone, *J. Geophys. Res.*, *111* (B10).

Pritchard, M. E., and M. Simons (2004), An InSAR-based survey of volcanic deformation in the central Andes, *Geochem. Geophys. Geosyst.*, *5* (QO2002), doi:10.1029/2003GC000610.

Rosen, P. A., et al. (2004), Updated Repeat Orbit Interferometry Package released, *Eos Trans. AGU*, *85* (5), 47.

Sambridge, M. (1998), Exploring multidimensional landscapes without a map, *Inverse problems in geophysics; closing the gap between theory and practice*, *14* (3), 427-440.

Smalley, R., Jr., and B. L. Isacks (1990), Seismotectonics of thin- and thick-skinned deformation in the Andean foreland from local network data; evidence for a seismogenic lower crust, *J. Geophys. Res.*, *95* (B8), 12,487-412,498.

Stein, S., and G. C. Kroeger (1980), Estimating earthquake source parameters from seismological data, in *The winter annual meeting of the American Society of Mechanical Engineers ; Solid earth geophysics and geotechnology*, edited by S. Nemat-Nasser, pp. 61-71, American Society of Mechanical Engineers Applied Mechanics Division.

Zwick, P., et al. (1994), MT5, IASPEI Software Library, 4, http://ees2.geo.rpi.edu/rob/mt5/.

CHAPTER 2

DEPTHS AND FOCAL MECHANISMS OF CRUSTAL EARTHQUAKES IN THE CENTRAL ANDES

Abstract

The depth distribution of earthquakes within the South American continental lithosphere is investigated to better understand crustal deformation of the Central Andes. 138 shallow (< 80 km depth), moderate-sized (7.0 > Mw ≳5.5) earthquake focal mechanisms throughout the Central Andes above the subducting Nazca plate were assembled from the Global CMT catalog and previously published sources spanning over 60 years of continental seismicity. To accurately constrain event depth for CMT solutions, teleseismic *P* and *SH* waveforms are modeled to obtain accurate strike, dip, rake, focal depth, and source time function. Earthquake hypocentral locations and focal mechanisms are then integrated with topographic and structural data to enable study of ongoing seismogenic crustal deformation.

The study area includes 5°S to 35°S latitudes of the Central Andes above three major segments of the subducted plate, the Peruvian and Chile-Argentine flat-slab segments and the intervening segment where the subducted Nazca plate dips more steeply. Seismically active structures of the Eastern Cordillera and foreland regions exhibit approximately east-west (oriented ~ 92°) oriented P axes and consistently involve deformation of basement rocks. The average orientation of the P axes is close to the direction of convergence (~ 77˚) between the Nazca and South American plates, while individual deviations from this average often indicate effects of inherited structural trends. Three distinct seismically active basement-involved structures are seen: (1)

shallow seismic activity associated with the near-surface expression of basement thrust blocks (e.g., Shira uplifts of Peru); (2) deep, diffusely distributed earthquake activity associated with a possible mid-crustal basement wedge creating a basement-cored anticline (e.g, Pie de Palo of Argentina); and (3) inverted relic Permo-Triassic rift structures deforming at deep depths beneath undeformed foreland basins (e.g., east of the Huallaga basin of Peru).

Normal and strike-slip earthquakes occur beneath the Altiplano plateau of southern Peru and northernmost Chile. These events are consistent with the effects of the increase in vertical compressive stress, due to high topography and thick crustal root of the plateau, superimposed on the stress orientations seen in the foreland.

Introduction

The Altiplano-Puna Plateau and surrounding mountains dominate the topography of the Central Andes in western South America (Figure 2.1). Plateau formation is broadly attributed to its location along a convergent plate margin involving subduction of the Nazca oceanic plate beneath the overriding South American continental plate. Subduction of the Nazca plate is illustrated in Figure 2.1 by the dashed contours lines, which show the depth in kilometers to the Wadati-Benioff zone of earthquakes within of the subducting Nazca oceanic plate [*Cahill and Isacks*, 1992]. The Andean margin displays major along-strike segmentations involving variations of angle of the subducting plate, foreland structural style, and upper plate foreland seismicity [*Barazangi and Isacks*, 1976; *Jordan, et al.*, 1983]. These corresponding relationships of segmentation have been known for some time now and many studies since have continued to study continental earthquakes in different locations throughout the Central Andes [*Alvarado and Beck*, 2006; *Alvarado, et al.*, 2005; *Alvarado, et al.*,

2004; *Assumpçao and Araujo*, 1993; *Dorbath, et al.*, 1987; *Kadinsky-Cade, et al.*, 1985; *Legrand, et al.*, 2007; *Regnier, et al.*, 1992; *Smalley and Isacks*, 1990; *Smalley, et al.*, 1993; *Stauder*, 1975; *Suarez, et al.*, 1983]. However, not since 1983 [*Chinn and Isacks*, 1983] has there been an overview study of continental seismicity of the entire Central Andes. The purpose of this chapter is to do so by gathering the most recent earthquake, topographic, and structural datasets to explore the relationship of upper plate seismicity to Andean segmentation.

In addition to tectonic segmentation along the strike of the Central Andes, lateral segmentation occurs as well [*Jordan, et al.*, 1983]. The "forearc" region is located between the trench and the continental drainage divide. The "magmatic arc" or "volcanic arc" is the zone of active volcanoes, or in the case of the flat slab segments, the zone of Miocene volcanism. The "hinterland" includes the Altiplano-Puna plateau, the Eastern Cordilleras of Peru, Bolivia, and Argentina, and the Principal and Frontal Cordilleras of Argentina. The "foreland" is the region of youngest deformation, located east of the main cordillera, and bounded to the east by the undeformed craton. Examples of foreland regions are the Subandean zone, Bolivian fold and thrust belt, and the Sierras Pampeanas.

Along-strike segmentation of subduction angle is illustrated in Figure 2.1 by the changes in distance between the contour lines. The terms "flat slab" or "flat subduction" are used to describe where the distance between the contour lines are large, indicating that the Nazca plate subducts at a relatively low angle (0 - 10°) [e.g., *Cahill and Isacks*, 1992]. Flat subduction occurs from 2° to 15°S in Peru and from 27° to 33°S in Argentina. In the intervening section of the Central Andes, from 15° to

Figure 2.1: Generalized map of the Central Andes. Dashed contours lines show the depth (labeled in km) to the Wadati-Benioff zone of earthquakes within the subducting Nazca oceanic plate [*Cahill and Isacks*, 1992]. An approximate outline of the Altiplano-Puna, or Central Andean, Plateau is the thick black line, which represents the ~ 4 km contour line derived from SRTM (Shuttle Radar Topography Mission) topography. Black triangles illustrate recently active volcanic edifices [*de Silva and Francis*, 1991]. Shaded topography is from SRTM topography.

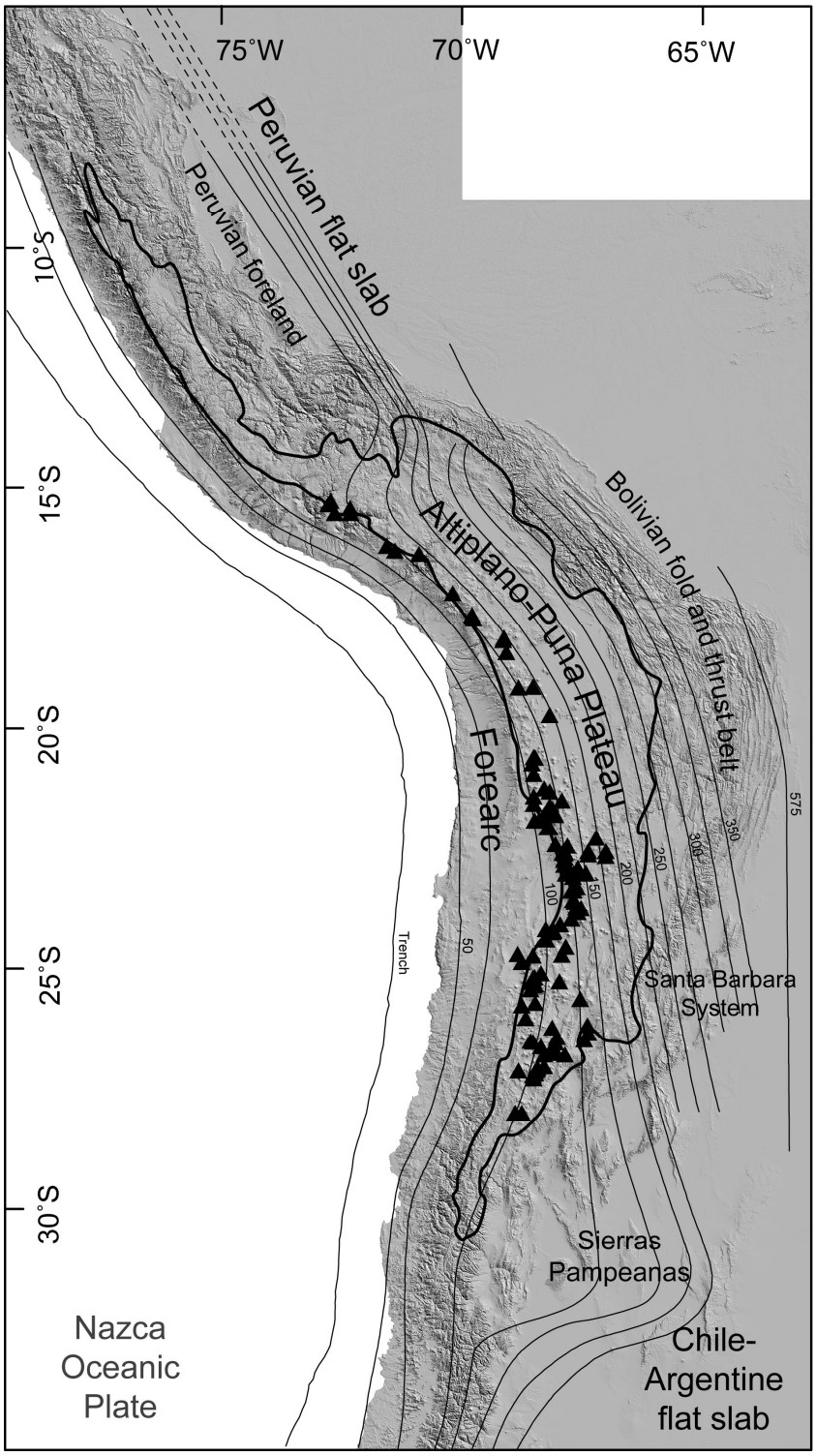
75°W
70°W
65°W
10°S
15°S
20°S
25°S
30°S
Peruvian flat slab
Peruvian foreland
Altiplano-Puna Plateau
Bolivian fold and thrust belt
Forearc
Trench
575
350
300
250
200
150
100
50
Santa Barbara System
Sierras Pampeanas
Nazca Oceanic Plate
Chile-Argentine flat slab

27°S, subduction occurs at a steeper angle of ~ 30°. The dip in subduction angle correlates with the absence or existence of Quaternary volcanic activity. Flat subduction occurs beneath regions were no significant Quaternary activity has occurred and evidence for such activity does exist in the intervening region. Because a steeper subduction angle and volcanic activity occur between 15° and 27°S, the region is described as exhibiting "normal subduction". It is referred to as "normal" because the subduction angle and related volcanic activity are typical of most other subduction zones around the world, rather than having a geometry consistent with flat slab subduction.

Along-strike segmentation of foreland deformation is comprised of three different types of foreland structural styles [e.g., *Jordan, et al.*, 1983; *Kley, et al.*, 1999]. Above flat subduction, foreland basement reverse faults dominate the deformational style. Basement reverse faults are considered thick-skinned structures because they deform basement rock on steep reverse faults. In map view, these faults tend to be widely spaced and when folding occurs it has long wavelengths. The Sierras Pampeanas of Argentina are examples of basement reverse faulted, thick-skinned deformational structures (Figure 2.1). Percent shortening accommodated in broad zones of basement thrusts typically does not exceed 10% [e.g., *Jordan and Allmendinger*, 1986]. Thin-skinned fold and thrust belt structures predominate in the foreland regions above normal subduction. This deformation typically involves detachment along a décollement level within the upper crust. Their map pattern is characterized by long, continuous along-strike thrust faults and folds at regular spacing. Thin-skinned belts can accommodate much more shortening (> 40%) than basement thrust structures. The third type of structural style is a combination of the first two. Thick-skinned thrust belts are known to occur above where the subducting plate transitions from flat to

normal at around 25°S latitude. These belts exhibit décollements in basement rocks at mid-crustal (10–20 km) depths, fold and thrust structures are relatively broad and short, and transverse structures are common. Shortening in well-developed thick-skinned thrust belts ranges from 20 to 35%. The Santa Barbara system of Argentina is considered a thick-skinned thrust belt (Figure 2.1). The primary control on structural style is often interpreted to be inherited stratigraphic and structural features of the South American plate [*Allmendinger, et al.*, 1983; *Kley, et al.*, 1999]. Where thick ($\gtrsim$ 3 km), relatively conformable sedimentary covers exists, thin-skinned structures dominate foreland deformation. Basement thrusts tend to form where there is thin sedimentary cover. Areas that experienced Mesozoic rifting now have reactivated thick-skinned thrust belt deformation.

Regarding segmentation of continental foreland seismicity, previous studies [e.g., *Chinn and Isacks*, 1983; *Jordan, et al.*, 1983] have noted that the two most seismically active segments of the central Andes are the forelands of Argentina and Peru. The crust of these regions is seismogenic from the surface to near Moho depth, and the structural style is dominated by basement thrusts. Outside of these two foreland regions, the South American plate has previously appeared nearly aseismic. Two earthquakes were determined to have occurred in the region of the plateau and three events have occurred in the transition zone between the Bolivian fold and thrust belt and the Santa Barbara system [*Chinn and Isacks*, 1983]. In other words, the forearc, the fold and thrust belts, and the plateau appeared aseismic with respect to earthquake of magnitude Mw $\gtrsim$ 5.5, magnitudes appropriate for teleseismic recording. The apparent aseismic behavior of the Andean plateau contrasts with the seismicity the Tibetan Plateau. Earthquake focal mechanism orientations display patterns that

strongly correlate with topography and deformational style [e.g., *Andronicos, et al.*, 2007; *Langin*, 2003].

Earlier studies [*Alvarado and Beck*, 2006; *Alvarado, et al.*, 2005; *Alvarado, et al.*, 2004; *Assumpçao and Araujo*, 1993; *Dorbath, et al.*, 1987; *Kadinsky-Cade, et al.*, 1985; *Legrand, et al.*, 2007; *Regnier, et al.*, 1992; *Smalley and Isacks*, 1990; *Smalley, et al.*, 1993; *Stauder*, 1975; *Suarez, et al.*, 1983] estimated source parameters in smaller regions within the Central Andes, but not since Chinn and Isacks [1983] has there been a overview study of continental seismicity of the entire Central Andes. Since the majority of the earthquake record is limited to the last 50 years and large magnitude earthquake recurrence intervals are typically 100 years or more, continued monitoring of the seismologic activity reveals information about on-going deformational provinces not previously observed.

Accurate focal depths of earthquakes are critical to tectonic interpretations of seismicity and related structure. A number of global earthquake bulletins and catalogs exist that routinely report earthquake depths. However, they lack the ability to resolve the relatively subtle differences in focal depth distribution within depths $\lesssim$ 70 km [*Kagan*, 2004; *Maggi, et al.*, 2002], depths typical for earthquakes within continental regions. Therefore, continental earthquake depths must be constrained by analyses separate from those of global catalogs and bulletins. Because the Central Andes is a large area and not densely covered with seismographs, this study constrains earthquake source parameters via *P* and *SH* waveform inversion using seismograms recorded at globally distributed seismograph stations.

To address how the earthquakes fit with deformational structure, earthquake hypocentral locations are integrated with two additional datasets. The datasets are NASA's Shuttle Radar Topography Mission (SRTM) 90 m topography and previously published studies that describe surface and subsurface structures (e.g., seismic imaging, balanced cross-sections). Integration of the SRTM topography dataset with the earthquake focal mechanisms allow investigation of the topographic expression of the seismic activity, and subsurface imaging and geological interpretations allow us to place the earthquakes into a context of imaged or hypothesized subsurface structures.

Earthquake depth determination

Data sources

To determine earthquake depth distributions throughout the Central Andes, three sources of data are considered: previously published accurate event parameters, events recorded teleseismically by global seismograph stations for which earthquake source properties are constrained using waveform modeling or short-period depth phase identification, and InSAR. The earthquakes compiled for this study are listed in Table 2.1 and displayed in map view in Figure 2.2. There are 138 earthquakes listed. 38 event parameters were constrained in this study, 48 have only Global Centroid Moment Tensor (CMT) solutions (a global earthquake catalog), and 52 are reported from previous studies. Earthquakes with solutions from this study are labeled MT5 and/or SHZ in the References column of Table 2.1. The labels refer to the analysis method used for depth determination and are described in detail later in this chapter.

InSAR analysis was conducted for this study as well. Please refer to Chapter 1 for analysis method description. Depending on what is available, this study uses epicentral locations reported by previously published studies, the International Seismological

Table 2.1: Central Andean continental earthquakes. Reference codes are AB06 is Alvarado and Beck [2006], A05 is Alvarado et al. [2005], A04 is Alvarado et al. [2004]; AA93 Assumpçao and Araujo [1993], CI83 is Chinn and Isacks [1983], KC85 is Kadinsky-Cade et al. [1985], MT5 is from this study using *P* and *SH* waveform modeling, R92 is Regnier et al. [1992], SHZ is from this study using forward modeling of short-period depth phase arrival times, S75 is Stauder [1975], and S83 is Saurez et al. [1983]. Blank cells within beneath the MT5 solution columns indicate that an MT5 solution is not available for that earthquake. Descriptions of other columns are contained in the text of this chapter.

Table 2.1: Central Andean continental earthquakes

Date	Time	Location			Nodal Plane 1			Nodal Plane 2			Depth	Reference	MT5 solution			
mm/dd/yy	hh:mm:ss	longitude	latitude	Mw	strike	dip	rake	strike	dip	rake	(km)	code	Mw	strike	dip	rake
01/15/44	23:49:27	-68.5000	-31.5500	7.0	045	35	110	201	57	76	11	AB06				
06/11/52	00:31:37	-68.6000	-31.5050	6.8	040	75	30	301	61	163	12	AB06				
05/12/59	09:46:51	-65.0100	-23.1800		180	25		007	65		14	CI83				
05/18/63	05:33:29	-69.3500	-29.5900		181	40		323	60			CI83				
11/13/65	17:59:41	-68.0900	-29.3400		170	58		320	36		32	CI83				
04/25/67	10:36:00	-69.1700	-32.7200	5.4	159	41	97	330	49	84	27	AA93				
06/19/68	08:13:35	-77.2000	-5.5500	6.1	185	54		357	36		23	CI83				
					204	57		000	35		20	S83				
					185	54		357	36		89	S75				
06/20/68	02:38:38	-77.3000	-5.5100	5.8	182	26		002	64		14	CI83				
					014	62		143	40		16	S83				
12/01/68	13:14:55	-74.8100	-10.5400	5.4	065	80		334	86			CI83				
					351	50		171	40		18	S83				
07/18/69	23:17:09	-63.3400	-18.2900		180	45		000	45			CI83				
07/24/69	02:59:20	-75.1000	-11.8400	5.9	228	45		340	70		14	CI83				
					328	72		205	31		6	S83				
					228	45		340	70		1	S75				
10/01/69	05:05:50	-75.1500	-11.7500	5.8	220	45		332	70		14	CI83				
					315	68		160	25		5	S83				
					220	45		332	70		4	S75				
02/14/70	11:17:16	-75.5500	-9.8400	5.8	185	63		335	30			CI83				
					170	54		350	36		28	S83				
					185	63		335	30		35	S75				
10/15/71	10:33:46	-73.4547	-14.1980	5.7	218	80		310	80		8	S83				
					220	75		315	72			CI83				
					220	75		315	72		54	S75				

Table 2.1 continued

Date	Time	Location			Nodal Plane 1			Nodal Plane 2			Depth	Reference	MT5 solution			
mm/dd/yy	hh:mm:ss	longitude	latitude	Mw	strike	dip	rake	strike	dip	rake	(km)	code	Mw	strike	dip	rake
03/20/72	07:33:48	-76.7621	-6.7927	6.1	355	25		170	65		33	CI83				
					177	55		357	35		38	S83				
					355	25		170	65		64	S75				
09/26/72	21:05:43	-68.2096	-30.9073		192	51		000	40		20	CI83				
11/03/73	14:17:38	-67.7162	-25.9829		142	66		030	52		11	CI83				
11/19/73	11:19:31	-64.5880	-24.5781		195	5		015	85		26	CI83				
07/01/74	16:51:52	-64.7364	-22.1416		168	29		348	61		17	CI83				
05/15/76	21:55:05	-74.4548	-11.6162	5.9	162	10		342	80		18	CI83				
					326	80		062	66		18	S83				
01/25/77	00:50:48	-68.2700	-33.5900	5.3	180	45	147	295	67	50	18	AA93				
03/08/77	13:08:54	-74.1563	-12.3277	5.6	184	52	165	284	78	39						
11/02/77	14:47:59	-74.7261	-9.9982	5.3	111	67	25	011	67	155						
11/23/77	09:26:48	-67.7644	-31.0411	7.5	183	44	90	004	46	90	17	KC85				
11/23/77	09:26:48	-67.7644	-31.0411	7.5	166	40		346	50		17	CI83				
11/24/77	18:20:20	-67.6859	-31.3099	5.6	190	34	91	008	56	89						
11/28/77	04:19:39	-67.6500	-31.6782	5.6	150	52	27	043	69	139						
11/28/77	06:31:38	-67.4445	-31.4370	6.2	170	30		338	60		15	CI83				
12/05/77	15:43:35	-67.9596	-31.0998	5.8	103	65	-5	195	86	-154						
12/06/77	17:05:16	-67.9010	-31.2383	5.9	180	39		034	56			CI83				
12/10/77	07:11:58	-67.7027	-31.2665	5.5	199	29	117	348	65	76						
01/17/78	11:33:21	-67.9981	-31.2512	6.0	142	66	12	047	79	156						
08/21/78	00:28:30	-67.8624	-31.2806	5.3	218	9	79	049	81	92						
01/06/79	01:31:51	-75.7280	-8.9389	5.7	351	26	65	199	67	102						
08/30/79	18:59:54	-67.6945	-31.4731	5.5	354	31	35	233	73	116						
01/14/80	21:51:08	-69.4100	-33.1133	5.6	141	69	5	049	85	159						
04/09/80	08:17:59	-67.4818	-31.6455	5.4	340	37	136	108	65	61						

Table 2.1 continued

Date	Time	Location			Nodal Plane 1			Nodal Plane 2			Depth	Reference	MT5 solution			
mm/dd/yy	hh:mm:ss	longitude	latitude	Mw	strike	dip	rake	strike	dip	rake	(km)	code	Mw	strike	dip	rake
11/10/80	16:24:44	-67.4716	-31.6218	5.7	133	31	49	358	67	111						
04/18/81	17:05:01	-74.4073	-13.1615	5.3	197	18	123	343	75	80						
06/22/81	17:53:26	-74.4973	-13.2204	5.8	159	15	55	015	78	99						
11/19/82	04:27:21	-74.6854	-10.6120	6.7	000	34	116	150	60	74						
04/02/83	05:58:41	-66.5942	-28.5365	5.3	247	25	137	017	73	71						
06/03/84	04:10:30	-76.7831	-7.8095	5.2	199	35	113	351	58	75						
06/05/84	04:15:28	-76.7119	-7.8335	5.7	200	20	114	354	72	82						
01/26/85	03:07:05	-68.5833	-33.0667	6.0	158	38	65	009	56	108						
03/19/85	10:28:35	-63.5786	-18.6038	5.8	172	38	81	004	53	97						
03/22/85	14:02:41	-63.5641	-18.6251	5.4	018	41	115	167	53	70						
04/12/85	14:35:02	-60.5853	-24.0443	5.1	338	43	49	208	59	121						
01/11/86	05:04:44	-77.4954	-9.5137	5.1	330	48	-15	070	79	-137						
04/05/86	20:14:26	-71.8142	-13.4188	5.2	121	32	-65	273	61	-104	6	SHZ				
05/09/86	16:24:00	-65.6185	-17.1679	5.9	151	39	88	334	51	92						
06/19/86	21:57:33	-65.4641	-16.9648	5.3	327	45	106	125	47	74						
08/11/86	22:06:49	-67.6639	-30.9197	5.4	187	49	167	285	80	41						
12/20/86	05:04:44	-75.4587	-7.7162	5.2	057	9	-31	178	86	-97						
09/13/87	20:08:52	-69.9598	-34.3708	5.9	027	58	176	119	87	32						
10/02/87	22:27:58	-77.9397	-8.1524	5.6	296	43	-157	189	74	-49						
11/15/87	22:00:55	-75.6773	-9.4024	5.4	210	12	120	000	80	84						
03/25/88	17:20:52	-67.9890	-31.4030		063	45		181	65		25	R92				
03/16/89	17:12:26	-65.0112	-17.0025	5.3	171	9	127	313	83	85	20	SHZ				
05/04/89	10:30:13	-75.7479	-6.6329	5.2	130	35	66	338	58	106	24	MT5	5.4	f 130	f 35	f 66
06/24/89	12:58:47	-66.2984	-28.3488	5.5	088	77	-172	357	82	-13						
05/30/90	02:34:12	-77.2142	-6.0307	6.6	188	24	122	333	70	77	26	MT5	6.5	174	29	118
05/30/90	16:49:31	-77.1261	-6.0454	5.7	169	29	130	305	68	70	29	MT5	5.4	f 169	f 29	f 130

Table 2.1 continued

Date	Time	Location			Nodal Plane 1			Nodal Plane 2			Depth	Reference	MT5 solution			
mm/dd/yy	hh:mm:ss	longitude	latitude	Mw	strike	dip	rake	strike	dip	rake	(km)	code	Mw	strike	dip	rake
06/06/90	02:01:11	-77.2055	-6.1461	5.3	191	15	149	311	82	77						
04/04/91	15:23:27	-77.1296	-6.0402	6.4	171	20	77	005	71	95	29	MT5	6.6	157	24	90
07/23/91	19:44:54	-71.6262	-15.6679	5.3	118	77	0	208	90	-167						
08/02/93	15:44:34	-74.1691	-11.7301	5.4	293	61	4	201	86	151	24	MT5	5.3	f 293	f 61	f 4
10/02/93	00:06:10	-64.4684	-24.0571	5.4	237	56	179	327	89	34						
12/26/94	19:57:05	-71.8240	-15.5968	5.4	111	35	-79	277	56	-98						
06/12/95	03:35:53	-75.9129	-8.3190	5.4	359	29	85	185	61	93	33	MT5	5.4	350	31	82
03/10/96	08:56:28	-69.4367	-13.0547	5.7	305	36	87	129	54	92	31	MT5	5.7	300	40	74
04/06/96	09:18:54	-75.1436	-10.2249	5.2	299	26	72	139	65	99						
04/08/96	02:52:17	-73.9892	-12.7711	5.3	159	32	-52	296	66	-111						
06/17/97	22:14:23	-64.7354	-27.7071	5.6	267	25	86	091	65	92						
01/10/98	04:54:30	-72.0638	-12.0264	6.2	101	22	88	283	68	91	11	MT5	6.2	115	5	114
02/19/98	04:21:33	-74.4149	-10.9469	5.9	131	41	82	321	50	97	4	MT5	6	124	31	81
03/01/98	01:51:04	-65.9728	-18.4203	5.3	354	50	172	090	84	41						
03/06/98	03:56:23	-74.5700	-10.8956	5.3	142	17	106	306	74	85	3	MT5	5.6	86	72	61
03/10/98	20:57:45	-74.5109	-10.9436	5.3	146	36	105	307	56	79	4	MT5	5.8	146	36	105
04/12/98	23:49:36	-71.8814	-15.6617	5.8	313	44	-47	081	60	-123	10	MT5 SHZ	f 5.8	f 313	f 44	f -47
05/22/98	04:49:03	-65.5390	-17.8595	6.6	186	79	-178	096	88	-11	13	MT5	6.1	360	88	179
05/26/98	01:08:20	-65.3282	-17.8360	5.4	204	64	-168	109	79	269	13	MT5	5.2	206	86	180
05/29/98	11:23:54	-65.2530	-17.7067	5.4	084	81	2	353	88	171	5	MT5	5.4	f 84	f 81	f 2
10/04/98	13:41:11	-76.2993	-8.4390	5.5	188	28	113	343	64	78	4	MT5	5.7	f 188	f 28	f 113
10/25/98	03:54:41	-69.3942	-17.9729	5.3	155	60	115	246	89	30	9	SHZ				
10/04/99	13:57:42	-75.6070	-10.7010	5.6	159	15	64	006	77	97	12	MT5	5.8	176	33	90
12/25/99	18:19:35	-75.2970	-6.1700	5.5	166	36	115	315	57	73	24	MT5	5.6	176	54	113
12/30/99	14:50:07	-64.8790	-23.7990	5.3	169	28	110	326	64	79						
04/30/00	05:31:30	-66.0210	-27.0380	5.2	185	38	45	057	64	119						

Table 2.1 continued

Date	Time	Location			Nodal Plane 1			Nodal Plane 2			Depth	Refernce	MT5 solution			
mm/dd/yy	hh:mm:ss	longitude	latitude	Mw	strike	dip	rake	strike	dip	rake	(km)	code	Mw	strike	dip	rake
12/21/00	06:13:12	-68.9350	-29.4740	4.0	151	36	69	356	57	104	14	A05				
12/25/00	00:49:27	-68.0150	-31.5330	3.9	191	42	103	353	49	78	20	A05				
02/06/01	20:18:40	-69.4950	-33.4590	3.7	334	83	47	236	46	169	17	A05				
02/09/01	01:11:50	-67.8700	-31.3830	4.0	034	48	106	190	44	72	22	A05				
02/21/01	15:20:26	-74.5210	-11.3330	5.7	158	17	85	343	74	91	15	MT5	5.7	83	16	33
03/15/01	11:06:19	-69.5600	-34.8200	4.8	034	51	103	193	41	74	3	A04				
05/07/01	02:24:00	-69.0800	-33.0210	4.1	181	19	77	015	71	94	14	A05				
05/10/01	02:24:00	-67.9560	-32.0720	3.5	276	53	79	115	39	104	20	A05				
05/18/01	04:48:00	-67.7290	-31.7560	3.8	045	39	95	218	51	86	22	A05				
05/18/01	07:12:00	-64.9300	-31.0000	4.3	344	83	19	251	71	173	7	A05				
06/13/01	04:10:53	-66.4550	-27.1770	5.0	209	30	70	052	62	101						
06/20/01	01:26:24	-69.0120	-33.2110	3.8	133	53	33	022	64	138	21	A05				
06/28/01	04:48:00	-67.8730	-31.2470	3.5	023	40	89	204	50	91	15	A05				
06/29/01	22:33:21	-70.3110	-15.3060	5.4	320	36	-65	110	58	-107	10	MT5 SHZ	f 5.4	f 320	f 36	f -65
07/04/01	12:09:10	-65.7270	-17.1910	6.2	088	23	44	316	74	107	14	MT5	6.1	89	34	51
07/08/01	00:00:00	-68.9990	-33.1940	3.6	015	49	96	185	41	83	14	A05				
07/24/01	05:00:17	-69.2450	-19.5180	6.3	014	46	-169	276	82	-44	8	MT5 SHZ	6.4	23	71	187
08/09/01	02:07:01	-72.6810	-14.3120	5.8	305	77	-12	037	79	-167	12	MT5 SHZ	5.9	113	87	13
08/09/01	06:45:39	-71.9910	-15.5910	5.2	318	47	-5	052	86	-137						
08/10/01	17:39:42	-72.7480	-14.3690	5.4	276	46	-76	076	46	-104						
08/12/01	00:16:32	-70.0000	-16.7010	5.2	130	45	-108	334	48	-73	7	SHZ				
09/17/01	00:00:00	-67.7300	-31.5960	4.0	149	57	56	019	46	130	17	A05				
10/12/01	04:21:38	-69.7260	-33.3540	5.3	222	78	171	314	81	12						
11/12/01	02:24:00	-67.5340	-33.1310	4.1	055	48	104	215	43	75	13	A05				
11/24/01	00:00:00	-67.2140	-33.3460	3.6	098	27	147	218	76	66	25	A05				
11/29/01	19:12:00	-66.9630	-32.1130	4.0	016	46	58	238	52	119	15	A05				

Table 2.1 continued

Date	Time	Location			Nodal Plane 1			Nodal Plane 2			Depth	Reference	MT5 solution			
mm/dd/yy	hh:mm:ss	longitude	latitude	Mw	strike	dip	rake	strike	dip	rake	(km)	code	Mw	strike	dip	rake
12/04/01	05:57:19	-72.5210	-15.3740	5.8	239	73	-178	149	88	-17	17	MT5 SHZ	f 5.8	f 239	f 73	f -178
12/05/01	00:00:00	-64.4350	-32.7200	3.8	060	48	96	231	42	83	16	A05				
12/08/01	04:17:22	-72.7100	-15.4190	5.6	315	68	-2	045	88	-158	13	MT5 SHZ	5.7	296	88	329
12/14/01	00:00:00	-67.7600	-31.8500	4.7	024	69	91	201	21	87	21	A04				
12/15/01	07:12:00	-66.8570	-29.3370	4.0	014	41	82	204	49	97	20	A05				
12/18/01	07:12:00	-66.8590	-32.1240	4.5	166	47	88	349	43	92	17	A05				
01/05/02	07:12:00	-68.6100	-33.3130	4.7	061	22	175	156	88	68	26	A05				
01/19/02	19:12:00	-66.1750	-30.3600	4.0	279	61	-15	017	77	210	7	A05				
02/24/02	14:44:13	-70.1320	-16.3750	5.3	134	43	-111	342	51	-72	10	SHZ				
03/10/02	12:00:00	-67.9650	-31.6500	4.0	021	37	95	194	53	86	15	A05				
03/15/02	00:00:00	-64.0900	-30.9080	4.0	356	43	69	204	50	109	18	A05				
04/17/02	04:48:00	-67.8270	-30.3140	4.2	031	31	124	173	65	72	25	A05				
04/27/02	23:53:59	-67.6000	-30.9980	5.2	034	40	98	204	50	83	21	A05				
05/04/02	12:51:49	-64.5530	-23.2130	5.3	180	21	79	011	70	94						
05/28/02	04:04:28	-66.7680	-28.9420	6.0	180	19	55	036	74	101	12	MT5	6	214	31	97
07/02/02	20:21:05	-67.7240	-31.1640	5.5	156	40	1	054	81	129	18	MT5	5.4	143	58	12
08/11/02	12:09:16	-74.6240	-10.6890	5.1	127	42	100	294	49	81	10	MT5	5.2	129	38	122
12/04/02	21:03:07	-67.6379	-30.0902	4.9	285	28	62	135	65	104						
12/13/02	16:31:17	-71.7043	-15.5274	5.3	253	44	-88	071	46	-92	7	SHZ				
05/03/05	19:11:38	-74.6701	-14.8785	5.9	278	55	-4	010	87	-144	32	MT5	5.9	282	55	358
10/31/05	02:10:28	-78.8021	-5.8792	5.4	049	55	166	148	78	36	5	MT5	5.4	f 49	f 57	f 169
11/20/06	14:38:34	-70.2280	-17.6680	5.5	220	41	28	108	72	127	37	MT5	5.4	239	24	72
03/24/07	19:13:55	-70.1590	-19.7970	5.5	103	40	91	282	50	89	24	MT5	f 5.5	f 103	f 40	f 91

Figure 2.2: Continental seismicity of the Central Andes. Base map is 90 m SRTM topography. Earthquake focal mechanism solutions are represented in lower hemispheric projections, where dark quadrants contain compressional motions and the T axis. Accurate event depths are labeled in red. Contours lines represent the depth (labeled in km) below sea-level of the subducting Nazca Oceanic plate. Black points are the six subduction zone earthquakes discussed in Chapter 1.

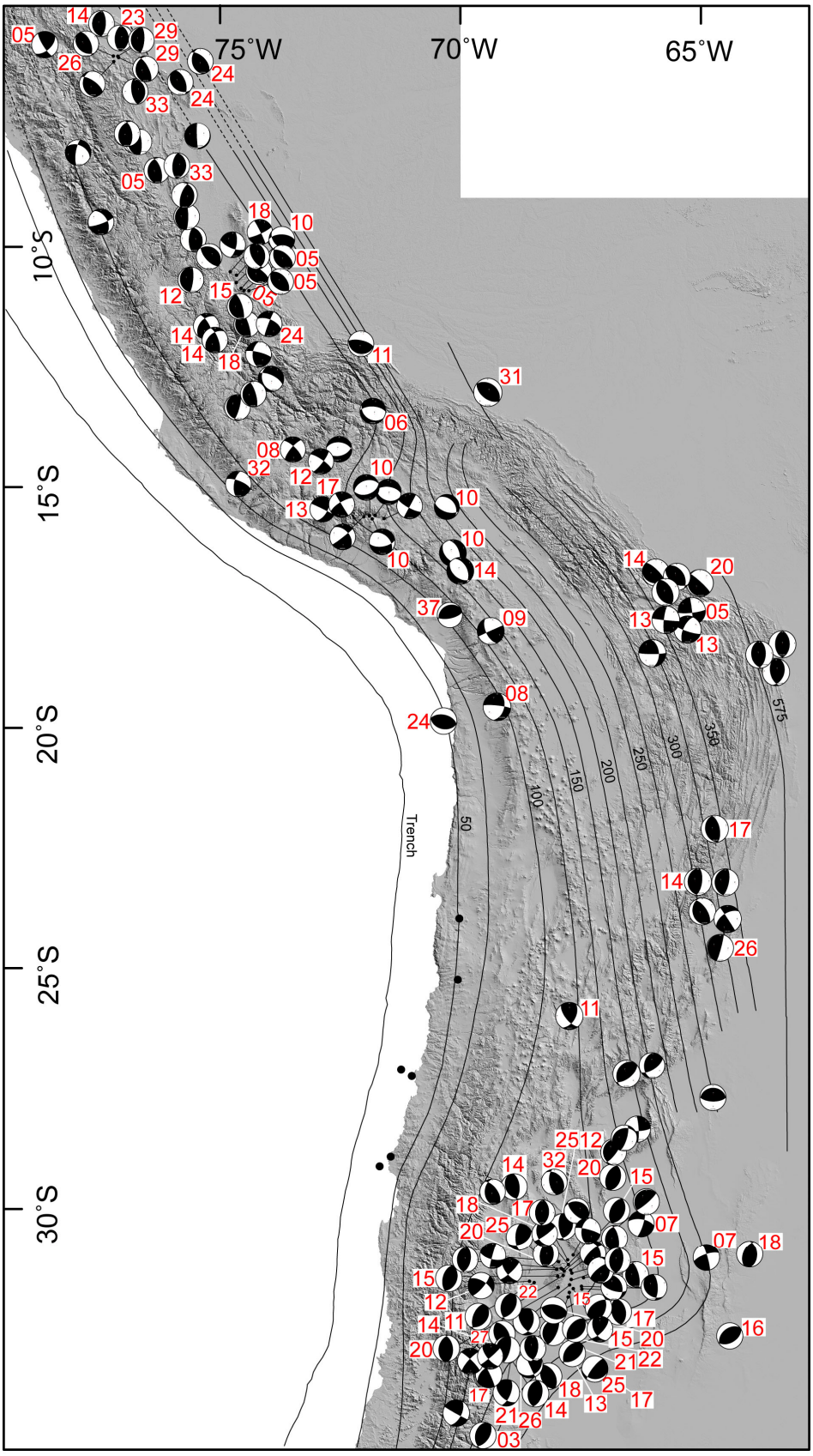
75°W
70°W
65°W
10°S
15°S
20°S
25°S
30°S
Trench
50
100
150
200
250
300
350
575

Centre (ISC), or from the U.S. Geological Survey's National Earthquake Information Center (NEIC). These locations are reported in Table 2.1. Earthquakes with only CMT solutions are included in the table. Their depths are left blank, because they lack accurate depth determination due to reasons such as poor data quality or insufficient data. The events are plotted on subsequent maps to help characterize tectonics of the Central Andes, but they are not considered during integration of subsurface structural data.

Teleseismic waveform analysis

P and SH waveform modeling

Of the 38 events with depths determined in this study, 32 earthquake solutions included *P* and *SH* teleseismic waveform modeling (labeled MT5 in Table 2.1 References column). The procedure involved broadband seismograms from the Global Digital Seismograph Network (GDSN) and change in the frequency response to that of a WWSSN 15–100 long-period instrument using a deconvolution procedure. For this range of periods, seismic waves are relatively insensitive to complexities in local velocity structure, and an event can be modeled as a point source.

The MT5 program [*Zwick, et al.*, 1994] of the algorithm developed by McCaffrey and Abers [1988] and McCaffrey et al. [1991] is used to forward model or invert *P* and *SH* waveform data depending on data quality. The inversion analysis estimates the source time function, moment, strike, dip, rake and depth. Constraining the source to be a pure double-couple, modeling includes *P*, *pP* and *sP* phases on vertical component seismograms in the epicentral distance range 30° to 90°, and *S* and *sS* phases on transverse components in the range 30° to 75°. MT5 corrects amplitudes for geometrical spreading and for anelastic attenuation using a Futterman *Q* operator with

a value t^* of 1.0 s for *P* and 4.0 s for *SH* waves. A simple half-space source structure was used with velocities V_P = 6.5 km/s, V_S = 3.7 km/s and density ρ = 2800 kg/m^3. The Global CMT focal mechanism solution [*Dziewonski, et al.*, 1981] or that reported by the NEIC are used as a starting models and are the initial input parameters into the MT5 program, the "seed" solution.

When data quality and azimuthal distribution is good, the MT5 program is permitted to invert for moment, strike, dip, rake, and depth, while a simple source time function is used (see Chapter 1 for details). Those solutions are reported in the MT5 solution column in Table 2.1, where seismic moment has been converted to moment magnitude, Mw. When data quality, quantity, or azimuthal distribution is poor, a full MT5 inversion solution can be difficult to determine due to factors such as high signal-to-noise ratio or poor focal sphere coverage. Three alternatives to a full solution inversion are then used to constrain source parameters, or at least better constrain source depth. One alternative holds moment, strike, dip, and rake fixed to that of the seed solution and only inverts for a best-fit depth. The second alternative is used when SHZ depth solutions are available (this solution determination is described below). Source depth is held fixed to the SHZ solution and inversion for best-fit focal mechanism and moment are then carried out. Thirdly, if a SHZ depth solution is determined but poor data quality limits inversion, forward modeling is preformed where the moment and focal mechanism are held fixed to the seed solution and the depth is held fixed to the SHZ solution. Quantities that are held fixed during the modeling procedure are labeled with the prefix "f" in the MT5 solution column in Table 2.1. Plots of the waveform inversion solution and sensitivity analyses (see Chapter 1 for examples and descriptions) are made to illustrate the *P* and *SH* waveform modeling solutions. The plots for each earthquake is contained in Appendix

A and ordered according to date. Typical uncertainties in depth solutions are ± 5 km, which is sufficient to describe the depth distribution of continental seismicity.

SHZ depth determination

To provide an additional constraint on focal depth by utilizing a complementary dataset, depth phases (the surface reflections *pP* and *sP*) from short-period, vertical component, teleseismic records are analyzed for some events. Depths determined through this method are labeled SHZ in the Reference column of Table 2.1. The separation times between *pP* and *P* and between *sP* and *P* provides a relatively well-constrained estimate of source depth. When phase arrivals are identified on waveform records, forward modeling using an average velocity structure is performed to determine source depth. The TTIMES program [*Kennett, et al.*, 1995; *Montagner*, 1996] performs the forward modeling of estimated phase arrival times. The differential travel times between *pP* - *P* and *sP* - *P* provided by TTIMES is then compared to the times picked on the seismic record and the depth reported by TTIMES is used as the SHZ depth solution, which was referred to earlier in this section.

Earthquakes in the foreland and Eastern Cordillera

The forelands and Eastern Cordillera of the Central Andes are more seismically active than the plateau or forearc regions (Figure 2.2). To see how deformation is accommodated in these regions along the entire orogen, Figure 2.3 was constructed. It shows P, B, and T axes for all foreland events from 5°S to 35°S in the Central Andes. Contours illustrate 4-sigma intervals after Kamb [1959] using the StereoWin program [*Allmendinger*, 2002]. Analysis of the P axes orientations is consistent with east-west shortening oriented ~ 92°. This orientation deviates from the direction of Nazca-South

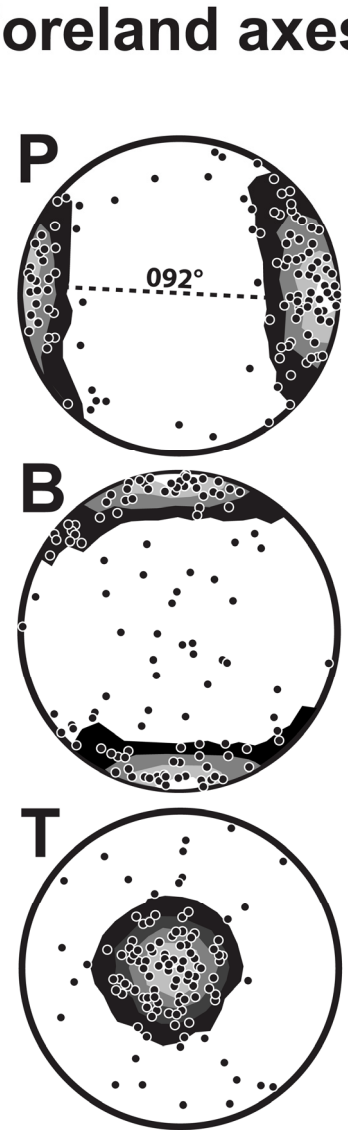

Figure 2.3: P, B, and T axis orientations of foreland earthquakes of the Central Andes. Black dots are the individual axis orientations on a Schmidt equal-area lower-hemisphere projection. Black, dark gray, light gray, and white contours illustrate 4-sigma intervals after Kamb [1959] using the StereoWin program [*Allmendinger*, 2002].

America plate convergence, which is ~ 77° [*Angermann, et al.*, 1999; *Norabuena, et al.*, 1998]. The ~ 15° difference in these directions could be due to the influence of local structure on focal mechanism orientation, the effects of oblique subduction along a curved plate boundary, or complex along-strike variability in Andean deformation. The influence of local structure on the orientation of focal mechanisms is shown to be important later in this chapter.

Continental seismicity above flat subduction

Figure 2.2 shows that the foreland regions above flat subduction remain two of the most seismically active regions of the central Andes consistent with previous findings [e.g., *Chinn and Isacks*, 1983; *Jordan, et al.*, 1983]. Dominant focal mechanism orientation in these regions is compressional with a few strike-slip mechanisms. Figure 2.4 plots the compressional (P) axis orientations for the earthquakes above flat subduction to assess whether orientation of plate convergence or mountain-front geometry control axis orientation. The figure shows individual P axes in gray, a rose diagram analysis of the data in black, and the colored arrows are the trend of plate convergence in red [~77°, *Angermann, et al.*, 1999; *Norabuena, et al.*, 1998] and the perpendicular line to the strike of the mountain front (blue). Each "petal" on the rose diagram is plotted according to axis trends and the size of the petals is proportional to how many axes fall with that trend direction. The strike of the mountain front was taken from the STRM topography. The comparisons do not illustrate a clear conclusion. The Peru P axes are more consistent with the trend of plate convergence, while the Argentine data is slightly more consistent with mountain front geometry.

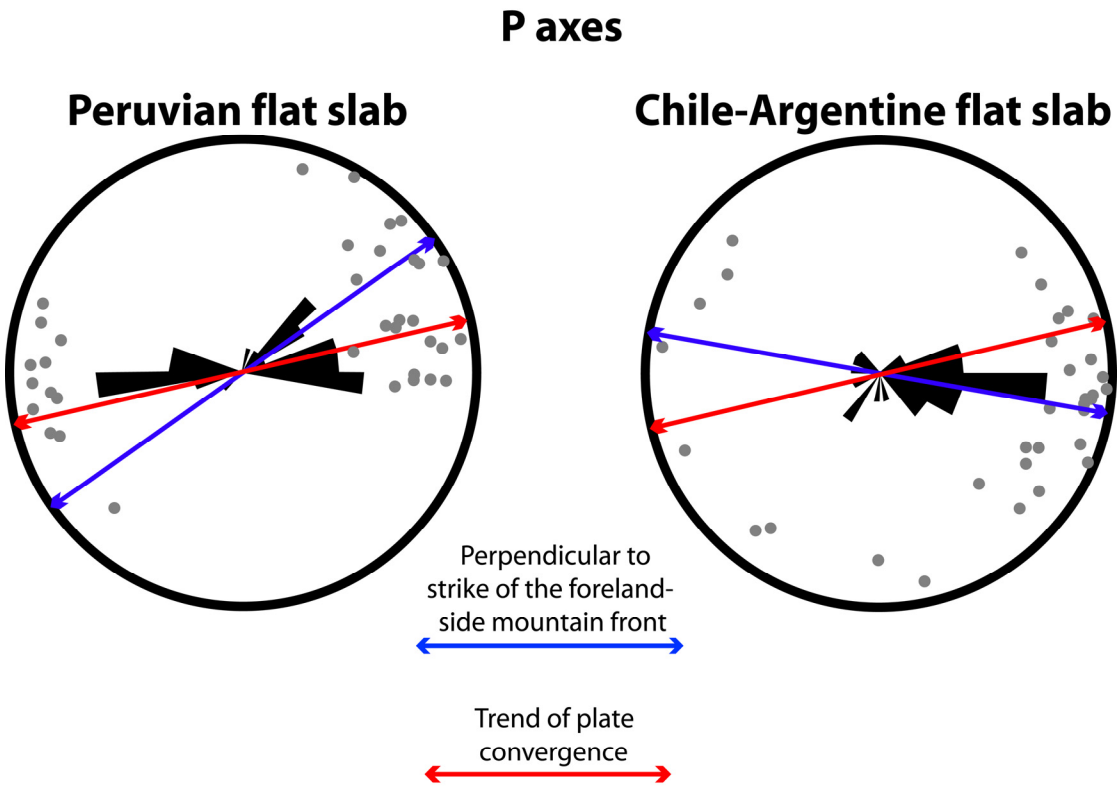

Figure 2.4: Analysis of focal mechanism P axes of Central Andean foreland earthquakes above regions of flat subduction. Plots are lower hemispheric projections. Gray dots are axis orientations for individual earthquakes. Black shapes illustrate a Rose Diagram describing P axis trends. The blue arrows represent the trend perpendicular to the strike of the foreland-side mountain front, which is ~055° for Peru and ~085° Argentina. The red arrows represent the trend of plate convergence between South America and Nazca , ~77° [*Angermann, et al.*, 1999; *Norabuena, et al.*, 1998].

Additionally, these two separate trends are consistent with principle infinitesimal strain axes resolved from GPS data [*Allmendinger, et al.*, 2007], where a dominant east-west compression direction is shown in the Argentine foreland and a roughly northeast-southwest compression direction is resolved in the Peruvian foreland. Therefore, these plots show that it is unclear whether the compressional axis orientation of these large regions is correlates with the trend of plate convergence or the geometry of the foreland-side mountain front, but the focal mechanism P axes orientations do appear consistent with strain directions resolved from GPS velocities. To understand how the individual earthquakes fit into more regional-scale structures, as opposed to broad plate boundary comparisons, the remaining parts of the section integrate the earthquakes with SRTM topography and subsurface structural data at smaller scales.

Argentina from 27° to 35°S

Continental seismicity between 27° and 35°S is predominately located in the foreland region of the Sierras Pampeanas, where reverse basement thrusts dominate the structural style and basement block uplifts dominate the topographic signature. The basement-cored structures are comprised of crystalline Precambrian–Early Palaeozoic rocks. Uplift resulted from compression during late Cenozoic time and the location of deformation appears largely controlled by older structural fabrics. Most of this area is made up of pre-Carboniferous accreted terranes. The major terrane sutures have experienced periods of extensional and compressional deformation since the Jurassic [e.g., *Ramos, et al.*, 2002 and references therein]. The Sierras Pampeanas province is composed of uplifted and tilted formations separated by broad and relatively undeformed basins [e.g., *Jordan, et al.*, 1983]. These uplifts are considered a modern

analogue to the Laramide uplifts of the western United States [*Jordan and Allmendinger*, 1986; *Jordan, et al.*, 1983].

Numerous studies have contributed to characterizing crustal seismicity in the region: Alvarado et al. [2005], Alvarado and Beck [2006], Assumpçao and Araujo [1993], Chinn and Isacks [1983], and Kadinsky-Cade et al. [1985], whose data are included in Table 2.1. Smalley and Isacks [1990], Regnier et al. [1992], and Smalley et al. [1993] analyzed data from local seismic networks. Although data (e.g., locations, magnitudes) from those studies was not available, their findings are also consistent with the following interpretations. Earthquakes in the region of the Sierras Pampeanas range in depth from the near surface to a maximum of ~ 45 km. Seismic imaging reveals Moho depths range from ~ 40 km in the east to ~ 60km in the west [*Calkins, et al.*, 2006; *Fromm, et al.*, 2004; *McGlashan, et al.*, 2008]. The deepest seismicity [~ 45 km, *Smalley and Isacks*, 1990] occurs beneath the Sierras Pampeanas basement uplifts where Moho depths reach ~ 50 km, so the entire crust appears seismically active.

This study analyzes structures of the Sierras Pampeanas in two places: at ~ 29°S in Figures 2.5 and 2.6 and at ~ 31°S in Figure 2.7 and 2.7, where each latitude has a map view image and accompanying cross sectional view image. Please note that cross section transect labels (A-A' through J-J') are ordered alphabetically north to south throughout the Central Andes. A-A' is located in northern Peru at ~ 6°S and will be discussed later in this chapter, and J-J', the southernmost transect, occurs at ~ 31°S. The map view images (Figures 2.4 and 2.6) illustrate the topographic expressions of the Sierras Pampeanas' uplifted and tilted formations separated by broad and relatively undeformed basins consistent with long wavelength deformational formations of basement thrust structures.

Figure 2.5: Map view of the Sierras Pampeanas at ~ 29°S. The black line and end labels illustrate the location of the cross section shown in Figure 2.6. The following description applies for each map view image in this chapter. For conciseness, the description is only explained once. SRTM 90 m topography base map with blue and green areas of low topography grading into areas of high topography in white and orange. Earthquake focal mechanism solutions are represented in lower hemispheric projections, where dark quadrants contain compressional motions. Accurate events depths are labeled in red. In accompanying cross sections, earthquake locations were projected into the transect perpendicular to the strike of the cross section. White dashed lines on maps indicated where non-perpendicular focal mechanism projections were used and the line shows the orientation of the projection. This is usually done when topographic trends indicated it is warranted.

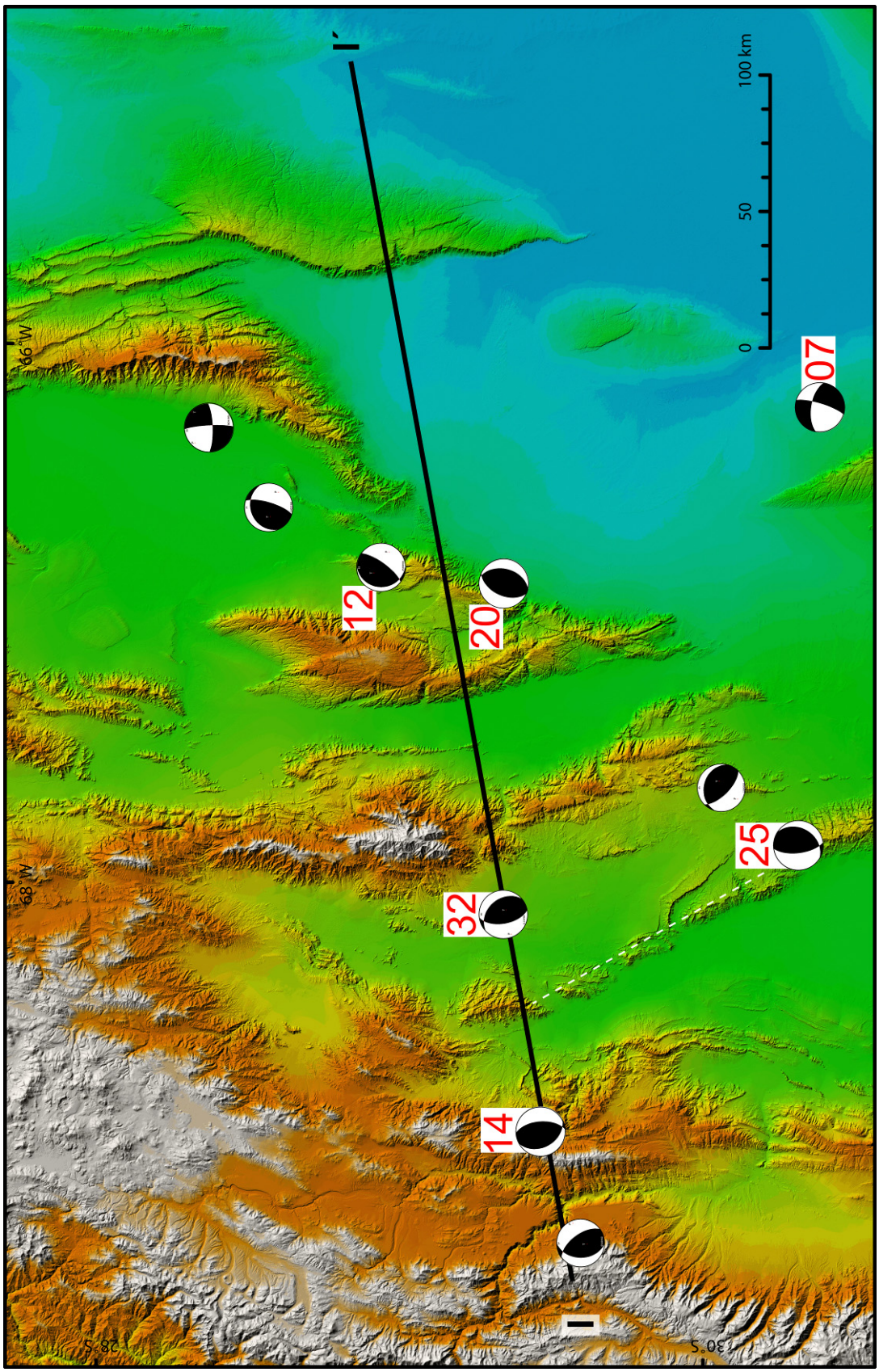
100 km
50
0
07
12
20
25
32
14
69°W
68°W
28°S
30°S

Figure 2.6: Cross sectional view of the Sierras Pampeanas at ~ 29°S, see Figure 2.5 for map location. (top) Ramos et al.'s [2002] structural interpretation at 29°S. (bottom) Topographic profiles at 10:1 and 1:1 elevation to length scales along with an interpretation of projected earthquake focal mechanism orientations and the structures illustrated in the top section. All profile images throughout this chapter have subsurface depth to length scales of 1:1, labels describe elevation to length scales, and dashed black lines are sometimes drawn on focal mechanisms to emphasize fault plane orientations.

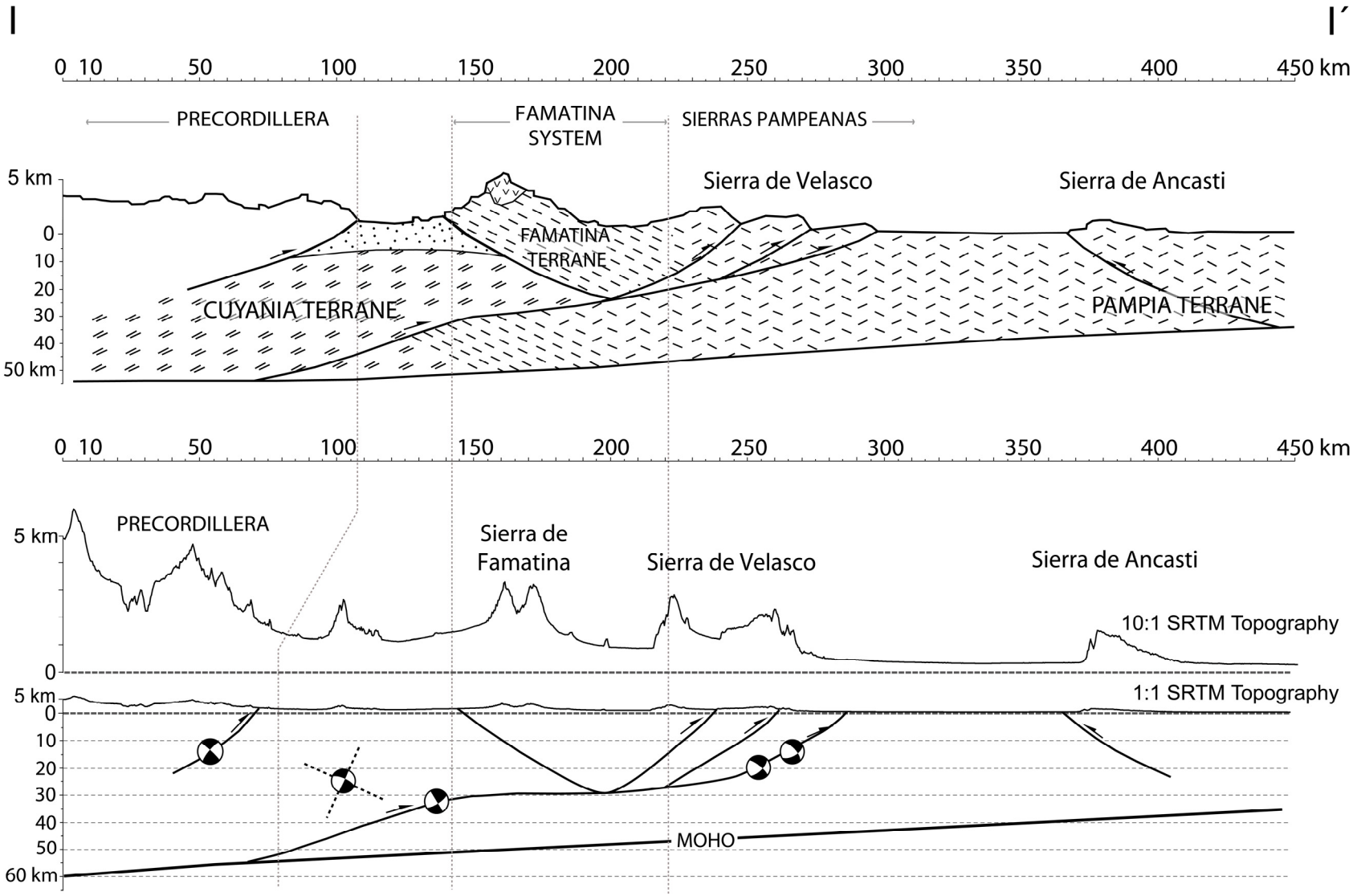
I
I´
0 10 50 100 150 200 250 300 350 400 450 km
PRECORDILLERA
FAMATINA SYSTEM
SIERRAS PAMPEANAS
5 km
0
10
20
30
40
50 km
Sierra de Velasco
Sierra de Ancasti
FAMATINA TERRANE
CUYANIA TERRANE
PAMPIA TERRANE
0 10 50 100 150 200 250 300 350 400 450 km
5 km
0
PRECORDILLERA
Sierra de Famatina
Sierra de Velasco
Sierra de Ancasti
10:1 SRTM Topography
5 km
0
10
20
30
40
50
60 km
1:1 SRTM Topography
MOHO

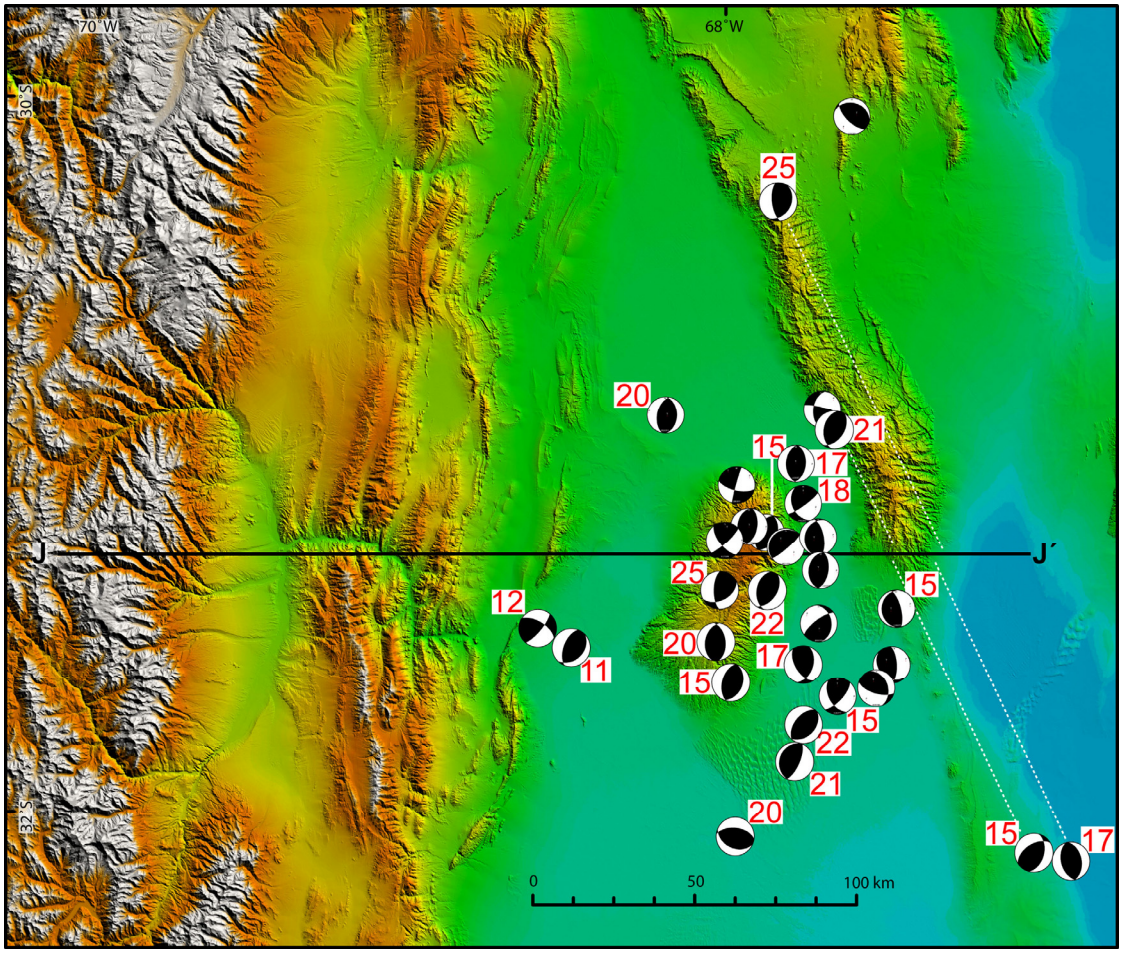

Figure 2.7: Map view of the Sierras Pampeanas at ~ 31°S. The black line and end labels illustrate the location of the cross section shown in Figure 2.8.

Figure 2.8: Cross sectional view of the Sierras Pampeanas at ~ 31°S, see Figure 2.7 for map location. (top) 10:1 topography with projected focal mechanisms. (bottom) 1:1 topography with projected focal mechanisms and select fault interpretations from Ramos et al.'s [2002] structural interpretation at 31°S.

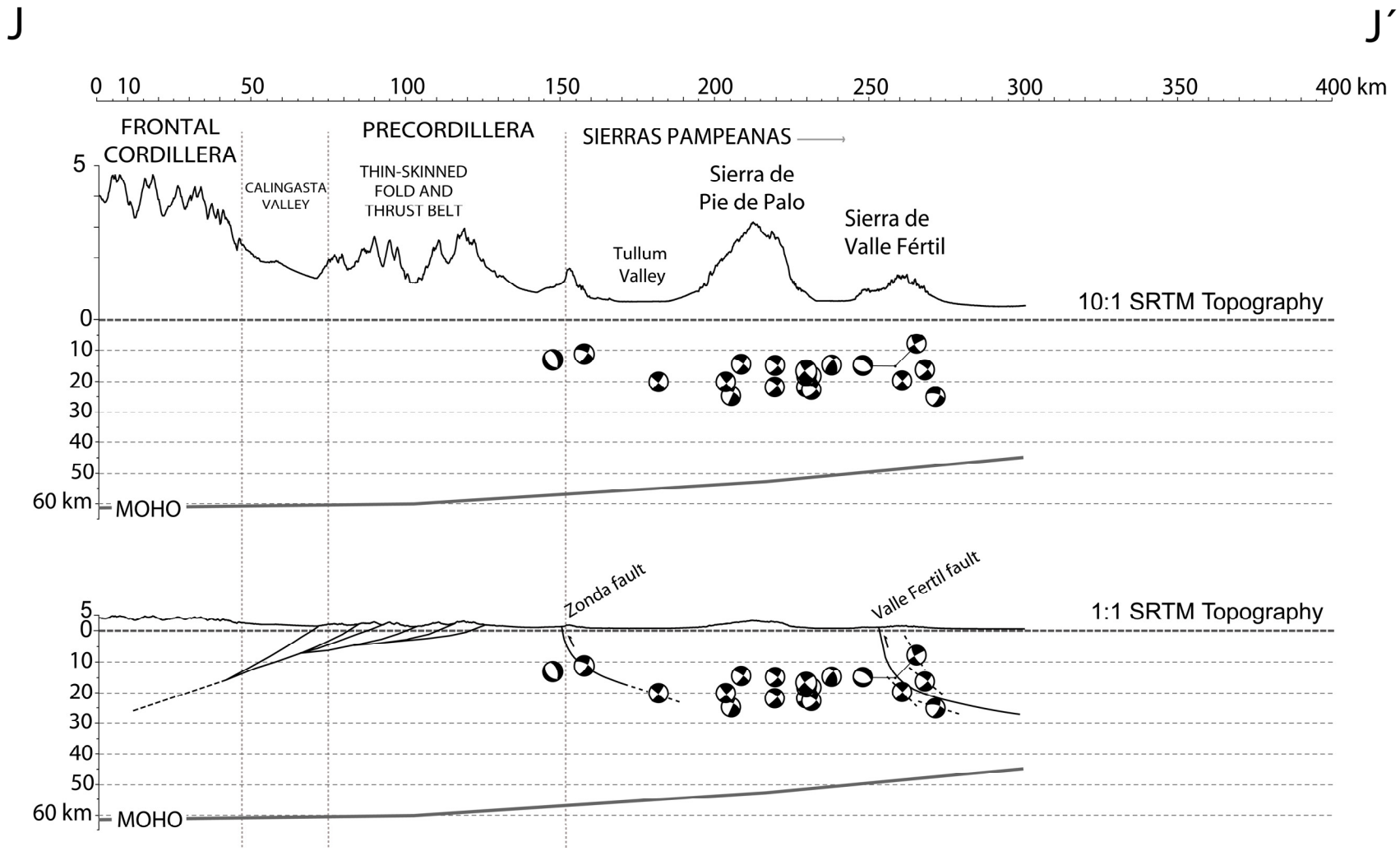
J
J´
0 10 50 100 150 200 250 300 350 400 km
FRONTAL CORDILLERA
PRECORDILLERA
SIERRAS PAMPEANAS
CALINGASTA VALLEY
THIN-SKINNED FOLD AND THRUST BELT
Tullum Valley
Sierra de Pie de Palo
Sierra de Valle Fértil
10:1 SRTM Topography
5
0
10
20
30
40
50
60 km
MOHO
Zonda fault
Valle Fertil fault
1:1 SRTM Topography

I-I' – Sierras Pampeanas at 29°S - Figure 2.5 is a map view image of the northern Sierras Pampeanas transect (I-I') at ~ 29°S and Figure 2.6 is the corresponding cross sectional view. The transect crosses the Sierras de Famatina, Velasco, and Ancasti and two interpreted terrane boundaries, one between the Cuyania and Famatina Terranes and one between the Famatina and Pampia Terranes (Figure 2.6). Five earthquakes with well-determined depths could potentially be related to structures controlling the uplift of these mountains and their depths range from 12 to 32 km (Figure 2.5). Ramos et al. [2002] developed a structural interpretation at 29°S, which is summarized in Figure 2.6. Earthquake mechanism orientations are predominantly thrust with steeply dipping fault planes of variable strike. Two strike-slip mechanisms occur along ~66°W longitude, one with at a depth of 7 km and the other with an unknown depth. They both occur well off the transect in flat basins, so distance from the cross section and lack of surface expression of fault-controlled structures give little indication how the strike-slip fault motions fit with the structural interpretation. Subsurface seismic imaging data are not available to constrain subsurface geometries through this area, but Ramos et al. [2002] reviewed surface geology that indicates a double-wedge thrust system likely controls the uplift of the mountains and coincides with major terrane boundaries (Figure 2.6). Four of the five events mapped on the cross section in Figure 2.6 have fault plane orientations and fault motions consistent with thrusting along Ramos et al.'s [2002] thrust system. Two events occurred beneath the Velasco system, an imbricate thrust system accommodating motion between the Famatina and Pampia terranes. One event occurred at 32 km depth consistent with the shoaling basement thrust between the Cuyania and Famatina terranes. Equally, it could be consistent with an east-dipping reverse fault bounding the west side of the Sierra de Maz located at ~ 100 km in the bottom section of Figure 2.6. The 14 km deep event maps at the décollement level of the thin-skinned structures of the Argentine Precordillera. An

event at ~ 25 km between the Precordillera and Famatina system does not correlate to any interpreted structures. However, the earthquake occurs below the Sierra de Maz consistent with the topographic trend of the Valle Fertil lineament shown in Figure 2.4 by the white dashed line. The high beneath the earthquake may relate to the high at approximately 110 km on Figure 2.6, bottom plot. The event was projected from the farthest distance onto the transect. This calls into question whether the event should be projected onto the section, but the map view topographic trends suggest that the event may be related to basement structures controlling topographic highs not captured in the Ramos et al. [2002] interpretation. One additional event (not pictured) occurred on 07 September 2004 at a depth of 8 km [Alvarado, personal communication] associated with thrusting beneath the Sierrra de Ambato, which is located between and slightly north of the Sierras de Velesco and Ancasti.

J-J' – southern Sierras Pampeanas at ~ 31°S - Figure 2.7 is a map view image of the southern transect (J-J') at ~ 31°S and Figure 2.8 is the corresponding cross sectional view. The transect is considered one of the most complete exposed sections of the entire Sierras Pampeanas [*Ramos, et al.*, 2002] and has been studied extensively by local seismic network studies [*Alvarado, et al.*, 2005; *Regnier, et al.*, 1992; *Smalley and Isacks*, 1990; *Smalley, et al.*, 1993]. Seismicity along the profile is concentrated between the Zonda and Valle Fértil fault systems, with the largest number of events occurring beneath Sierras de Pie de Palo (Figure 2.8). Neotectonic structures and Quaternary active faulting are known along the west-bounding fault of the Sierra de Valle Fértil and present-day tectonics and uplift are concentrated further west in the Sierra de Pie de Palo [*Ramos, et al.*, 2002]. Figure 2.7 and 2.8 are consistent with such similar neotectonic activity. Five earthquakes with well determined depths occurred beneath the Valle Fértil system, four of those events have thrust mechanisms with

fault planes consistent with compression along its west-bounding basement structure (Figure 2.8). Alvarado and Beck [2006] used teleseismic waveform modeling to determine source parameters for two historical earthquakes, the January 15, 1944 event (Mw 7.0) and the June 11, 1952 event (Mw 6.8). Both earthquakes have depths of < 12 km and are the two westernmost events in Figure 2.8. Alvarado and Beck's [2006] profile interpretation of the January 15, 1944 event is consistent with the geologic model proposed by Ramos et al. [2002] between the Precordillera and the Sierra Pie de Palo, where one major east-dipping thrust basement fault extending up to 10–15 km depth beneath the Tulum valley with several thrust branches as it becomes shallower, the Zonda fault system. A diffuse distribution of seismicity from ~ 5 to 15 km depth was also seen in the same region by Smalley et al. [1993], which may be related to the east-dipping thrust structures.

The most seismically active uplift of the Sierras Pampeanas is the Sierra de Pie de Palo [e.g., *Jordan and Allmendinger*, 1986; *Siame, et al.*, 2005]. This is illustrated in Figure 2.8, as well as in a more detailed view in Figure 2.9. Deformation of Pie de Palo started at approximately 3 Ma and continues to the present with a shortening rate of about 4 mm/yr and an uplift rate of 1mm/yr [*Brooks, et al.*, 2003; *Ramos and Vujovich*, 2000]. Beneath Pie de Palo the predominance of thrust-type focal mechanisms suggests active compression. Deformational structures with different geometries have been proposed to control deformation beneath Pie de Palo. Two bands of seismic activity constrained by a local network study was used to propose that two décollement levels may accommodate deformation beneath Pie de Palo, one at about 12 to 15 km depth and another at 22 to 25 km [*Regnier, et al.*, 1992]. Further, Ramos and Vujovich [2000] and Ramos et al. [2002] proposed the décollements were part of an east-vergent basement wedge (Figure 2.9 middle), so that Pie de Palo is a

Figure 2.9: Detailed cross sectional view of the seismicity and proposed structures beneath Sierre de Pie de Palo. Length scale on the top is the same as in Figure 2.8 and illustrates the subset of topographic data from that figure that was used to create these profiles. The events outlined in red, yellow, and blue are the three largest historic earthquakes to occur in this region. Their outline colors correspond to the red, yellow, and blue descriptions in the figure. (top) Profile shows earthquake focal mechanisms projected into a depth profile with limited structural interpretation. The Ramos et al., 2002 profile shows the earthquakes and how they relate relative to the structural interpretation of Ramos and Vujovich [2000] and Ramos [2002]. The Siame et al., 2005 profile shows how the earthquakes relate to the proposed structures of Siame et al. [2005]. Moho geometry was derived from Calkins et al. [2006] and McGlashan et al. [2008].

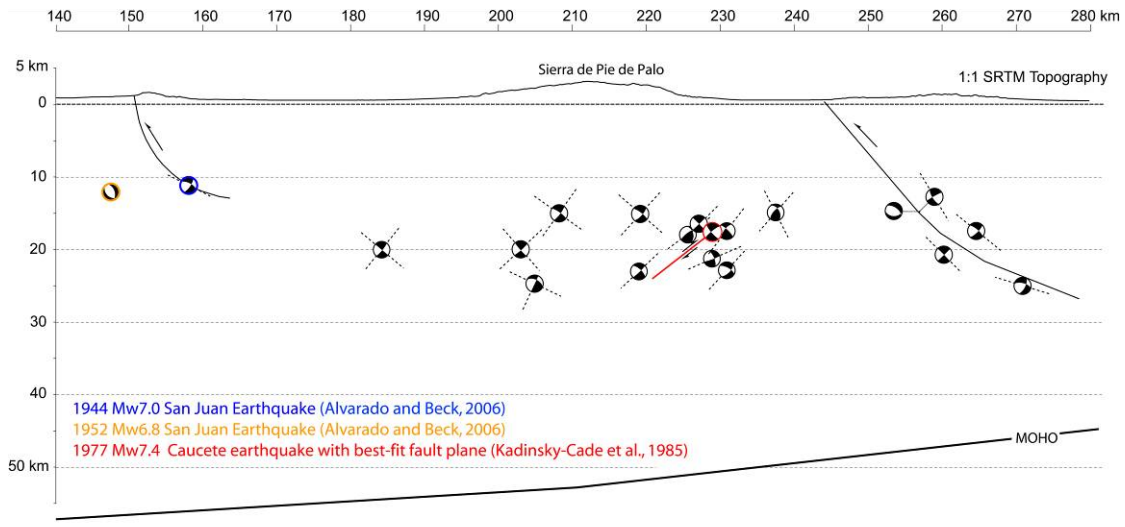
140 150 160 170 180 190 200 210 220 230 240 250 260 270 280 km
5 km
0
10
20
30
40
50 km
Sierra de Pie de Palo
1:1 SRTM Topography
1944 Mw7.0 San Juan Earthquake (Alvarado and Beck, 2006)
1952 Mw6.8 San Juan Earthquake (Alvarado and Beck, 2006)
1977 Mw7.4 Caucete earthquake with best-fit fault plane (Kadinsky-Cade et al., 1985)
MOHO

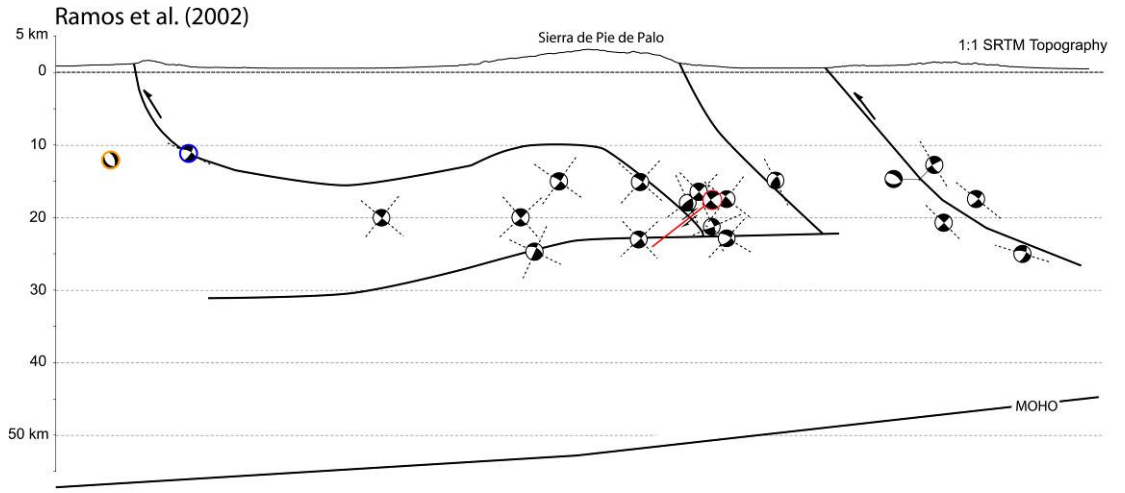
Ramos et al. (2002)
5 km
0
10
20
30
40
50 km
Sierra de Pie de Palo
1:1 SRTM Topography
MOHO

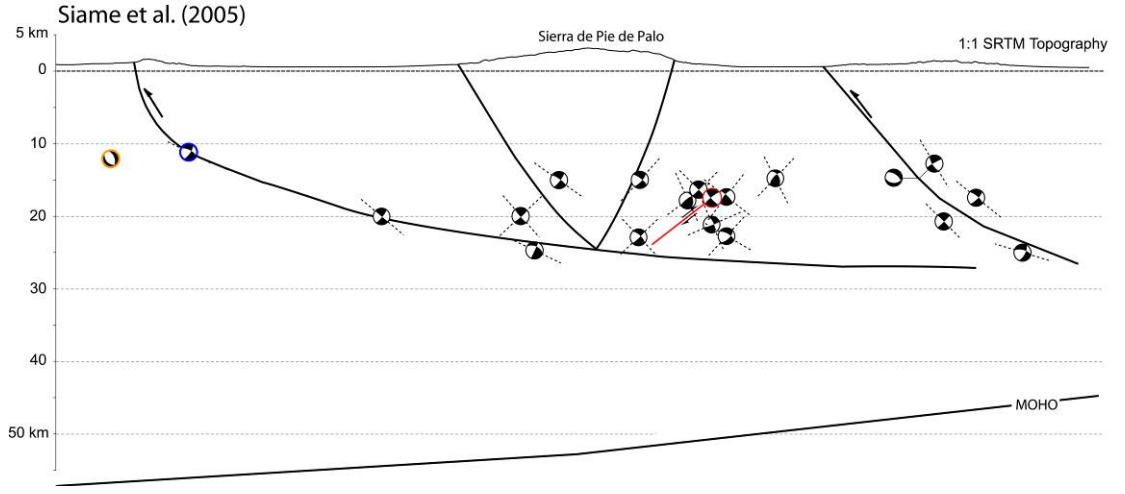
Siame et al. (2005)
5 km
0
10
20
30
40
50 km
Sierra de Pie de Palo
1:1 SRTM Topography
MOHO

basement anticline above a mid-crustal wedge. Ramos et al.'s interpretation is consistent with the rounded topography of Pie de Palo, which is suggestive of a large wavelength basement fold (Figure 2.7). Siame et al. [2005] proposed Pie de Palo is bounded to the east and west by faults with opposing dips, so that Pie de Palo is a pop-up basement block (Figure 2.9 bottom).

Earthquake hypocentral locations collected in this chapter do not resolve two bands of activity, as seen by Regnier et al. [1992]. The earthquakes show one band. Events occur from 15 to 25 km beneath Pie de Palo (Figure 2.8), roughly between the proposed décollement levels. Kadinsky-Cade et al. [1985] combined leveling data and seismic observations to study the 1977, Ms 7.4 Caucete and constrain rupture parameters. Best-fit fault rupture was determined to have occurred on a west-dipping fault from ~17 to 25 km depth (Figure 2.9). Neither structural interpretation illustrated in Figure 2.9 fits with focal mechanism fault plane orientations or the best-fit fault rupture geometry of the 1977 Caucete earthquake. However, as indicated by the range in depths of the earthquakes in local and teleseismic studies and the best-fit rupture geometry of the 1977 Caucete earthquake, the depth range between 12 to 25 km appears to be accommodating a significant about of diffuse deformation. Earthquake focal planes do not map into a simple geometry, but the depths of the earthquakes and the mid-crustal depth of the proposed basement wedge structure are consistent. So an interpretation may be that the earthquakes are reflecting diffuse deformation associated with the proposed basement wedge structure of Ramos and Vujovich [2000] and Ramos et al. [2002] rather than illustrating controlling master faults.

Peru from 5°S to 14°S

The foreland of Peru is largely dominated by the Subandean zone, which includes the Santiago and Huallaga basins, the Ucayali basin, and the basement highs of the Shira uplift (Figure 2.10). The Subandean zone is considered an active fold and thrust belt that developed since the Miocene [*Mathalone and Montoya R*, 1995; *Megard*, 1987]. It is made up of thrust-related anticlines spaced ~ 25 km apart. Elevations reach ~ 2 km near the Eastern Cordillera and decrease to the east. The Ucayali basin extends between 7° and 12°S latitudes and belongs to the greater Amazonian foreland basin. South of Ucayali, basement-involved thrusting builds the Shira uplifts. The Eastern Cordillera bounds the hinterland side of the foreland region, where elevations can reach ~ 6 km and vast basement blocks are cut by numerous subvertical longitudinal and transverse faults [*Megard*, 1987].

Figure 2.10 is a map view of continental seismicity of the Peruvian Andes above flat subduction. A-A' through E-E' are different cross sectional views used to interpret how crustal seismicity relates to the deformational structure zones. Most earthquakes are located in the foreland regions, while a lesser number appear in the hinterland. Two oblique normal fault events with undetermined depths appear associated with Cordillera Blanca detachment fault of western Peru. This detachment fault has unroofed an ~ 8 Ma batholith, which now creates the highest mountain range in Peru [*McNulty and Farber*, 2002; *McNulty, et al.*, 1998]. Mechanisms are predominantly thrust in the foreland regions with three strike-slip events occurring west of the Shira uplift. In contrast to the foreland regions, six oblique slip events, two thrust events, and two normal-type earthquakes occurred beneath the hinterland regions elucidating a mixture of possible stress regimes at high elevations. Earthquakes range in depth

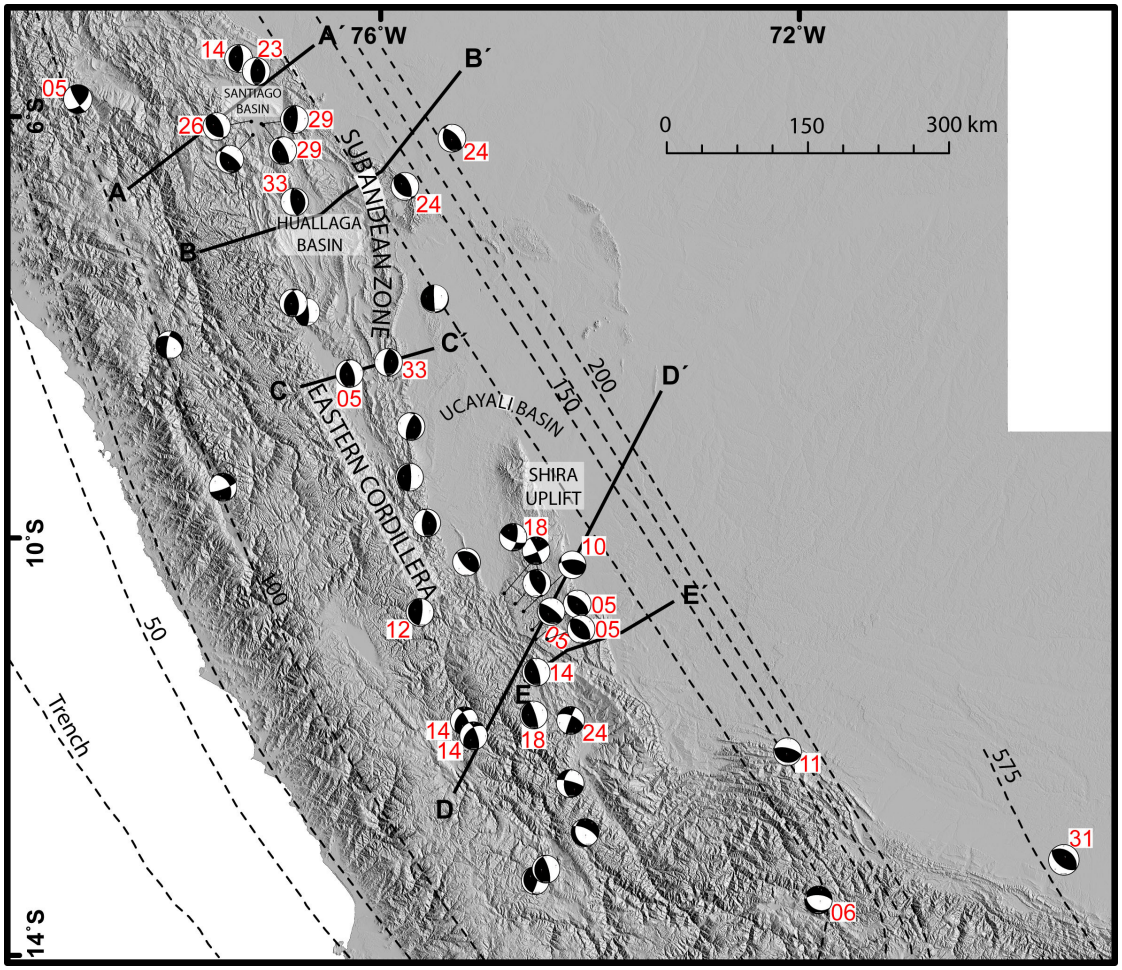

Figure 2.10: Continental seismicity of the Peruvian Andes above flat subduction. A-A' and B-B', C-C', D-D', and E-E' are different cross sectional views shown in Figures 2.11 and 2.12, 2.13, 2.14 and 2.15, and 2.16 and 2.17, respectively.

from 5 to 33 km in the foreland regions and from 5 to 14 km beneath the Eastern Cordillera.

A-A' and B-B' – the Santiago and Huallaga basin regions - Figures 2.11 and 2.12 are maps and cross section images of the northernmost extent of this study's area of interest, so they show areas involving cross sections A-A' and B-B'. These sections capture relationships between seismicity and deformational structures of the Subandean regions of the Santiago and Huallaga basins. These regions are comprised of broad, Triassic-salt-related thin-skinned fold and thrust belt with inverted basement thrusts at their eastern edge which also underlie the thin-skinned structures in some places [*Hermoza, et al.*, 2005; *Mathalone and Montoya R*, 1995]. The basement thrusts are interpreted as inverted graben structures of Permian-Triassic age [*Hermoza, et al.*, 2005; *Mathalone and Montoya R*, 1995]. Earthquakes occurred at mid- to lower crustal depths, from 14 to 33 km, and one event occurred in the Eastern Cordillera at a shallow depth (5 km).

Four earthquakes occurred beneath the Santiago basin and two additional events occurred at it northern edge (A-A'). Although the basin shows little surface expression of deformational structure, deformation from mid- to lower crustal depths beneath the basin appears to be occurring. No interpretation of subsurface structure beneath the basin could be found, but farther north Mathalone et al. [1995] interprets a décollement at a depth of ~ 10 km underlying the northern Santiago basin, so the thrust earthquakes at depths of 14 to 29 km would locate in basement thrusts underlying the thin-skinned basin. Additionally, seismic imaging beneath the neighboring Huallaga basin provides indications of what types of blind fault structures may be rupturing at these depths. Lastly, A-A' illustrates that the 5 km deep

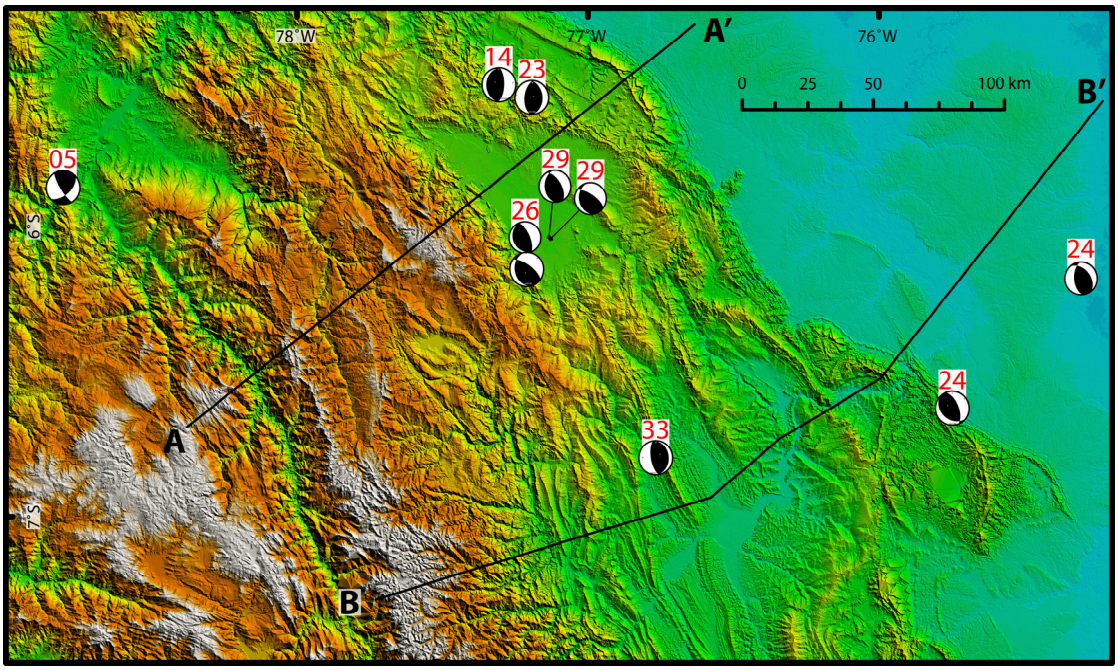

Figure 2.11: Map view of the cross sections A-A’ and B-B’ shown in Figure 2.12.

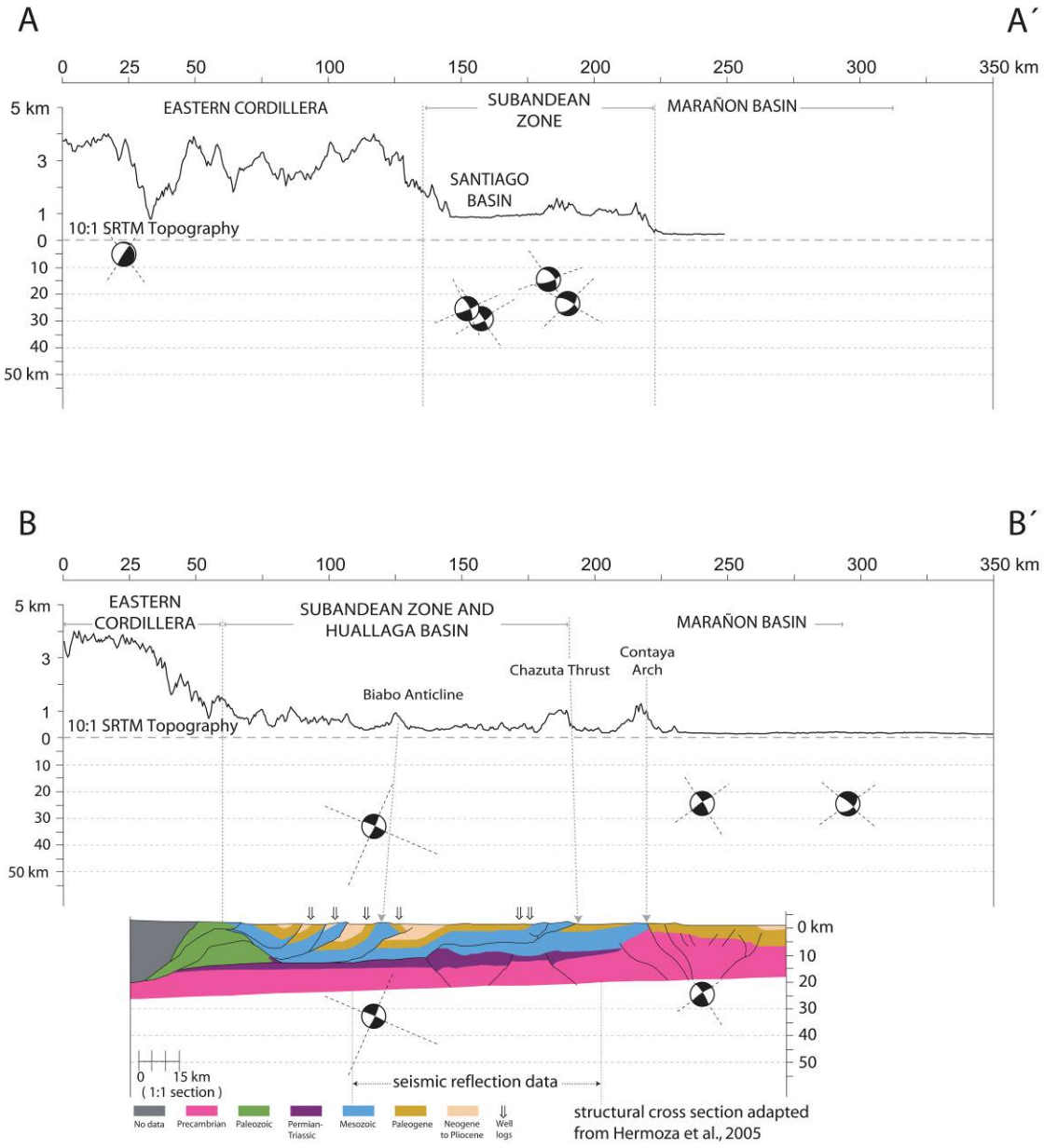

Figure 2.12: Cross section views of A-A' and B-B', see Figure 2.11 for map locations. (A-A') 10:1 elevation with projected focal mechanisms. (B-B') 10:1 elevation with projected focal mechanisms. Beneath B-B' is the balanced cross section interpretation of Hermoza et al. [2005] and projected earthquake mechanisms with respect to structures.

earthquake beneath the Eastern Cordillera has steep focal plane solutions consistent with subvertical faults typical of this region and a strong NW-SE linear topographic trend is apparent on the SRTM topography suggesting that the NW-SE oriented focal plane is likely the fault plane of this earthquake.

B-B' crosses the Eastern Cordillera, the Subandean zone of the Huallaga basin, and the bounding basement structures of the Contaya arch. Hermoza et al. [2005] constructed a balanced cross section along this transect based on subsurface seismic imaging. The section maps near where three moderate-sized earthquakes occurred at mid- to lower crustal depths, so the events are likely the result of basement deformation. Of these events, the westernmost earthquake occurs beneath the well imaged décollement of characteristic Subandean thin-skinned fold and thrust belt structures indicating basement shortening beneath the shallow features. Another earthquake maps within the Contaya arch basement structure that bounds the Subandean zone in the area. The third event is located off the Hermoza et al. section, but its hypocentral location places the event at 24 km depth beneath the relatively undeformed Marañon basin. This event likely indicates basement-involved deformation with minimal surface expression. These findings are consistent with the interpretation that thrust-type seismic deformation at mid- to lower crustal depths beneath the Santiago, Huallaga, and Marañon basins occurs in basement rocks along inverted Permo-Triassic rift structures.

C-C' – Peruvian foreland at 8°S - Transect C-C' (Figure 2.13) is located from approximately 8.5° to 8°S crossing from the Eastern Cordillera into the Subandean zone. This section location was chosen because two earthquakes with well-determined depths occurred along it. No associated known subsurface structural data exist for this

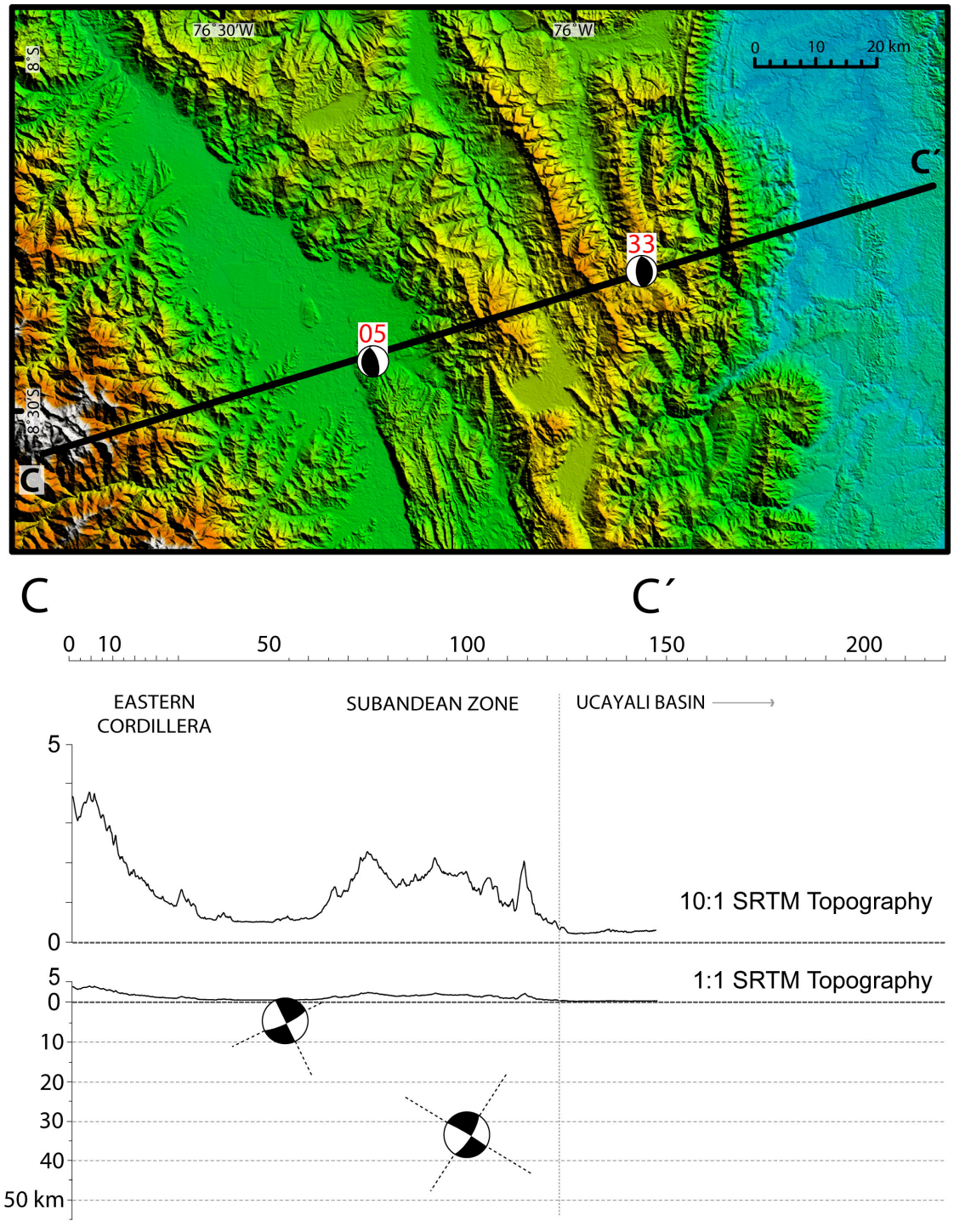

Figure 2.13: (top) map view location of cross section C-C' (bottom).

region, but some information can be gleaned from relating the events within the topography profile and map. The two earthquakes occurred at 5 and 33 km depth. The 33 km depth event occurs beneath Subandean-type structures. The wavelength of these ranges is < 25 km consistent with thin-skinned structures similar to interpreted thin-skinned structures around the Huallaga basin in Figure 2.11. The depth of this event places this event in the lower crust, so similar to events beneath Santiago and Huallaga this event indicates basement deformation of the lower crust beneath thin-skinned structures. The 5 km deep event occurs in a transitional area between the Subandean zone and Eastern Cordillera. The event also occurs were a basin to the north meets a presumed thin-skinned range system to the south. With these four different types of provinces intersecting, it is difficult to categorize whether this event occurred beneath a Subandean-type region or that of the Eastern Cordillera. Hermoza et al.'s [2005] regional structural map figure shows an east-dipping fault bounding this range. With regard to the earthquake focal planes, this is consistent with slip on the steeply dipping focal plane and subvertical shallow deformation is consistent with patterns seen in the Eastern Cordillera and not the Subandean zone. Therefore, the topography and seismicity suggest that the 5 km event is likely associated with Eastern Cordillera-type deformational structures.

D-D' – the Shira uplifts - From southwest to northeast, profile D-D' crosses the Eastern Cordillera, Subandean zone, Shira uplifts, and the Ucayali basin (Figure 2.14). The profile is oriented perpendicular to the western boundary of the large Shira uplift, also referred to as Shira mountain. Figure 2.14 shows the profile map orientation on the top and the 10:1 and 1:1 topographic cross sections on the bottom. North of the section James and Snoke [1994] calculated estimates of depth to the base of the crust and found Moho depth of 35 km beneath the Ucayali basin deepening to 50 km at the

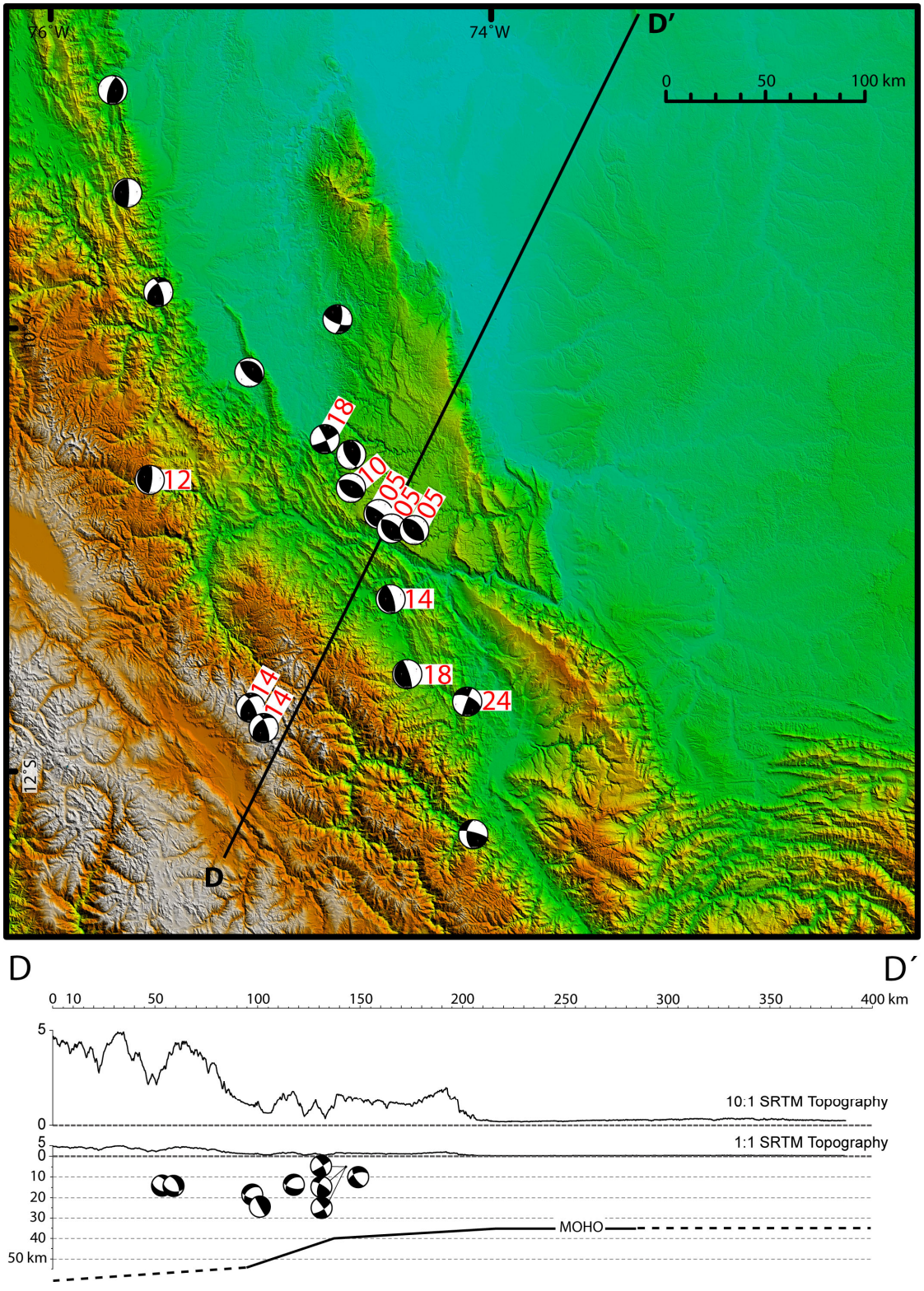

Figure 2.14: (top) map view location of cross section D-D' (bottom).

edge of the Eastern cordillera. Eleven earthquakes in this region have well-constrained depth estimates. Five of those events cluster around the western side of the Shira mountain and have shallow to mid-crustal depths of 5 to 18 km. Three events occur within the Subandean zone between Shira and the Eastern Cordillera at mid-crustal depths of 14 to 24 km likely occurring on décollement or within basement structures beneath the thin-skinned Subandean structures. Three events with well-determined depths occur beneath the Eastern Cordillera. The events occur from 12 to 14 km depth.

The Shira uplifts provide a unique opportunity for integration of seismic, topographic, and structural data (Figure 2.15). The uplifts are a series of tilted fault blocks. The short wavelength (< 25 km) of the tilted blocks along E-E' suggests they are fault-controlled at a shallow level, but the larger Shira mountain has a longer topographic wavelength which may indicate deeper controlling structures. Shallow and mid-crustal seismicity are clearly associated with its tectonic structures with youthful topographic expression. Although the extremely wet climate in this rain forest region would rapidly erode sharp topography, the tectonic signature is quite strong. Fluvial incision into the low relief surfaces of the uplifted and tilted thrust blocks is clearly youthful and the bounding fault scarps are sharp and little eroded. Six earthquakes trace the western side of the Shira mountain and four of those are thrust mechanisms with well-determined depths and fault plane consistent with the trend of the western edge of Shira.

Nodal plane geometries of the three 5 km depth events and the 10 km event were used to investigate Shira's south-bounding structure using fault geometry reconstruction by assuming a tilted fault block and listric fault geometry [e.g., *Jordan and Allmendinger*, 1986]. This is illustrated in the d-d' profile (Figure 2.16). d-d' is a subset of profile

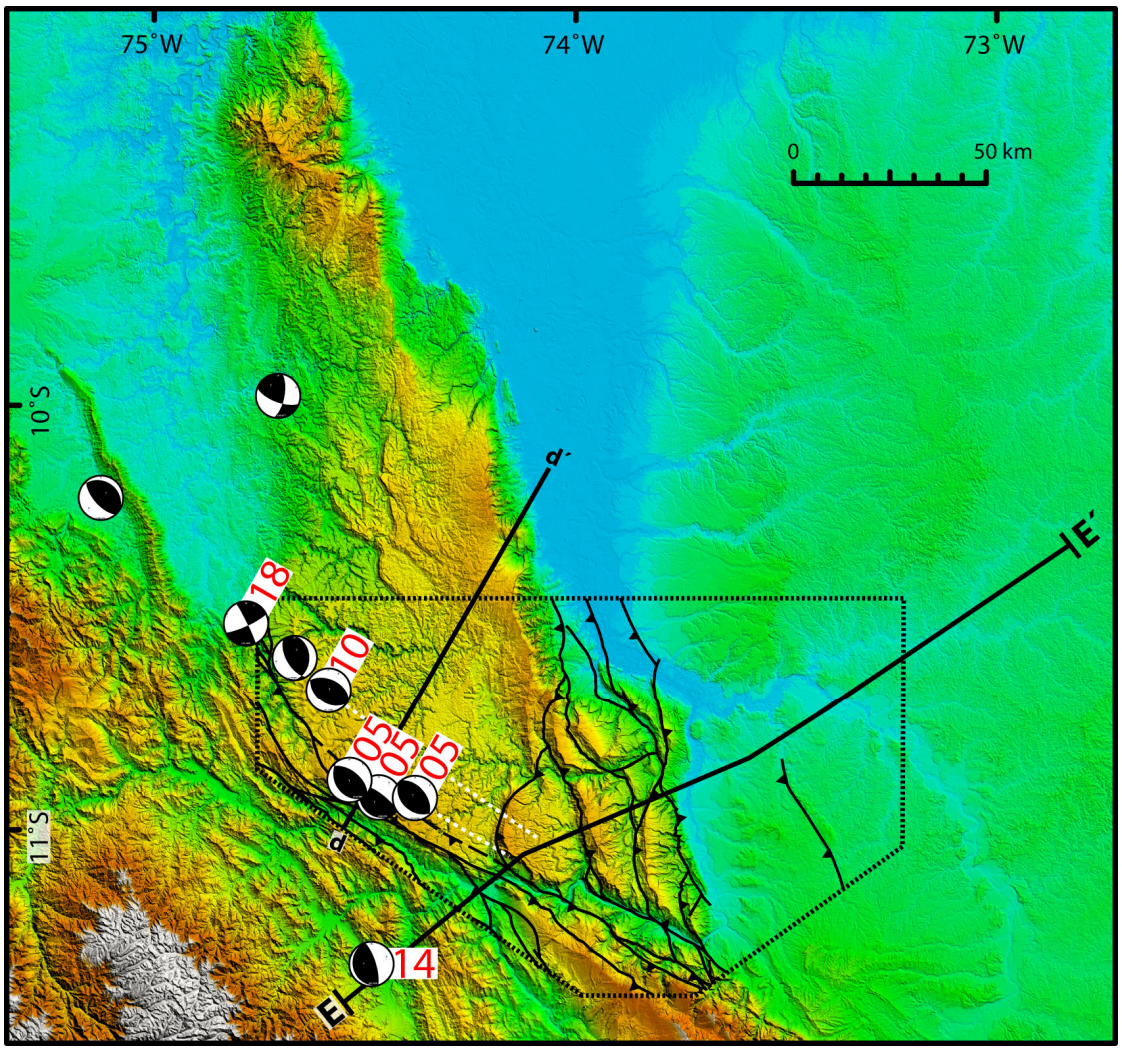

Figure 2:15: Detail map of the Shira uplifts. Profile d-d' is a subset of D-D' from Figure 2.14 and is shown in Figure 2.15. Profile E-E' is found in Figure 2.17. Dashed polygon illustrates the map outline from Espurt et al.'s [2008] Figure 10 from which the interpreted fault orientations shown in thin black lines were taken.

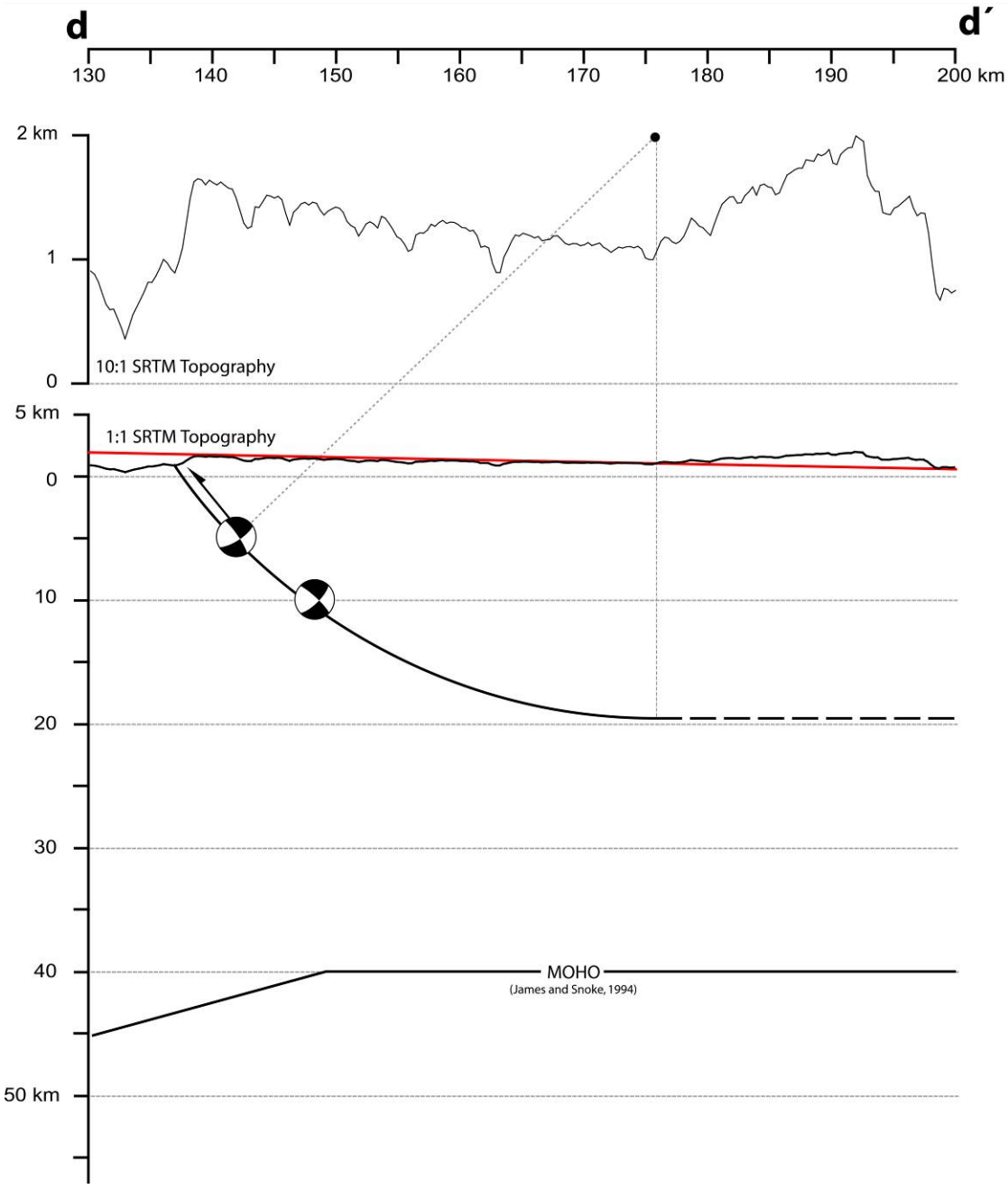

Figure 2.16**:** Fault geometry reconstruction by assuming a tilted fault block and listric fault geometry performed on the south-bounding structure of the Shira mountain. See text for modeling constrains and results.

D-D' in Figure 2.14. A composite focal mechanism solution was used of the three 5 km events. A listric, arc fault geometry was assumed and constrained by Shira's topographic tilt (Figure 2.16 red line) and the earthquake focal plane orientations. The analysis predicts a west-vergent thrust fault dipping 56° that shoals at a depth of 20 km controls the uplift of the southern boundary of the Shira uplift. Both Hermoza et al. [2005] and INGEMMET [1999] illustrate Shira's south-bounding structure as an east-dipping thrust fault, consistent with the reconstruction. However, Espurt et al. [2008] interpret Shira's southern structure differently (Figure 2.17). Espurt et al. [2008] generated regional balanced cross sections from surface and subsurface seismic imaging lines to investigate deformation throughout the region (Figure 2.15 and 2.17). They interpret deep deformation along basement thrusts controlling thin-skinned thrust sheets of the Shira uplifts. Their seismic data imaged the thin-skinned structures of the Subandean zone and the Atalaya back-thrust system (Figure 2.17), but limited fault exposure and no seismic imaging is available for the Shira's south-bounding structure where the earthquakes are located. Figure 2.17 illustrates profile E-E' with a topographic 10:1 profile (a) and Espurt et al.'s balanced cross section with projected earthquake focal mechanisms in (b). The 5 km deep earthquakes do not map onto interpreted structures, while the 10 km event may be consistent with Espurt et al.'s Shira thrust 2 geometry. However, since the southern structure of Shira has not been seismically imaged and the 5 km earthquakes are not consistent with Espurt et al.'s interpretation, part (c) and (d) of Figure 2.17 illustrate an alternative geometry for the south-bounding structure of the Shira mountain using the fault reconstruction geometry from Figure 2.16. (c) shows the analysis superimposed on the Espurt et al.'s balanced cross section and (d) shows a new interpretation of basement structure geometry where the Shira mountain acts as a pop-up basement block bounded on both side by faults of opposing dips. This new geometry is consistent with Hermoza et al.

Figure 2.17: Detailed cross section view of the Shira uplifts, E-E'. Map view is in Figure 2.15. (a) 10:1 topography with depth-projected focal mechanisms. (b) balanced cross section from Espurt et al. [2008] and depth-projected focal mechanisms. (c) balanced cross section from Espurt et al. [2008], super-positioned fault reconstruction from Figure 2.16, and depth-projected focal mechanisms. (d) new interpretation of Shira mountain as a pop-up basement block structure.

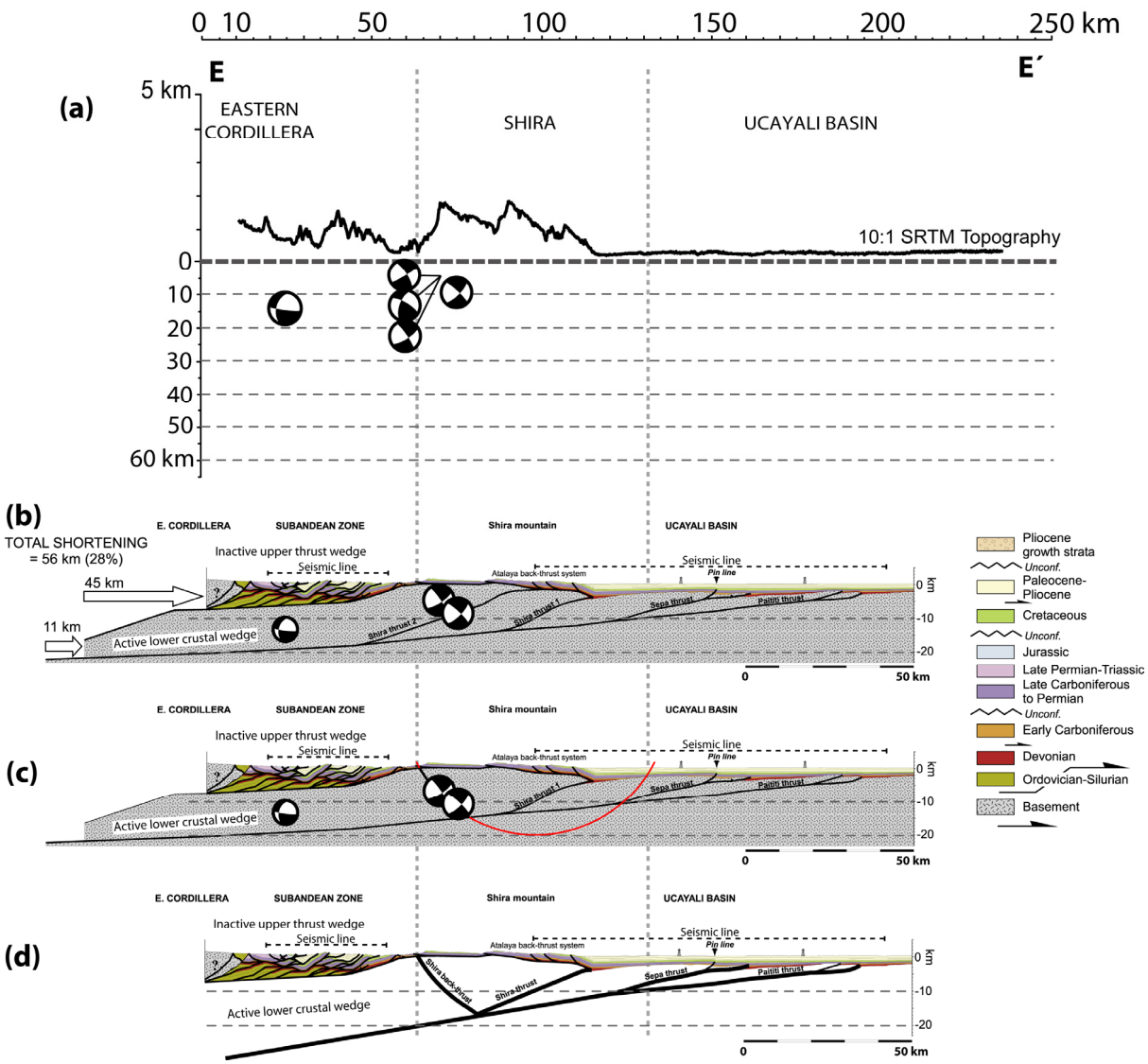
0 10 50 100 150 200 250 km
E
E´
(a)
5 km
EASTERN CORDILLERA
SHIRA
UCAYALI BASIN
10:1 SRTM Topography
0
10
20
30
40
50
60 km
(b)
TOTAL SHORTENING
= 56 km (28%)
45 km
11 km
E. CORDILLERA
SUBANDEAN ZONE
Shira mountain
UCAYALI BASIN
Inactive upper thrust wedge
Seismic line
Active lower crustal wedge
Shira thrust 2
Shira thrust 1
Atalaya back-thrust system
Pin line
Sepa thrust
Paititi thrust
(c)
(d)
Shira back-thrust
Pliocene growth strata
Unconf.
Paleocene-Pliocene
Cretaceous
Jurassic
Late Permian-Triassic
Late Carboniferous to Permian
Early Carboniferous
Devonian
Ordovician-Silurian
Basement
km
0
-10
-20
50 km

[2005] and INGEMMET [1999] and is similar to the bounding structures of the Famatina system in the thick-skinned Sierras Pampeanas (Figure 2.6). Additionally, Figure 2.17 shows that the 14 km deep earthquake beneath the Subandean zone maps beneath the < 10 km deep décollement level, so the event occurred in basement structures without known geometries. Two strike-slip events occurred along the western side of the Shira uplift. One event has a depth of 18 km and the other depth is unknown. It is not clear how these motions fit into the thrust structure of Shira, but their existence suggests the mountains are accommodating some transpressional stresses.

Continental seismicity in the Eastern Cordillera and foreland above steep subduction

Foreland regions above normal subduction are characterized by thin-skinned fold and thrust structures topographically expressed as a series of subparallel ridges. Folding has small wavelengths (5-10 km) and generally faults are steep thrust fault (45-60°). There are two foreland regions above areas of normal subduction that exhibit seismicity. One is located from 15° to 19°S near the cities of Cochabamba and Santa Cruz, Bolivia. The other is located between 22° and 25°S just north of the Santa Barbara system (Figure 2.2). Both regions are located where changes in foreland structural style occur (Figure 2.1 and 2.2). The northern zone occurs where the Subandean fold and thrust belt decreases significantly in width accompanied by a 45-degree change in trend of the fold-thrust structures creating an elbow shape (the Santa Cruz bend) in the landscape. South of that region, the Subandean zone is a pronounced thin-skinned fold and thrust belt with north-south trending structures mapping a large zone over 200 km wide and 500 km long. At 17°S, this belt reduces significantly in width to about 100 km and fold-thrust structures begin trending NW-SE (Figure 2.18). In the southern seismically active region, the Bolivian thin-skinned structures to the

Figure 2.18: Seismicity of the Bolivian foreland, map (left) and P axis orientations (right). Profile F-F' is located in Figure 2.19. Earthquakes break up into three distinct groups according to focal mechanism orientation and location of the events. These groupings are designated by three different colored circles that surround the earthquake groups – red, yellow, and blue. Analysis of the different groups' P axis orientations is shown on the right, and the color of the analyses correspond to the earthquake group colors. Lines on the P axis plots are the average trend of the axes, the value of which is labeled.

66°W
64°W
F´
17°S
18°S
Cochabamba
F
Santa Cruz bend
20
14
05
13
13
0
50
100 km
P axes
050
058
088

north transition and foreland deformational style changes to the thick-skinned thrust belt structures of the Santa Barbara system. Elsewhere, thin-skinned structures of the Central Andean foreland remain aseismic (Figure 2.1). Since continental earthquakes above normal subduction occur where major structural transitions occur, it is possible that stresses are concentrating in these zones due to structural complexities which cause the higher level of seismic activity. This study will now explore how seismicity integrates into the regional structures of these areas.

From 15° to 19°S, the Cochabamba and Santa Cruz region - The topography in Figure 2.18 illustrates the changes in width and trend of the Bolivian Subandean zone. In the south a broad zone of N-S trending thin-skinned structures narrow into a smaller zone trending NW-SE in the north around the Santa Cruz bend. In addition to the bent geometry of the fold-thrust belt, another distinct topographic feature are the basins near the city of Cochabamba. These basins lay within the Interandean zone between the fold-thrust belt and the Eastern Cordillera around 17.5°S. The basins are considered a thin-skinned pull-part system controlled by bounding tear faults that accommodate E-W left-lateral motion [*Allenby*, 1987; *Dewey and Lamb*, 1992; *Sheffels*, 1995].

Earthquakes break up into three distinct groups according to focal mechanism orientation and location of events. These groupings are designated by three different colored circles that surround the earthquake groups. The events circled in red are thrust events with nodal plane orientations consistent with the NW to SE trending structures and earthquakes circled in blue have planes oriented with local N-S trends. Further west, in areas of high elevations, strike-slip earthquakes (yellow circle) dominate event orientations. Averaging of group P axis orientations (Figure 2.18)

illustrates rotation of dominant focal mechanism orientation around the Subandean band suggesting that structural trends and strike of the mountain front geometry influence compressional axis orientation in this region.

14 and 20 km are the two well-determined depths for the Subandean events. These events occurred near where subsurface imaging and interpretations have been done [*Baby, et al.*, 1995; *Baby, et al.*, 1997; *McQuarrie and Davis*, 2002] (Figure 2.19 F-F'). A generalized version of the McQuarrie and Davis [2002] interpretation is shown in Figure 2.19. This is used to elucidate a few consistent features among the multiple interpretations that have been published [*Baby, et al.*, 1995; *McQuarrie and Davis*, 2002; *Roeder and Chamberlain*, 1995]. The short-wavelength structures of the Subandean fold-thrust belt are bound to the east by undeformed plains. West are the Interandean zone and Eastern Cordillera where increases in topography occur along with involvement of basement deformational structures. The 20 km deep event occurs beneath an undeformed basin consistent with where Sheffels [1995] has proposed a Paleozoic basin margin impinges on the edge of the Subandean zone and is responsible for the bent foreland geometry. Compression between the basin margin and Subandean zone may be reflected with this event. The 14 km event occurs were Interandean basement-involved deformation occurs. Décollement depth interpretations beneath the Interandean zone are around 15 km [*Baby, et al.*, 1997; *McQuarrie and Davis*, 2002], so the thrust event at ~ 14 km with a shallow west-dipping fault plane could have occurred along the décollement.

Determined depths for the strike-slip events are 5 and 13 km. One of these events was the Mw 6.6 Aiquile, Bolivia event that occurred in 1998. The best-fit waveform modeling solution appears in Figure 2.20, which shows a relatively good waveform fit

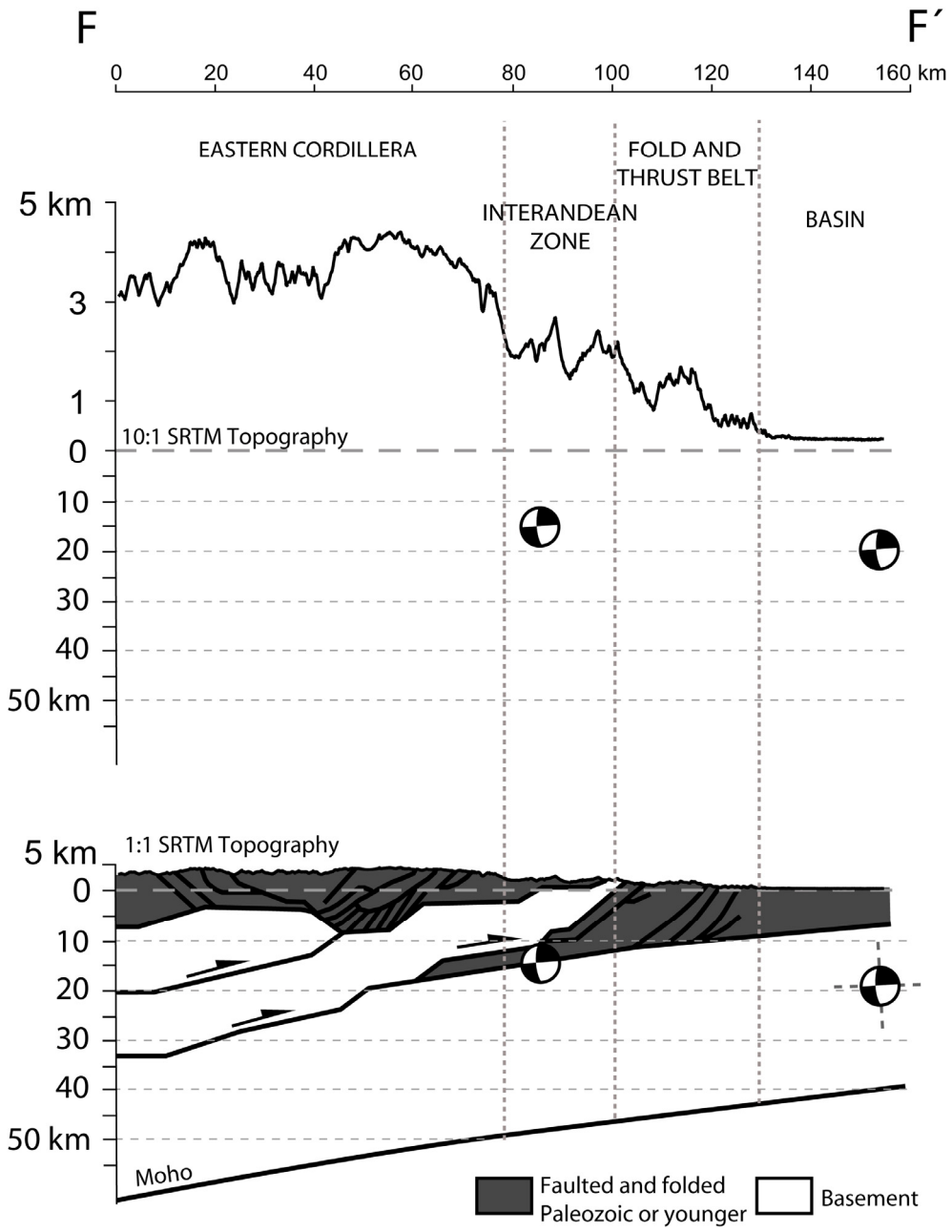

Figure 2.19: Cross section F-F' for interpretation of the seismicity of the Bolivian foreland from Figure 2.18. (top) 10:1 topographic profile and earthquakes projected into the profile. (bottom) 1:1 topographic profile, subsurface structural interpretation modified from McQuarrie and Davis [2002], and earthquakes projected into the profile.

Table 2.2: 5/22/1998 Mw 6.6 Aiquile, Bolivia

method	Longitude (deg)	Latitude (deg)	depth (km)	Mw	strike (deg)	dip (deg)	rake (deg)	length (km)	width (km)
CMT	-65.2000	-17.6000	15.0	6.6	186	79	-178	n/a	n/a
Funning et al. (2005)	-65.1770	-17.8970	2 – 12	6.6	7	79	171	14.5	15.0
InSAR (this study)	-71.1534	-17.8924	2 – 8	6.4	181	110	182	19.7	5.0
MT5	-65.5390	-17.8595	13 ± 5	6.7	360	88	179	n/a	n/a

Figure 2.20: Waveform inversion solution for the 1998 Aiquile, Bolivia earthquake. Figure conventions are those described in Figures 1.3 and 1.5. The bottom line of the sensitivity analysis plot tests the waveform fit of the solution from Figure 2.21 and listed in Table 2.2 as InSAR (this study).

1998/05/22
360/88/179/13/1.564E19

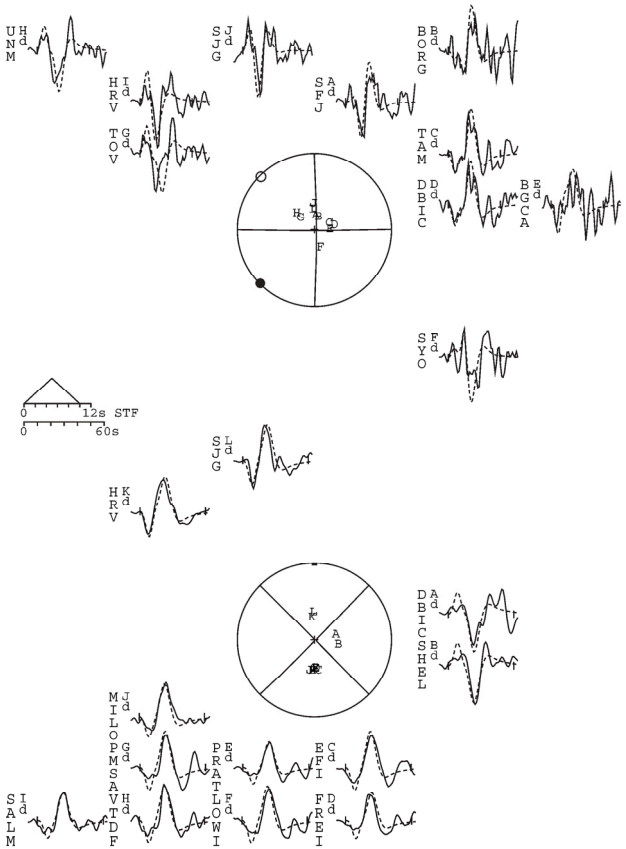

1998/05/22 04:48:50.46 (-17.85, -65.53) Mw6.6

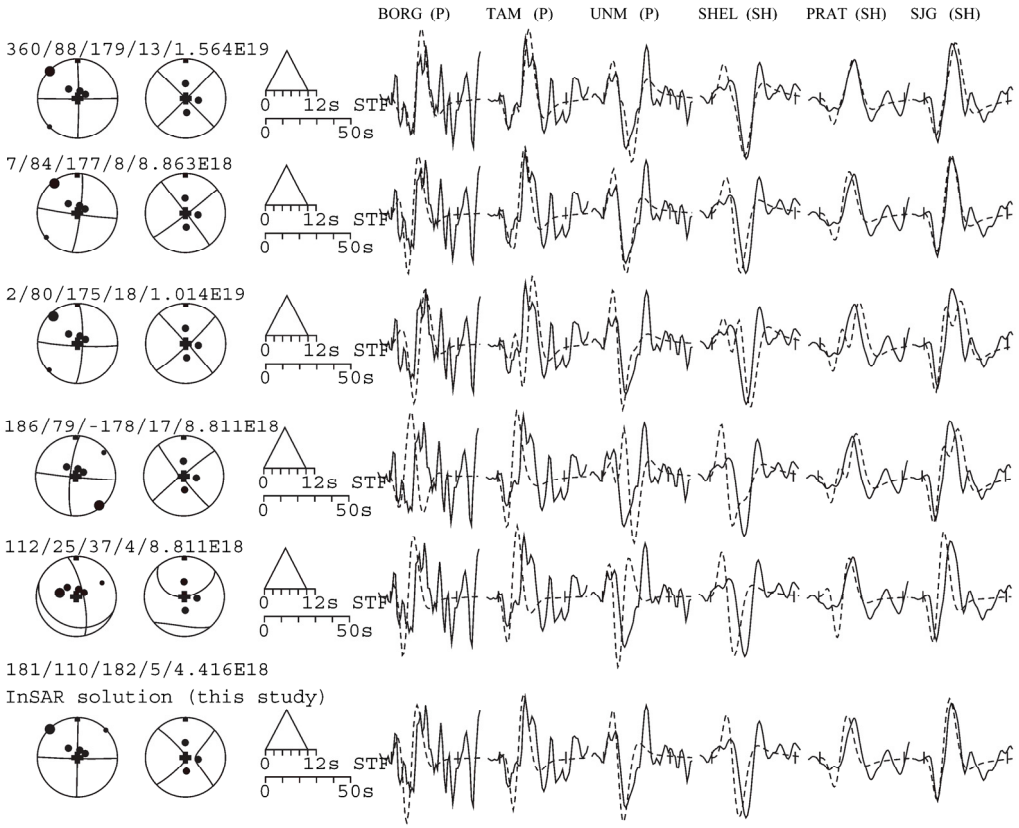

for an azimuthal range of stations. It shows a strike-slip event with subvertical fault solutions at 13 ± 5 km depth. InSAR analysis of the event was also done in this study to provide and independent constraint on rupture properties (Figure 2.21) and was separately also conducted by Funning et al. [2005]. The two InSAR solutions used different data frames for their analyses (Figure 2.21 caption). These provide an independent test of source properties from waveform analysis. Table 2.2 lists the solutions from each analysis, which were roughly consistent among the methods. InSAR analysis conducted for this study (procedural method is described in Chapter 1) found a slightly shallower solution with fault rupture occurring from ~ 2 to 8 km depth. Funning et al.'s depth solution lies between the MT5 and InSAR just reported, and their best-fit fault ruptured at depths between 2 and 12 km. The waveform inversion solution and the two InSAR solutions illustrate a potential depth range between 2 to 18 km for this event when you include error bounds of the MT5 solution and the entire rupture areas of the InSAR solutions. All three solutions overlap at 8 km, so this is likely the depth of the earthquake. Both InSAR analyses determined that the north-south right-lateral plane is likely the fault plane. The shallow depth of the event is consistent with interpretations of shallow tear faults around Cochabamba. East-west structures bound the pull-part basin [*Allenby*, 1987; *Dewey and Lamb*, 1992; *Sheffels*, 1995], but the best-fit fault plane of the 1998 event does not reflect this deformation. Consistent with the findings of Funning et al. [2005], it may instead reflect right-lateral motions along north-south structures proposed by Dewey and Lamb [1992]. Alternatively, the three strike-slip events are consistent with EW left-lateral motion, which is consistent with shearing accommodating the Santa Cruz bend and Cochabamba pull apart basins.

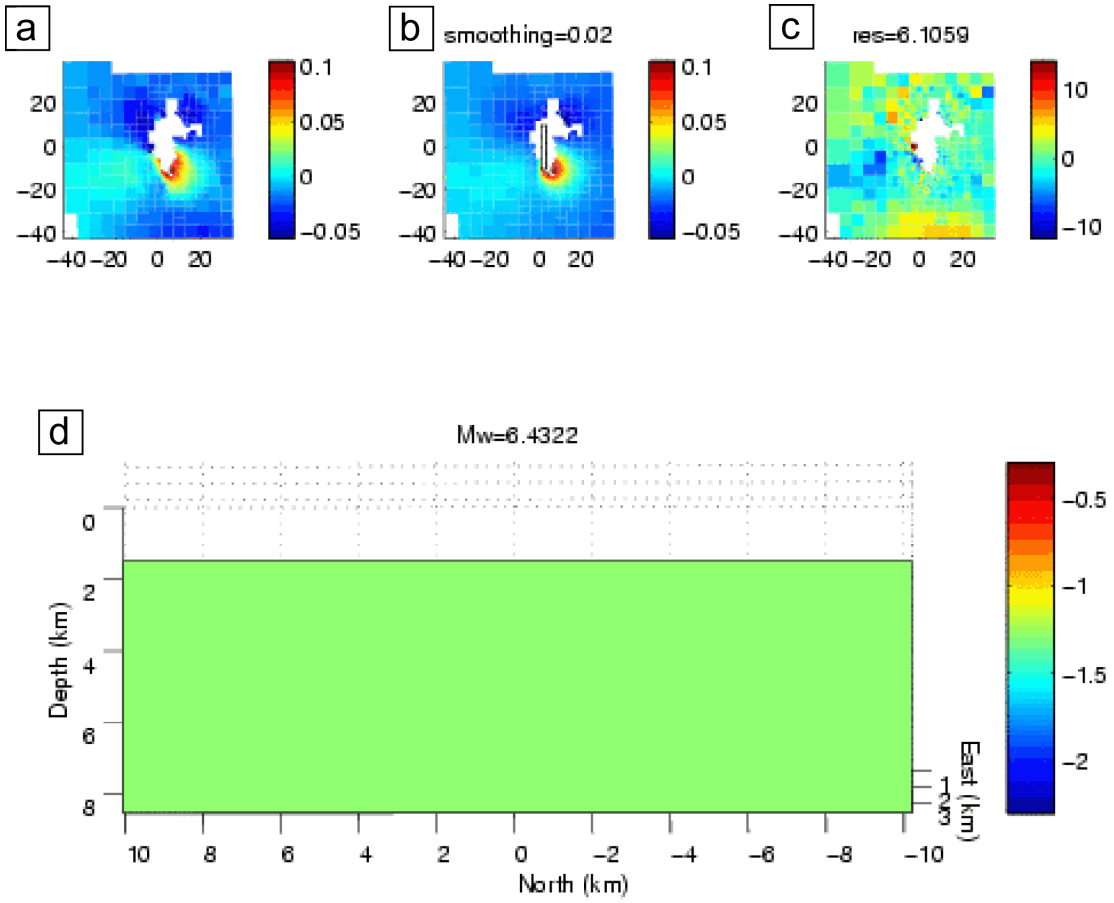

Figure 2.21: InSAR solution from this study of the 1998 Aiquile, Bolivia earthquake. (a) Resampled unwrapped interferogram where phase differences were converted to meters. The boxes outline the resampled points, and white areas show no data (either because the data did not successfully unwrap or was there was none to start with). (b) Predicted interferogram from our model. (c) The difference between the data and the model (residual) where the scale bar is cm. The residual value is shown above this figure value and has been weighted during the resampling procedure so it doesn't simply relate to the RMS. (d) The fault model and predicted slip is shown. Data used: ERS track 239 19980730-19960411 Bperp 15 m. Two frames (3969 3987) were used instead of the one frame (3962) used by Funning et al. [2005].

From 22° to 25°S, the Santa Barbara system - The existence and depth determination of foreland seismicity between 22° to 25°S was documented by Chinn and Isacks [1983]. Three additional earthquakes have occurred in the region with CMT-reported magnitudes between 5.3 and 5.4 (Figure 2.22). Due to small magnitudes and subsequent low amplitude phase arrivals, depth determinations were not possible for these events. Previous works have integrated seismicity and subsurface interpretations in this region [*Allmendinger, et al.*, 1983; *Allmendinger and Zapata*, 2000; *Cahill, et al.*, 1992; *Grier*, 1990; *Jordan, et al.*, 1983; *Kley and Monaldi*, 2002]. Their findings are reviewed here and combined with the three events not reported by Chinn and Isacks [1983].

This region is where foreland structures transition from creating a thin-skinned fold and thrust belt in the north to being the thick-skinned thrust belt structures of the Santa Barbara system in the south (Figure 2.22 and 2.23). Earthquake depths indicate décollement-level deformation beneath thin-skinned structures (Figure 2.23 G-G') [*Jordan, et al.*, 1983] and deformation along unknown structures below the thrust blocks of the Santa Barbara system [*Jordan, et al.*, 1983; *Kley and Monaldi*, 2002]. Cahill et al.'s [1992] local seismic network study found peak foreland seismicity levels occurred between 20 and 25 km depth. The more recent events (those without depth determinations) are consistent with continued thrusting within the foreland and some strike-slip motion beneath the Santa Barbara. Dextral strike-slip movement along faults of the northernmost Santa Barbara System has been reported [*Bianucci, et al.*, 1982; *Kley and Monaldi*, 2002]. Northeast trending fault and folds accommodate the motion [*Kley and Monaldi*, 2002] and the NE striking nodal plane is consistent with dextral slip. Therefore, that plane is likely the fault plane of the earthquake.

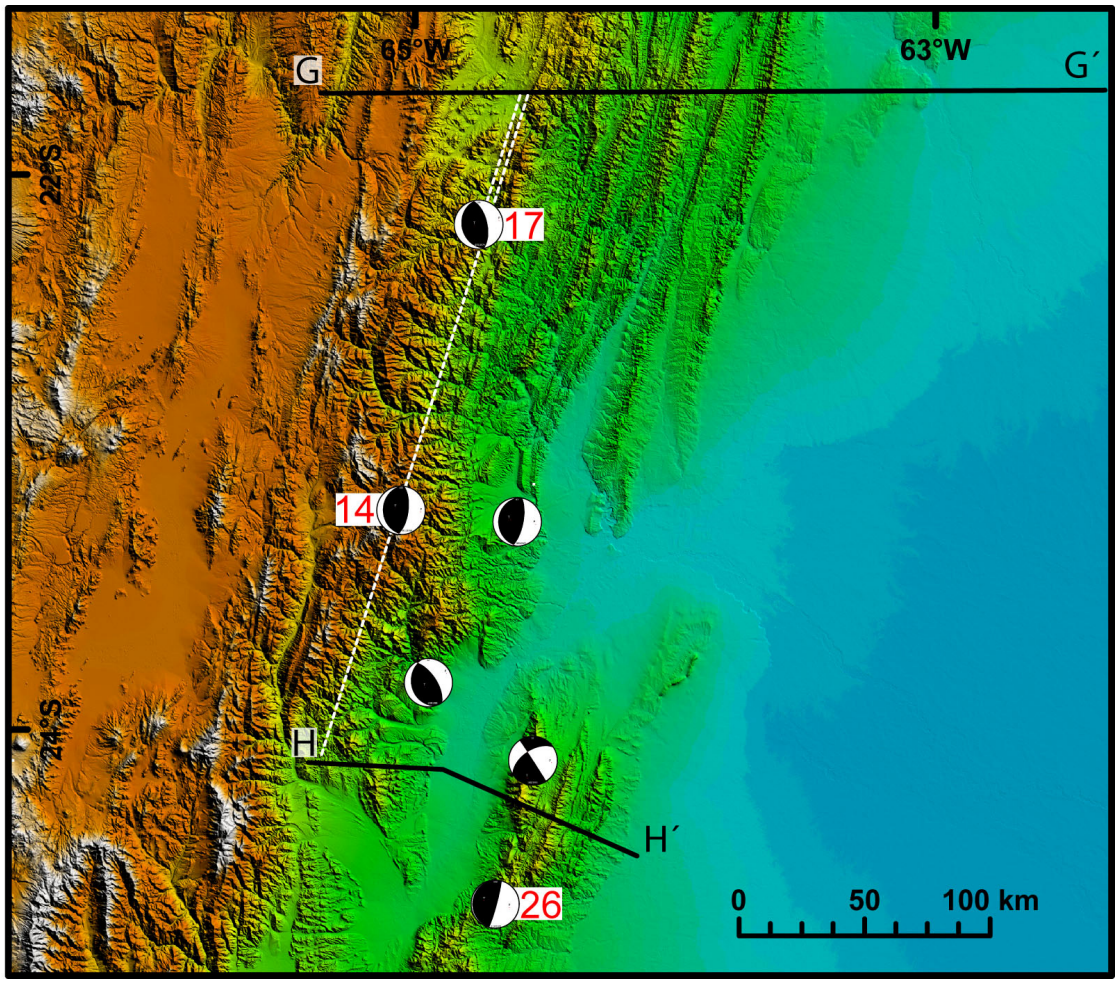

Figure 2.22: Seismicity of the foreland between 22° to 25°S. Profiles G-G' and H-H' are located in Figure 2.23. The two white lines intersecting the event with a 14 km depth, one to the north and one to south, indicate that this event was projected onto both the G-G' and H-H' profiles in Figure 2.23.

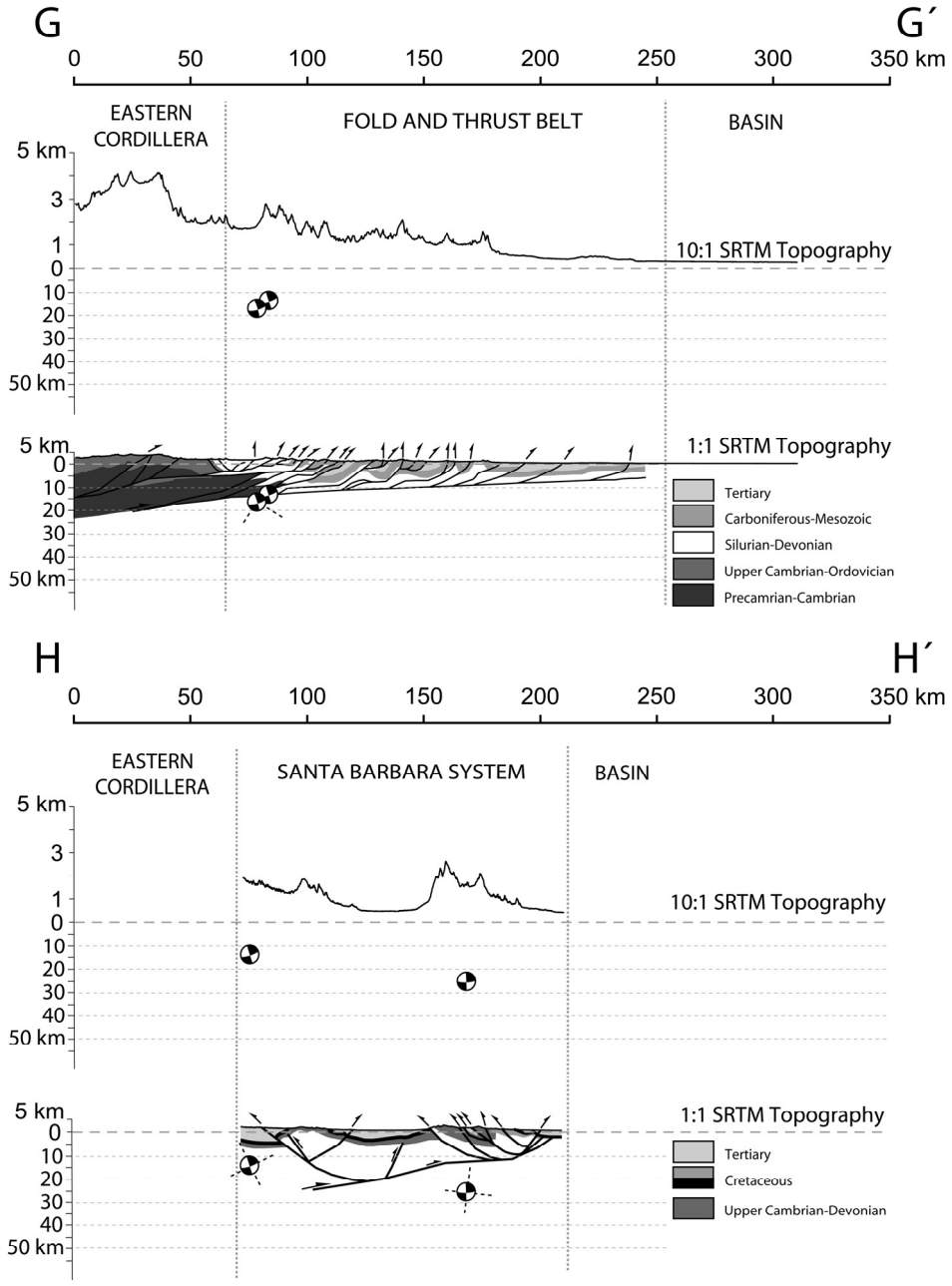

Figure 2.23: Cross section interpretations and foreland seismicity between 22° to 25°S. The structural interpretation along G-G' is a composite section [*Baby, et al.*, 1992; *Dunn, et al.*, 1995; *Kley*, 1996] constructed by Kley et al. [1999]. H-H' comes from Kley and Monaldi [*Kley and Monaldi*, 1998]. Profile locations can be found in Figure 2.22.

Plateau earthquakes

The Altiplano-Puna plateau is a 400 km wide orogenic plateau of elevations greater than 3 km. This distinctive topographic structure contains a large internally drained basin of moderate relief. The widest segment of the plateau is located above normal Nazca plate subduction (Figure 2.1). While the majority of the plateau does not exhibit seismicity, the Altiplano of southern Peru and northernmost Chile has experienced earthquakes with magnitudes large enough for waves to be recorded teleseismically (Figure 2.24). The mechanisms reveal a mixture of normal and strike-slip fault orientations with approximate north-south T axis orientations (Figure 2.25), where B and P axes appear interchangeably associated with the east-west and vertical orientations. Of the fifteen earthquakes located on the plateau, eight of the events occurred from 29 June 2001 to 24 February 2002. A Mw 8.5 subduction zone earthquake occurred in this area on 23 June 2001, just prior to these plateau events, and two large subduction zone aftershocks also followed during this period of time (Figure 2.26). The portion of the subduction zone that ruptured during the interplate events [*Pritchard, et al.*, 2007] is schematically drawn in Figure 2.26. The timing and spatial correlation between the plateau earthquakes and the subduction zone activity suggests that stresses associated with the seismic cycle along the subduction zone may influence stresses on the plateau to induce north-south extension. Earthquakes range in depth from 8 to 17 km. Extension on the plateau is consistent with field observations and interpretations from satellite images of youthful faulting reported in the literature [e.g., *Fielding*, 1989; *Sebrier, et al.*, 1985]. However, distinguishable topographic features indicative of pervasive extensional deformation are not apparent on the SRTM topography with the exception of the Cuzco area (Figure 2.27).

Figure 2.24: Plateau-wide view of plateau and forearc seismicity. Forearc earthquakes are haloed in white to ease identification.

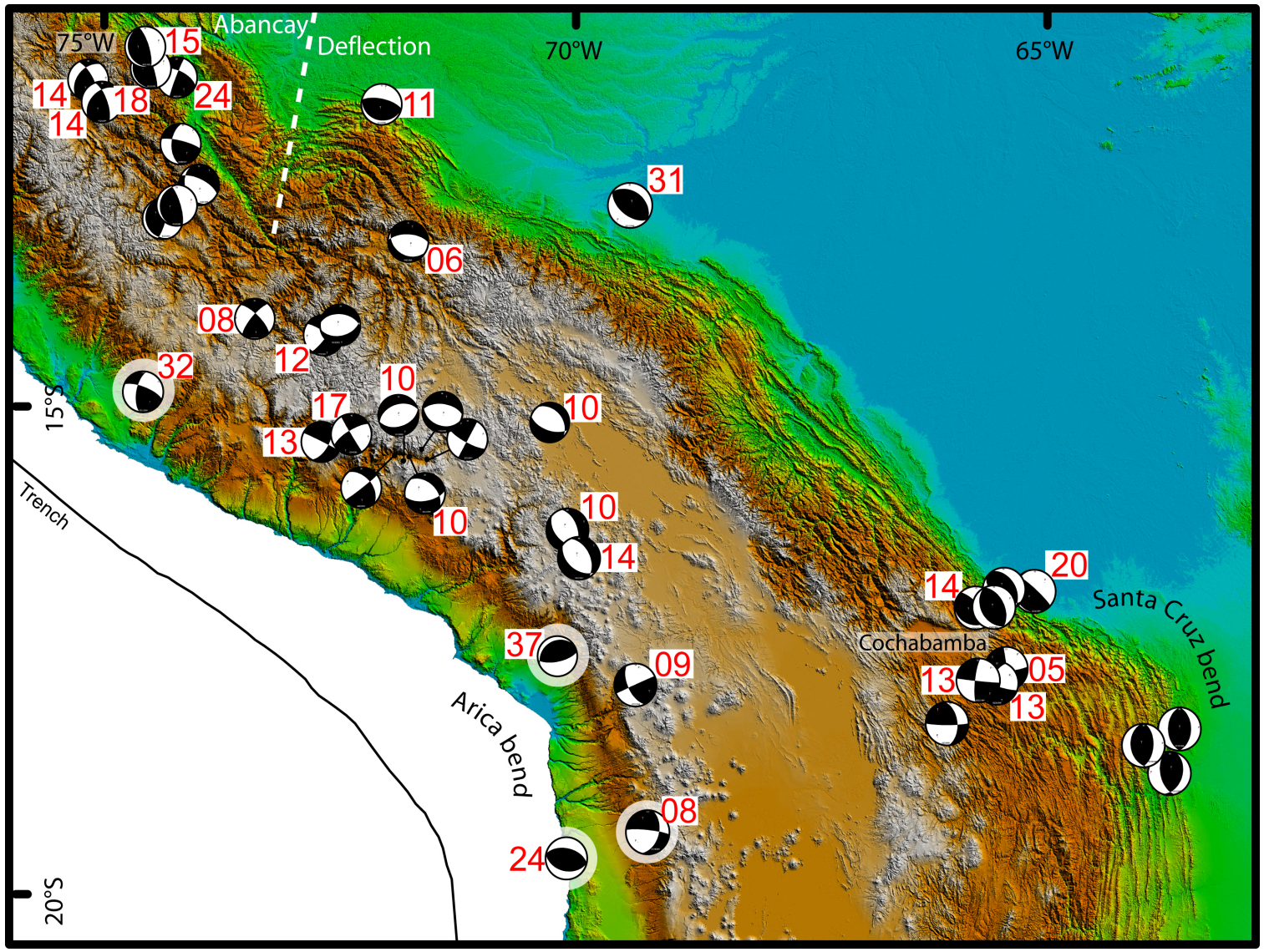
75°W
70°W
65°W
15°S
20°S
Abancay
Deflection
Trench
Arica bend
Santa Cruz bend
Cochabamba
15
14
18
24
14
11
31
06
08
12
32
10
17
13
10
10
10
14
37
09
14
20
13
05
13
08
24

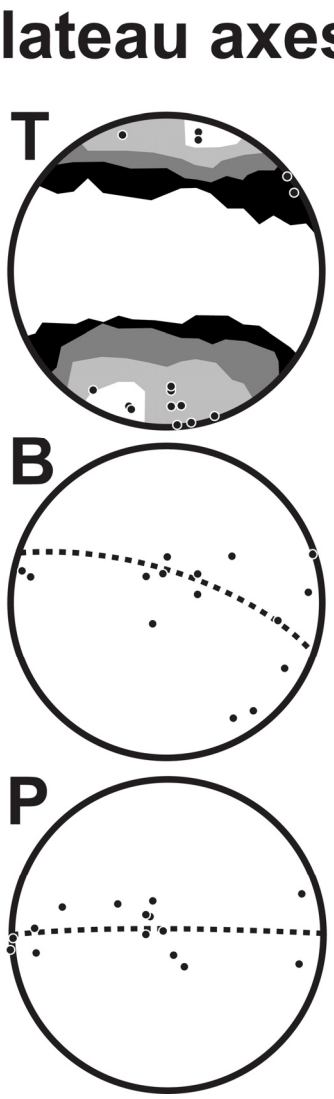

Figure 2.25: Plateau focal mechanism axis plots. Black dots show axes plotted in a Schmidt equal-area lower-hemisphere projection. Black, dark gray, light gray, and white contours illustrate 2-sigma intervals after Kamb [1959] using the StereoWin program [*Allmendinger*, 2002]. Dashed great circles on the P and B axis plots show the cylindrical best fit to the axes. Axes plotted are from the plateau events shown in Figure 2.24. This excludes events from the forearc, Santa Cruz bend, foreland, events north and west of the Abancay Deflection, and the 9-km deep earthquake beneath are arc at the Arica bend (Figure 2.24).

Figure 2.26: Plateau and forearc earthquakes that occurred from 29 June 2001 to 24 February 2002, after a Mw 8.5 subduction zone earthquake occurred in this area on 23 June 2001. The portion of the subduction zone that ruptured during the interplate events is schematically shown as a dashed rectangle [*Pritchard, et al.*, 2007].

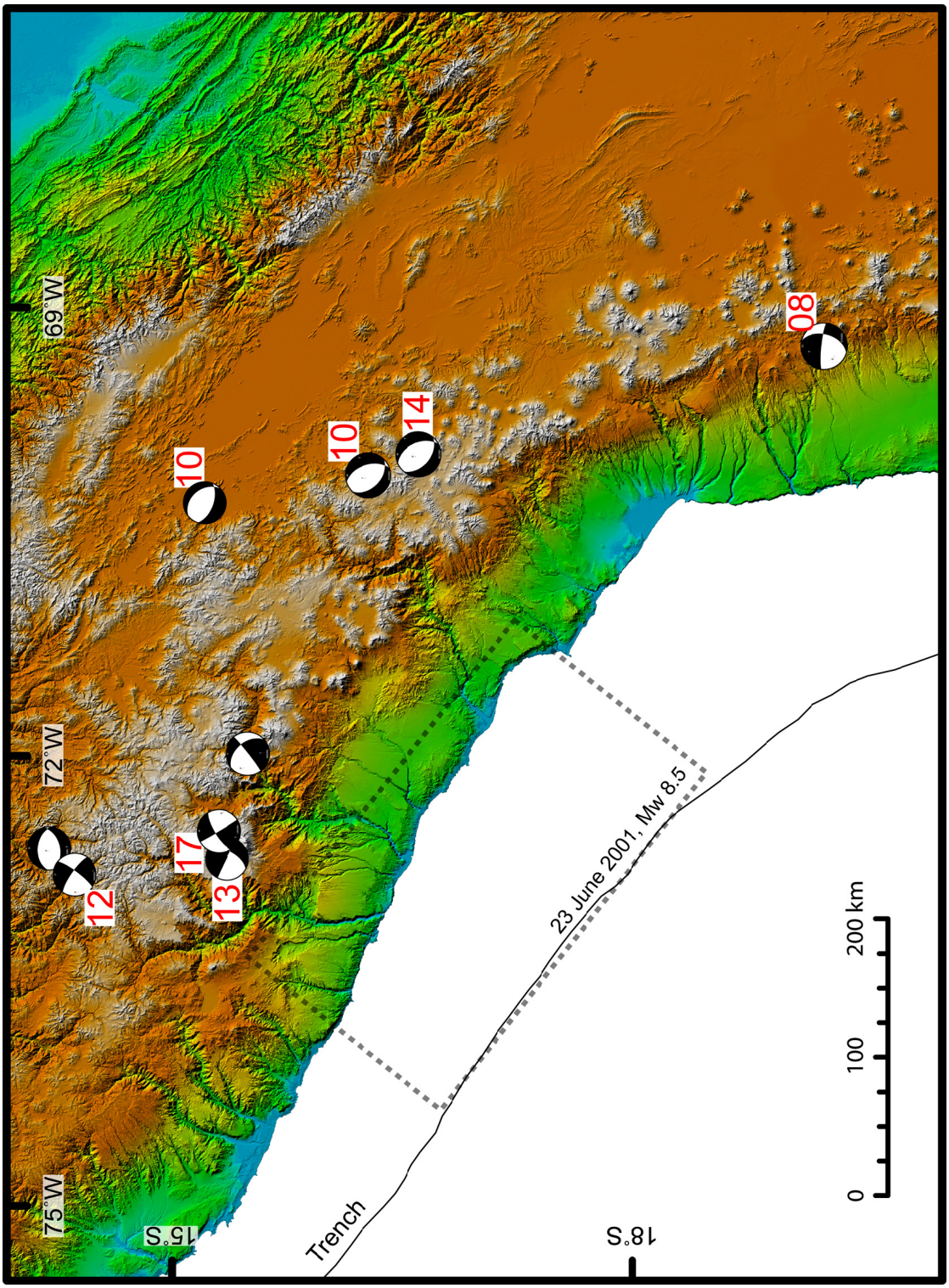
69°W
72°W
75°W
15°S
18°S
Trench
23 June 2001, Mw 8.5
0
100
200 km
08
10
14
10
17
13
12

Figure 2.27: Earthquakes around the Cuzco region. Black dashed line approximates the structural boundary between Paleozoic rocks to the north and Mesozoic-Cenozoic rocks to the south, which is the approximate structural sketch of the Ayacucho, Cuzco, and Vilcanota fault systems separating Paleozoic rocks in the north and Mesozoic-Cenozoic rocks to the south.

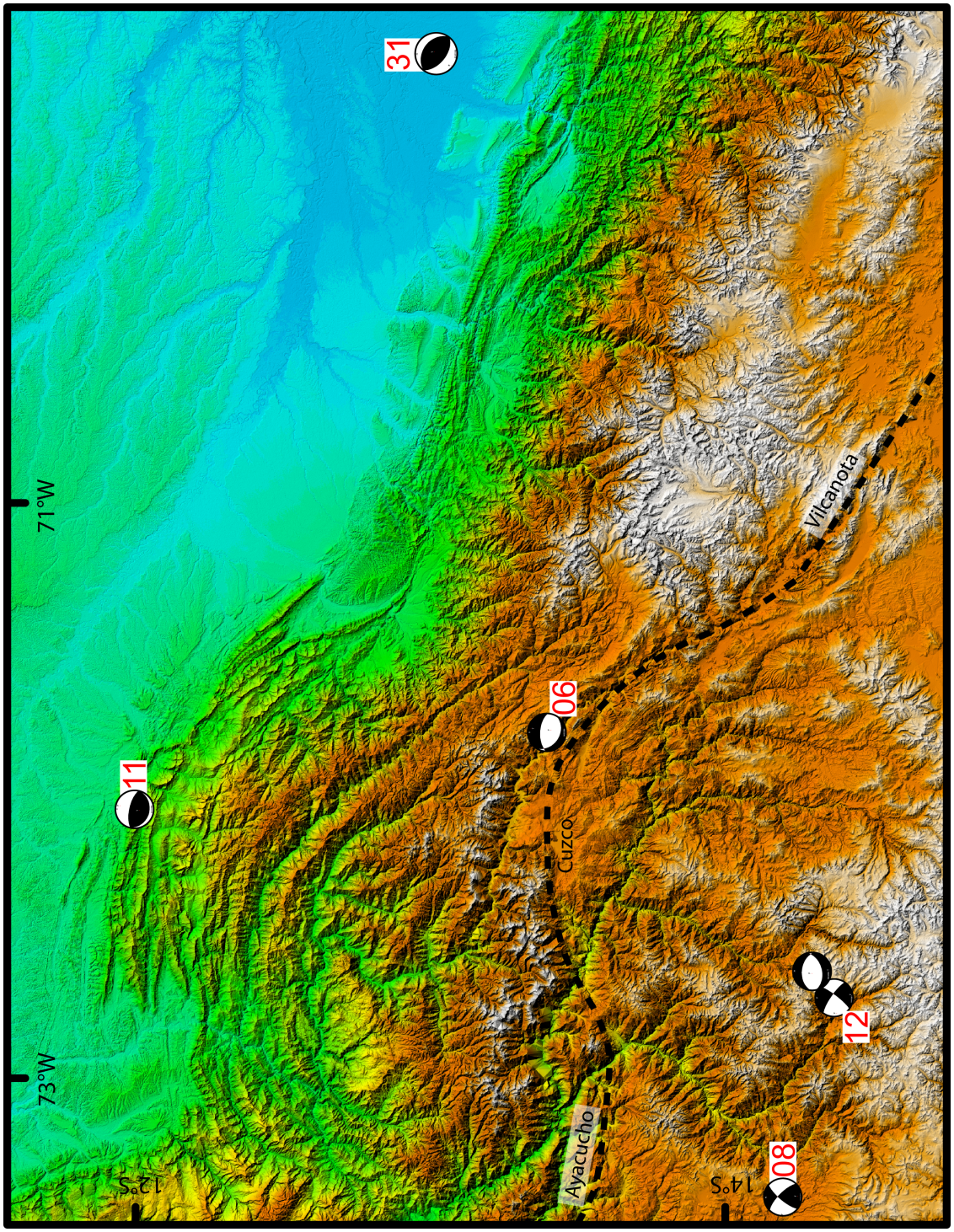
31
71°W
Vilcanota
06
11
Cuzco
12
73°W
Ayacucho
08
12°S
14°S

The Abancay deflection denotes an abrupt change in structural trends in the Andes of southern Peru from curvilinear trends around the Cuzco region to northwest-southeast farther north (Figure 2.24). The Cuzco fault system is part of a more than 200 km long, approximately east-west striking fault zone located between the northwest-southeast striking Ayacucho and Vilcanota fault systems (Figure 2.27). The transition from the Ayacucho to Cuzco fault systems occurs roughly at the Abancay deflection, where the east-west trends around Cuzco transition to the northwest-southeast trends of the Ayacucho system. These three fault systems present major structural control in the area and define the boundary between Paleozoic and Mesozoic-Cenozoic rocks (Figure 2.27 black-dashed line). Superimposed families of striations on fault planes of the Cuzco fault system allowed Mercier et al. [1992 and references therein] to establish a succession of tectonic regimes in the Cuzco region from the Pliocene to present: (1) Pliocene east-west extension, (2) early Pleistocene east-west or north-south compression, and (3) mid-Pleistocene to present north-south extension. Approximate present-day north-south extension around Cuzco is consistent with the 6 km deep event just northeast of Cuzco (Figure 2.27). This focal mechanism T axis was included in the plateau focal axes plots in Figure 2.25 and is consistent with north-south extension of the plateau regions of southern Peru.

Also captured in Figure 2.27 are two foreland earthquakes, which were not easily discussed in any other section but, nonetheless, warrant mention. In the foreland region north of Cuzco, an 11 km deep thrust event occurred and the orientations of the nodal planes are consistent with the roughly northwest-southest orientation of topographic structures. East of Cuzco a 31 km deep event occurred beneath a relatively undeformed basin. At such a deep depth and with no close topographic

features, this event likely involved basement structures similar to those found farther north, east of the Huallaga basin.

Forearc earthquakes

The forearc region of the Chilean Central Andes is characterized by the monocline-shaped western flank of the Altiplano. This simple topographic feature is interrupted in northern Chile and southern Peru around the Arica bend (Figure 2.24). Four earthquake depths were determined for this study that occurred in the forearc and they range from 8 to 37 km in depth (Figure 2.24 haloed earthquakes). Shallow crustal seismic activity has previously been reported along the forearc in northern Chile and southern Peru [*Comte, et al.*, 2003; *David, et al.*, 2003], but few of the earthquakes previously studied are of large enough magnitude to be recorded teleseismically. The crustal seismicity of the forearc suggests that tectonic activity is important in this region.

The 24 July 2001 Mw 6.3 Aroma earthquake was an expression of forearc seismicity. That event has a depth of 8 km as determined by waveform inversion (Figure 2.28) and that is consistent with the local seismic network analysis of Legrand et al. [2007] and with InSAR analysis done for this study (Figure 2.29 and Table 2.3). Like the plateau events, this earthquake was related to heightened seismic activity throughout the region following to the Mw 8.5 subduction zone earthquake on 23 June 2001 (Figure 2.26). Using different seismological data (short-period, broadband, strong-motion) and aftershock distributions, Legrand et al. determined the earthquake occurred on a steeply dipping fault striking NE-SW. InSAR analysis of this event is also consistent with a shallow NE striking fault rupture.

Figure 2.28: Waveform inversion solution for the 2001 Aroma, Chile earthquake. Figure conventions are those described in Figures 1.3 and 1.5.

2001/07/24
018/75/187/8/2.003E18

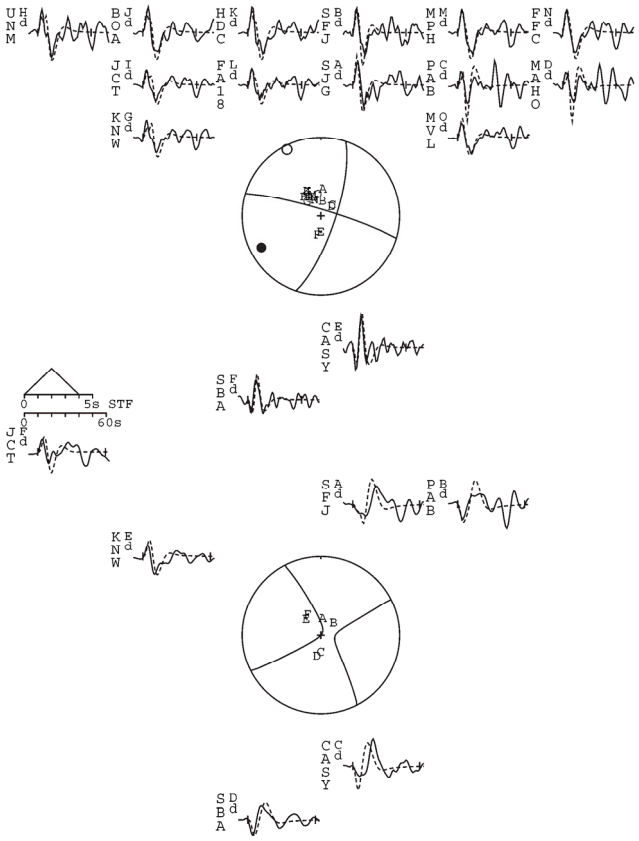

2001/07/24 05:00:08.94 (-19.5180, -69.2450) Mw6.4

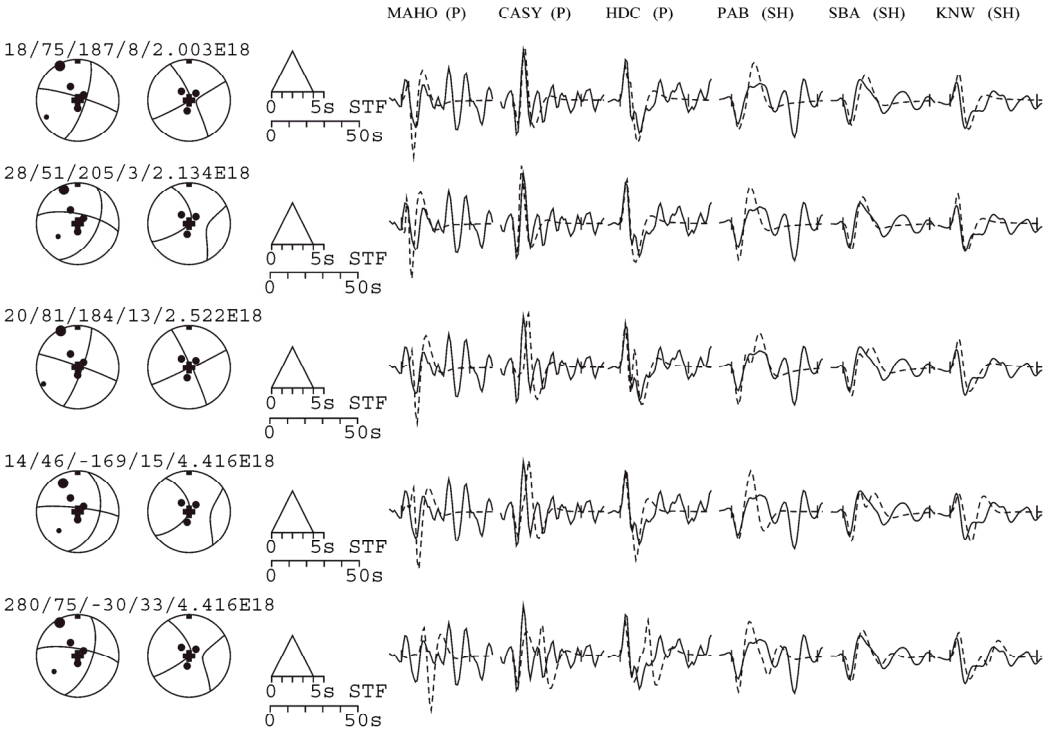

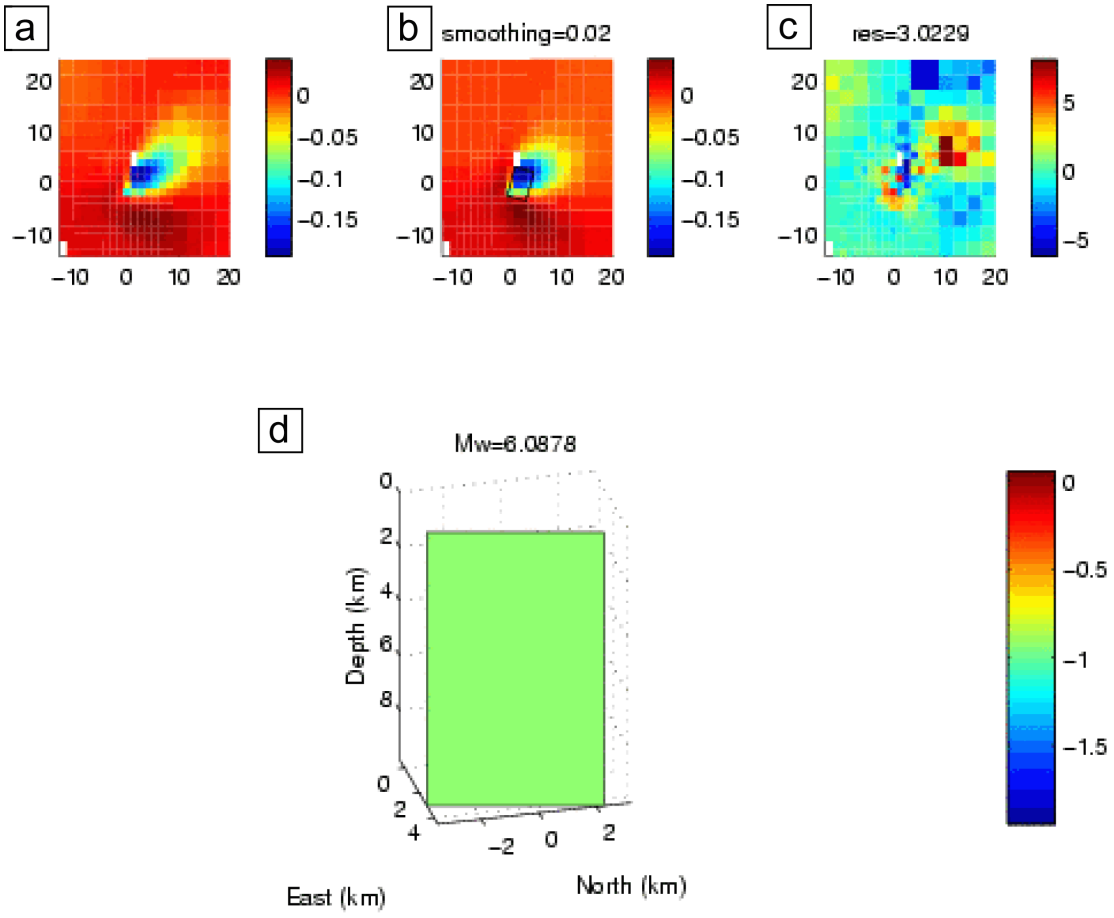

Figure 2.29: InSAR analysis of the 24 July 2001 Mw 6.3Aroma earthquake. (a) Resampled unwrapped interferogram where phase differences were converted to meters. The boxes outline the resampled points, and white areas show no data (either because the data did not successfully unwrap or was there was none to start with). (b) Predicted interferogram from our model. (c) The difference between the data and the model (residual) where the scale bar is cm. The residual value is shown above this figure value and has been weighted during the resampling procedure so it doesn't simply relate to the RMS. (d) The fault model and predicted slip is shown.

Table 2.3: 24 July 2001 Mw 6.3 Aroma earthquake

	method	Longitude (deg)	Latitude (deg)	depth (km)	Mw	strike (deg)	dip (deg)	rake (deg)	length (km)	width (km)
07/24/01 Mw 6.3 Aroma, Chile	Global CMT catalog	-69.1800	-19.4400	15.0	6.3	14	46	-169	n/a	n/a
	Legrand et al. [2007]	-69.3140	-19.5890	5.0	6.3	14	53	-163	16	11
	InSAR (this study)	-69.2749	-19.5923	2 → 9	6.1	14	62	213	5.6	8.6
	MT5 (this study)	-69.2450	-19.5180	8	6.4	23	71	187	n/a	n/a

Two deep earthquakes, at 24 and 37 km depths, indicate north-south compression. The southern event at 19.80°S is consistent with interpretations of trench parallel shortening in the forearc [*Allmendinger, et al.*, 2005; *Bevis and Martel*, 2001; *McCaffrey*, 1996]. McCaffrey [1996]showed through kinematic modeling that arc-parallel strain in the forearc can be geological significant at 23.5°S and predicted a similar pattern for all of northern Chile from 18° to 30°S. Bevis et al.'s [2001] elastic modeling predicted arc-parallel shortening along a locked, plate boundary with a concave seaward geometry. Allmendinger et al. [2005] reported evidence of a suite of EW topographic scarps located between 19° and 21.6°S latitude. The 24 km deep event occurred at latitudes roughly consistent with findings of those studies, but the offshore location and deep depth of the event limits relating it to a specific scarp structure. The northern event that indicates north-south shortening in the forearc is consistent with the broad interpretation that north-south compression accompanies concave plate boundary convergence. However, the event's location, more than 200 km from the trench, is inconsistent with surface velocity fields predicted by Bevis et al. [2001]. Surface velocities decrease in magnitude and rotate to parallel orientations with distance from the plate boundary. Parallel surface velocity orientations at distances ~ 200 km from the plate boundary are not consistent with north-south compression. Therefore, this forearc event is not easily explained by the Bevis model.

Discussion and implications

All earthquakes were found to occur at depths within the crust, so no lithospheric mantle seismicity was found. Deep crustal events occur beneath the forearc and in regions where basement thrust structures dominate foreland structural style. In the forelands above flat subduction, deformation of basement thrust structures take many forms and most focal mechanisms are consist with horizontal shortening. Examples of

deforming basement structures include: (1) shallow seismic activity associated with the near-surface expression of basement thrust blocks (e.g., Shira uplifts), (2) deep diffuse earthquake activity associated with a possible mid-crustal basement wedge creating a basement-cored anticline (e.g, Pie de Palo), and (3) inverted relic rift structures deforming at deep depths beneath undeformed foreland basins (e.g., east of the Huallaga basin). Basement-involved deformation also appears to accompany seismic activity beneath the Subandean zone and Eastern Cordillera above normal and flat subduction. The one region that is an exception to this and that exhibits shallow seismic deformation not likely associated with basement rocks, is the area of strike-slip earthquakes near the Cochabamba region of Bolivia. The earthquakes there are in some way accommodating deformations related to the neighboring shallow pull-apart basin, but linking of these events to specific faults expressed at the surface is not possible at this time.

Analysis of focal mechanism P axes long the entire Central Andean foreland (Figure 2) shows orientations that are consistent with east-west shortening (~ 92°), which is ~ 15° from the direction of plate convergence (~77°). The difference in these directions is consistent with compressional infinitesimal strain directions resolved from GPS velocities [*Allmendinger, et al.*, 2007]. Allmendinger et al. [2007] found that infinitesimal shortening axes in the hinterland and forelands of the Central Andes are oriented perpendicular to the strike of local structures, which is also clearly resolved in focal mechanisms orientations around the region of the Santa Cruz bend (Figure 2.18).

Seismic activity on the Altiplano-Puna plateau is limited to regions of southern Peru and northernmost Chile. Only shallow to mid-crustal depth events occur on the plateau and, in contrast to foreland earthquakes, focal mechanisms indicate normal and strike-

slip faulting rather than thrust faulting. Assuming that regional stress and strain axes directions are coaxial, thrusting in the forelands suggests that the maximum compressive stress there is horizontal and is oriented approximately east-west (Figure 2.3). Plateau extensional earthquakes suggest a maximum compressive stress direction oriented vertical, a minimum compressive stress direction oriented north-south (Figure 2.25), and an intermediate stress direction is east-west. Consistent with the plateau horizontal focal mechanism axis orientations, the two dimensional infinitesimal strain directions derived from GPS velocities illustrate roughly east-west compression and north-south extension across the plateau of southern Peru and northernmost Chile [*Allmendinger, et al.*, 2007].

A vertically oriented maximum stress direction in areas of high topography has previously been related to stress differentials in the crust needed to maintain the high topography and crustal root of the plateau [e.g., *Dalmayrac and Molnar*, 1981; *Froidevaux and Isacks*, 1984; *Mercier, et al.*, 1992; *Molnar and Lyon-Caen*, 1988]. North-south extension in the plateau is consistent with structural analysis of southern Peru that concluded north-south extension occurs in the region [e.g., *Mercier*, 1980; *Mercier, et al.*, 1992; *Sebrier, et al.*, 1985]. Models predict a rotation in orientation of principle stress directions from the plateau to its bounding regions (i.e., the trench and foreland). Crustal thickness estimates beneath the Altiplano-Puna plateau reach upwards of 80 km [*Beck and Zandt*, 2002; *Beck, et al.*, 1996; *McGlashan, et al.*, 2008; *Yuan, et al.*, 2000; *Yuan and Sobolev*, 2002; *Zandt, et al.*, 1996; *Zandt, et al.*, 1994]. A first-order effect of thickened crust and associated high topography is to perturb vertical lithospheric stresses. In compressional regions of relatively low topography, the direction of maximum horizontal stress corresponds to the direction of maximum lithospheric compression and the vertical stress corresponds to the direction of

minimum compression. In areas of thickened crust, lithospheric stress orientations can change because of increasing vertical stresses due to the thickened crustal mass. If large elevations and corresponding large crustal thicknesses are reached the direction of maximum lithospheric compression could become vertical causing extension. This theory provides one possible explanation for plateau extension.

For the strike-slip focal mechanisms in the northern Altiplano, the T axes also trend north-south, while the P and B axes have interchanged, with the P axis nearly horizontal and trending east-west, similar to the trends of the foreland focal mechanisms. In terms of a foreland thrust-type focal mechanism, the superposition of an increased vertical compressive stress can either produce normal faulting if that component becomes the maximum compressive stress component (P axis), or strike-slip faulting if that vertical stress only manages to become the intermediate compressive component (B axis).

The Tibetan plateau can act as a point of comparison with the Andean plateau. Tibet, like the Altiplano-Puna, is a vast plateau associated with a subduction zone setting, but, unlike the Andes, the setting involves continent-continent collision. Tibet exhibits pervasive seismic activity covering the plateau. Earthquake focal mechanism orientations display kinematic domains that strongly correlate with topography and deformational style in Tibet [e.g., *Andronicos, et al.*, 2007; *Langin*, 2003]. Southern Tibet has a zone where predominantly extensional earthquakes and graben north-south faults occur. A number of studies have concluded that normal earthquakes and extensional grabens are generally restricted to elevations above 4.5 km on the Tibet plateau [*Molnar and Lyon-Caen*, 1988]. The role of gravity in producing Tibetan extension has also been suggested [e.g., *Molnar and Tapponnier*, 1978]. Alternatively,

several workers have suggested that Tibetan east-west extension is driven by crustal flow away from high topography centered in western Tibet [e.g., *Andronicos, et al.*, 2007; *Clark and Royden*, 2000; *Royden, et al.*, 1997]. And, Kapp and Guynn [2004] explained the two dimensional spatial pattern of normal-fault orientations solely by collisional stresses localized along a southern part of the Himalayan arc. These alternative theories provide scenarios through which to the study extension events on the Altiplano-Puna.

T axis orientations of normal fault earthquake mechanisms on the Andean plateau display a consistent north-south orientation, which is perpendicular to the approximately east-west direction of tectonic compression. Similarly, the extensional zone of Tibet shows extension oriented perpendicular to the direction of plate convergence. The existence of a ductile lower crust has been suggested to occur beneath the Andean plateau [e.g., *Beck and Zandt*, 2002; *Isacks*, 1988] and evaluation of crustal shortening estimates and subsequent crustal thicknesses suggest along-strike lower crustal flow may occur beneath the Andean plateau [*Hindle, et al.*, 2002; *Hindle, et al.*, 2005; *Kley*, 1999]. The case for lower crustal flow beneath Tibet is much stronger than for beneath the Altiplano-Puna. Modeling of GPS velocity vectors and dynamic topography are both consistent with along-strike crustal flow out the region of the Eastern Syntaxis [e.g., *Clark and Royden*, 2000; *Royden, et al.*, 1997]. Previously however, crustal shortening and the thermal effects of a thin lithosphere were used to explain the majority of crustal thickening creating the Andean plateau [*Allmendinger, et al.*, 1997; *Isacks*, 1988], so, although conditions exist for a ductile lower crust, the existence of flow beneath the Altiplano-Puna remains debatable. Collisional stresses modeled by Kapp and Guynn [2004] in a semicircular elastic plate predict along-strike trench-parallel extension. Tibet's plate boundary geometry,

concave towards the orogen, is the opposite to that of the Andes, concave towards the trench. Reversing the concavity of the plate geometry would produce along-strike trench parallel shortening, rather than the roughly trench-perpendicular extension seen in the Andes, similar to patterns seen in interseismic surface velocity fields model by Bevis et al. [2001]. Also, as mentioned earlier, the modeled velocity fields do not predict trench-parallel deformation into the plateau. It lies too far from the locked plate boundary used for modeling. Finally, as discussed earlier, the potential gravitational effects of thickened crust and high topography of the Andean plateau, along with the east-west convergence as demonstrated in the foreland regions, is consistent with the Altiplano plateau of southern Peru and northern-most Chile experiencing north-south oriented extension due to lithospheric stress perturbations from buoyant thickened crust [e.g., *Dalmayrac and Molnar*, 1981].

Conclusions

Basement-involved deformation is consistently associated with seismically active structures of the Eastern Cordillera and foreland regions. Three types of seismically active structures are: (1) shallow seismic activity associated with the near-surface expression of basement thrust blocks (e.g., Shira uplifts), (2) deep diffuse earthquake activity associated with a possible mid-crustal basement wedge creating a basement-cored anticline (e.g, Pie de Palo), and (3) inverted relic rift structures deforming at deep depths beneath undeformed foreland basins (e.g., east of the Huallaga basin).

Central Andean foreland regions exhibit a roughly east-west direction of convergence. Local structures seem to be influencing earthquake focal mechanism orientations in the region of the Santa Cruz bend, so deviation of the dominant direction of foreland

compression from the direction of Nazca-South America plate convergence is likely due to the influence of local structure.

Normal and strike-slip earthquakes occur beneath the Altiplano plateau of southern Peru and northernmost Chile. These events are consistent with the effects of the increase in vertical compressive stress, due to high topography and thick crustal root of the plateau, superimposed on the stress orientations seen in the foreland.

REFERENCES

Allenby, R. J. (1987), Origin of the Bolivian Andean orocline: a geologic study utilizing Landsat and shuttle imaging radar, *Tectonophysics*, *142* (2-4), 137-154.

Allmendinger, R. W. (2002), Stereonet for Windows v. 1.2, http://www.geo.cornell.edu/geology/faculty/RWA/programs.html.

Allmendinger, R. W., et al. (2005), Trench-parallel shortening in the Northern Chilean Forearc: Tectonic and climatic implications, *Geol. Soc. Am. Bull.*, *117* (1/2), 89–104.

Allmendinger, R. W., et al. (1997), The Evolution of the Altiplano-Puna Plateau of the Central Andes, in *Annu. Rev. Earth Planet. Sci.*, edited, pp. 139-174, Annual Reviews Inc.

Allmendinger, R. W., et al. (1983), Paleogeography and Andean structural geometry, northwest Argentina, *Tectonics*, *2*, 1-16.

Allmendinger, R. W., et al. (2007), Strain and rotation rate from GPS in Tibet, Anatolia, and the Altiplano, *Tectonics*, *26* (3), doi: 10.1029/2006tc002030.

Allmendinger, R. W., and T. R. Zapata (2000), The footwall ramp of the Subandean decollement, northernmost Argentina, from extended correlation of seismic reflection data, *Tectonophysics*, *321* (1), 37-55.

Alvarado, P., and S. Beck (2006), Source characterization of the San Juan (Argentina) crustal earthquakes of 15 January 1944 (Mw 7.0) and 11 June 1952 (Mw 6.8), *Earth Planet. Sci. Lett.*, *243* (3-4), 615–631, doi:10.1016/j.epsl.2006.01.015.

Alvarado, P., et al. (2005), Crustal deformation in the south-central Andes backarc terranes as viewed from regional broadband seismic waveform modeling, *Geophys. J. Int.*, *163* (2), 580–598, doi: 10.1111/j.1365-246X.2005.02759.x.

Alvarado, P. M., et al. (2004), Modeling of Andean backarc (30°-36°S) crustal earthquake waveforms using a portable regional broadband seismic network, in *Tópicos de Geociencias. Un volumen de estudios sismológicos, geodésicos y geológicos en homenaje al Ing. Fernando Séptimo Volponi*, edited by S. A. Miranda, et al., pp. 53-93, UNSJ Editorial, San Juan, Argentina.

Andronicos, C. L., et al. (2007), Large-scale deformation in the India-Asia collision constrained by earthquakes and topography, *19* (2), 105-119, doi:10.1111/j.1365-3121.2006.00714.x.

Angermann, D., et al. (1999), Space-geodetic estimation of the Nazca-South America Euler vector, *Earth Planet. Sci. Lett.*, *171* (3), 329-334.

Assumpçao, M., and M. Araujo (1993), Effect of the Altiplano-Puna Plateau, South America, on the regional intraplate stresses, *Tectonophysics*, *221* (3-4), 475-496.

Baby, P., et al. (1992), Geometry and kinematic evolution of passive roof duplexes deduced from cross section balancing; example from the foreland thrust system of the southern Bolivian subandean zone, *Tectonics*, *11* (3), 523-536.

Baby, P., et al. (1995), Petroleum system of the northern and central Bolivian Sub-Andean zone, in *Petroleum Basins of South America, AAPG Memoir 62*

edited by R. S. A. J. Tankard, H. J. Welsink, pp. 445-458, AAPG.

Baby, P., et al. (1997), Neogene shortening contribution to crustal thickening in the back arc of the Central Andes, *Geology*, *25* (10), 883-886.

Barazangi, M., and B. L. Isacks (1976), Spatial distribution of earthquakes and subduction of the Nazca Plate beneath South America, *Geology*, *4* (11), 686-692.

Beck, S. L., and G. Zandt (2002), The nature of orogenic crust in the Central Andes, *J. Geophys. Res.*, *107* (10).

Beck, S. L., et al. (1996), Crustal-thickness variations in the Central Andes, *Geology*, *24* (5), 407-410.

Bevis, M., et al. (2001), On the strength of interplate coupling and the rate of back arc convergence in the Central Andes; an analysis of the interseismic velocity field, *Geochem. Geophys. Geosyst.*, *2*, 20011101.

Bevis, M., and S. J. Martel (2001), Oblique plate convergence and interseismic strain accumulation, *Geochem. Geophys. Geosyst.*, *2*, 2000GC000125.

Bianucci, H., et al. (1982), Inversion tectonica y plegamientos resultantes en la comarca Puesto Guardian-Dos Puntitas, Departamento de Oran, Provincia de Salta, in *Primer Congreso Nacional de Hidrocarburos; Exploracion*, edited, Inst. Argent. Petrol., Buenos Aires.

Brooks, B. A., et al. (2003), Crustal motion in the Southern Andes (26–36S): Do the Andes behave like a microplate?, *Geochem. Geophys. Geosyst.*, *4* (10), 1085, doi:1010.1029/2003GC000505.

Cahill, T., et al. (1992), Seismicity and tectonics in Jujuy Province, northwestern Argentina, *Tectonics*, *11* (5), 944-959.

Cahill, T. A., and B. L. Isacks (1992), Seismicity and shape of the subducted Nazca Plate, *J. Geophys. Res.*, *97* (B12), 17,503-517,529.

Calkins, J. A., et al. (2006), Crustal images from San Juan, Argentina, obtained using high frequency local event receiver functions, *Geophys. Res. Lett.*, *33* (7), L07309, doi:10.1029/2005GL025516.

Chinn, D. S., and B. L. Isacks (1983), Accurate source depths and focal mechanisms of shallow earthquakes in western South America and in the New Hebrides island arc, *Tectonics*, *2* (6), 529-563.

Clark, M. K., and L. H. Royden (2000), Topographic ooze: Building the eastern margin of Tibet by lower crustal flow, *Geology*, *28* (8), 703-706.

Comte, D., et al. (2003), Distribucion temporal y en profundidad de las replicas del sismo superficial de Armoa, norte de Chile del 24 de Julio de 2001, paper presented at 10th Congreso Geologico Chileno 2003, Universidad de Concepcion Departamento de Ciencias de la Tierra.

Dalmayrac, B., and P. Molnar (1981), Parallel thrust and normal faulting in Peru and constraints on the state of stress, *Earth Planet. Sci. Lett.*, *55* (3), 473-481.

David, C., et al. (2003), Analisis sismotectonico en torno al codo de Arica: resultados preliminares, paper presented at 10th Congreso Geologico Chileno 2003.

de Silva, S. L., and P. W. Francis (1991), Volcanoes of the Central Andes, 216 p, Springer-Verlag, New York.

Dewey, J. F., and S. H. Lamb (1992), Active Tectonics of the Andes, *Tectonophysics*, *205* (1-3), 79-95.

Dorbath, C., et al. (1987), On crustal seismicity of the Amazonian foothill of the Central Peruvian Andes, *Geophys. Res. Lett.*, *13* (10), 1023-1026.

Dunn, J. F., et al. (1995), Structural styles and hydrocarbon potential of the sub-Andean thrust belt of southern Bolivia, *Petroleum basins of South America*, *62*, 523-543.

Dziewonski, A. M., et al. (1981), Determination of earthquake source parameters from waveform data for studies of global and regional seismicity, *J. Geophys. Res.*, *86* (B4), 2825-2852.

Espurt, N., et al. (2008), Paleozoic structural controls on shortening transfer in the Subandean foreland thrust system, Ene and southern Ucayali basins, Peru, *Tectonics*, *27* (TC3009), doi:10.1029/2007TC002238.

Fielding, E. J. (1989), Neotectonics of the central Andean Cordillera from satellite imagery, 228 pp, Cornell University, Ithaca, NY.

Froidevaux, C., and B. L. Isacks (1984), The mechanical state of the lithosphere in the Altiplano-Puna segment of the Andes, *Earth Planet. Sci. Lett.*, *71* (2), 305-314.

Fromm, R., et al. (2004), Crustal thickness beneath the Andes and Sierras Pampeanas at 30°S inferred from Pn apparent phase velocities, *Geophys. Res. Lett.*, *31* (6), 1-4.

Funning, G. J., et al. (2005), The 1998 Aiquile, Bolivia earthquake; a seismically active fault revealed with InSAR, *Earth Planet. Sci. Lett.*, *232* (1-2), 39-49.

Grier, M. E. (1990), The influence of the Cretaceous Salta Rift basin on the development of Andean structural geometries, NW Argentine Andes, 192 pp.

Hermoza, W., et al. (2005), The Huallaga foreland basin evolution: Thrust propagation in a deltaic environment, northern Peruvian Andes, *J. S. Am. Earth Sci.*, *19* (1), 21-34.

Hindle, D., et al. (2002), Consistency of geologic and geodetic displacements during Andean orogenesis, *Geophys. Res. Lett.*, *29* (8), 20020415.

Hindle, D., et al. (2005), Crustal balance and crustal flux from shortening estimates in the Central Andes, *Earth Planet. Sci. Lett.*, *230* (1-2), 113-124, doi: 10.1016/j.epsl.2004.11.004.

INGEMMET (1999), 1:1,000,000 Mapa Geologico del Peru,, Lima, Peru.

Isacks, B. L. (1988), Uplift of the Central Andean Plateau and bending of the Bolivian Orocline, *J. Geophys. Res.*, *93* (B4), 3211-3231.

James, D. E., and J. A. Snoke (1994), Structure and tectonics in the region of flat subduction beneath central Peru; crust and uppermost mantle, *J. Geophys. Res.*, *99* (B4), 6899-6912.

Jordan, T. E., and R. W. Allmendinger (1986), The Sierras Pampeanas of Argentina; a modern analogue of Rocky Mountain foreland deformation, *Am. J. Sci.*, *286* (10), 737-764.

Jordan, T. E., et al. (1983), Andean tectonics related to geometry of subducted Nazca plate, *Geol. Soc. Am. Bull.*, *94*, 341-361.

Kadinsky-Cade, K., et al. (1985), Surface deformation associated with the November 23, 1977, Caucete, Argentina, earthquake sequence, *J. Geophys. Res.*, *90* (B14), 12,691-612,700.

Kagan, Y. Y. (2004), Short-term properties of earthquake catalogs and models of earthquake source, *B. Seismol. Soc. Am.*, *94* (4), 1207-1228.

Kamb, W. B. (1959), Ice petrofabric observations from Blue Glacier, Washington, in relation to theory and experiment, *J. Geophys. Res.*, *64* (11), 1891-1909.

Kapp, P., and J. H. Guynn (2004), Indian punch rifts Tibet, *Geology*, *32* (11), 993-996.

Kennett, B. L. N., et al. (1995), Constraints on seismic velocities in the earth from travel times, *Geophys. J. Int.*, *122*, 108-124, doi:10.1111/j.1365-246X.1995.tb03540.x

Kley, J. (1996), Transition from basement-involved to thin-skinned thrusting in the Cordillera Oriental of southern Bolivia, *Tectonics*, *15* (4), 763.

Kley, J. (1999), Geologic and geometric constraints on a kinematic model of the Bolivian orocline, *J. S. Am. Earth Sci.*, *12* (2), 221-235.

Kley, J., and C. R. Monaldi (1998), Tectonic shortening and crustal thickness in the Central Andes; how good is the correlation?, *Geology*, *26* (8), 723-726.

Kley, J., and C. R. Monaldi (2002), Tectonic inversion in the Santa Barbara System of the central Andean foreland thrust belt, northwestern Argentina, *Tectonics*, *21* (6).

Kley, J., et al. (1999), Along-strike segmentation of the Andean foreland; causes and consequences, *Tectonophysics*, *301* (1-2), 75-94.

Langin, W. R. (2003), Seismicity, tectonics, and lithospheric structure of the Tibetan Plateau, Ph.D. thesis, 162 pp, Cornell University, Ithaca, NY.

Legrand, D., et al. (2007), Source parameters of the M-w=6.3 Aroma crustal earthquake of July 24, 2001 (northern Chile), and its aftershock sequence, *J. S. Am. Earth Sci.*, *24* (1), 58-68.

Maggi, A., et al. (2002), Focal Depths of Moderate to Large Magnitude Earthquakes in Iran, *J. Seism. Earthq. Eng.*, *4* (2-3), 1-10.

Mathalone, J. M. P., and M. Montoya R (1995), Petroleum geology of the sub-Andean basins of Peru, *Petroleum basins of South America*, *62*, 423-444.

McCaffrey, R. (1996), Estimates of modern arc-parallel strain rates in fore arcs, *Geology*, *24* (1), 27-30.

McCaffrey, R., and G. A. Abers (1988), SYN3: A program for inversion of teleseismic body waveform on microcomputers., Air Force Geophysics Laboratory Technical Report, AFGL-TR-88-0099.

McCaffrey, R., et al. (1991), Inversion of teleseismic body waves in *Digital Seismogram Analysis and Waveform Inversion*, edited by W. H. K. Lee, pp. 81-166, Int. Assoc. Seismol. Phys. Earth Inter. Software Library.

McGlashan, N., et al. (2008), Crustal thickness in the Central Andes from teleseismically recorded depth phase percursors, *Geophys. J. Int.*, *in press*.

McNulty, B., and D. Farber (2002), Active detachment faulting above the Peruvian flat slab, *Geology*, *30* (6), 567-570.

McNulty, B. A., et al. (1998), Role of plate kinematics and plate-slip-vector partitioning in continental magmatic arcs: evidence from the Cordillera Blanca, Peru, *Geology*, *26*, 827-830.

McQuarrie, N., and G. H. Davis (2002), Crossing the several scales of strain-accomplishing mechanisms in the hinterland of the central Andean fold-thrust belt, Bolivia, *J. Struct. Geol.*, *24* (10), 1587-1602.

Megard, F. (1987), *Structure and evolution of the Peruvian Andes*, Princeton, NJ.

Mercier, J. L. (1980), Extensional-compressional tectonics associated with the Aegean Arc; comparison with the Andean Cordillera of South Peru-North Bolivia, in *Extensional tectonics associated with convergent plate boundaries; Discussion meeting | Extensional tectonics associated with convergent plate boundaries Discussion meeting*, edited by F. J. Vine and A. G. Smith, pp. 337-355, Royal Society of London.

Mercier, J. L., et al. (1992), Changes in the tectonic regime above a subduction zone of Andean type: the Andes of Peru and Bolivia during the Pliocene-Pleistocene, *J. Geophys. Res.*, *97* (B8), 11,945-911,982.

Molnar, P., and H. Lyon-Caen (1988), Some simple physical aspects of the support, structure, and evolution of mountain belts, *Geol. Soc. Am. Spec Pap.*, *218*, 179-207.

Molnar, P., and P. Tapponnier (1978), Active tectonics of Tibet, *J. Geophys. Res.*, *83* (B11), 5361-5375.

Montagner, J.-P. K., B.L.N. (1996), How to reconcile body-wave and normal-mode reference earth models, *Geophys. J. Int.*, *125* (1), 229-248, doi:10.1111/j.1365-246X.1996.tb06548.x

Norabuena, E., et al. (1998), Space geodetic observations of Nazca-South America convergence across the Central Andes, *Science*, *279* (5349), 358-362.

Pritchard, M. E., et al. (2007), Geodetic, teleseismic, and strong motion constraints on slip from recent southern Peru subduction zone earthquakes, *J. Geophys. Res.*, *112, no. B3* (B3).

Ramos, V. A., et al. (2002), The Pampean flat-slab of the Central Andes, *J. S. Am. Earth Sci.*, *15* (1), 59-78.

Ramos, V. A., and G. Vujovich (2000), Hoja Geologic San Juan, escala 1:250000, 82, Servicio Geologico Minero Argentino, Boletin, Buenos Aires.

Regnier, M., et al. (1992), Seismotectonics of Sierra Pie de Palo, a basement block uplift in the Andean foreland of Argentina, *Bull. Seismol. Soc. Am.*, *82* (6), 2549-2571.

Roeder, D., and R. L. Chamberlain (1995), Structural geology of sub-Andean fold and thrust belt in northwestern Bolivia, in *Petroleum Basins of South America*, edited, pp. 459-479, AAPG.

Royden, L. H., et al. (1997), Surface deformation and lower crustal flow in eastern Tibet, *Science*, *276* (5313), 788-790.

Sebrier, M., et al. (1985), Quaternary normal and reverse faulting and the state of stress in the Central Andes of South Peru, *Tectonics*, *4* (7), 739-780.

Sheffels, B. M. (1995), Is the bend in the Bolivian Andes an orocline?, *Petroleum basins of South America*, *62*, 511-522.

Siame, L. L., et al. (2005), Deformation partitioning in flat subduction setting: Case of the Andean foreland of western Argentina (28S–33S), *Tectonics*, *24* (TC5003), 24.

Smalley, R., Jr., and B. L. Isacks (1990), Seismotectonics of thin- and thick-skinned deformation in the Andean foreland from local network data; evidence for a seismogenic lower crust, *J. Geophys. Res.*, *95* (B8), 12,487-412,498.

Smalley, R., Jr., et al. (1993), Basement seismicity beneath the Andean Precordillera thin-skinned thrust belt and implications for crustal and lithospheric behavior, *Tectonics*, *12* (1), 63-76.

Stauder, W. (1975), Subduction of Nazca Plate under Peru as Evidenced by Focal Mechanisms and by Seismicity, *J. Geophys. Res.*, *80* (8), 1053-1064.

Suarez, G., et al. (1983), Seismicity, Fault Plane Solutions, Depth of Faulting, and Active Tectonics of the Andes of Peru, Ecuador, and Southern Colombia, *J. Geophys. Res.*, *88* (B12), 403-428.

Yuan, X., et al. (2000), Subduction and collision processes in the Central Andes constrained by converted seismic phases, *Nature*, *408* (6815), 958-961.

Yuan, X., and S. V. K. R. Sobolev (2002), Moho topography in the Central Andes and its geodynamic implications, *Earth Planet. Sci. Lett.*, *199* (3-4), 389-402.

Zandt, G., et al. (1996), Anomalous crust of the Bolivian Altiplano, Central Andes: Constraints from broadband regional seismic waveforms, *Geophys. Res. Lett.*, *23*, 1159-1162.

Zandt, G., et al. (1994), Composition and thickness of the southern Altiplano crust, Bolivia, *Geology*, *22* (11), 1003-1006.

Zwick, P., et al. (1994), MT5, IASPEI Software Library, 4, http://ees2.geo.rpi.edu/rob/mt5/.

CHAPTER 3

EARTHQUAKES IN THE LOWER CONTINENTAL CRUST: A GLOBAL SYNTHESIS

Abstract

Continental seismogenic thickness (T_S), the depth to which earthquakes occur, defines the thickness where stress relaxation is accommodated in some part by seismic rupture. The jelly sandwich model of lithospheric strength postulates an aseismic, ductile lower crust between a seismic, brittle upper crust and mantle lid. In many continental areas, crustal seismicity is restricted to the upper crust consistent with the crustal portion of the model. However, studies in other localities have documented lower crustal earthquakes to near-Moho depth, which is contrary to the model. Here we investigate in what tectonic settings lower crustal earthquakes occur in an attempt to understand their significance to lithospheric strength and deformation. We compiled a global dataset from previously published sources of accurately determined continental earthquake depths (± 5 km or better).

Results indicate that deep crustal earthquakes are not restricted to any one type of Late Cenozoic tectonically active setting and that a relationship exists between variations in T_S and variations in lithospheric thickness and amount of crustal deformation. Lower crustal earthquakes beneath continents are well-documented to occur in areas experiencing extension (e.g., East African Rift System, North Island New Zealand, Baikal Rift System, Upper Rhine Graben Region), compression (e.g., Tien Shan, Alpine Foreland, Western Pyrenees, Andean Foreland), and one transtensional region (Dead Sea Fault System). Additionally, deep crustal earthquakes are documented to

occur in seismically active, stable cratonic areas (e.g., Bhuj and Jabalpur in India, St. Lawrence River region near the US–Canadian border, Aswan Egypt). Within tectonically active regions, deep continental crustal earthquakes occur where the lithosphere is in an intermediate state between being primarily thick and tectonically stable (e.g., shields) and being thin and highly deformed (e.g., Basin and Range or Southern California). Lower crustal earthquakes in tectonically active regions occur where lithospheric thicknesses are between about 80 and 160 km thick and where the crust has experienced less than 30% strain. Therefore, earthquakes in the lower continental crust can occur within stable lithosphere and within tectonically active lithosphere at a transitional state of lithospheric thickness and crustal deformation.

In order to understand what controls the occurrence of these deep crustal earthquakes and reconcile the variety of tectonic settings in which they occur, we discuss possible lower crustal deformation mechanisms. Common interpretations of crustal strength profiles are that earthquakes occur only where slip on pre-existing faults is dominant (i.e., in the middle to upper crust). Deformation mechanisms such as ductile instabilities, fluid embrittlement, and eclogitic phase transitions highlight the fact that not only can earthquakes occur within the brittle portion of the continental crust, but, consistent with observations, they can also occur where power-law creep is the dominant method of deformation (i.e., in the lower crust). However, fluid-enhanced embrittlement is likely to be the only deformation mechanism capable of explaining continental lower crustal earthquakes in the wide variety of settings where these events occur.

Introduction

A fundamental question in geology is how the strength and deformation of the lithosphere vary spatially and temporally [e.g., *Jackson*, 2002; *Thatcher and Pollitz*, 2008; *Watts and Burov*, 2003]. The seismogenic thickness (T_S) of continental lithosphere is one parameter we can use to understand where and how the lithosphere is deforming. T_S is the depth over which earthquakes occur, which defines the thickness where stress relaxation is accommodated in some part by seismic rupture. Earthquakes are one of the most easily observable indicators of on-going lithospheric deformation and thus far, in continental regions, they mainly occur within the crust and not the mantle lid [e.g., *Maggi, et al.*, 2000a]. Seismic activity occurs with varying frequency throughout the entire seismogenic thickness (i.e., T_S typically defines a continuous seismic layer from the surface of the Earth to a depth equal to T_S) and T_S is generally found to be less than or equal to the thickness of the continental crust. This paper investigates earthquakes occurring in the continental lithosphere with a specific concentration on those occurring in the lower crust. Lower crustal earthquakes are phenomena that have become increasingly well documented in the scientific literature in many places around the world, but are not predicted by popular theories of lithospheric strength and dominant modes of deformation. The purpose of this chapter is to review the global distribution of accurately determined lower crustal earthquakes beneath continents, and from this to better understand the relationship of these earthquakes to lithospheric properties.

Earthquakes in the oceanic lithosphere occur within both the crust and uppermost mantle [e.g.,*Chen and Molnar*, 1983; *Wiens and Stein*, 1983]. There is a simple relationship of T_S to temperature, and therefore age, of the oceanic lithosphere, as supported by numerous studies [e.g., *Chen and Molnar*, 1983; *McKenzie, et al.*, 2005;

Wiens and Stein, 1983]. T_S increases from very thin in young, hot lithosphere to approximately 50 km in older, cooler oceanic lithosphere. Chen and Molnar [1983] and Wiens and Stein [1983] found limiting isotherms around 600 to 800°C, while McKenzie et al. [2005] came to a similar result, about 600°C. In McKenzie et al.'s [2005] study, only earthquakes beneath the outer rises of trenches occur in oceanic lithosphere hotter than 600°C. They attributed the occurrence of these outlying events to large strain rates.

T_S within continental lithosphere has not proven to be as simple. In 1983, Chen and Molnar published an influential study relating focal depth distributions of intraplate earthquakes to the mechanical strength of the oceanic and continental lithospheres. Chen and Molnar used the depth distribution of earthquakes to support the idea that continental lithosphere consists of a weak, aseismic lower crust located between the stronger, seismic upper crust and mantle lid. This "jelly sandwich" model of the strength of continental lithosphere has largely influenced our understanding of tectonic deformation since its publication. Chen and Molnar predicted and observationally supported a bimodal earthquake distribution in continental lithosphere coincident with lithospheric mechanical strength. Within the jelly sandwich model, crustal seismicity is limited to depths of $\lesssim$ 15 km, aseismic deformation would occur from ~ 15 km to the Moho, and the mantle lid is predicted to exhibit seismic activity. The model's corresponding lithospheric mechanical strength profile is based on assumptions of rheology and dominant modes of deformation. The interpretation made by Chen and Molnar is that earthquakes should only outline the portion of the profile where frictional slip is the prevailing deformation mechanism (i.e., in the upper crust and mantle lid). Because deformation in the lower crust is understood to be dominated by ductile creep, the lower crust remained aseismic. Many seismically active regions

around the world are partially consistent with the jelly sandwich model. That is, the upper continental crust is seismogenic to a depth of about 15 to 20 km and the lower crust is aseismic, as in the San Andreas Fault System and the Zagros mountains [e.g., *Maggi, et al.*, 2000a; *Nazareth and Hauksson*, 2004]. However, two problems with the jelly sandwich model have since emerged.

First, no clear global continental pattern of reliably determined earthquake hypocenters with depths in the upper mantle has appeared [*Jackson*, 2002; *Maggi, et al.*, 2000a]. Studies have documented possible mantle lid seismicity in several locations, but the events are often few in number and small in magnitude. The Himalayan collisional belt exhibits possible mantle seismicity beneath the subducted Indian plate, but this region, in a unique tectonic setting, is difficult to extrapolate to a global pattern of continental crustal seismicity.

The second problem with the jelly sandwich model is the discovery in a number of regions of accurately determined seismicity in the lower crust where the weak ductile layer was hypothesized. T_S in those regions covers nearly to the entire crust. Globally, these events occur much more frequently and with higher magnitudes than the possible continental mantle lid events. Therefore, the focus of this paper is to survey the regions where reliably observed lower crustal seismicity beneath the continents has been found. By conducting this survey, we want to understand what the many regions exhibiting lower crustal seismicity have in common and how they are relevant to our understanding of lithospheric strength and deformation.

The foundation of this research is a literature review of accurate depth parameters of intraplate lower crustal earthquakes throughout the continents. Bulletin and catalog

depths are insufficiently accurate to resolve focal depth distributions within the crust [e.g., *Maggi, et al.*, 2002]. For that reason, reviewing published studies that report accurate depths of continental crustal earthquakes is the best data source for a global study. With the explosion of earthquake waveform modeling and local network studies since Chen and Molnar's [1983] publication, it is timely to review global continental earthquake depths and associated lithospheric strength. To date, no other study has compiled a review of earthquakes occurring in the lower continental crust as extensive as that presented here. While studies in individual areas have noted the occurrence of lower crustal earthquakes, no recent study has collected the data to investigate these phenomena globally.

Earthquakes occur in the lower continental crust at a variety of tectonic settings, as in East Africa and near Lake Baikal associated with extension, within the subducting Indian lithosphere and the forelands of Peru and Argentina associated with compression, and along the Dead Sea fault system associated with transtension. This paper discusses lower crustal earthquakes in their regional tectonic frameworks. We want to understand what tectonic settings appear to be associated with the deep crustal seismicity and how this seismicity integrates with other methods of deformation to create lithospheric scale deformation. We try to understand if and why these regions may deviate from popular understanding of lithospheric deformation (i.e., the jelly sandwich model) and address what that means for geologists' broader understanding of lithospheric strength and seismicity. Finally, we propose a model that relates continental lithospheric structure and deformation to deep crustal seismicity.

Earthquake data selection

Depths of earthquakes are particularly difficult to constrain, especially when the events are shallow (< 70 km) as they are in the continental crust. Local network studies provide the most reliable depths, however global coverage of local networks is sparse and deployment at any one location is sporadic when compared to the almost 50 years of recording by the combined operation of the World-Wide Standardized Seismograph Network (WWSSN) and Global Seismographic Network (GSN). Earthquake hypocenter determination in most places around the world is done using WWSSN and/or GSN data from stations located at regional and teleseismic distances from the event.

A number of global earthquake bulletins and catalogs exist that routinely report earthquake depths, such as the International Seismological Centre Bulletin (ISC), the Preliminary Determination of Epicenters (PDE) from the US Geological Survey's National Earthquake Information Center, the Global Centroid Moment Tensor Catalog (CMT) [*Dziewonski, et al.*, 1981], and the Centennial Earthquake Catalog (CEC) [*Engdahl, et al.*, 1998; *Engdahl and Villaseñor*, 2002]. However, technique limitations affecting parameter determination or the lack of teleseismic depth phase identification decreases these compilations' ability to resolve the relatively subtle differences in focal depth distribution within the continental crust [*Kagan*, 2004; *Maggi, et al.*, 2002]. Locations based on teleseismic *P* wave arrival times suffer from a trade-off between origin time and depth (ISC and PDE). CMT analysis of body waves, based on a very long-period (> 40 s) waves, filters out the short-period waves needed to accurately determine depth for shallow events. In principle, CEC earthquake locations should be more accurate than reported by the other bulletins and catalogs due in particular to the inclusion of teleseismic depth phase arrival times (*pP*, *sP*, and *pwP*).

However, Maggi et al. [2000a; 2002] compared CEC (referred to as EHB in those articles) depths to depths determined via teleseismic depth phase modeling (this technique is discussed below) and found inconsistencies as large as 40 km. Therefore, these global catalogs and bulletins do not report accurate enough depths to study shallow events and we must look elsewhere to compile a dataset of well-determined depths for continental earthquakes.

There are a variety of alternative methods utilized by seismologists to constrain earthquake depths and these depth determinations are the basis for this review study. As mentioned above, local network studies, where epicentral distances are $\lesssim 1°$, provide the most reliable depths due to proximal station location. Studies that report earthquakes from local seismograph deployments were incorporated into this study [e.g., *Aldersons, et al.*, 2003; *Langin, et al.*, 2003; *Reyners, et al.*, 2007], as well as events reported from analysis of waveforms recorded at dense permanent networks (e.g., the New Madrid Earthquake Catalog from CERI, the Southeast US Seismic Network, the Southern California Earthquake Catalog from SCEDC). We have a specific interest in local network studies that recorded lower crustal events, but we also included a number of studies that did not record such activity. These localities serve as counter examples. We limited all local network data to events with hypocenter vertical uncertainties of ± 5 km or better, which is consistent with errors from other depth determination methods (see below).

For earthquakes with magnitudes with Mw $\gtrsim$ 5.5 and recorded by long-period or broadband seismographs, the *P* and *S* wave arrivals can be modeled by including the effects of the focal mechanism orientation and moment release time function together with the direct *P* and *S* phases and surface-reflected *P* and *S* phases (*pP*, *sP*, and *sS*)

[e.g., *Foster and Jackson*, 1998; *Molnar and Lyon-Caen*, 1989; *Nelson, et al.*, 1987]. Such analyses typically yield depth uncertainties of ± 5 km, which is sufficient to describe general patterns of T_S within the continental crust. In addition, modeling of *Pn* and *Sn* coda at regional stations (epicentral distance $\lesssim 30°$) [e.g., *Brazier, et al.*, 2005; *Ghose, et al.*, 1998] and forward modeling and phase identification of short-period records has also produced accurate focal depths. Depth phase identification can be difficult on broadband or long-period records, higher frequency short-period waveforms can reveal differential traveltimes of *pP–P* and *sP–P*, thereby allowing a depth estimate to be made [e.g., *Maggi, et al.*, 2000a; *Nyblade and Langston*, 1995].

In this review, we highlight earthquake datasets that document the occurrence of lower crustal seismicity beneath continents. All event depths were determined by studies utilizing the above-described methods and have vertical uncertainties of ± 5 km or better.

Continental seismogenic thickness (T_S)

By compiling accurate continental earthquake depths and analyzing depth distribution histograms, we define three types of continental regions that exhibit seismic activity (Figure 3.1): tectonically active continental areas that exhibit a seismic lower crust (Figure 3.1 in red and Figure 3.2), tectonically active continental areas that exhibit an aseismic lower crust (Figure 3.1 in blue and Figure 3.3), and stable continental regions (SCRs) (Figure 3.1 in yellow). Most SCRs do not have significant earthquake activity, but to understand the seismic character of these regions we compiled data for a few SCRs that are seismically active (Figure 3.4). For each earthquake depth histogram in Figures 3.2, 3.3, and 3.4, earthquake depth uncertainties are ± 5 km or better and approximate Moho depths are illustrated as red dashed lines. If Moho depths vary

Figure 3.1: Location map of three types of seismically active continental regions. Global topographic base map showing the color-coded locations of each area with an earthquake depth histogram reported in this paper.

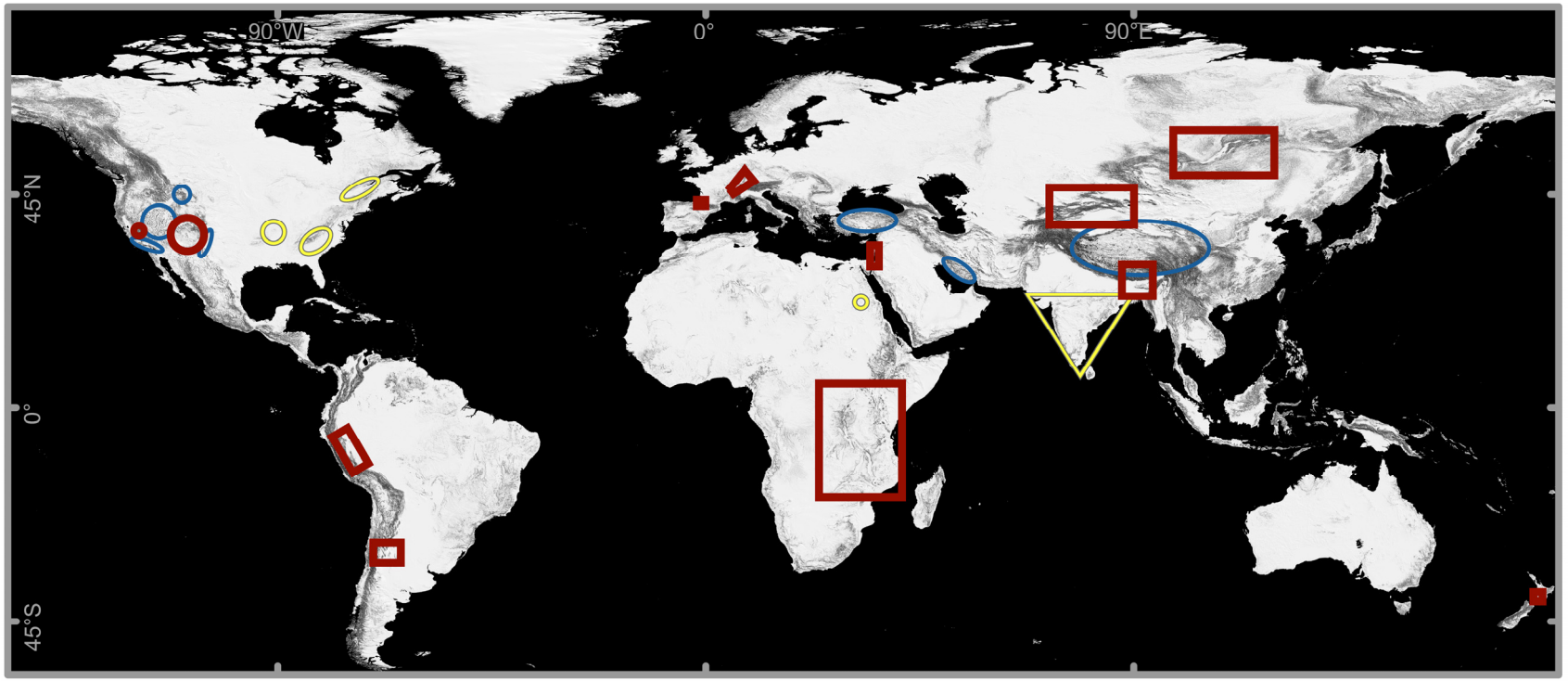

Tectonically active continental areas that exhibit a seismic lower crust (Figure 3.2)
Tectonically active continental areas that exhibit an aseismic lower crust (Figure 3.3)
Stable Continental Regions (Figure 3.4)

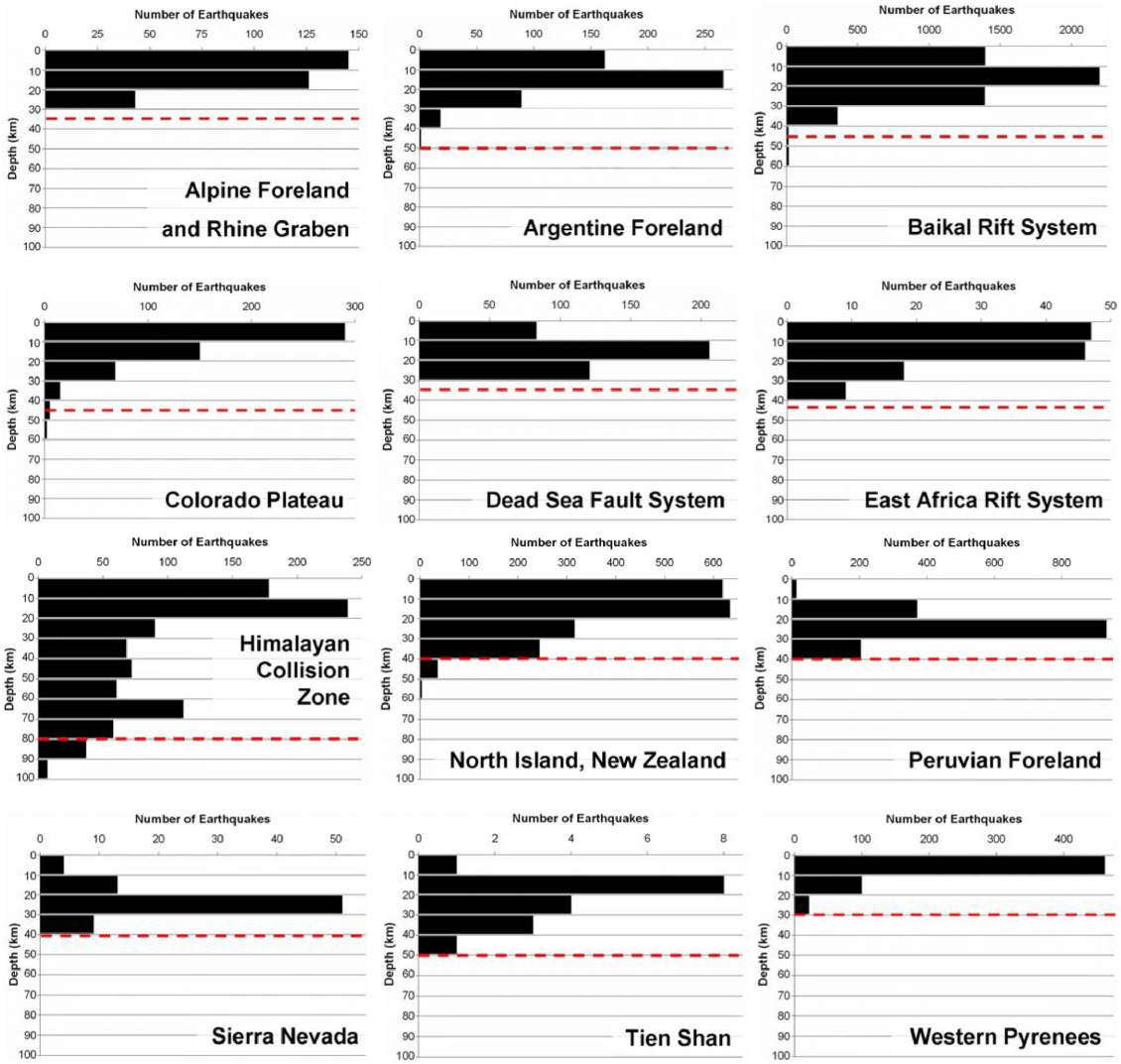

Figure 3.2: Earthquake depth histograms for tectonically active continental areas that exhibit a seismic lower crust. Dashed red line indicates approximate Moho depth. See Appendix B for earthquake depth and Moho references.

Figure 3.3: Earthquake depth histograms for tectonically active continental areas that exhibit an aseismic lower crust. Dashed red line indicates approximate Moho depth for each region. Earthquake depth and Moho references: Basin & Range – Earthquakes: UNR Historical Catalog 1990 → 1999, M_W 3.5 → 10; Moho: Gilbert and Sheehan [2004]. North Anatolian Fault – Earthquakes: Gurbuz et al. [2000], Polat et al. [2002], Turkelli et al. [2003], and Biryol et al. [2006]; Moho: Karahan et al. [2001], Ozacar et al. [2006], and Erduran et al. [2007]. Rio Grande Rift – Earthquakes: King [1986]; Moho: Olsen et al. [1987] and Wilson et al. [2005]. Southern California – Earthquakes: Southern California Earthquake Catalog from the SCEDC, 1999 → present, >Mw3 and Nazareth and Hauksson [2004]; Moho: Zhu and Kanamori [2000]. Tibet – Earthquakes are those north of the Indus-Tsangpo Suture, Earthquakes: Molnar and Chen [1983], Zhou et al. [1983], Jones et al. [1984], Molnar and Lyon-Caen [1989], Chen and Molnar [1990], Zhu and Helmberger [1996], Langin et al. [2003], Monsalve et al. [2006], and Torre et al. [2007]; Moho: Brown et al. [1996], Nelson et al. [1996], and Zhao et al. [2001]. Yellowstone – Earthquakes: UUSS Yellowstone National Park Earthquake Catalog, 1995 to 2006, EHZ ≤ 5 km; Moho: Schilly et al. [1982] and Peng and Humphreys [1998]. Zagros – Earthquakes: Ni and Barazangi [1986], Baker [1993], Baker et al. [1993], and Maggi et al. [2000a]; Moho: Snyder and Barazangi [1986], Paul et al. [2006] and see Maggi and Priestley [2005] for review of other references.

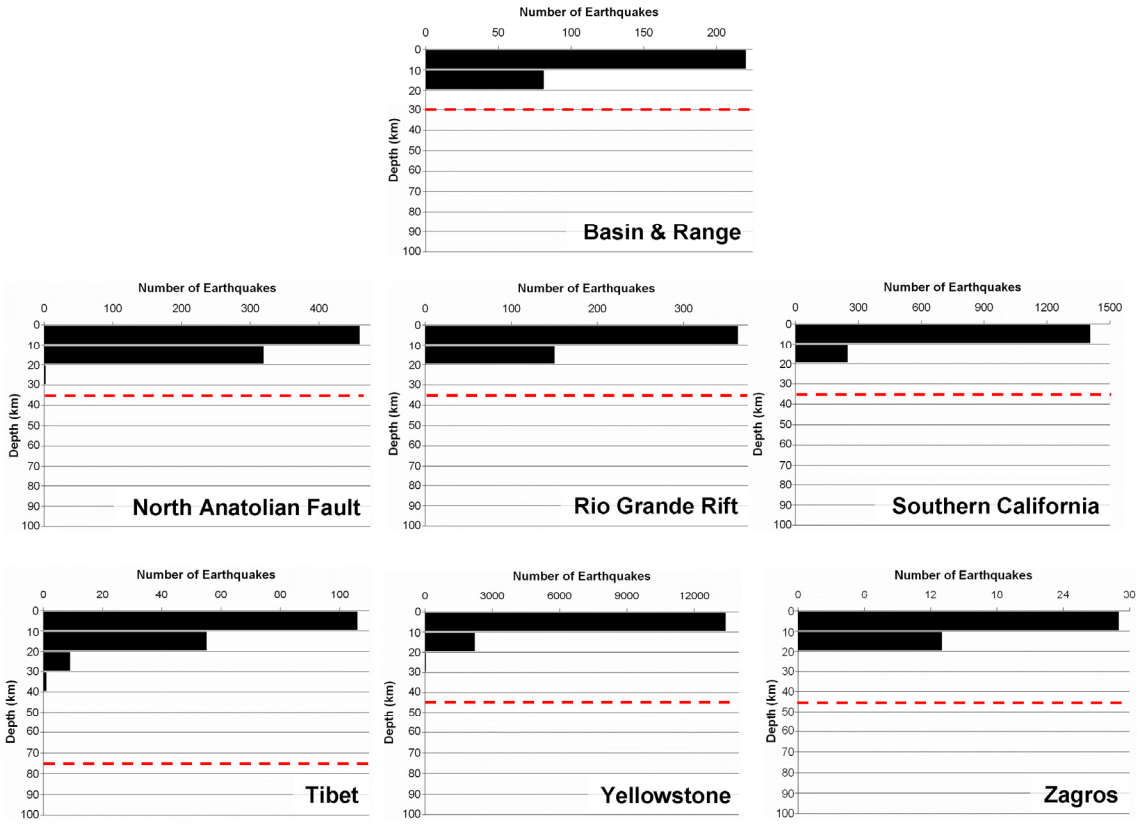
Number of Earthquakes
Depth (km)
Basin & Range
North Anatolian Fault
Rio Grande Rift
Southern California
Tibet
Yellowstone
Zagros

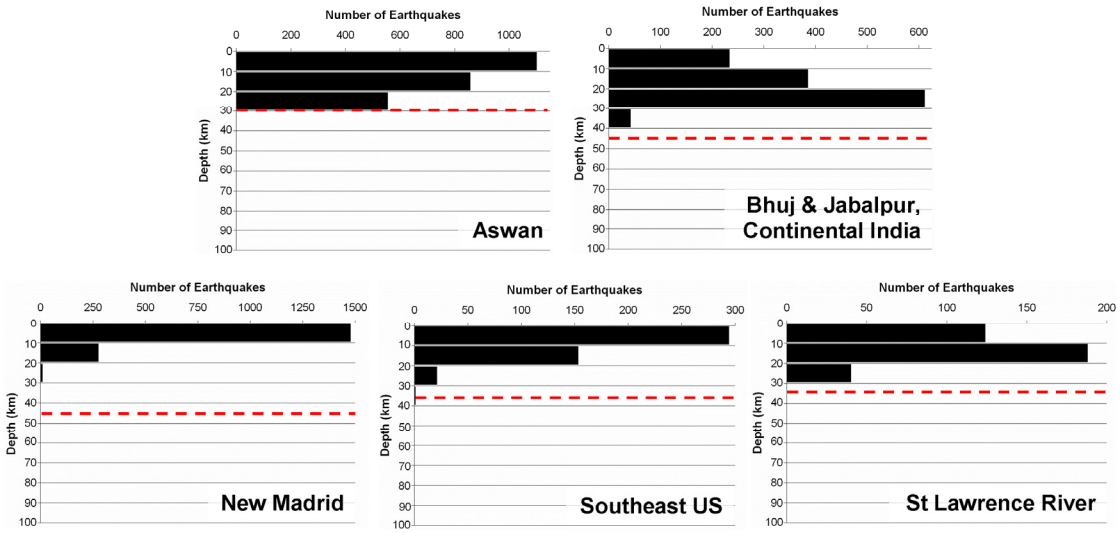

Figure 3.4: Earthquake depth histograms for stable continental regions (SCRs). Dashed red line indicates approximate Moho depth. Earthquake depth and Moho references: Aswan, Egypt – Earthquakes: Awad et al. [2005]; Moho: Gharib [1991] and Kebeasy et al., [1991]. Bhuj & Jabalpur, India – Earthquakes: Bodin & Horton [2004] and Rao & Rao [2006]; Moho: Saikia [2006]. New Madrid – Earthquakes: CERI Earthquake Catalog, 1993 → present; Moho: Catchings [1999]. Southeast United States – Earthquakes: Southeast US Seismic Network (SEUSS), 1990-present, Magnitude ≥ 2; Moho Reference: Nelson et al. [1985]. St. Lawrence River – Earthquakes: Lamontagne et al. [1994] and Ma & Atkinson [2006]; Moho: Ma & Atkinson [2006].

across a region, then the deepest Moho depth estimate is displayed. We consider an area to be experiencing earthquakes in the lower continental crust when T_S reaches to near-Moho depth (i.e., Moho depth minus $T_S \lesssim 10$ km), while the lower crust is considered aseismic if the deepest 10 km or more of crust is void of seismic activity. Figure 3.2 displays earthquake depth histograms of tectonically active continental regions for which event depths have been accurately determined to occur in the lower crust. The purpose of this section is to establish that deep crustal earthquakes beneath continents are in fact a global phenomenon which is not restricted to any one tectonic setting. These type of events occur in continental areas experiencing extension (e.g., East African Rift System, North Island New Zealand, Baikal Rift System, Upper Rhine Graben Region), compression (e.g., Tien Shan, Alpine Foreland, Western Pyrenees, Andean Foreland), and one transtensional region (Dead Sea Fault System). For the sake of conciseness, detailed discussion of the studies that were reviewed to construct and understand Figure 3.2 (e.g., earthquake and Moho depth estimates, regional tectonic settings, and regional maps) is contained in Appendix B.

In contrast to Figure 3.2, Figure 3.3 shows tectonically active continental areas that exhibit an aseismic lower crust and Figure 3.4 highlights a few SCRs that are seismically activity. Earthquakes reach near the Moho in each SCR with the exception of the New Madrid Seismic Zone. In Jabalpur, India one moderate-sized (Mw 5.7) event on May 21, 1997 occurred deep within the relatively stable crust at 35 km depth [*Bhattacharya, et al.*, 1997; *Rao, et al.*, 2002]. Therefore, T_S in SCRs can reach to Moho depth albeit the seismicity does not appear to be associated with current tectonic activity. The three types of continental regions exhibit different depths of maximum earthquake occurrence, such that tectonically active areas with aseismic lower crusts all have peak earthquake occurrence in the upper 10 km of crust. SCRs and

tectonically active areas with seismic lower crusts exhibit variable depths of peak earthquake occurrence, anywhere in the ≤ 25 km of crust depending on what area the histogram describes.

One interesting feature in Figure 3.2 is the possible indication of mantle lid seismicity in four locations, beneath the Baikal Rift System (BRS), the Colorado Plateau, the Himalayan collision zone, and the North Island of New Zealand. Beneath the BRS and the Colorado Plateau the mantle lid events are very few in number and tend to be small in magnitude (<Mw 4), so they provide little evidence that mantle lid deformation via seismic slip is an important tectonic process. The Moho beneath New Zealand's North Island in the area where potential mantle seismicity is occurring is poorly constrained to ≳ 40 km (see Appendix B). Therefore, all events beneath that island many in fact be within continental crust and not in the mantle lid. Recently, the Himalayan Nepal Tibet Seismic Experiment located more than 100 event depths beneath their independently constrained Moho [*de la Torre, et al.*, 2007; *Monsalve, et al.*, 2006; *Schulte-Pelkum, et al.*, 2005]. These studies have located the largest number of continental mantle lid earthquakes. The Himalayan collision zone is where continent-continent collision occurs between India and Eurasia as India underthrusts beneath the Himalayas. So, mantle lid seismicity of this zone is not necessarily representing a global phenomenon on which to base a general understanding of continental earthquake depth distributions and lithospheric deformational processes. Additional examples of continental subcrustal seismicity not shown in Figure 3.2 occur in areas of proposed delamination, such as beneath the Carpathians [e.g., *Knapp, et al.*, 2005], the Alboran Sea [e.g., *Seber, et al.*, 1996], and the Atlas mountain region [e.g., *Ramdani*, 1998]. Overall, the potential for subcrustal seismicity still exists beneath continents. However, an encompassing theory as to why they may occur in limited numbers in some areas and

why they do not occur in others remains unclear. Also their existence at all in some areas remains a matter of debate. For these reasons, the focus of this chapter is lower crustal seismicity and its role on lithospheric deformation.

Lastly, lower crustal and upper mantle seismicity is determined to occur beneath South Island, New Zealand [*Kohler and Eberhart-Phillips*, 2003; *Reyners*, 1987]. These events have not been included events in our study, because this study contends they occur in oceanic lithosphere and not in continental. Please refer the Appendix B section on New Zealand for an explanation.

Deformation mechanisms of the lower continental crust

Jackson [2002] asked whether it is time for geologists to abandon the jelly sandwich model, and this is addressed in this section. The role of seismic deformation in the continental mantle lid is spatially sporadic and its significance with respect to lithospheric deformation remains unclear, while the results of our survey clearly shows reliably documented seismicity in the lower continental crust in a broad variety of tectonic settings. Apparent from this is that the observational evidence that Chen and Molnar [1983] used to support the jelly sandwich model (i.e., earthquake focal depths) no longer outlines the predicted bimodal depth distribution the way they hypothesized. What then remains to be determined is what lower crustal conditions and deformation mechanisms control the occurrence of the deep crustal seismicity. Is the lower crust inherently brittle and capable of deforming seismically, contrary to our rheological understanding? Has the lower crust in these areas been modified to induce brittle deformation? Or is the assumption that earthquakes only occur within brittle continental crust incorrect? To address these questions, this section discusses deformation mechanisms that have been proposed to influence crustal seismicity

within continents and how these mechanisms are expressed in different tectonic settings.

Brittle fault slip

At low temperatures, and therefore shallow depths, the dominant mode of deformation of geological materials is often assumed to be brittle slip on pre-existing fault surfaces, which is governed by Byerlee's Law [*Byerlee*, 1967; 1968; 1978] and controls the linear portion of the jelly sandwich model. Therefore, models of fault friction dominate characterizations of earthquake slip mechanisms, as opposed to models of brittle fracture. As temperature increases with depth in the crust, ductile flow replaces brittle fault slip as the primary mode of deformation. The brittle-ductile transition occurs where pressure-sensitive brittle fault slip is replaced by temperature-sensitive ductile flow [*Brace and Kohlstedt*, 1980; *Kirby*, 1983; *Sibson*, 1982; 1986]. Since the development of Byleree's Law, scientists have tried to use extremely cold geotherms to limit the onset of bulk ductile flow and maintain the crust's deformation via frictional fault slip to deep crustal depths. For example, geothermal gradients approximating 10 to 15°C/km to 35 km depth have been calculated to explain earthquakes deep beneath the East African Rift System (EARS) [*Nyblade and Langston*, 1995]. Such cold geotherms predict temperatures of ≤ 550°C at 35 km in the lower crust, which seems abnormally cold for a region of active rifting and probable superplume activity. Comparable geotherms have been calculated for the Canadian and Siberian shields and orogenic regions near the BRS [*Emmerson and McKenzie*, 2007; *McKenzie, et al.*, 2005]. Xenoliths entrained in kimberlites were used to constrain the geothermal gradient calculations to ~ 250 km depth. Moho temperatures for the stable shields are typically ≤ 600°C [*Emmerson and McKenzie*, 2007; *McKenzie, et al.*, 2005]. In the two orogenic regions near BRS, however, Moho

temperatures reached temperatures of 750°C and 860°C [*Emmerson, et al.*, 2006], values significantly highly than those suggested for the EARS. Additionally, the EARS lithosphere is expected to be hotter than that of the BRS. The EARS experiences higher strain rates (~ 6 mm/yr), more substantial Holocene volcanism, sits on top of the African Superplume, and is considered an active rift system. On the other hand, the BRS experiences strain rates of ~ 4.5 ± 1.2 mm/yr [*Calais, et al.*, 1998], significantly less Holocene volcanism, and is thought of as a pull-apart rift system. Baikal Rift tectonics and magmatic history are related to accommodating continental scale deformation associated with the evolution of the India-Asia collision [*Petit and Déverchère*, 2006], rather than mantle upwelling or triple junction rifting as in East Africa. Therefore, it is geologically unreasonable to expect the EARS and similarly tectonized areas to have geothermal gradients of ~ 10 to 15°C/km.

Forcing the lithosphere's dependence on simple frictional fault slip into the lower crust to explain deep seismicity within the continents is unnecessary. In the following subsections, we discuss additional deformation mechanisms. Each is a process that could allow bulk ductile deformation to occur in the middle and lower crust consistent with general rheological understanding, while episodes of seismogenic slip or rupture can still explain the anomalously deep seismic events documented in the literature.

Ductile instabilities

In 1986, Hobbs et al. studied pseudotachylytes (glassy rock generated by frictional melting during seismic slip) and ultramylonitic rocks from an exhumed, high-grade crustal shear zone in Central Australia. The rocks developed in a cyclical manner where pseudotachylytes experienced ductile deformation, which was later overprinted by another cycle of brittle deformation. They proposed that both deformational events

occurred entirely within the ductile regime and that the embrittlement resulted from unstable ductile shearing. These and other similar observations [*Kirby*, 1983; *McNulty*, 1995; *Sibson*, 1980] are consistent with a zone of long-term creep experiencing rapid, transient slip and rupture. The momentary deformation is called a ductile instability. It occurs when a creeping shear zone is perturbed by a change in temperature, stress, or strain-rate. The instability is a localization of deformation in a discrete area that results in rapid stress relaxation. This temperature-dependent phenomenon is a deformational mechanism that could explain some earthquakes in the lower continental crust below the brittle-ductile transition [*Hobbs, et al.*, 1986 Figure 17].

Ord and Hobbs [1989] combined lithospheric strength profiles with calculations of the temperatures limiting ductile instability to determine the constraints imposed on the strength of the continental crust by rheological properties and tectonic setting. They found earthquakes due to frictional slip or ductile instabilities are unlikely to occur deeper than ~ 25 km for strike-slip and thrust-type settings with geothermal gradient hotter than 20°C/km. For normal fault settings, the lithosphere should be aseismic at depths greater than 10 km. Seismicity is documented to occur to near-Moho depths beneath East Africa and the Lake Baikal region, which are both continental rift systems. Therefore, the theory of ductile instabilities is incapable of explaining the existence of lower crustal seismicity in every tectonic setting, but it is a mechanism that could contribute in some part to the occurrence of earthquakes beneath the brittle-ductile transition.

The assumption often associated with the jelly sandwich model, that earthquakes occur only in the brittle regimes, may be untrue. It may be incorrect to assume that continental seismicity is an indicator of the frictional-slip deformation mechanism.

The occurrence of earthquakes via ductile instabilities would not invalidate the lithospheric strength profile associated with the jelly sandwich model, but would invalidate the idea that earthquakes only outline the portion of the crust where frictional slip is the prevailing deformation mechanism.

Fluid-enhanced embrittlement

Surface derived pore fluid pressure changes – Scientists have long understood that earthquakes can be triggered by natural or human-caused changes in pore fluid pressure [*Gibbs, et al.*, 1973; *Raleigh, et al.*, 1976]. Reservoir filling, subsurface fluid injection, oil reservoir or aquifer withdrawal, earthquakes, and possibly changes in groundwater recharge rates can induce these pressure changes. The best correlations between deep seismicity induced from changes in near surface pore fluid pressures are those associated with reservoir-induced seismicity as summarized by Simpson [1986] and Simpson et al. [1990; 1988]. One case study of particular interest is that of the Aswan Reservoir in Egypt. That region experienced a significant increase in earthquake activity following the filling of the reservoir. The mainshock associated with the increased activity occurred at a depth of ~ 19 km, while aftershock hypocenters are reported as deep as 27 km. The magnitude 5.3 (Ms) mainshock on November 14, 1981 is historically the largest seismic event to occur in the Aswan region. In addition, the timing of the increased seismicity correlates well with expansion of the reservoir area into the seismically activated area in 1976, six years prior to the mainshock event. This time delay between lateral spreading of the reservoir and deep earthquake occurrence is likely due to gradual diffusion of water from the reservoir region to depth. Either the water traveled to hypocentral depths during the delay time and simulated seismicity, or it took time to induce an increase in pore fluid pressures at hypocentral depths resulting in fault slip [*Simpson*, 1986;

Simpson, et al., 1990; *Simpson, et al.*, 1988 and references therein]. Also, magnetotelluric imaging of a seismogenic fault in the Aswan region correlates areas of high conductivity with seismic clustering. Imaging suggests crustal fluids are influencing both geoelectrical conductivity and seismic activity levels [*Mekkawi, et al.*, 2005].

Constain et al. [1987] studied the transmission of pore fluid pressure changes downward in crystalline permeable crust as a possible trigger of earthquakes in the southeastern United States. They suggest that transient increases in water-table elevation of as little as 1 m can modify fluid pressure and ambient chemical conditions to depths of 20 km in fractured crust already under tectonic stresses based on an electrical conductivity study and a groundwater flow model . At hypocentral depths, seismic triggers can be pressure changes at depth due to natural increases in hydraulic head, the dissolution of minerals in water, or the solubility of water in minerals leading to structural weakening. What Constain et al. provide is a conceptual physical model to transmit fluid pressure transients from surface recharge areas down to depths of 20 km. The occurrence of "hydroseismicity" [*Costain, et al.*, 1987] at these deep depths is supported by the mainshock Aswan reservoir-induced seismicity reaching depths of 20 km and smaller aftershocks reaching greater depths, 27 km.

Melt-related embrittlement – Melt-related activity in the crust is also hypothesized to facilitate seismic activity through the processes of magma migration, partial melting, or fluids released in dehydration or other metamorphic reactions. Seismic monitoring of active volcanic centers around the globe confirms examples of seismic activity associated with active magmatic systems at depth. Davidson et al. [1994] discussed the end member scenarios where melt was injected into the deep crust or melt was

produced *in situ*. They utilize thermal models of injected melts, as well as a natural example of *in situ* melting from migmatites of the Central Gneiss belt in British Columbia. The authors conclude embrittlement of the lower crust can occur in both environments. The injected melt works by weakening the surrounding rock and temporarily concentrating strain where the melt is present, while during *in situ* partial melting space problems arise due to the positive volume change in most melting reactions. Both processes lower the effective pressure in discrete areas, thereby localizing deformation along narrow shear zones.

Rushmer [1995] supported theoretical models of melt-enhanced embrittlement by presenting experimental results of deformation of partially molten natural amphibolite from the Ivrea Zone in Italy, a typical mid- to lower crustal mafic rock [*Voshage, et al.*, 1990]. Rushmer [1995] performed experiments under fluid-absent conditions with 1.8 GPa pressure and temperatures between 650°C to 1000°C, conditions likely similar to those of thickened lower continental crust. At low melt fractions (< 15 vol %), results show melting reactions can induce fracture in previously ductile rocks. Therefore, melt-enhanced embrittlement, like ductile instabilities, is a mechanism that could facilitate brittle deformation in the lower continental crust below the brittle-ductile transition.

One example of where deep crustal earthquakes are most likely due to melt embrittlement in the lower continental crust comes from North Island, New Zealand. The Taupo Volcanic Zone (TVZ) is a back-arc spreading rift system related to the Hikurangi subduction zone beneath the island. Reyners et al. [2007] used data from a dense seismic network to combine accurately located crustal earthquakes and three-dimensional tomographic images of seismic velocities and seismic attenuation to

propose a common explanation for upper and lower crustal seismicity. They observe a continuous band of seismicity along the rift region. Earthquake distributions deepen from events located at depths of ≤ 10 km beneath the TVZ to lower crustal depths (30 – 40 km deep) southwest of the termination of the volcanic zone (Figure B.12). Reyners et al. hypothesize migration of subduction-related hot fluids along the margin of an otherwise dry, mafic New Zealand continental crust causes both the deep and shallow events. Seismicity in all areas often occurs in swarms, which suggests the influence of fluid movement [e.g., *Nur and Booker*, 1972]. Additionally, the earthquakes occur within seismic velocities that are consistent with the presence of fluids ($V_P/V_S \approx 1.70$) and the deepening band of events parallels the boundary between zones of high and low seismic attenuations. These contrasting attenuation zones are interpreted as the boundary between an anomalous concentration of partial melt beneath the TVZ and the over-thickened crust of the southwestern North Island (~ 10 km thicker than beneath the TVZ). The authors suggest that subduction-related melts from the limited mantle wedge beneath the thickened crust in the southwest is entrained toward the northeast due to the relatively high mantle corner flow in the northeast and restricted flow to the southwest. The melt entrainment could feed the partial melt concentrations of the TVZ.

If this hypothesized entrainment is true, then the seismicity appears to outline the regions where subduction-related melts meet resistance in upward migration. The crust beneath the TVZ exhibits high attenuation values, which suggests high temperatures and therefore weak rock. Melts generated beneath the TVZ meet little resistance and aseismically migrate through the weak lower and middle crust until they reach the upper crust. There the crust is brittle. The melts are able to weaken preexisting faults or increase stress concentrations to facilitate seismic slip from ~ 10 km and shallower.

The melt generated southwest of the TVZ, however, encounters an overly thickened, dry, mafic crust, which has low seismic attenuation properties to 40 km depth. This crust may limit melt migration and subsequent seismic activity to within the middle and lower crust, leaving the upper crust relatively aseismic. A limitation of melt migration upward could also force melts to migrate laterally. Reyners et al. suggest that this may explain the dipping band of seismicity that connects the deep events in the southwest to the shallow earthquakes in the northeast along the attenuation contrast boundary. Within this model for the North Island, the region southwest of the TVZ containing the lower crustal seismicity is likely less deformed than the crust beneath the TVZ. The earthquake swarms are indicative that the southwest is experiencing ongoing deformation, while lateral migration of melts and high attenuation to the northeast suggests more pervasive melt emplacement and deformation beneath the TVZ. Lastly, the North Island is experiencing back-arc rifting, so unlike ductile instabilities, melt-enhanced lower crustal seismicity is not limited to strike-slip and thrust settings. Effects of melting can explain deep crustal earthquakes in normal-type tectonic settings as well.

Eclogite phase transitions – A special case for fluid-enhanced embrittlement involves eclogite phase transitions in very thick crust in collisional tectonic settings. Pseudotachylytes containing eclogite facies assemblages from the Bergen Arcs of Western Norway have been used to support the hypothesis that rapid faulting and seismic activity can occur during eclogite phase transitions in the deep continental crust [*Austrheim*, 1987; *Austrheim and Boundy*, 1994; *Austrheim, et al.*, 1996; *Bjørnerud, et al.*, 2002; *Lund and Austrheim*, 2004]. The high- and ultrahigh-pressure rocks formed in a shear zone at depths of 60 km or more beneath the continental collision zone of the Caledonian orogeny. The presence of pseudotachylytes within the

Grenvillian granulite host-rock indicates that the lower parts of the thickened crust deformed via rapid brittle failure, while the eclogitic microlites contained in the fractures suggest coeval brittle failure and eclogitic phase formation. The mechanism driving granulite to eclogite conversion is fundamental to our understanding of the evolution and metamorphism of deep mountain roots, and these researchers have shown it now may be critical to our understanding of deep continental seismicity.

Austrheim and Boundy [1994] inferred that the pseudotachylytes formed at depth during fluid-enhanced eclogitization. The eclogites formed at temperatures of ~ 700°C deep within the over-thickened continental crust [*Austrheim and Griffin*, 1985; *Boundy, et al.*, 1992; *Jamtveit, et al.*, 1990; *Perchuk*, 2002] and other calculations suggested that the surrounding anhydrous, and subsequently strong, granulites also experienced similar temperatures. Austrheim and Boundy [1994] concluded that fluids played the integral role in bringing about the eclogitization reaction. Infiltration of water, possibly from the breakdown of pressure-sensitive hydrous phases in the continental mantle, hydrated the dry granulite and facilitated rapid changes in rheology and density resulting in eclogite-filled pseudotachylyte formation. Austrheim and Boundy [1994], and later Jackson et al. [2004] and Priestley et al. [2008], used the development of the Bergen Arc eclogites from anhydrous, strong granulites as an analogy to processes possibly at work beneath Tibet within the subducting Indian lithosphere.

Camacho et al., 2005, however, interpret the Norwegian rocks differently. These authors used thermal modeling combined with volume-diffusion argon ($^{40}Ar - ^{39}Ar$) gradient modeling to concluded that hot (700°C) fluids injected co-seismically into surprisingly colder (400°C) crust. Their data suggests that the brittle strength of the

host-rock granulite did not come from its anhydrous composition, but rather its anomalously cold temperature. They suggest fluid migration and eclogitization was triggered by multiple, short-lived deformational pulses associated with earthquakes within the cold granulite.

Both hypotheses conclude that fracture-hosted fluids are essential components and catalysts in the eclogite phase transition. However, they greatly differ on their conclusions of an embrittlement mechanism for the host-rock. Did the granulite exist at cold, brittle temperatures and seismic faulting allowed hot fluid infiltration, or did hydration of the anhydrous granulite facilitate such rapid deformation it forced the hot rock to deform seismically? It does not seem intuitive that crust at 60 km depth within a tectonized collision zone would be at temperatures $\leq 400°C$, but, as of yet, Camacho et al.'s [2005] argon isotopic data has not seriously been contested. Each hypothesis, however, relies heavily on the transport of fluids into the lower crust. Whether hydrous phases introduce eclogitic melts into lower crust or induce granulite to eclogite phase transitions, the existence of fluids in the lower crust remains a decisive factor in determining the dominate mode of deformation. Finally, however the relationship between seismic faulting and granulite to eclogite phase transitions occurs, this deformation mechanism is limited to the lower crust of overly-thickened mountain roots, where pressure-temperature conditions are reached that can facilitate the granulite to eclogite transition.

Summary

Through this review of the deformation mechanisms in the continental crust, we find the influence of fluids is the only mechanism capable of encouraging earthquake occurrence throughout the continental crust in any tectonic setting. Whether sourced

from the surface or from beneath the crust, fluids can facilitate seismic failure in brittle and ductile rocks. Near surface derived changes in pore fluid pressure observationally and theoretically can penetrate at least to depths of 20 km, while melt-assisted seismic slip is thought to occur from shallow depths in highly modified lithosphere to lower crustal depths in stronger, less tectonized crust. Embrittlement of the continental crust by fluids, water or melt, is capable of explaining the depth distribution of earthquakes in all types of tectonic environments. It is unnecessary to assume questionably cold temperatures or strong rocks in the lower crust in order to drive velocity-dependant fault slip to great depth, although it may occur in some settings. Ductile instabilities are a viable mechanism that can stimulate rapid, brittle failure within weak rocks experiencing bulk plastic flow and therefore explain lower crustal earthquakes beneath the brittle-ductile transition. On a global scale, however, fluid-enhanced embrittlement is not limited by depth or tectonic environment, as are ductile instabilities. Therefore, fluid-enhanced embrittlement, where fluids are derived from a variety of processes, is likely to be the dominant deformation mechanism controlling seismicity within continental crust.

The deformation mechanisms discussed above seriously challenge the validity of the assumption that earthquakes are indicative of a specific dominant mode of deformation. The jelly sandwich model of lithospheric strength was developed from experimental data on rheology and dominant modes of deformation [*Brace and Kohlstedt*, 1980]. Common interpretations of the strength profiles were that earthquakes occurred within the lithosphere only where slip on pre-existing faults was dominant, which was where the crust could sustain the largest stresses (i.e. was the strongest). However, this review highlights the fact that by means of different mechanisms, earthquakes can occur within the ductile portion of the continental

profile where power-law creep is dominant, in the region which was often considered to be the weak part of the crustal column. Through some combination of ductile instabilities, fluid embrittlement, and eclogite phase transitions, the continental crust seems to deform seismically wherever rocks are capable of sustaining sufficient stress differentials. Within this framework, earthquakes are possible throughout continental crust until the rock is sufficiently weakened that it permanently deforms under differential stress too small for earthquakes to occur. When such a stage is reached in the lower crust, temperatures are likely to be high, processes such as crustal flow are likely to be dominant, and the lower crust is most likely decoupled from the brittle upper crust and, if present, the underlying mantle lid. In this situation the lower crust is the weak layer often called upon to explain tectonic and geomorphic observations in tectonically active, highly deformed belts such as the Basin and Range or the Tibetan Plateau [e.g., *Gans*, 1987; *Royden, et al.*, 1997].

Lithospheric rheology and deformation

Having challenged the validity of the jelly sandwich model of continental lithospheric strength, we now ask the question: how do earthquakes relate to the strength of the lithosphere? In this section, we address this topic by placing earthquakes occurring in the lower continental crust into a broad geophysical framework. We summarize the current state of knowledge of continental seismicity regarding lithospheric properties and measured estimates of continental deformation.

First, we discuss the connections between T_S and effective elastic thickness (T_e) and between T_S and temperature that have been proposed. We find that at this time an ongoing debate about how to estimate continental T_e hinders a scientific consensus from forming with regard to comparisons of T_e and T_S. Additionally, a simple

relationship between focal mechanism distribution and flexural stresses has not been clearly documented in any continental region, as is seen in oceanic lithosphere. Therefore, it is difficult to reconcile a relationship between T_S and T_e in continents. Concerning a relationship between T_S and temperature, we find that earthquake depth distributions often mimic lithospheric strength profile distributions (i.e., earthquake occurrence increases to a maximum in the upper crust, $\lesssim$ 25 km, and decreases quasi-exponentially at greater depths). Since temperature controls the exponential decay in lithospheric strength at such depths, temperature may then control the thickness of continental seismicity. However, it remains unclear how temperature directly controls rapid slip along a fault surface within the lower crust. Finally, T_S is discussed with respect to estimates of lithospheric deformation to address whether continental lower crustal earthquakes occur in relatively strong or weak lithosphere. We compiled calculations of percent strain mainly from surficial constraints and lithospheric thermal thickness estimates largely from seismic imaging studies in order to relate lithospheric structure and the amount of deformation to continental T_S. Results are consistent with lower crustal earthquakes occurring in stable lithosphere, as well as tectonically active lithosphere with characteristics intermediate between thick, tectonically stable cratons and thin, highly mobile Late Cenozoic orogens.

Estimated effective elastic thickness

There is on-going debate about a possible relationship between T_S and the lithosphere's estimated effective elastic thickness (T_e) [e.g., *Burov and Watts*, 2006; *Jackson*, 2002]. T_e is the thickness of the lithosphere modeled as flexure of an elastic plate above a fluid mantle. The plate can be subjected to surface and/or internal loads, which may be gravitationally compensated via elastic plate bending with wavelengths up to a few hundred kilometers. Bending stresses associated with flexure can act as a

one possible cause of earthquakes. Flexural compensation requires bulk elastic rheologies to accommodate recoverable plate bending. Likewise, the Reid earthquake rebound model of seismic rupture involves rocks capable of elastic recovery during an abrupt release of accumulated strain. So theoretically, bending stresses and elastic rheologies may sustain a relationship between T_e and T_S.

Watts [2001] reviewed one simple relationship that exists in oceanic lithosphere. As T_S increases with lithospheric age, tensional events consistently occur shallower than compressional events in regions seaward of deep-sea trenches [*Watts*, 2001 Figure 6.37]. This distinct pattern in focal mechanisms is easiest explained by seismic slip caused by outer-rise flexural stresses. Additionally, when estimates of T_e and T_S for the entire oceanic lithosphere are compared [*Watts*, 2001 Figure 6.40a], the majority of calculations for both thicknesses are $\leq$ 50 km. Therefore, earthquakes within oceanic lithosphere are generally distributed throughout the lithosphere's elastic layer.

A consensus has not been reached, however, regarding the relationship between the seismogenic layer and the effective elastic thickness in continental regions. Much of the ambiguity fueling the debate comes from the fact that geodynamicists currently disagree on how to calculate T_e correctly in the continents. Scientists have estimated T_e using both forward and inverse (spectral) methods. Differences in T_e estimates arise between forward and inverse modeling largely because they yield measurements corresponding to different times. Forward models commonly calculate elastic thicknesses corresponding to the time of a specific loading event by reconstructing surface and subsurface loads and their associated flexures (e.g., Lyon-Caen and Molnar [1983], Royden [1988], and Stewart and Watts [1997]). Spectral methods are based on present-day topography and gravity anomalies yielding estimates of the

current T_e. Therefore, forward and spectral methods estimate similar T_e's in young tectonic provinces but are understood to differ in areas with older deformational histories [*Grotzinger and Royden*, 1990; *Perez-Gussinye and Watts*, 2005].

More troublesome discrepancies have been reported, however, between T_e estimates based on the spectral methods. Two spectral methods are currently at the center of the debate, one based on analysis of the Bouguer anomaly–topography coherence [*Forsyth*, 1985] and the other on free air anomaly–topography admittance [*McKenzie and Fairhead*, 1997]. Both methods utilize present-day topography and gravity anomaly datasets and therefore should result in equivalent T_e values. Patterns of Bouguer coherence can yield T_e estimates of 100 km or more suggesting both the crust and mantle can contribute to the lithosphere's long-term flexural strength, while the free-air admittance function often calculates T_e everywhere within continents as typically < 25 km. The latter is often interpreted to suggest that the mantle is weak and that long-term continental lithospheric strength resides solely in the crust. McKenzie and Fairhead [1997] combined continental T_S and T_e estimates from free air anomaly–topography admittance to hypothesize that both thicknesses may be restricted to the crust and involve no significant lithospheric mantle contribution. Maggi et al. [2000b] took the idea further by observing that variations in T_S correlate with variations in T_e calculated from free air–topography admittance and that usually $T_e < T_S$. Jackson [2002] then proposed that continental lithospheric strength resides solely in the seismogenic layer (i.e., in the crust). The concept that continental tectonics and mechanics are controlled by strength that resides mainly in the crust, rather than in the mantle was thereafter dubbed the crème brûlée model of lithospheric strength [*Burov and Watts*, 2006], in contrast to the jelly sandwich model.

Pérez-Gussinyé et al. [2004] investigated the methodological discrepancy between effective elastic thickness calculations from Bouguer–topography coherence and free air–topography admittance using synthetic topography and gravity anomaly data for which the elastic thickness was prescribed. They showed that differences arise in T_e calculations when the admittance and coherence have not been comparably formulated. Often with the free air–topography admittance analyses, an infinite data window is used to calculate the predicted spectra, while a finite data window is used to calculate the observed spectra. Pérez-Gussinyé et al. [2004] show that using these different data windows [*McKenzie and Fairhead*, 1997] can lead to an underestimation of T_e by a factor of 2 when effective elastic thickness is large (> 30 – 40 km). "However, when the observed and predicted admittance functions are calculated in the same data windows, as is usually the case in the coherence method, then the results from the two techniques are equivalent" [*Perez-Gussinye, et al.*, 2004; *Perez-Gussinye and Watts*, 2005]. Their results, other results from the Bouguer anomaly–topography coherence method and forward modeling estimates of T_e support the concept that the lithospheric mantle contributes significantly to continental strength and that the effective elastic thickness can be much larger than T_S. However, other studies [*Crosby*, 2007; *Emmerson, et al.*, 2006; *Jackson, et al.*, 2008] continue to challenge the validity of the Bouguer anomaly–topography coherence method. Crosby [2007] conducted a range of tests to analyze errors resulting from spectral leakage, noise, and lateral T_e variations on T_e estimates from synthetic surface data, free-air admittance and Bouguer coherence, and synthetic line-of-sight satellite accelerations. Crosby found that the effect of noise, such as internal loads, on the Bouguer coherence–topography analysis strongly increases estimation of T_e, as well as lateral variations in T_e introduce a large bias in T_e estimates from analysis of free-air admittance functions. Since lateral variations can be relatively easily minimized by not including actively deforming

regions within analysis of stable regions or vise versa, Crosby contents the whole-box admittance technique [*McKenzie and Fairhead*, 1997] is the simplest of the spectral methods. Jackson et al. [2008] briefly reviewed this debate and explained that incompatible estimates of T_e from spectral analysis result from different assumptions of where the flexed plate is broken, and hence where the bending moment of the plate is zero. Unfortunately, the location of the break is not well constrained by geophysical observation leaving T_e poorly constrained with a broad minimum and unconstrained upper bound. At the time of this review, a scientific consensus has not been reached regarding accurately calculating T_e in continental regions, thereby leaving the debate, thus far, unsettled.

Regardless of the question as to how to calculate T_e, the relationship between T_S and T_e in continents does not appear to be as simple as that found in oceanic lithosphere. If the crème brûlée-type deformation was dominant in continental lithosphere and therein T_S and T_e have similar values and are both contained within the crust, then we would expect to see earthquake distributions in bending continental crust consistent with flexural stresses (e.g., normal fault events in the upper half of the crust and thrust events in the lower parts of the crust or vise versa). Yet most intraplate stress distributions are characterized by large horizontal compressive stress regimes that correlate with absolute-plate-velocity directions on these plates [*Reinecker, et al.*, 2005; *Sykes and Sbar*, 1973; *Zoback, et al.*, 1989]. Therefore, the stresses are likely due to broad-scale plate tectonic forces and not local stresses like that of flexural loading. Additionally, within any tectonically active region included in this study, upper and lower crustal earthquakes are largely consistent with each other and with the regional tectonic stresses (e.g., within extensional and compressional environments focal mechanism throughout the crust are dominantly normal and thrust, respectively).

Flexural stress patterns have been hypothesized to explain focal mechanism distributions within the Indian plate as it subducts beneath Tibet [*Bilham, et al.*, 2003; *Chen and Kao*, 1996; *de la Torre, et al.*, 2007; *Molnar, et al.*, 1977]. The topography, structure, and gravity of the Central Indian Plateau, Ganges Basin, and Himalayas show that the Indian plate does flex as is descends beneath Tibet [*Molnar, et al.*, 1977]. But, very few earthquakes occur south of the Himalaya Main Central Thrust which would be the region equivalent to oceanic regions seaward of deep-sea trenches and no pervasive and clear focal mechanism distribution has yet to emerge. Therefore, a simple relationship between focal mechanism distribution and flexural stresses has not been clearly documented in any continental region and subsequently it is difficult to reconcile a relationship between T_S and T_e.

Temperature

Chen and Molnar [1983] studied continental earthquake focal depths and estimated temperatures at the depth of the deepest earthquakes to investigate possible limiting temperatures for the occurrence of earthquakes. McKenzie et al. [2005] revisited the question of a limiting temperature for earthquakes. The authors derived geotherms for the Canadian and Siberian shields from surface heat flow, radioactivity, and pressure and temperature calculations from xenoliths entrained in kimberlites. They conclude that seismicity is limited by the 600°C isotherm in both oceanic and continental lithosphere. In stable continental lithosphere they estimated Moho temperatures to be $\leq$ 600°C, implying that stable continental crust is capable of deforming seismically throughout its thickness if subjected to tectonic stresses. That study sampled only relatively aseismic, stable cratons, so it is unclear how those calculations extrapolate to active orogens. Emmerson et al. [2006] combined observations of seismicity,

gravity, and topography and estimations of thermal and velocity structures to investigate the rheological properties of the lithosphere in the Lake Baikal region. They used two kimberlite sites within orogenic belts. Estimated temperatures were 750°C and 860°C at Moho depths of 40 and 45 km, respectively. Moderate- to large-magnitude seismicity reaches depths of 30 km in the Lake Baikal region, so seismicity there appears also limited to temperatures ≤ 600°C. Xenoliths record elevated geothermal gradients beneath both the Basin and Range and Tibet, where the aseismic lower crust (Figure 3.3) exhibits temperatures ≳ 700°C. Temperatures are ~ 900° to 1050°C at Moho depth beneath the Basin and Range province and subsequently ≲ 700°C at depths ≤ T_S assuming surface heat flow of 90 to 100 mW m^{-2} [*McGuire*, 1994]. For Tibet, temperatures reach 800° to 1000°C at a depth of 30 to 50 km where T_S ≲ 30 km [*Hacker, et al.*, 2000]. These temperatures are not consistent with seismicity limited by the 600°C isotherm, although they are consistent with aseismic lower crust experiencing elevated geothermal conditions (≳ 700°C) when compared to lower crustal temperatures beneath SCRs (≲ 600°C) [*McKenzie, et al.*, 2005].

Within oceanic lithosphere simple relationships do exist between temperature, elastic thickness, and T_S [*Chen and Molnar*, 1983; *Emmerson and McKenzie*, 2007; *McKenzie, et al.*, 2005; *Molnar and Chen*, 1983; *Watts*, 2001 section 6.9 for review; *Wiens and Stein*, 1983]. However, young ages (< 200 Ma), relatively simple tectonic histories, and homogeneous rheologies may facilitate such simple correlations. The complex deformational histories and compositional heterogeneity of the continental crust is likely to establish varying geothermal structures beneath continents. Chapman and Furlong [1992] investigate geological processes that modify modeled steady-state geotherms of stable continental crust. They used simple thermal models of tectonism and found that relaxation times (the time required for geothermal gradients to return to

the previous state or to establish a new steady-state geotherm) are 100 Ma or more following the cessation of most thermally altering tectonic events (e.g. burial by thrusting, magmatic underplating). Therefore, it is not intuitive that comparable lower crustal temperatures exist in all the numerous tectonically active environments reviewed in this study.

Almost all continental crust exhibits a similar pattern of earthquake depth distribution which may suggest seismicity is temperature controlled. Histograms show event occurrence typically increasing to a maximum in the upper crust ($\leq$ 25 km depth) and decreases quasi-exponentially at greater depths. This pattern of earthquake frequency versus depth is generally consistent with profiles of crustal strength (e.g., that used in the jelly sandwich model). The transition from increasing to decreasing crustal strength occurs at the brittle-ductile transition and the exponential decrease in strength below the transition is described by the failure criterion for power-law creep, the dominant deformation mechanism of the lower continental crust as predicted by theory and experiment [*Brace and Kohlstedt*, 1980 and references therein]. Creep is a temperature-dependant deformation mechanism. As a result, the strength of the lower crust is thought to be largely dependant on rheology and temperature. Earthquake depth distributions mimic crustal strength profiles [e.g., *Petit and Déverchère*, 2006 Figure 6], which implies a possible relationship between crustal strength and crustal earthquakes. Therefore, observations make it plausible that since temperature controls strength in the lower crust and earthquake distributions follow the pattern of crustal strength, temperature may control seismogenesis. However, as discussed above, geotherm calculations do not appear to outline a specific temperature that defines an earthquake depth limit in continental crust, although it is likely that where the lower crust is aseismic it is experiencing elevated geothermal conditions ($\gtrsim$ 700°C).

Lithospheric structure

The most striking observation about the global distribution of lower crustal earthquakes is the variety of tectonic settings in which they occur. The dominant deformational character, whether compressional, extensional, or strike-slip, is not the determining factor. In this section we show that correlated measures of lithospheric thickness and deformation appear to be the important factors. The key observation is that, in contrast to tectonically active continental areas that have lower crustal events (Figure 3.2), there also exist tectonically active continental areas that exhibit an aseismic lower crust (Figure 3.3). The other important observation is that stable, cratonic regions, although relatively quiet seismically, in fact appear to exhibit lower crustal seismicity (Figure 3.4). Figures 3.2, 3.3, and 3.4 show examples of these three types of regions for which we have accurate data on crustal earthquake depths. We hypothesize that the difference between these types of regions is related to a difference in the thermal thickness of the lithosphere, which is in turn related to the strength of the lithosphere and amount of deformation the lithosphere has experienced. Thinner, weaker lithosphere is associated with more deformation and the absence of lower crustal earthquakes, while somewhat thicker, stronger lithosphere is associated with lower crustal earthquakes. This hypothesis implies a spectrum of lithospheric strengths and thicknesses, including at one extreme cratonic regions with a thick lithosphere and little or no post-Paleozoic deformation, and at the other end of the spectrum highly deformed orogens subjected to large amounts of Cenozoic deformation with a relatively thin lithosphere due to extensive magmatism, heating, and possibly delamination. In between are areas with intermediate strength, thickness, and degree of Cenozoic deformation. We hypothesize that the tectonically active regions with lower crustal earthquakes (Figure 3.2) fit into this intermediate category.

Figure 3.5 shows a simple block model incorporating the proposed hypothesis connecting T_S to variations in lithospheric thickness and related deformation. It is broken into a top and bottom section illustrating compressional and extensional tectonic regimes, respectively. These two cases were chosen to illustrate that the model is consistent with data from any continental deformational environment regardless of whether crustal thickness is increasing, decreasing, or remaining relatively constant (i.e., in strike-slip settings). From left to right, lithospheric blocks illustrate the spectrum of lithospheric thermal thickness, deformation, and strength, where SCRs with thick, strong lithosphere are represented in the leftmost column and tectonically active areas with an aseismic lower crust and a thin, weak lithosphere are in the rightmost column. The intermediate-type lithosphere is represented in the middle column, where we hypothesize tectonically active areas with a seismic lower crust correspond to lithosphere that has intermediate thickness and has experienced only moderate amounts of deformation. Each region's seismogenic thickness is illustrated by the white arrow and is defined by the earthquake depth histograms in Figures 3.4, 3.2, and 3.3 (from left to right respectively).

While brittle fault slip and ductile instabilities are capable mechanisms to facilitate seismic slip, fluid-enhanced embrittlement is unique because it can induce earthquakes at deep crustal depths and in any tectonic environment when water or melts are present. Thus, we argue fluid embrittlement is likely the most influential method of inducing earthquakes in continental crust and is the only mechanism represented in Figure 3.5. The green arrows illustrate the influence of surface water on seismogenesis and the purple arrows illustrate the influence of in situ melting or injected melts. It is doubtful that melt is inducing earthquakes within SCRs, because volcanic activity is

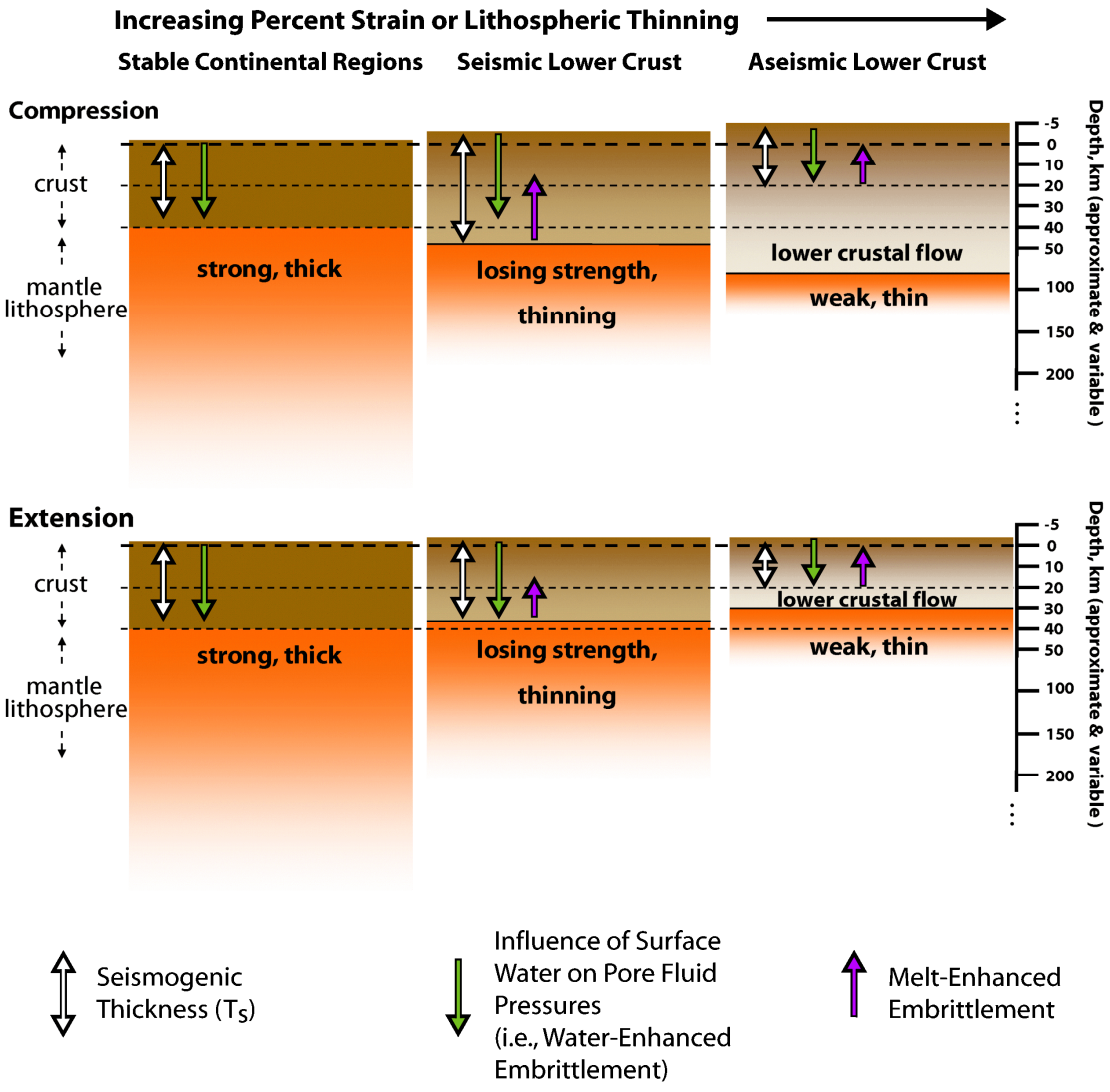

Figure 3.5: Lithospheric block model of variations in continental lithospheric thickness and strength, corresponding seismogenic thickness, and dominant earthquake deformation mechanism.

rarely present and mantle lid thicknesses are large. Therefore, T_S within SCRs is accompanied solely by the green arrow that illustrates the influence of surface water, implying that in some regions meteoric water can reach depths throughout the crust. Increased deformation and thinning of the lithosphere would raise lithospheric temperatures and increase the possibility of melt involvement in the lower crust, so we employ both surface water and melt-enhanced embrittlement to explain T_S in the middle and right columns. However, the combination of extremely thin lithosphere, high percent strain, and limited T_S in the rightmost column implies that the lower crust can become aseismic when continental lithosphere is sufficiently deformed and thinned at which point the lower crust is weak and may flow without any kind of brittle failure.

In order to test the proposed hypothesis, below we examine whether T_S can be correlated with measures of lithospheric strength and thermal thickness. As a proxy for lithospheric strength we compile estimates of the amount of Late Cenozoic crustal deformation, based on estimates of the percent strain, for the regions where T_S is reliably estimated. For lithospheric thermal thickness we use mainly available results for seismic velocity structure and, where available, correlate those estimates with geochemical and geothermal constraints.

Percent strain – The tectonically active regions in this study (Figures 3.2 and 3.3) have experienced significant periods of deformation during the last ~ 35 Ma. Percent strain measurements included in this section reflect those deformations and not any that occurred prior to the mid-Cenozoic, although the Western Pyrenees is one exception. The Pyrenees formed due to convergence between the Iberian and European plates from ~ 85 to 25 Ma. The period of time involving the height of

deformations for these many regions (Figures 3.2 and 3.3) varies. By this we mean, in a few regions current tectonic activity appears to be waning from what it once was (e.g., Alps and Pyrenees), whereas in other regions deformations initiated very recently (< 5 Ma) and are more vigorous then during previous Cenozoic times (> 5 Ma) (e.g., Argentine Foreland and North Island, New Zealand). A question may then be whether comparing strains across these regions is reasonable given the differences in timing of the main periods of deformation. The findings of Chapman and Furlong [1992] support that it would take $\gtrsim$ 100 Ma after the cessation of most tectonic events which modify the thermal structure of the crust (e.g., exhumation, burial by thrusting, extensional unroofing, and magmatic underplating) for continental crust to return geothermal gradients to a steady-state geotherm of stable continental lithopshere. It is then likely that all regions considered tectonically active in this study are still experiencing the thermal effects of tectonic deformations, where the Pyrenees has the earliest tectonic cessation age of ~ 25 Ma. We contend it is reasonable to compare estimates of percent strain across the many tectonically active regions, because in each area the structures included in the percent strain estimates are likely part of the tectonic deformations that are still affecting lithospheric thermal structure. Additionally, our goal is to establish where the different regions fit into the broad, global range of crustal deformations rather than attempting to establish precise values, rates, and durations of deformations.

To quantify the amount of deformation that has occurred in a region, we compiled estimates of percent strain, where percent strain is:

$$\left|e\%\right| = \left|\frac{\Delta L}{L} * 100\%\right|$$

and e is strain, ΔL is the change in length, L is the original length, and the | | symbols indicate that we take the absolute value. Percent strain can be negative or positive depending on whether deformation is compressional or extensional. We use absolute percent strain to eliminate the importance of the sign, since we are comparing the deformation in both compressional and extensional tectonic environments. Percent strain estimates have been compiled from previously published sources (Figure 3.6). The reported values result from a variety of data and analyses, which are described within Appendix C. Strike-slip settings are discussed separately later in this section. Percent strain is not a readily applicable quantity to those environments, because it does not fully capture the complex tectonic histories of the strike-slip settings included in this study (e.g., Southern California and Anatolia).

A pattern emerges when comparing percent strain estimates from areas with an aseismic or seismic lower crust (Figure 3.6). Seismically active continental areas with an aseismic lower crust generally exhibit larger regional percent strains (Figure 3.6 black bars) than areas with a seismic lower crust (Figure 3.6 gray bars). Presumably, negligible deformation has occurred in SCRs, so percent strains in those areas are not plotted. The pattern suggests a change in the seismic character of the continental lower crust with increasing deformation, such that at limited to moderate percent strains the continental lower crust is capable of deforming seismically and with increased deformation (i.e., more percent strain) the lower crust is aseismic. From Figure 3.6, it appears that at approximately 30 % strain the lower crust under goes this transition from being seismically active at strains < 30% to being aseismic at strains > 30 %. However, regional percent strain measurements can have significant errors due to limited knowledge of structure at mid- to lower crustal depths, so at this time 30 % is a very rough estimate of where the lower crust may transition from being seismically

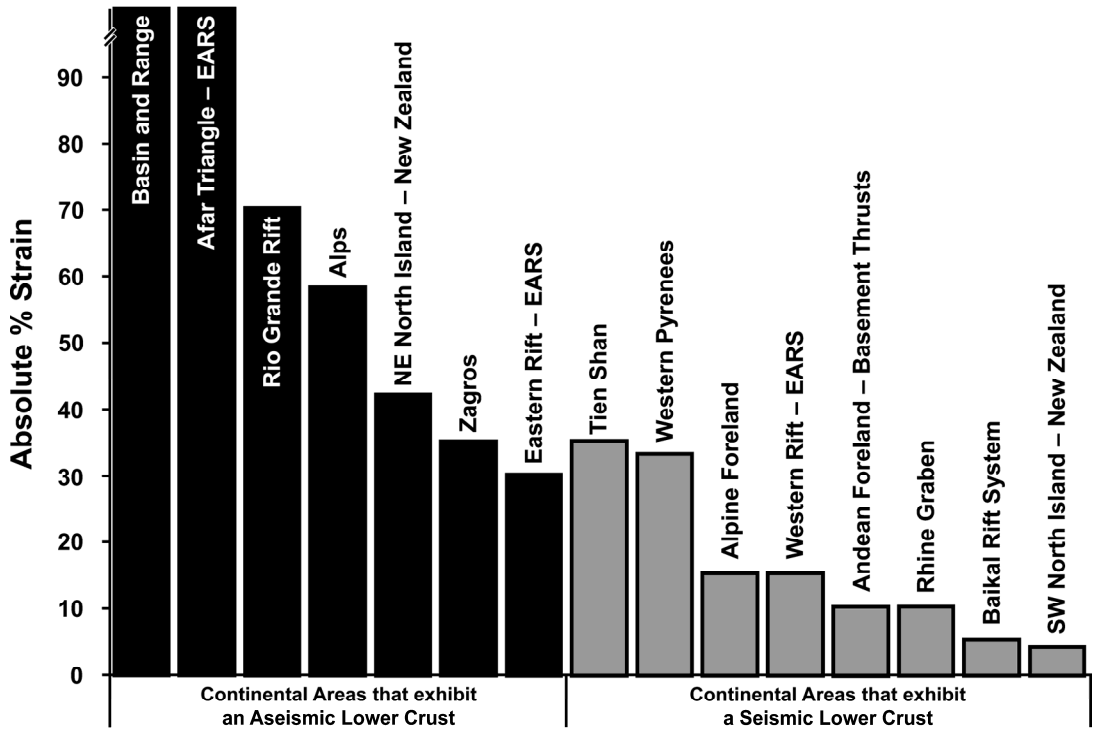

Figure 3.6: Absolute percent strain estimates. References are contained in Appendix C.

active to becoming aseismic. These inaccuracies may explain why percent strains of the Zagros, Eastern Rift, Tien Shan, and Western Pyrenees are very similar yet the Zagros and Eastern Rift exhibit an aseismic lower crust and the Tien Shan and Western Pyrenees exhibit a seismic lower crust. Each region also has different thermal and rheological conditions that could influence such a transition. With regard to the percent strain estimate for the Western Pyrenees, the region experienced tectonic cessation at ~ 25 Ma, so that it is plausible that the region has experienced some stabilization (e.g., crustal cooling) since that time, albeit not enough for it to be considered a SCR. Therefore, when compared to the Zagros and the Eastern Rift, the Western Pyrenees' percent strain calculation may be a slight over estimate, because it does not take into account effects since the tectonic cessation. Other strains shown on Figure 3.6 differ by an order of magnitude or more (e.g., 5 % in the Baikal Rift System and $\gtrsim$ 100 % in the Afar Triangle) and have not experienced tectonic cessation, so that the overall pattern appears robust. Therefore, Figure 3.6 illustrates a possible relationship between T_S and amount of deformation, where T_S is thick and reaches to near-Moho depth when limited to intermediate amounts of deformation have occurred and percent strains are lowest (< 30% strain), and when larger amounts of deformation have occurred (> 30 % strain) T_S thins and is restricted to upper and middle crust leaving the lower crust aseismic.

The general pattern of a seismic lower crust limited to where moderate to little amounts of deformation have occurred and an aseismic lower crust where larger deformations have occurred is also apparent in strike-slip tectonic environments. Three large continental strike-slip provinces are included in the histograms in Figures 3.2 and 3.3 – Dead Sea Fault System (DSFS), North Anatolian Fault (NAF), and the San Andreas Fault System (SAFS) (included within the Southern California histogram in

Figure 3.3). The DSFS exhibits lower crustal seismic activity, while both the NAF and SAFS demonstrate an aseismic lower crust. In concert with the pattern revealed by the percent strain data compilation, the respective tectonic histories of these strike-slip regions suggests that lower crustal seismic activity is restricted to areas that experienced moderate to limited tectonic deformation (i.e., the DSFS), while the massive tectonic reworking and large amounts of deformation of Anatolia and Southern California over much of the Cenozoic is reflected by aseismic lower crusts.

The region of Southern California and that of the SAFS experienced subduction of the Farallon oceanic plate through the Paleogene which resulted in subduction of an oceanic spreading center beneath the margin around 30 Ma. This subduction set up a triple junction that migrated northward to become today's Mendocino triple junction, while a slab window developed beneath Southern California ~ 28 Ma. The establishment of the SAFS occurred during that time and movement continues today. First, transform plate motion was accommodated offshore along the margin approximately where subduction previously occurred and later ($\lesssim$ 20 Ma) the motion migrated inland to set up the intraplate continental transform fault system of the San Andreas (e.g., Atwater [1970]). Studies have shown that ~ 255 km of right-lateral motion occurred since ~ 6 Ma in southern California associated with the regional SAFS, while about 175 km of slip has occurred on the San Andreas Fault itself [*Dickinson*, 1996; *Matti, et al.*, 1992].

Likewise, Anatolia has an extensive tectonic history which is not simply limited to Neogene motion along the transform system (i.e., NAF). The lithosphere of the Anatolian Plate is comprised of an amalgamation of continental fragments that resulted from subduction and accretionary processes associated with the convergence

between Africa and Eurasia since the Cretaceous. Subduction processes continued beneath the Mediterranean Sea south of Anatolia and to the east in eastern Turkey. Ultimately, this convergence resulted in middle Miocene continent-continent collision between the Arabian and Eurasian Plates in eastern Anatolia forcing the extrusion of the Anatolian Plate westward. The NAF accommodates motion associated with the extrusion tectonics and formed at ~ 13 to 11 Ma [*Barazangi, et al.*, 2006; *Bozkurt*, 2001; *Golonka*, 2004; *Sengor*, 1979; *Sengor, et al.*, 2005]. It has accumulated ~ 85 km of offset since its formation [*Sengor*, 1979].

Relative to the regions of the SAFS and NAF, the region of the DSFS has not experienced as much tectonic deformation. The Dead Sea region was part of a relatively stable platform since the early Mesozoic. To accommodate relative motion between the African and Arabian continental breakup, the DSFS formed during the Late Cenozoic (~ 17 Ma) interrupting the previous tectonic stability. Accumulated offset is estimated to be ~ 105 km [*Freund, et al.*, 1970; *Quennell*, 1958]. Of these three intra-continental transform fault systems, the DSFS seems to have experienced moderate amounts of Neogene deformation, while the regions of the SAFS and the NAF experienced more pervasive tectonic reworking from the Early Cenozoic to present. The relative tectonic histories are consistent with the DSFS region exhibiting a seismic lower crust as well as having experienced limited to moderate amounts of deformation, while the SAFS and NAF regions exhibit aseismic lower crusts and have experienced large amounts of tectonic deformation. Therefore, intraplate transform tectonic environments exhibit a similar pattern to that revealed by the percent strain compilation shown in Figure 3.6, such that a relationship between T_S and amount of deformation possibly exists. T_S is thick and reaches to near-Moho depth when limited to intermediate amounts of deformation have occurred, and when larger amounts of

deformation have occurred T_S thins and is restricted to upper and middle crust leaving the lower crust aseismic.

Lithospheric thickness – Lithospheric thermal thickness estimates for most areas are based on seismic imaging analyses, such as surface wave tomography and receiver functions, with a number of areas also having corroborating calculations from geotherm modeling and geochemical constraints. Estimates of T_e are excluded from this compilation.T_e is a measure of elastic thickness and not lithospheric thermal thickness, as well as, debate about how to estimate continental T_e hinders analysis of that quantity at this time (as discussed above). For interested readers, a full discussion of the background data and analyses used to construct our lithospheric thickness compilation (Figure 3.7) is contained in Appendix D. Figure 3.7 plots estimated lithospheric thicknesses in decreasing order from left-to-right with each estimate color-coded according to type of continental region. Figure 3.7 illustrates an apparent relationship between lithospheric thickness and seismogenic thickness, T_S. Seismogenic and lithospheric thickness are thinnest where the lower crust is aseismic, ~20 km and < 80 km, respectively. Intermediate lithospheric thicknesses ranging from ~80 to ~ 160 km correspond to tectonically active regions where T_S reaches to the Moho and lower crustal earthquakes occur. In SCRs, lithospheric thicknesses are the largest (> 200 km). The pattern in Figure 3.7 suggests that within lithosphere of thick or intermediate thickness ($\gtrsim$ 80 km thick) the lower crust is seismogenic.

Summary – Figures 3.6 and 3.7 are consistent with our proposed hypothesis of a spectrum of corresponding changes in lithospheric thickness, deformation, and seismogenic thickness (Figure 3.5). They illustrate a relationship between whether the lower continental crust is seismically active and the Cenozoic evolution of the

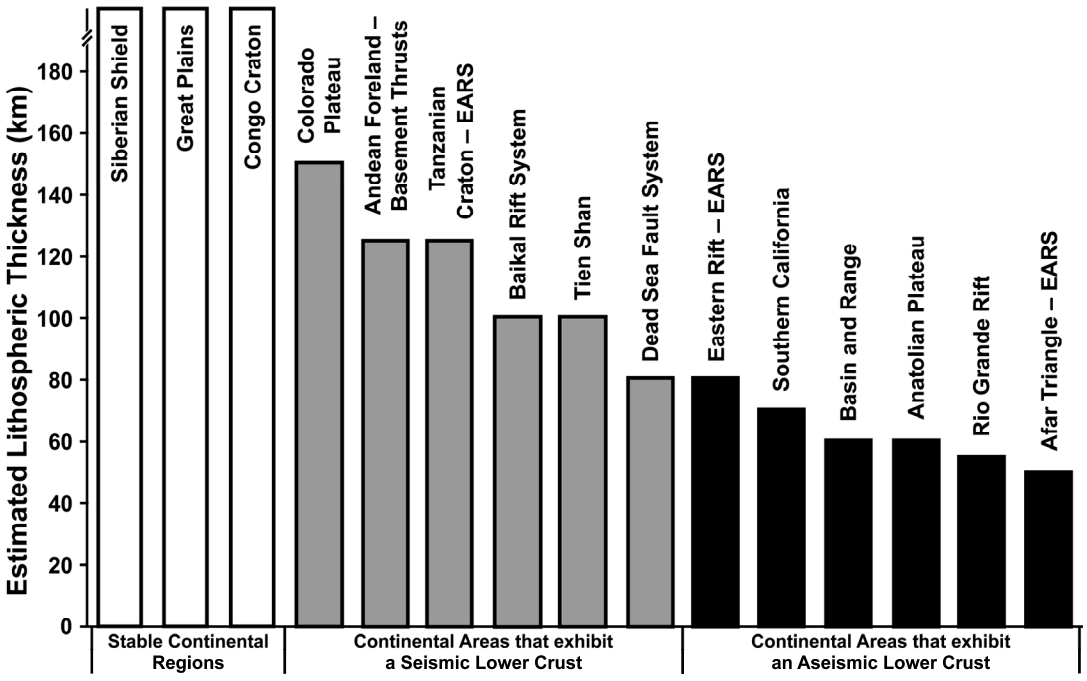

Figure 3.7: Estimated lithospheric thickness (km). References are contained in Appendix D.

lithosphere in deformational environments. SCRs have the thickest lithosphere of 200 km or more, no measurable percent strain, and the lowest level of seismic activity. In the few areas where it is possible to describe T_S in a SCR, T_S can reach to near-Moho depth. When tectonically active areas are considered, earthquakes occur in the lower continental crust of lithosphere with intermediate thickness (between ~ 80 and ~ 160 km) and that has experienced limited to moderate amounts of percent strain (< 30 %). Figure 3.6 and 3.7 also show that within thinner continental lithosphere (< 80 km thick) that has experienced larger percent strains (> 30 %), the lower crust is aseismic. These relationships suggest a transition in earthquake occurrence in the lower continental crust associated with the evolution of lithosphere as it thins, weakens, and deforms.

Africa, specifically the Congo Craton together with the EARS, can be used as an example of where all three stages captured in the lithospheric block model are displayed, as shown in Figure 3.6 (labeled Afar Triangle – EARS, Eastern Rift – EARS, and Western Rift – EARS) and 3.7 (labeled Congo Craton, Tanzanian Craton – EARS, Eastern Rift – EARS, and Afar Triangle - EARS). In addition to the percent strain and lithospheric thickness data, the timing of the onset of volcanism and seismic imaging analysis are consistent with the northern EARS (i.e., the Afar Triangle and the Eastern Rift of Ethiopia and Kenya) having experienced more extensive and longer-lived crustal modification by the addition of mafic material then the areas of the southern EARS (i.e., the Western Rift and the Eastern Rift in Tanzania), where the northern EARS exhibits $T_S \lesssim 20$ km [*Braunmiller and Nabelek*, 1990; *Foster and Jackson*, 1998; *Gaulon, et al.*, 1992; *Keir, et al.*, 2006; *Wagner and Langston*, 1988] and the southern EARS exhibits T_S to Moho depths (as deep as ~ 40 km) (see Figure B.9 of the Appendix).

Deformation has propagated from north to south with volcanism initiating in southern Ethiopia around 45 to 37 Ma, 35 to 30 Ma in northern Kenya, 15 Ma in central Kenya, and 8 Ma in northern Tanzania [*Ebinger*, 1989; *George, et al.*, 1998; *Nyblade and Brazier*, 2002 and references therein]. Since all of these areas continued to experience volcanism into the Holocene, it is likely that the northern EARS has experienced longer-lived weakening due to magmatic addition then in the southern EARS. In 2005, Dugda et al. reported results from receiver function analysis that determined crustal thicknesses and Poisson's ratios for the crust throughout the Eastern Rift. Analyses showed that in Ethiopian the crust is thin (Moho depths between ~ 27 and 38 km) and has elevated Poisson's ratios (0.27 to 0.35) consistent with crust that has been extensively modified by the addition of mafic rock. The crust of Kenya and Tanzania has thicknesses between 33 and 42 km and Poisson's ratios of 0.24 to 0.28 consistent with felsic to intermediate composition crust. Therefore, deep crustal earthquakes in the southern EARS are coincident with a later onset of volcanism and moderate crustal modification relative to the thin T_S, longer volcanic record, and more pervasive crustal modification of the northern EARS. These findings are consistent with the percent strain and lithospheric thickness relationships in Figures 3.6 and 3.7. Such that, the Congo Craton is an example of a SCR (left block in Figure 3.5), the southern EARS is an example of lithosphere at the intermediate stage (center block), and the northern EARS at the more advanced stage (right block).

Implications

The previous interpretation of continental lithospheric strength profiles, that continental earthquakes only occur where brittle fault slip is the dominant deformation mechanism (i.e., the jelly sandwich model), seems incorrect. It now appears that

earthquakes can occur throughout the continental crust, from the near surface to Moho depths within the dominantly brittle and ductile portions of continental crust, such that the entire continental crust is likely capable of brittle failure on time scales consistent with the seismic cycle. Similar assertions have been made by other studies [*Handy and Brun*, 2004; *Jackson, et al.*, 2008 and references therein; *Thatcher and Pollitz*, 2008], however our study has quantified that the lower crustal earthquakes associated with tectonic activity are restricted to areas where the lithosphere has an intermediate thickness (between ~ 80 and ~ 160 km) and moderate to limited amounts of deformation (< 30 %) have occurred. Continental earthquake depth histograms exhibit patterns consistent with this new interpretation of lithospheric strength profiles (i.e., earthquakes can occur in ductile as well as brittle crust). Earthquake depth distributions mimic crustal strength profiles, such that they increase to a maximum in the upper crust (≤ 25 km depth) and decrease quasi-exponentially to Moho depths. Within lithosphere that has experienced large amounts of thinning (lithospheric thickness ≲ 80 km) and deformation (percent strain > 30%), the lower crust does not support seismic rupture. Therefore, whether a tectonically active area exhibits lower crustal seismicity appears to depend on the lithospheric thermal thickness and amount of accumulated lithospheric deformation and therefore the strength of the continental lithosphere. Thicker, less deformed lithosphere is stronger and demonstrates lower crustal seismicity, while thinner, more deformed lithosphere is weaker and exhibits the absence of lower crustal earthquakes.

A thin lithospheric thermal thickness causes elevated lower crustal temperatures due to the proximity of hot asenthospheric mantle, which provides a potential source of melts and heat into the lower crust. This may explain how the lower crust becomes aseismic and weak enough to possibly flow without any kind of brittle failure. Beneath the

Basin and Range province and the Tibetan Plateau, arguments have been made that the lower crust flows and Figure 3.3 illustrates the aseismic behavior of the lower crust in these areas. Within the Basin and Range province, distributions of strain can vary spatially from $\lesssim$ 15 % strain in some areas to $\gtrsim$ 100 % in others, while a relatively flat Moho at ~ 30 km depth lies beneath all areas. The contrasting crustal structure of spatially sporadic distributions of strain and the simple Moho geometry suggest lower crustal compensation via ductile flow [*Gans*, 1987; *Goodwin and Mccarthy*, 1990; *McCarthy, et al.*, 1991 and references therein]. Also, the flat topography of Tibet and long wavelength topographic slopes along its edges are consistent with flow beneath the plateau [*Clark, et al.*, 2005; *Clark and Royden*, 2000]. Thermal conditions that decrease lower crustal viscosities (e.g., igneous underplating, intrusion, or by addition of water-rich fluids) likely govern whether the lower crust flows in extensional environments [*McKenzie and Jackson*, 2002]. Within compressional settings, crustal thickening may alone provide enough heat to generate metamorphic transformations in the lower crust that enable ductile flow, while coincident lithospheric thinning would likely accelerate such a process [*England and Thompson*, 1984; *Le Pichon, et al.*, 1997]. Therefore, tectonically and seismically active regions exhibiting an aseismic lower crust may be places where the lower crust is weak and may flow.

Conclusions

By compiling accurately located earthquake depths (± 5 km or better), we investigated the tectonic settings in which continental lower crustal earthquakes occur to understand their significance with respect to lithospheric properties and deformation. Deep crustal events are not restricted to any one tectonic environment and fluid-enhanced embrittlement is the only deformation mechanism capable of inducing seismicity in the wide variety of settings where these events occur. In addition to fluid-

enhanced embrittlement, ductile instabilities is another viable mechanisms that can stimulate rapid, brittle failure within weak rocks experiencing bulk plastic flow, which explains the occurrence of lower crustal earthquakes beneath the brittle-ductile transition. These mechanisms are not consistent with the classic jelly sandwich model of lithospheric strength and deformation, where seismic slip is restricted to the upper crust and mantle lid leaving the lower crust aseismic. Our results are consistent with the entire continental crust being capable of seismic rupture unless extreme heating, melting, and/or fluid injection have occurred at which point the lower crust becomes aseismic. In such a case, percent strains are likely to be high (> 30%) and lithospheric thicknesses are likely to be thin ($\lesssim$ 80%).

REFERENCES

Aldersons, F., et al. (2003), Lower-crustal strength under the Dead Sea basin from local earthquake data and rheological modeling, *Earth Planet. Sci. Lett.*, *214* (1-2), 129-142.

Atwater, T. (1970), Implications of plate tectonics for the Cenozoic tectonic evolution of western North America, *Geol. Soc. Am. Bull.*, *81* (12), 3513-3535.

Austrheim, H. (1987), Eclogitization of lower crustal granulites by fluid migration through shear zones, *Earth Planet. Sci. Lett.*, *81* (2-3), 221-232, doi: 10.1016/0012-821X(87)90158-0.

Austrheim, H., and T. M. Boundy (1994), Pseudotachylytes generated during seismic faulting and eclogitization of the deep crust, *Science*, *265* (5168), 82-83, doi: 10.1126/science.265.5168.82.

Austrheim, H., et al. (1996), Garnets recording deep crustal earthquakes, *Earth Planet. Sci. Lett.*, *139* (1-2), 223-238, doi: 10.1016/0012-821X(95)00232-2.

Austrheim, H., and W. L. Griffin (1985), Shear Deformation and Eclogite Formation within Granulite-Facies Anorthosites of the Bergen Arcs, Western Norway, *Chem. Geol.*, *50*, 267-281.

Awad, H., et al. (2005), Temporal and three dimensional spatial analysis of seismicity in the Lake Aswan area, Egypt, *Acta Geophys.*, *53* (2), 153-166.

Baker, C. (1993), The active seismicity and tectonics of Iran, PhD thesis, 228 pp, University of Cambridge, UK.

Baker, C., et al. (1993), Earthquakes on the Kazerun Line in the Zagros Mountains of Iran: strike-slip faulting within a fold-and-thrust belt, *Geophys. J. Int.*, *115* (1), 41-61, doi:10.1111/j.1365-246X.1993.tb05587.x.

Barazangi, M., et al. (2006), Structure and tectonic evolution of the Anatolian Plateau in eastern Turkey, *Geol. Soc. Am. Spec Pap.*, *409*, 463-473.

Bhattacharya, S. N., et al. (1997), Source parameters of Jabalpur earthquake of 22 May 1997, *Curr. Sci.*, *73* (10), 855-863.

Bilham, R., et al. (2003), Flexure of the Indian plate and intraplate earthquakes, *Proc. Indian Acad. Sci. (Earth Planet Sci.)*, *112* (3), 315-329.

Biryol, C. B., et al. (2006), Preliminary Results from the North Anatolian Fault Passive Seismic Experiment: Seismicity and Anisotropy, *Eos Trans. AGU, Fall Meet. Suppl., Abstract #T43D-1667*.

Bjørnerud, M. G., et al. (2002), Processes leading to eclogitization (densification) of subducted and tectonically buried crust, *J. Geophys. Res.*, *107* (B10), 2252, doi:10.1029/2001JB000527.

Bodin, P., and S. Horton (2004), Source Parameters and Tectonic Implications of Aftershocks of the Mw 7.6 Bhuj Earthquake of 26 January 2001, *B. Seismol. Soc. Am.*, *94* (3), 818-827, 10.1785/0120030176.

Boundy, T. M., et al. (1992), Structural Development and Petrofabrics of Eclogite Facies Shear Zones, Bergen Arcs, Western Norway - Implications for Deep Crustal Deformational Processes, *J. Metamorph. Geol.*, *10* (2), 127-146, doi:10.1111/j.1525-1314.1992.tb00075.x.

Bozkurt, E. (2001), Neotectonics of Turkey - a synthesis, *Geodin. Acta*, *14* (1-3), 3-30.

Brace, W. F., and D. L. Kohlstedt (1980), Limits on lithospheric stress imposed by laboratory experiments, *J. Geophys. Res.*, *85* (B11), 6248-6252.

Braunmiller, J., and J. Nabelek (1990), Rupture Process of the Macquarie Ridge Earthquake of May 23, 1989, *Geophys. Res. Lett.*, *17* (7), 1017-1020.

Brazier, R. A., et al. (2005), Focal mechanisms and the stress regime in NE and SW Tanzania, East Africa, *Geophys. Res. Lett.*, *32* (14), L14315, doi:10.1029/2005GL023156.

Brown, L. D., et al. (1996), Bright spots, structure, and magmatism in southern Tibet from INDEPTH seismic reflection profiling, *Science*, *274* (5293), 1688-1690.

Burov, E. B., and A. B. Watts (2006), The long-term strength of continental lithosphere; "jelly sandwich" or "creme brulee"?, *GSA Today*, *16* (1), 4-10.

Byerlee, J. D. (1967), Frictional characteristics of granite under high confining pressure, *J. Geophys. Res.*, *72* (14), 3639-3648.

Byerlee, J. D. (1968), Brittle-ductile transition in rocks, *J. Geophys. Res.*, *73* (14), 4741-4750.

Byerlee, J. D. (1978), Friction of rocks, *Pure Appl. Geophys.*, *116* (4-5), 615-626.

Calais, E., et al. (1998), Crustal deformation in the Baikal Rift from GPS measurements, *Geophys. Res. Lett.*, *25* (21), 4003-4006.

Camacho, A., et al. (2005), Short-lived orogenic cycles and the eclogitization of cold crust by spasmodic hot fluids, *Nature*, *435* (7046), 1191-1196.

Catchings, R. D. (1999), Regional Vp, Vs, Vp/Vs, and Poisson's ratios across earthquake source zones from Memphis, Tennessee, to St. Louis, Missouri, *B. Seismol. Soc. Am.*, *89* (6), 1591-1605.

Chapman, D. S., and K. P. Furlong (1992), Thermal state of the continental crust, in *Continental Lower Crust*, edited by D. M. Fountain, et al., pp. 179-199, Elsevier, New York.

Chen, W.-P., and H. Kao (1996), Seismotectonics of Asia: some recent progress, *Bull. Inst. Earth Sci. Acad. Sin.*, *16*, 23-24.

Chen, W.-P., and P. Molnar (1983), Focal depths of intracontinental and intraplate earthquakes and their implications for the thermal and mechanical properties of the lithosphere, *J. Geophys. Res.*, *88* (B5), 4183-4214.

Chen, W.-P., and P. Molnar (1990), Source parameters of earthquakes and intraplate deformation beneath the Shillong Plateau and the northern Indoburman Ranges, *J. Geophys. Res.*, *95* (B8), 12527-12552.

Clark, M. K., et al. (2005), Late Cenozoic uplift of southeastern Tibet, *Geology*, *33* (6), 525-528.

Clark, M. K., and L. H. Royden (2000), Topographic ooze: Building the eastern margin of Tibet by lower crustal flow, *Geology*, *28* (8), 703-706.

Costain, J. K., et al. (1987), Hydroseismicity - A hypothesis for the role of water in the generation of intraplate seismicity, *Geology*, *15* (7), 618-621.

Crosby, A. G. (2007), An assessment of the accuracy of admittance and coherence estimates using synthetic data, *Geophys. J. Int.*, *171* (1), 25-54, doi:10.1111/j.1365-246X.2007.03520.x.

Davidson, C., et al. (1994), Role of melt during deformation in the deep crust, *Terra Nova*, *6* (2), 133-142.

de la Torre, T. L., et al. (2007), Earthquake processes of the Himalayan collision zone in eastern Nepal and the southern Tibetan Plateau, *Geophys. J. Int.*, *171* (2), 718-738, doi:10.1111/j.1365-246X.2007.03537.x.

Dickinson, W. R. (1996), Kinematics of transrotational tectonism in the California Transverse Ranges and its contribution to cumulative slip along the San Andreas transform fault system, *Geol. Soc. Am. Spec Pap.*, *305*, 46.

Dugda, M. T., et al. (2005), Crustal structure in Ethiopia and Kenya from receiver function analysis; implications for rift development in eastern Africa, *J. Geophys. Res.*, *110* (B1), B01303, doi:10.1029/2004JB003065.

Dziewonski, A. M., et al. (1981), Determination of earthquake source parameters from waveform data for studies of global and regional seismicity, *J. Geophys. Res.*, *86* (B4), 2825-2852.

Ebinger, C. J. (1989), Tectonic development of the western branch of the East African rift system, *Geol. Soc. Am. Bull.*, *101* (7), 885-903.

Emmerson, B., et al. (2006), Seismicity, structure and rheology of the lithosphere in the Lake Baikal region, *Geophys. J. Int.*, *167* (3), 1233-1272, doi:10.1111/j.1365-246X.2006.03075.x.

Emmerson, B., and D. McKenzie (2007), Thermal structure and seismicity of subducting lithosphere, *Phys. Earth Planet. In.*, *163* (1-4), 191-208.

Engdahl, E. R., et al. (1998), Global teleseismic earthquake relocation with improved travel times and procedures for depth determination, *B. Seismol. Soc. Am.*, *88* (3), 722-743.

Engdahl, R. E., and A. Villaseñor (2002), Global Seismicity: 1900–1999, in *International Handbook of Earthquake and Engineering Seismology*, edited by W. H. K. Lee, et al., pp. 665–690, Academic Press.

England, P. C., and A. B. Thompson (1984), Pressure Temperature Time Paths of Regional Metamorphism .1. Heat-Transfer during the Evolution of Regions of Thickened Continental-Crust, *Journal of Petrology*, *25* (4), 894-928.

Erduran, M., et al. (2007), Anatolian surface wave evaluated at GEOFON Station ISP Isparta, Turkey, *Tectonophysics*, *434* (1-4), 39-54.

Forsyth, D. W. (1985), Subsurface loading and estimates of the flexural rigidity of continental lithosphere, *J. Geophys. Res.*, *90* (B14), 12,623-612,632.

Foster, A. N., and J. A. Jackson (1998), Source parameters of large African earthquakes; implications for crustal rheology and regional kinematics, *Geophys. J. Int.*, *134* (2), 422-448.

Freund, R., et al. (1970), The shear along the Dead Sea rift, *Philos. Mag. A*, *267* (1181), 107-130.

Gans, P. B. (1987), An open-system, two layer crustal stretching model for the eastern Great Basin, *Tectonics*, *6* (1), 1-12.

Gaulon, R., et al. (1992), Regional Geodynamic Implications of the May July 1990 Earthquake Sequence in Southern Sudan, *Tectonophysics*, *209* (1-4), 87-103, doi:10.1016/0040-1951(92)90012-U.

George, R., et al. (1998), Earliest magmatism in Ethiopia: Evidence for two mantle plumes in one flood basalt province, *Geology*, *26* (10), 923-926.

Gharib, A. A. (1991), The crust and upper mantle structure in the Lake Nasser area from seismic waves generated by earthquakes and explosions, Ph.D. Thesis thesis, Cairo University, Cairo, Eygpt.

Ghose, S., et al. (1998), Source parameters of moderate-size earthquakes in the Tien Shan, Central Asia from regional movement tensor inversion, *Geophys. Res. Lett.*, *25* (16), 3181-3184.

Gibbs, J. F., et al. (1973), Seismicity in the Rangely, Colorado, area: 1962-1970, *B. Seismol. Soc. Am.*, *63* (5), 1557-1570.

Gilbert, H. J., and A. F. Sheehan (2004), Images of crustal variations in the intermountain west, *J. Geophys. Res.*, *109* (B3), doi:10.1029/2003JB002730.

Golonka, J. (2004), Plate tectonic evolution of the southern margin of Eurasia in the Mesozoic and Cenozoic, *Tectonophysics*, *381* (1-4), 235-273.

Goodwin, E. B., and J. Mccarthy (1990), Composition of the Lower Crust in West Central Arizona from 3-Component Seismic Data, *J. Geophys. Res.*, *95* (B12), 20097-20109.

Grotzinger, J., and L. Royden (1990), Elastic strength of the Slave craton at 1.9 Gyr and implications for the thermal evolution of the continents, *Nature*, *347* (6288), 64-66.

Gurbuz, C., et al. (2000), The seismotectonics of the Marmara region (Turkey): results from a microseismic experiment, *Tectonophysics*, *316* (1-2), 1-17.

Hacker, B. R., et al. (2000), Hot and Dry Deep Crustal Xenoliths from Tibet, *Science*, *287* (5462), 2463-2466, doi: 10.1126/science.287.5462.2463.

Handy, M. R., and J.-P. Brun (2004), Seismicity, structure and strength of the continental lithosphere, *Earth Planet. Sci. Lett.*, *223* (3-4), 427-441.

Hobbs, B. E., et al. (1986), Earthquakes in the Ductile Regime, *Pure Appl. Geophys.*, *124* (1-2), 309-336.

Jackson, J. (2002), Strength of the continental lithosphere; time to abandon the jelly sandwich?, *GSA Today*, *12* (9), 4-10.

Jackson, J., et al. (2008), New views on the structure and rheology of the lithosphere, *J. Geol. Soc. London*, *165* (2), 453-465, doi: 10.1144/0016-76492007-109.

Jackson, J. A., et al. (2004), Metastability, mechanical strength, and the support of mountain belts, *Geology*, *32* (7), 625-628.

Jamtveit, B., et al. (1990), Fluid Controlled Eclogitization of Granulites in Deep Crustal Shear Zones, Bergen Arcs, Western Norway, *Contrib. Mineral. Petrol.*, *104* (2), 184-193.

Jones, L. M., et al. (1984), Focal mechanisms and aftershock locations of the Songpan earthquakes of August 1976 in Sichuan, China, *J. Geophys. Res.*, *89* (B9), 7697-7707.

Kagan, Y. Y. (2004), Short-term properties of earthquake catalogs and models of earthquake source, *B. Seismol. Soc. Am.*, *94* (4), 1207-1228.

Karahan, A. E., et al. (2001), Crustal structure at the western end of the North Anatolian fault zone from deep seismic sounding, *Ann. Geofis.*, *44* (1), 49-68.

Kebeasy, R. M., et al. (1991), Crustal Structure Modeling for the Northern Part of the Aswan Lake Area Using Seismic-Waves Generated by Explosions and Local Earthquakes, *J. Geodyn.*, *14* (1-4), 159-182.

Keir, D., et al. (2006), Strain accommodation by magmatism and faulting as rifting proceeds to breakup; seismicity of the northern Ethiopian Rift, *J. Geophys. Res.*, *111* (B5), doi:10.1029/2005JB003748.

King, K. M. (1986), Investigation of the Seismogenic Zone in the Vicinity of Socorro, New Mexico, from an Analysis of Focal Depth Distributions - Open File, New Mexico Institute of Mining and Technology Geophysics, Socorro, New Mexico.

Kirby, S. H. (1983), Rheology of the lithosphere, *Rev. Geophys. Space Phys.*, *21* (6), 1458-1487.

Knapp, J. H., et al. (2005), Crustal constraints on the origin of mantle seismicity in the Vrancea zone, Romania: The case for active continental lithospheric delamination, *Tectonophysics*, *410* (1-4), 311-323.

Kohler, M. D., and D. Eberhart-Phillips (2003), Intermediate-depth earthquakes in a region of continental convergence: South Island, New Zealand, *B. Seismol. Soc. Am.*, *93* (1), 85-93.

Lamontagne, M., et al. (1994), The Mont-Laurier, Quebec, earthquake of 19-October-1990 and its seismotectonic environment, *B. Seismol. Soc. Am.*, *84* (5), 1506-1522.

Langin, W. R., et al. (2003), Seismicity of central Tibet from Project INDEPTH III seismic recordings, *B. Seismol. Soc. Am.*, *93* (5), 2146-2159.

Le Pichon, X., et al. (1997), Uplift of Tibet: From eclogites to granulites - Implications for the Andean Plateau and the Variscan belt, *Tectonophysics*, *273* (1-2), 57-76.

Lund, M. G., and H. E. M. Austrheim (2004), Earthquakes in the deep continental crust; insights from studies on exhumed high-pressure rocks, *Geophys. J. Int.*, *158* (2), 569-576.

Lyon-Caen, H., and P. Molnar (1983), Constraints on the structure of the Himalaya from an analysis of gravity anomalies and a flexural model of the lithosphere, *J. Geophys. Res.*, *88* (B10), 8171-8191.

Ma, S. T., and G. M. Atkinson (2006), Focal depths for small to moderate earthquakes (mN $\geq$ 2.8) in western Quebec, southern Ontario, and northern New York, *B. Seismol. Soc. Am.*, *96* (2), 609-623.

Maggi, A., et al. (2000a), A re-assessment of focal depth distributions in southern Iran, the Tien Shan and northern India: do earthquakes occur in the continental mantle?, *Geophys. J. Int.*, *143* (3), 629–661.

Maggi, A., et al. (2000b), Earthquake focal depths, effective elastic thickness, and the strength of the continental lithosphere, *Geology*, *28* (6), 495-498.

Maggi, A., and K. Priestley (2005), Surface waveform tomography of the Turkish-Iranian Plateau, *Geophys. J. Int.*, *160* (3), 1068-1080.

Maggi, A., et al. (2002), Focal Depths of Moderate to Large Magnitude Earthquakes in Iran, *J. Seism. Earthq. Eng.*, *4* (2-3), 1-10.

Matti, J. C., et al. (1992), The San Andreas fault system in the vicinity of the central Transverse Ranges province, Southern California, U. S. Geological Survey, Reston, VA and Tucson, AZ.

McCarthy, J., et al. (1991), Anatomy of a Metamorphic Core Complex - Seismic Refraction Wide-Angle Reflection Profiling in Southeastern California and Western Arizona, *J. Geophys. Res.*, *96* (B7), 12259-12291.

McGuire, A. V. (1994), Southern Basin and Range Province crust-mantle boundary; evidence from gabbroic xenoliths, Wikieup, Arizona, *J. Geophys. Res.*, *99* (B12), 24,263-224,273.

McKenzie, D., and J. Jackson (2002), Conditions for flow in the continental crust, *Tectonics*, *21* (6), doi:10.1029/2002TC001394.

McKenzie, D., et al. (2005), Thermal structure of oceanic and continental lithosphere, *Earth Planet. Sci. Lett.*, *233* (3-4), 337- 349.

McKenzie, D. P., and D. Fairhead (1997), Estimates of the effective elastic thickness of the continental lithosphere from bouguer and free-air gravity anomalies, *J. Geophys. Res.*, *102* (B12), 27,523–527,552, doi: 10.1029/97Jb02481.

McNulty, B. A. (1995), Pseudotachylyte generated in the semi-brittle and brittle regimes, Bench Canyon shear zone, central Sierra Nevada, *J. Struct. Geol.*, *17* (11), 1507-1521.

Mekkawi, M., et al. (2005), Electrical structure of the tectonically active Kalabsha Fault, Aswan, Egypt, *Earth Planet. Sci. Lett.*, *240* (3-4), 764-773.

Molnar, P., and W.-P. Chen (1983), Focal depths and fault plane solutions of earthquakes under the Tibetan Plateau, *J. Geophys. Res.*, *88* (B2), 1180-1196.

Molnar, P., et al. (1977), Structure and tectonics of the Himalaya; a brief summary of relevant geophysical observations, in *Ecologie et geologie de l'Himalaya*, edited by C. Jest, pp. 269-294, Centre National de la Recherche Scientifique.

Molnar, P., and H. Lyon-Caen (1989), Fault plane solutions of earthquakes and active tectonics of the Tibetan Plateau and its margins, *Geophys. J. Int.*, *99* (1), 123-153.

Monsalve, G., et al. (2006), Seismicity and one-dimensional velocity structure of the Himalayan collision zone: Earthquakes in the crust and upper mantle, *J. Geophys. Res.*, *111* (B10), doi:10.1029/2005JB004062.

Nazareth, J. J., and E. Hauksson (2004), The Seismogenic Thickness of the Southern California Crust, *B. Seismol. Soc. Am.*, *94* (3), 940-960, doi: 10.1785/0120020129.

Nelson, K. D., et al. (1985), New COCORP profiling in the southeastern United States; Part I, Late Paleozoic suture and Mesozoic rift basin, *Geology*, *13* (10), 714-718.

Nelson, K. D., et al. (1996), Partially molten middle crust beneath southern Tibet: Synthesis of project INDEPTH results, *Science*, *274* (5293), 1684-1688.

Nelson, M. R., et al. (1987), Source Parameters for 11 earthquakes in the Tien Shan, Central Asia, determined by P and SH waveform inversion, *J. Geophys. Res.*, *92* (B12), 12,629-612,648.

Ni, J., and M. Barazangi (1986), Seismotectonics of the Zagros Continental Collision Zone and a Comparison with the Himalayas, *J. Geophys. Res.*, *91* (B8), 8205-8218.

Nur, A., and J. R. Booker (1972), Aftershocks Caused by Pore Fluid Flow?, *Science*, *175* (4024), 885-887, 10.1126/science.175.4024.885.

Nyblade, A. A., and R. A. Brazier (2002), Precambrian lithospheric controls on the development of the East African Rift system, *Geology*, *30* (8), 755-758.

Nyblade, A. A., and C. A. Langston (1995), East African earthquakes below 20 km depth and their implications for crustal structure, *Geophys. J. Int.*, *121* (1), 49-62.

Olsen, K. H., et al. (1987), Rio Grande Rift: An overview, *Tectonophysics*, *143*, 119-139.

Ord, A., and B. E. Hobbs (1989), The strength of the continental crust, detachment zones and the development of plastic instabilities, *Tectonophysics*, *158* (1-4), 269-289.

Ozacar, A. A., et al. (2006), North Anatolian Fault Passive Seismic Experiment: Receiver Functions Along a Major Strike-Slip Fault, *Eos Trans. AGU, Fall Meet. Suppl., Abstract #T43D-1668*.

Paul, A., et al. (2006), Seismological evidence for crustal-scale thrusting in the Zagros mountain belt (Iran), *Geophys. J. Int.*, *166* (1), 227-237.

Peng, X. H., and E. D. Humphreys (1998), Crustal velocity structure across the eastern Snake River Plain and the Yellowstone swell, *J. Geophys. Res.*, *103* (B4), 7171-7186.

Perchuk, A. L. (2002), Eclogites of the Bergen Arcs complex, Norway: Petrology and mineral chronometry, *Petrology*, *10* (2), 99-118.

Perez-Gussinye, M., et al. (2004), On the recovery of effective elastic thickness using spectral methods; examples from synthetic data and from the Fennoscandian Shield, *J. Geophys. Res.*, *109* (B10), doi:10.1029/2003JB002788.

Perez-Gussinye, M., and A. B. Watts (2005), The long-term strength of Europe and its implications for plate-forming processes, *Nature*, *436* (7049), 381-384.

Petit, C., and J. Déverchère (2006), Structure and evolution of the Baikal rift: A synthesis, *Geochem. Geophys. Geosyst.*, *7* (11), Q11016, doi:10.1029/2006GC001265.

Polat, O., et al. (2002), Analysis and interpretation of the aftershock sequence of the August 17, 1999, Izmit (Turkey) earthquake, *J. Seismol.*, *6* (3), 287-306.

Priestley, K., et al. (2008), Lithospheric structure and deep earthquakes beneath India, the Himalaya and southern Tibet, *Geophys. J. Int.*, *172* (1), 345-362, doi:10.1111/j.1365-246X.2007.03636.x.

Quennell, A. M. (1958), The structural and geomorphic evolution of the Dead Sea rift, *Quart. J. Geol. Soc., Lond.*, *114* (453), 1-24.

Raleigh, C. B., et al. (1976), An Experiment in Earthquake Control at Rangely, Colorado, *Science*, *191* (4233), 1230-1237, 10.1126/science.191.4233.1230.

Ramdani, F. (1998), Geodynamic implications of intermediate-depth earthquakes and volcanism in the intraplate Atlas mountains (Morocco), *Phys. Earth Planet. In.*, *108* (3), 245-260.

Rao, B. R., and V. K. Rao (2006), Influence of fluids on deep crustal Jabalpur earthquake of 21, May 1997: Geophysical evidences, *J. Seismol.*, *10* (3), 301-314.

Rao, N. P., et al. (2002), Deep lower crustal earthquakes in central India: inferences from analysis of regional broadband data of the 1997 May 21, Jabalpur earthquake, *Geophys. J. Int.*, *148* (1), 132-138.

Reinecker, J., et al. (2005), The 2005 release of the World Stress Map, www.world-stress-map.org.

Reyners, M. (1987), Subcrustal Earthquakes in the Central South Island, New-Zealand, and the Root of the Southern Alps, *Geology*, *15* (12), 1168-1171.

Reyners, M., et al. (2007), The role of fluids in lower-crustal earthquakes near continental rifts, *Nature*, *446* (7139), 1075-1078.

Royden, L. (1988), Flexural behavior of the continental lithosphere in Italy; constraints imposed by gravity and deflection data, *J. Geophys. Res.*, *93* (B7), 7747-7766.

Royden, L. H., et al. (1997), Surface deformation and lower crustal flow in eastern Tibet, *Science*, *276* (5313), 788-790.

Rushmer, T. (1995), An experimental deformation study of partially molten amphibolite; application to low-melt fraction segregation, *J. Geophys. Res.*, *100* (B8), 15,681-615,695.

Saikia, C. K. (2006), Modeling of the 21 May 1997 Jabalpur earthquake in central India; source parameters and regional path calibration, *B. Seismol. Soc. Am.*, *96* (4A), 1396-1421, doi: 10.1785/0120050120.

Schilly, M. M., et al. (1982), The 1978 Yellowstone-Eastern Snake River Plain Seismic Profiling Experiment - Data and Upper Crustal Structure of the Yellowstone Region, *J. Geophys. Res.*, *87* (B4), 2692-2704.

Schulte-Pelkum, V., et al. (2005), Imaging the Indian subcontinent beneath the Himalaya, *Nature*, *435* (7046), 1222-1225.

Seber, D., et al. (1996), Geophysical evidence for lithospheric delamination beneath the Alboran Sea and Rif-Betic mountains, *Nature*, *379* (6568), 785-790.

Sengor, A. M. C. (1979), The North Anatolian transform fault: its age, offset and tectonic significance, *J. Geol. Soc. Aust.*, *136* (3), 269-282, doi: 10.1144/gsjgs.136.3.0269.

Sengor, A. M. C., et al. (2005), The North Anatolian Fault; a new look, *Annu. Rev. Earth Pl. Sc.*, *33*, 37-112.

Sibson, R. H. (1980), Transient Discontinuities in Ductile Shear Zones, *J. Struct. Geol.*, *2* (1-2), 165-171.

Sibson, R. H. (1982), Fault zone models, heat flow, and the depth distribution of earthquakes in the continental crust of the United States, *B. Seismol. Soc. Am.*, *72* (1), 151-163.

Sibson, R. H. (1986), Earthquakes and Rock Deformation in Crustal Fault Zones, *Annu. Rev. Earth Pl. Sc.*, *14*, 149-175, doi:10.1146/annurev.ea.14.050186.001053.

Simpson, D. W. (1986), Triggered earthquakes, *Annu. Rev. Earth Pl. Sc.*, *14*, 21-42.

Simpson, D. W., et al. (1990), Induced seismicity and changes in water level at Aswan Reservoir, Egypt, *Gerl. Beitr. Geophys.*, *99* (3), 191-204.

Simpson, D. W., et al. (1988), Two types of reservoir-induced seismicity, *B. Seismol. Soc. Am.*, *78* (6), 2025-2040.

Snyder, D. B., and M. Barazangi (1986), Deep crustal structure and flexure of the Arabian Plate beneath the Zagros collisional mountain belt as inferred from gravity observations, *Tectonics*, *5* (3), 361-373.

Stewart, J., and A. B. Watts (1997), Gravity anomalies and spatial variations of flexural rigidity at mountain ranges, *J. Geophys. Res.*, *102* (B3), 5327-5253.

Sykes, L. R., and M. L. Sbar (1973), Intraplate Earthquakes, Lithospheric Stresses and Driving Mechanism of Plate Tectonics, *Nature*, *245* (5424), 298-302.

Thatcher, W., and F. F. Pollitz (2008), Temporal evolution of continental lithospheric strength in actively deforming regions, *GSA Today*, *18* (4), 4-11, doi: 10.1130/GSAT01804-5A.1.

Turkelli, N., et al. (2003), Seismogenic zones in eastern Turkey, *Geophys. Res. Lett.*, *30* (24), 8039, doi:10.1029/2003GL018023.

Voshage, H., et al. (1990), Isotopic evidence from the Ivrea Zone for a hybrid lower crust formed by magmatic underplating, *Nature*, *347* (6295), 731-736.

Wagner, G. S., and C. A. Langston (1988), East-African Earthquake Body Wave Inversion with Implications for Continental Structure and Deformation, *Geophys. J. Int.*, *94* (3), 503-518, doi:10.1111/j.1365-246X.1988.tb02271.x.

Watts, A. B. (2001), *Isostasy and flexure of the lithosphere*, 458 pp., University of Cambridge, Cambridge.

Watts, A. B., and E. B. Burov (2003), Lithospheric strength and its relationship to the elastic and seismogenic layer thickness, *Earth Planet. Sci. Lett.*, *213* (1-2), 113-131, doi: 10.1016/S0012-821X(03)00289-9.

Wiens, D. A., and S. Stein (1983), Age Dependence of Oceanic Intraplate Seismicity and Implications for Lithospheric Evolution, *J. Geophys. Res.*, *88* (B8), 6455-6468.

Wilson, D., et al. (2005), Lithospheric structure of the Rio Grande Rift, *Nature*, *433* (7028), 851-855, doi:10.1038/nature03297.

Zhao, W., et al. (2001), Crustal structure of central Tibet as derived from project INDEPTH wide-angle seismic data, *Geophys. J. Int.*, *145* (2), 486-498, doi: 10.1046/j.0956-540X.2001.01402.x.

Zhou, H., et al. (1983), Source processes of large earthquakes along the Xianshuihe Fault in southwestern China, *B. Seismol. Soc. Am.*, *73* (2), 537-551.

Zhu, L., and D. V. Helmberger (1996), Intermediate depth earthquakes beneath the India-Tibet collision zone, *Geophys. Res. Lett.*, *23* (5), 435-438, doi: 10.1029/96GL00385.

Zhu, L., and H. Kanamori (2000), Moho depth variation in Southern California from teleseismic receiver functions, *J. Geophys. Res.*, *105* (B2), 2969-2980, doi: 10.1029/1999JB900322.

Zoback, M. L., et al. (1989), Global patterns of tectonic stress, *Nature*, *341* (6240), 291-298, doi:10.1038/341291a0.

APPENDIX A

EARTHQUAKE DEPTH DETERMINATION RESULTS

This section contains waveform figures of the 38 earthquakes with properties that were determined through this study and described in Chapter 2. Waveform plots are ordered according to date. Events that occurred first in time occur first in this chapter and the most recent events are placed last. Plots come in two forms: *P* and *SH* waveform modeling plots and SHZ phase identification plots. Examples of *P* and *SH* waveform modeling plots were shown in Chapter 2. These plots are broken into two halves, the left halves are the waveform solution plots and the right halves are the sensitivity analysis plots. Convention for these plots is described in Figures 1.3 and 1.5, respectively. Conventions for the SHZ phase identification plots have not been described before. These plots show one or more short-period waveform record, the SHZ record. The titles contain the date and origin time of the earthquake. Forward modeling of *pP* and *sP* phase arrival times are superimposed on the SHZ waveforms. In the upper right of the waveform plots the network, station, waveform type, and distance, in degrees, from event to station are listed. When particular descriptions are needed, they are contained within the figure captions.

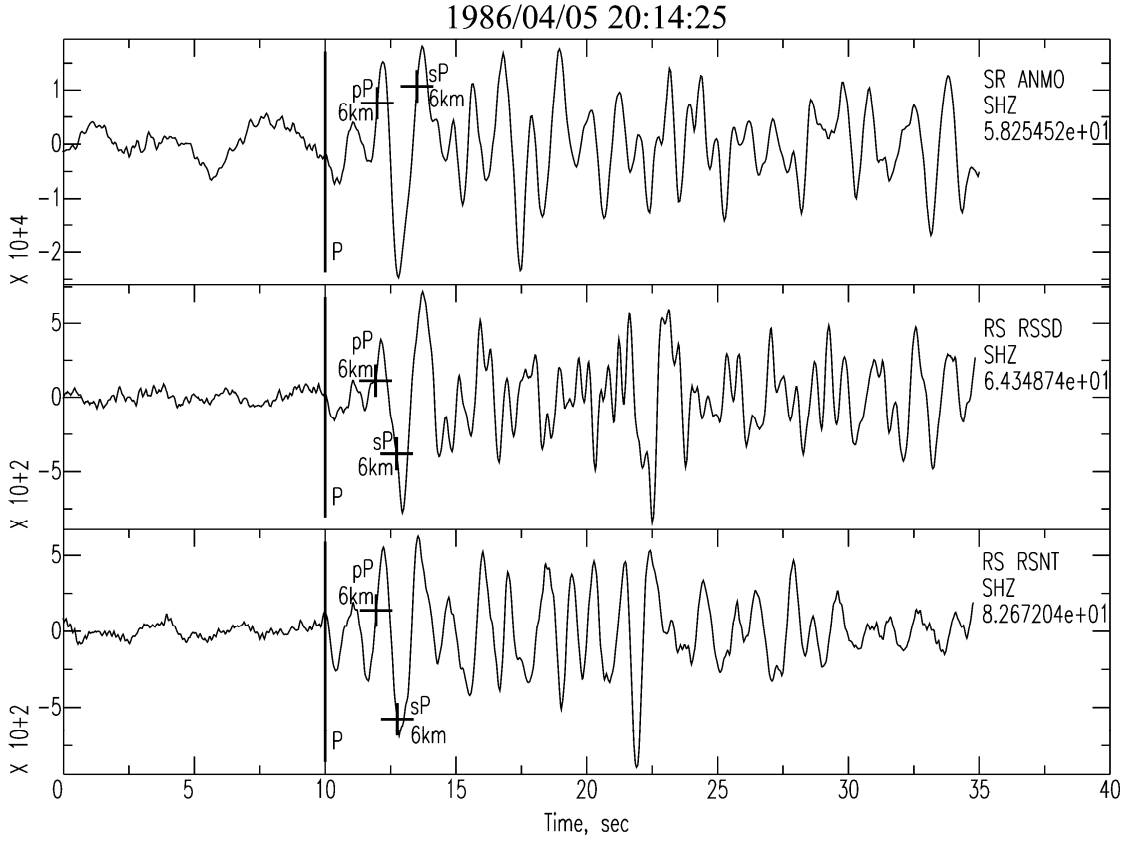

Figure A.1: SHZ analysis plot for the 1986/04/05 earthquake. Event depth was found to be 6 km.

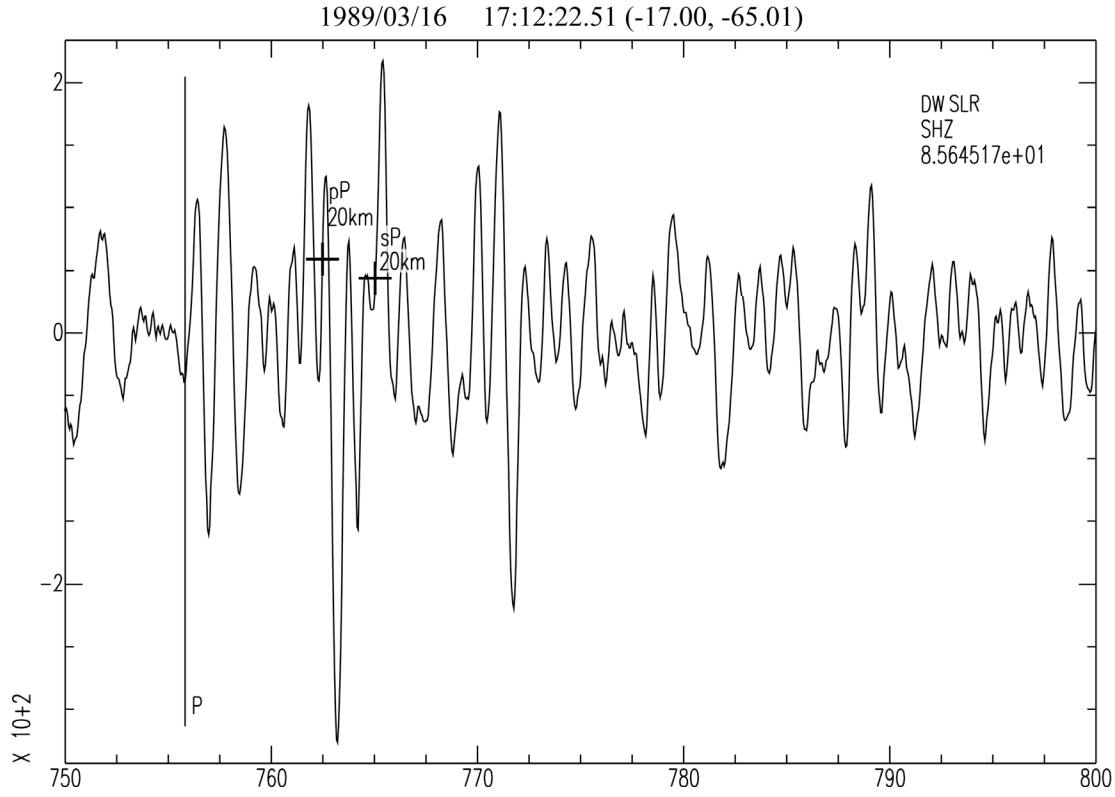

Figure A.2: SHZ analysis plot for the 1989/03/16 earthquake. Event depth was found to be 20 km.

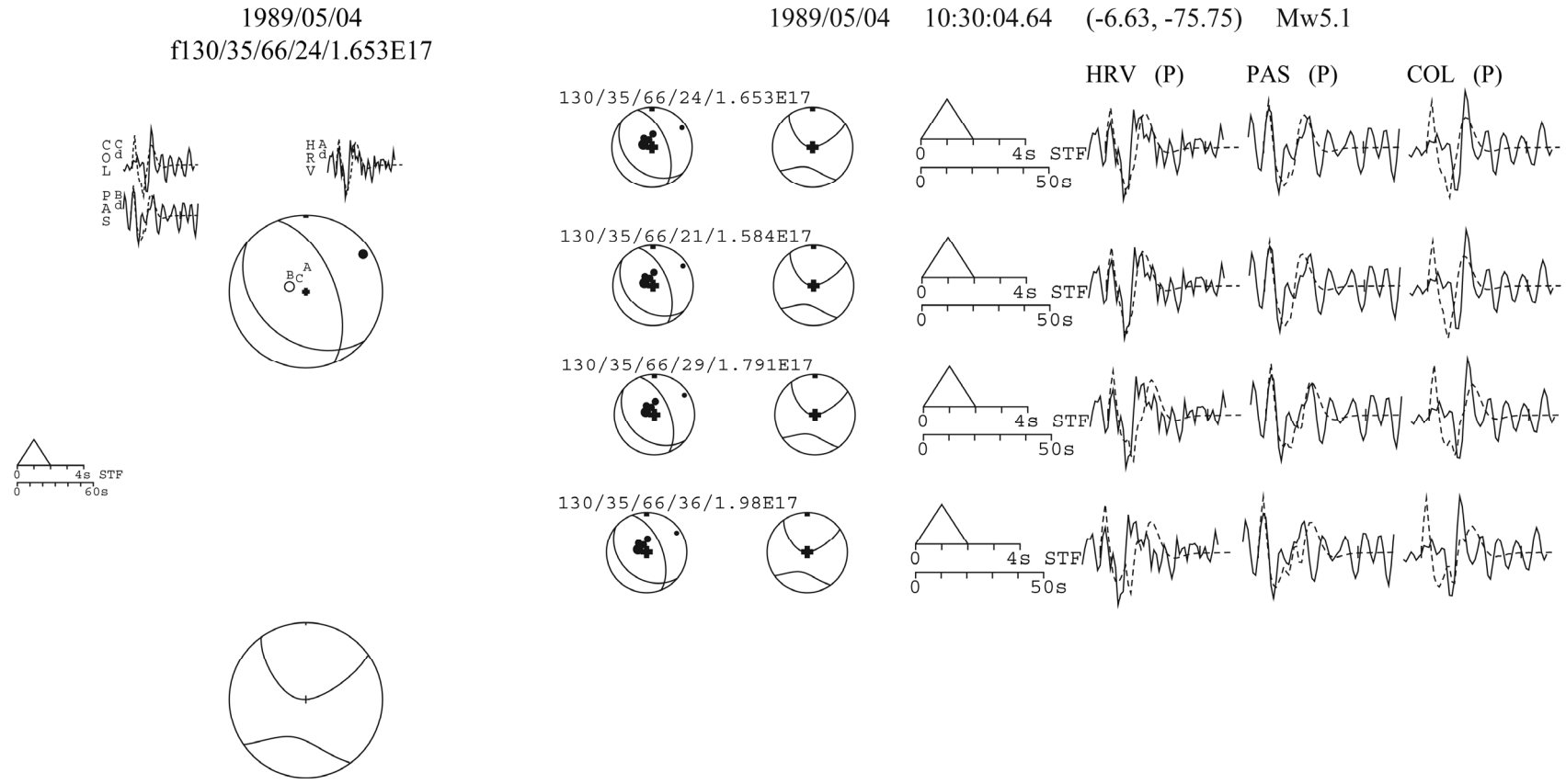

Figure A.3: MT5 waveform inversion solution plot for the 1989/05/04 earthquake. Focal mechanism was held fixed to that reported by the Global CMT catalog. Event depth was found to be 24 km.

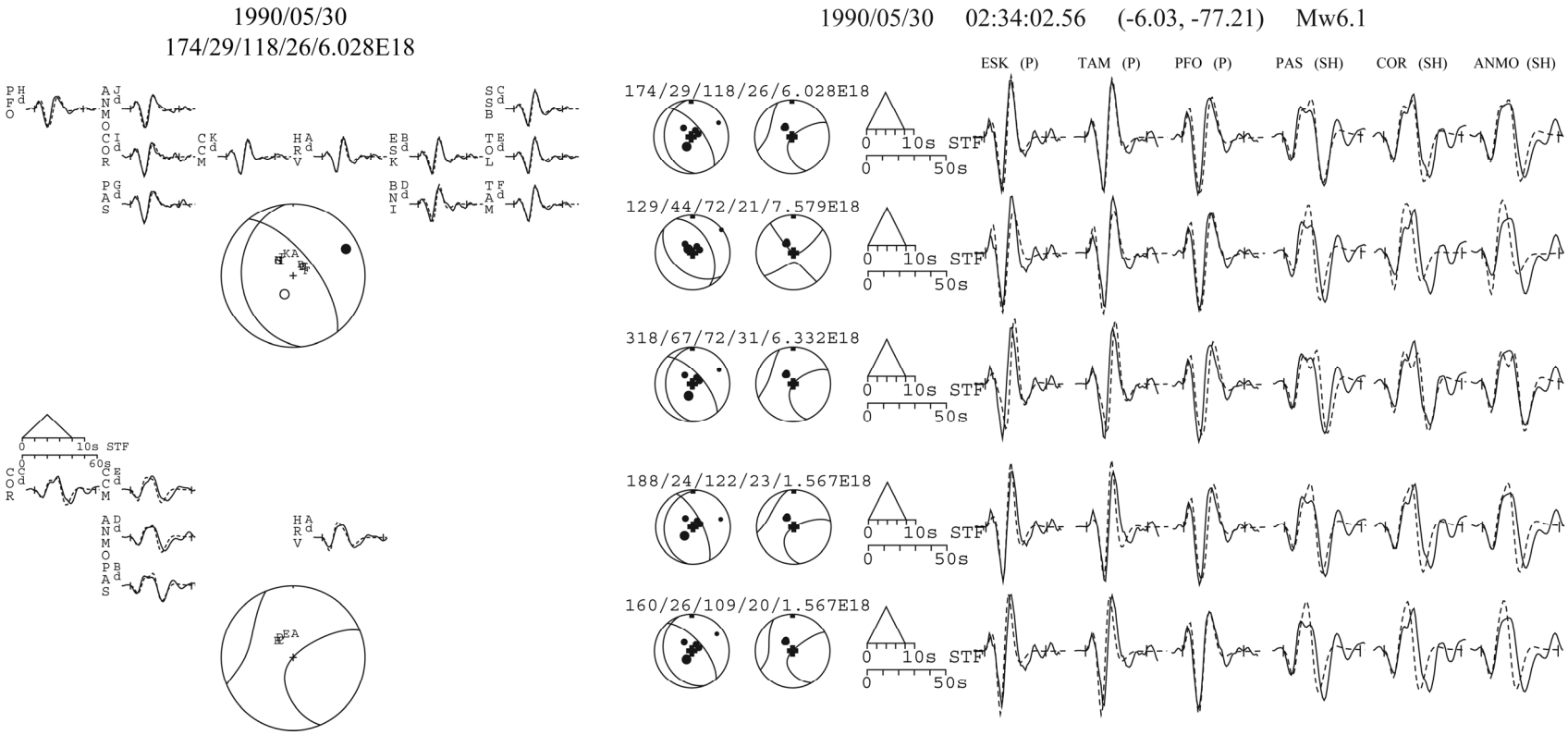

Figure A.4: MT5 waveform inversion solution plot for the 1990/05/30 02:34:02.56 earthquake. Minimum misfit solution: strike 174°, dip 29°, rake 118°, depth 26 km, and Mw 6.5.

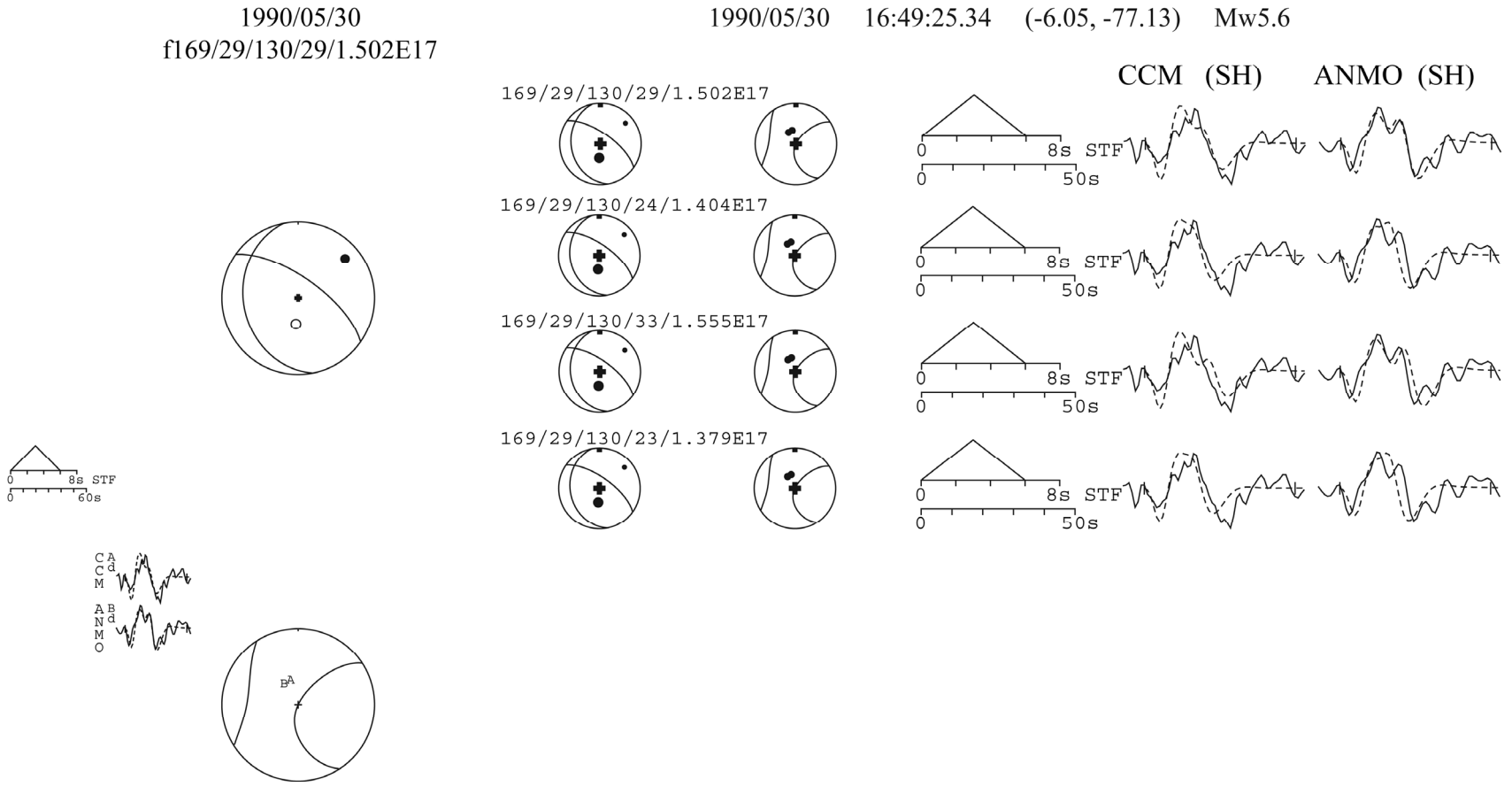

Figure A.5: MT5 waveform inversion solution plot for the 1990/05/30 16:49:25.34 earthquake. Focal mechanism was held fixed to that reported by the Global CMT catalog. Event depth was found to be 29 km.

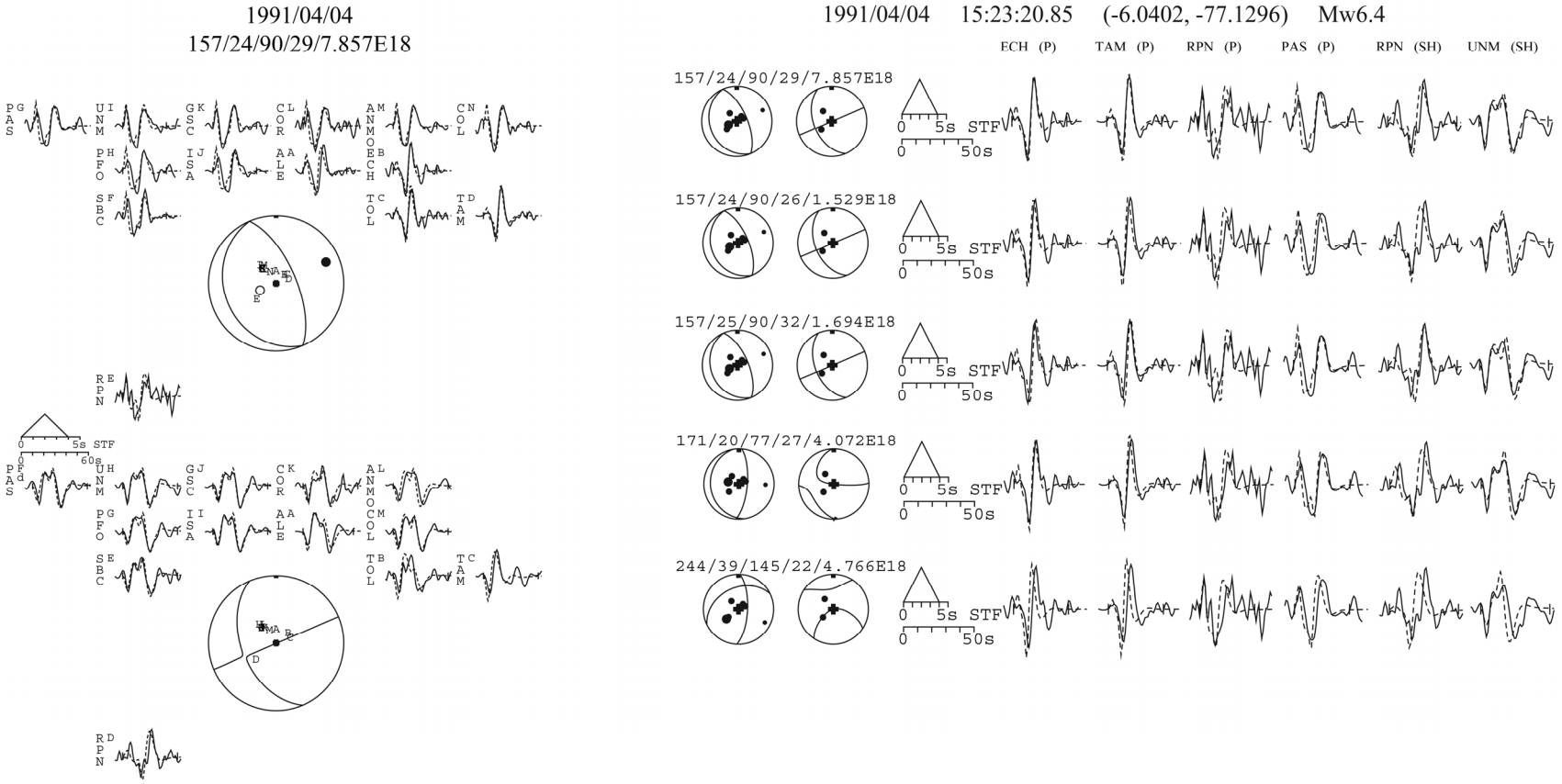

Figure A.6: MT5 waveform inversion solution plot for the 1991/04/04 earthquake. Minimum misfit solution: strike 157°, dip 24°, rake 90°, depth 29 km, and Mw 6.6.

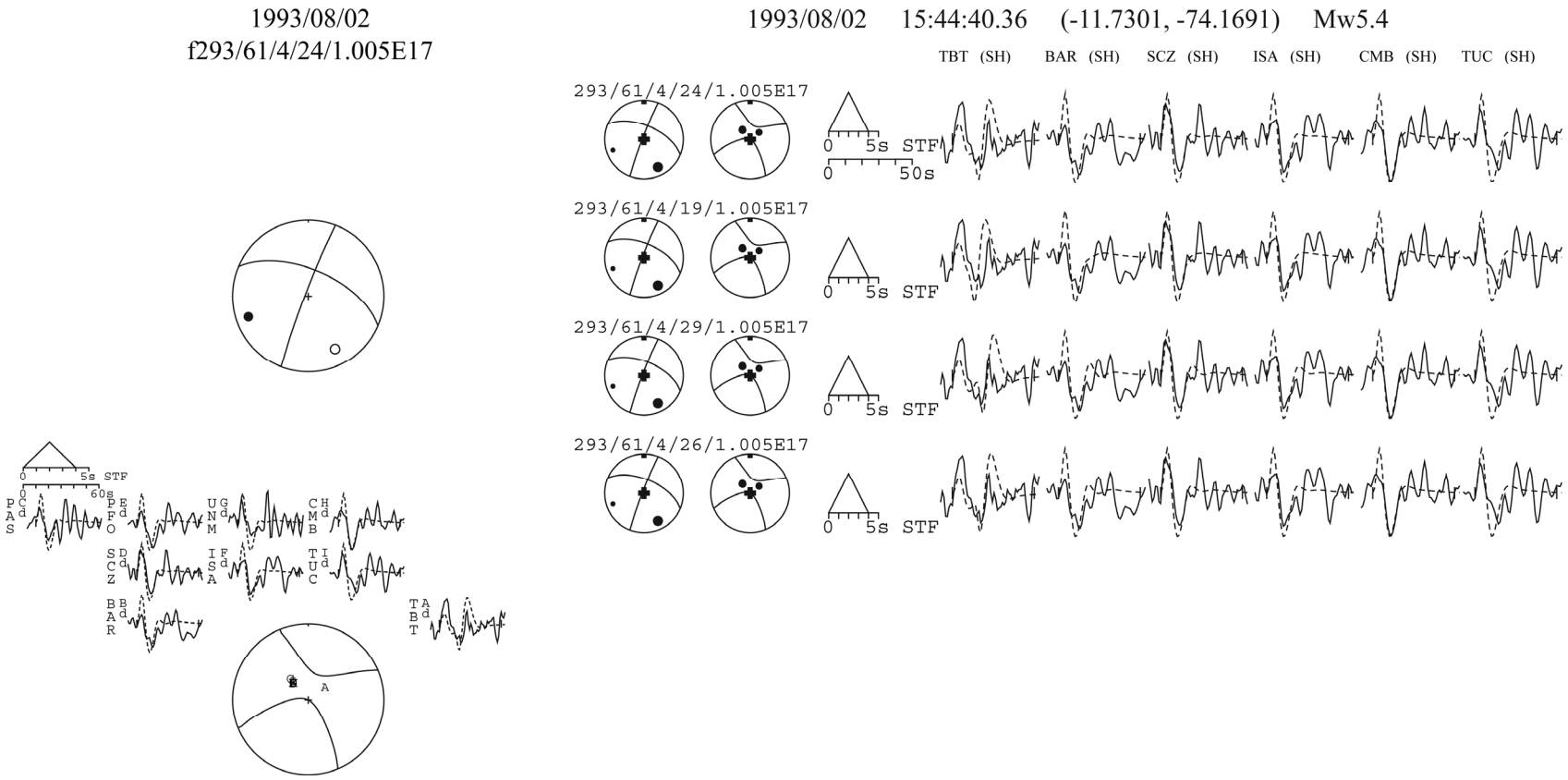

Figure A.7: MT5 waveform inversion solution plot for the 1993/08/02 earthquake. Focal mechanism was held fixed to that reported by the Global CMT catalog. Event depth was found to be 24 km.

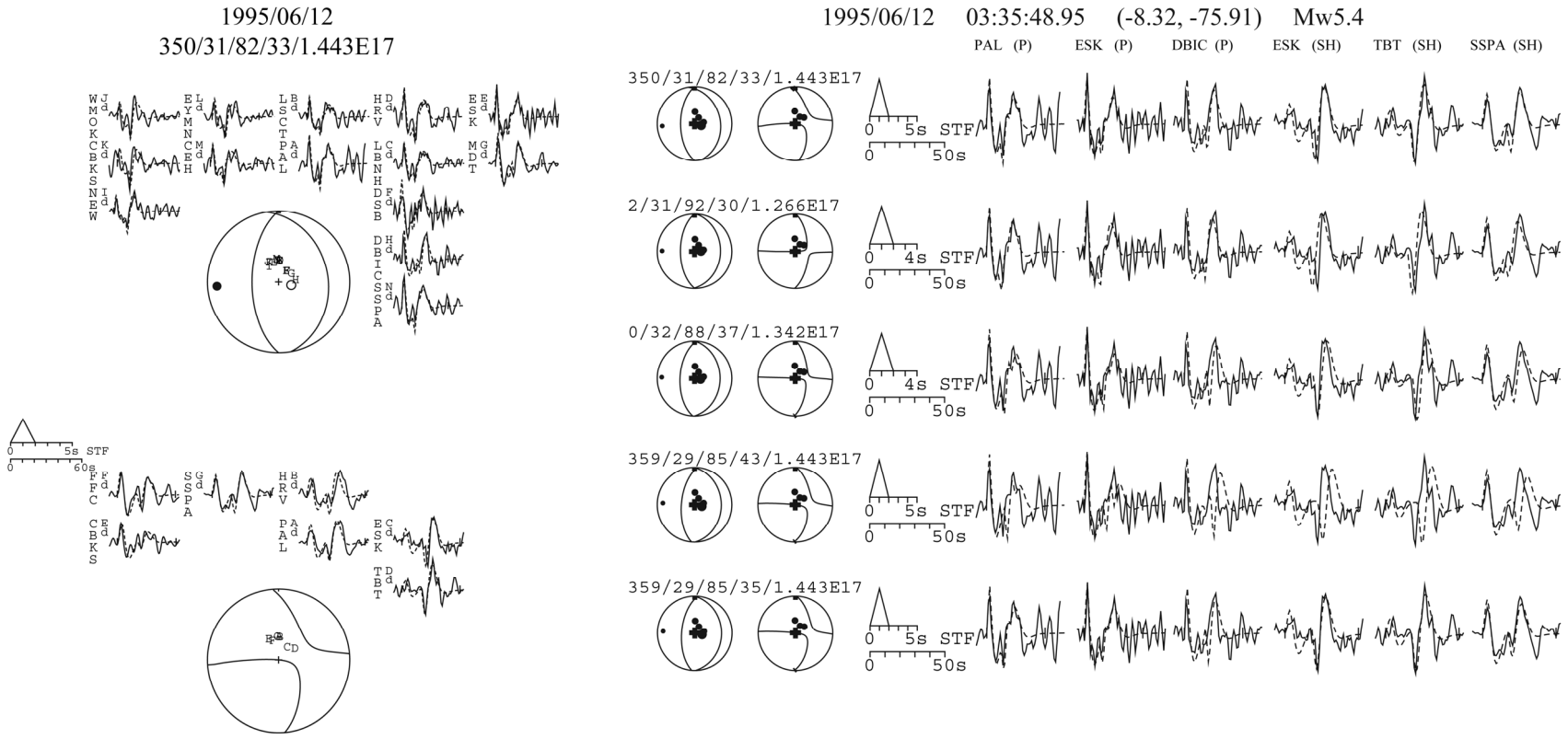

Figure A.8: MT5 waveform inversion solution plot for the 1995/06/12 earthquake. Minimum misfit solution: strike 350°, dip 31°, rake 82°, depth 33 km, and Mw 5.4.

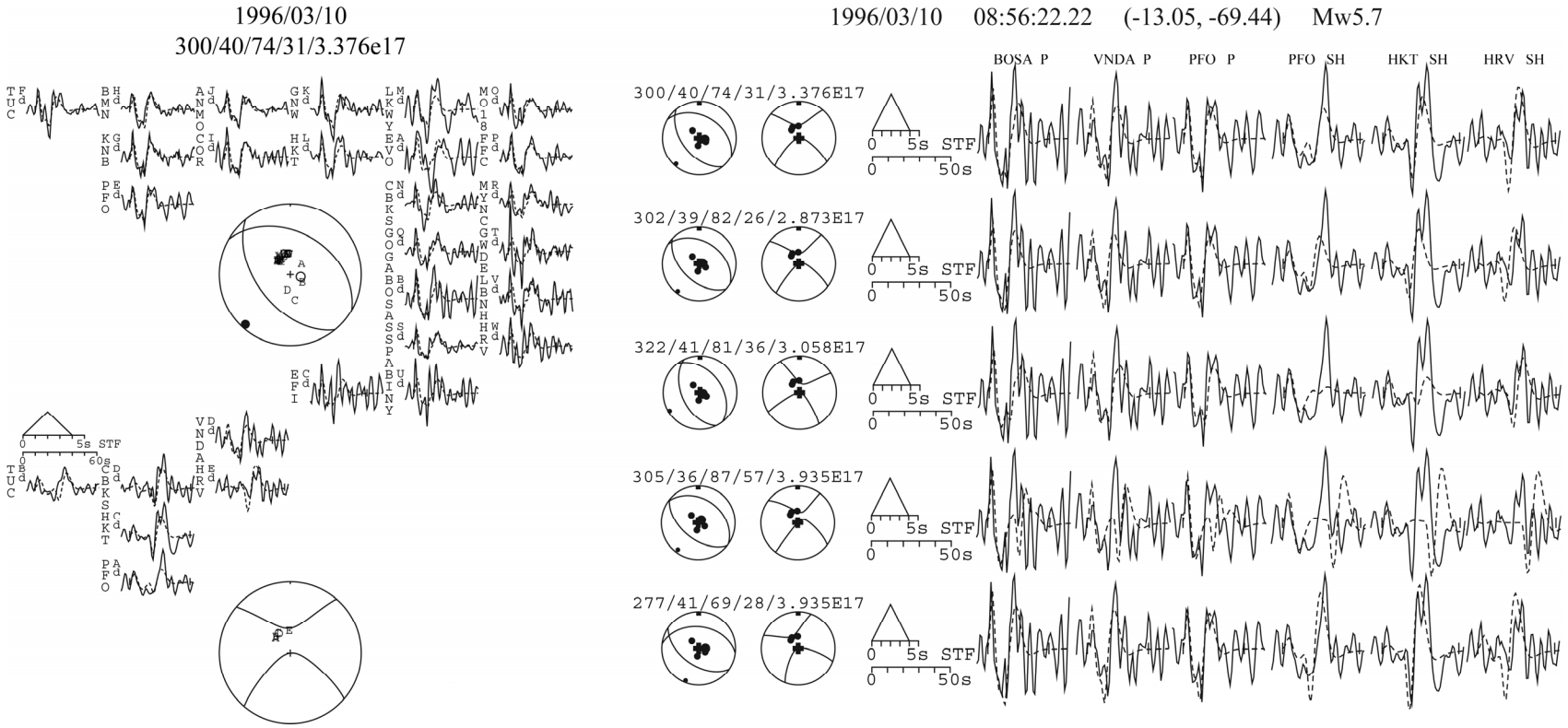

Figure A.9: MT5 waveform inversion solution plot for the 1996/03/10 earthquake. Minimum misfit solution: strike 300°, dip 40°, rake 74°, depth 31 km, and Mw 5.7.

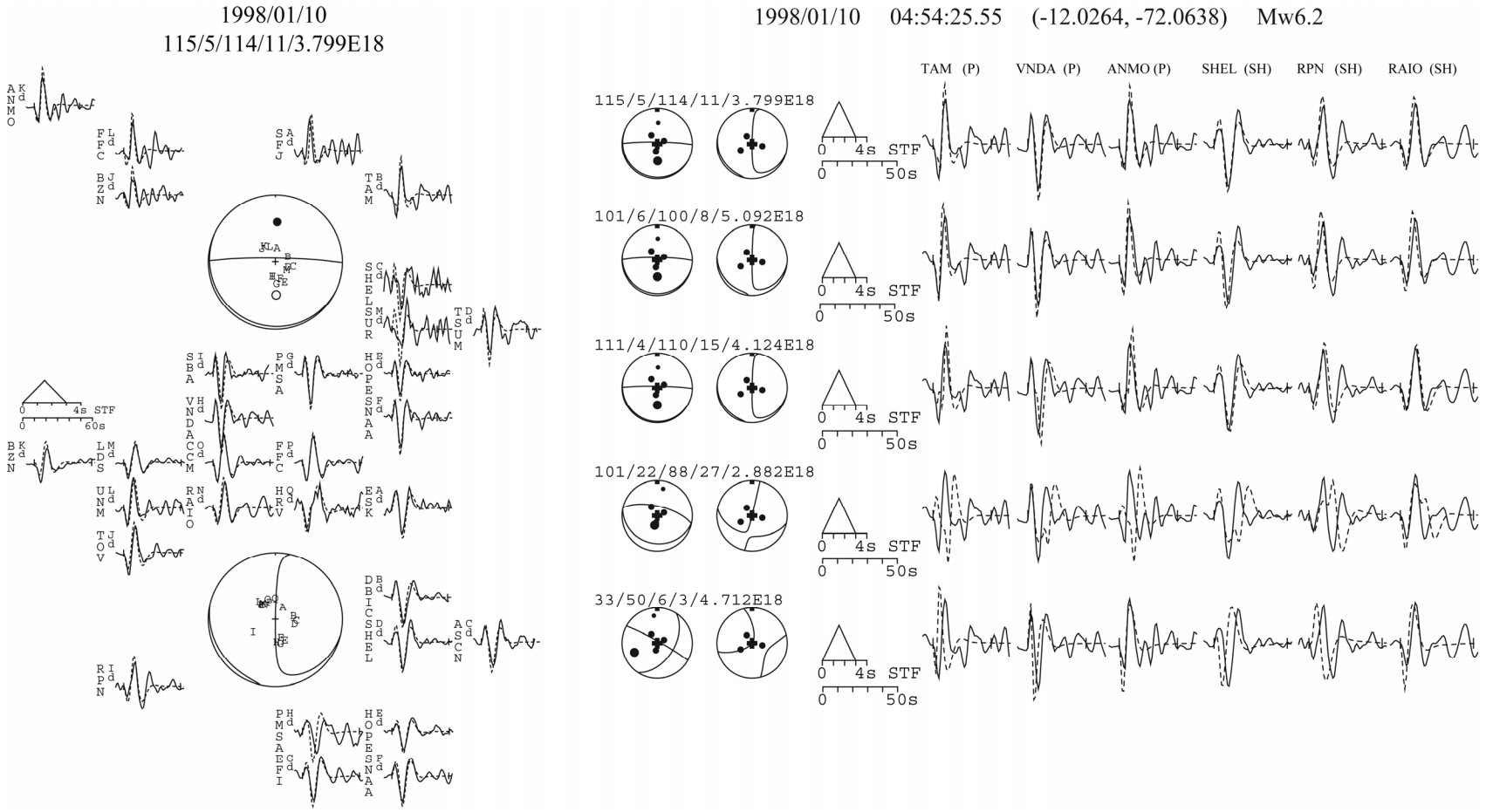

Figure A.10: MT5 waveform inversion solution plot for the 1998/01/10 earthquake. Minimum misfit solution: strike 115°, dip 5°, rake 114°, depth 11 km, and Mw 6.2.

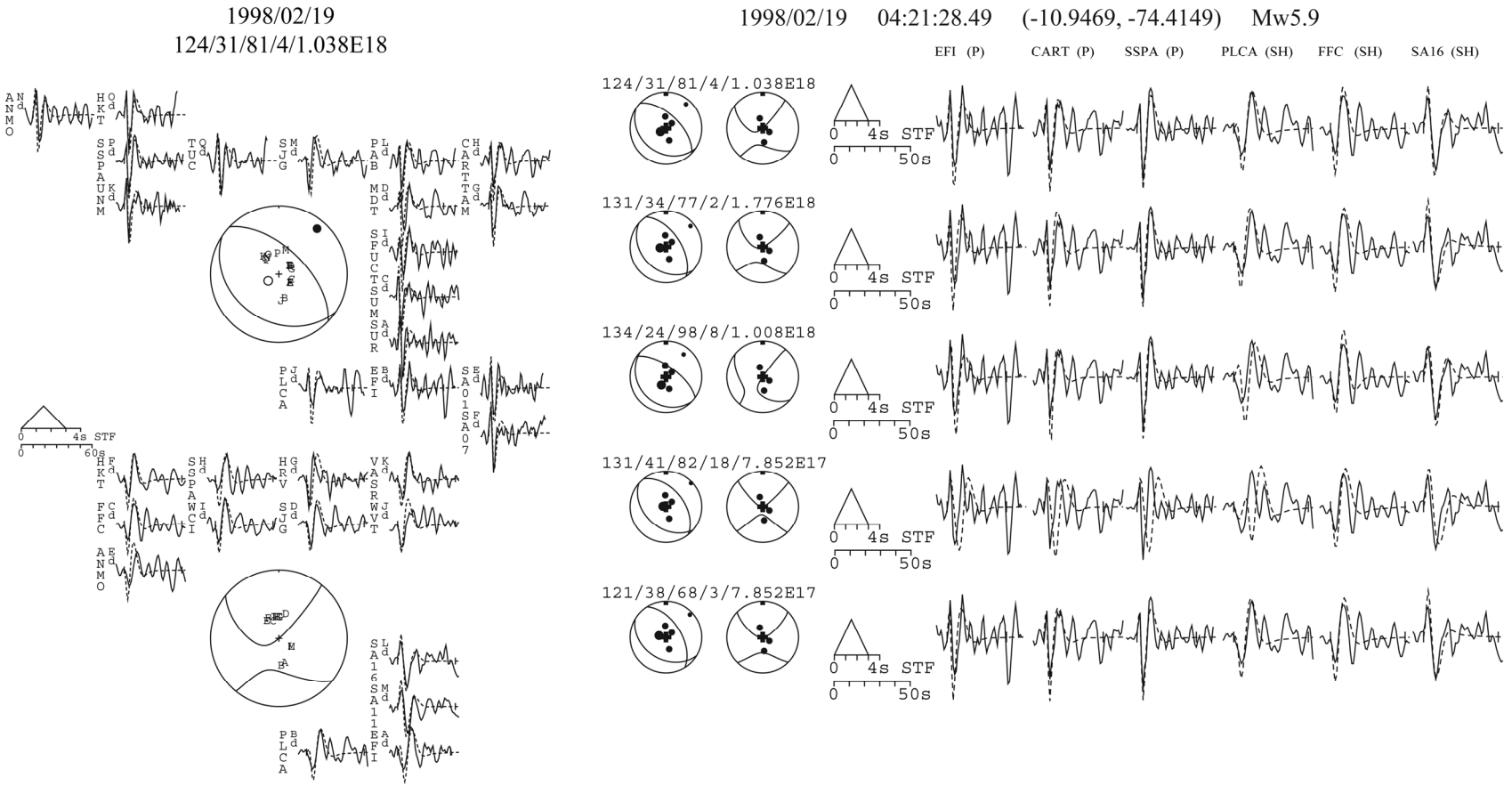

Figure A.11: MT5 waveform inversion solution plot for the 1998/02/19 earthquake. Minimum misfit solution: strike 124°, dip 31°, rake 81°, depth 4 km, and Mw 6.0.

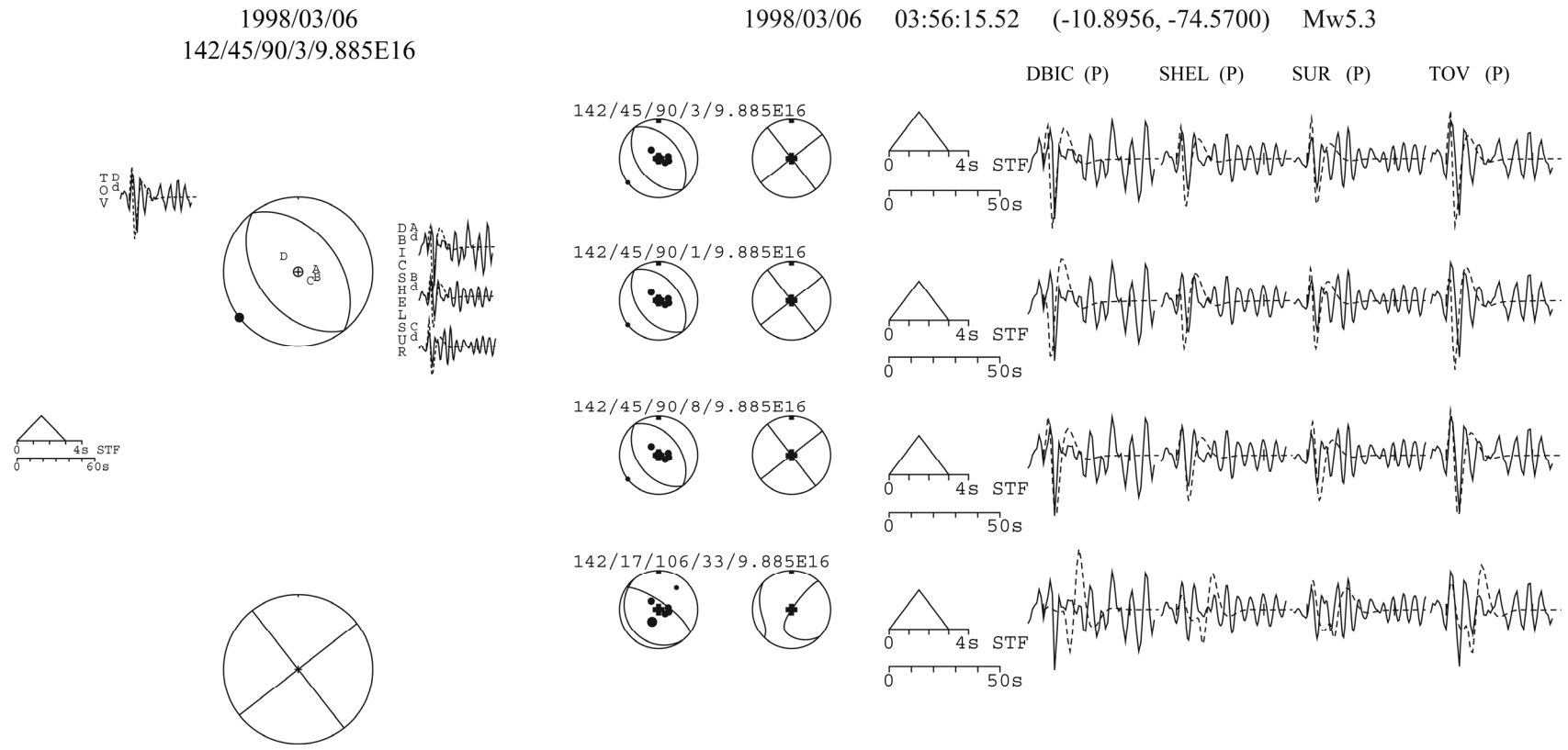

Figure A.12: MT5 waveform inversion solution plot for the 1998/03/06 earthquake. Minimum misfit solution: strike 142°, dip 45°, rake 90°, depth 3 km, and Mw 5.6.

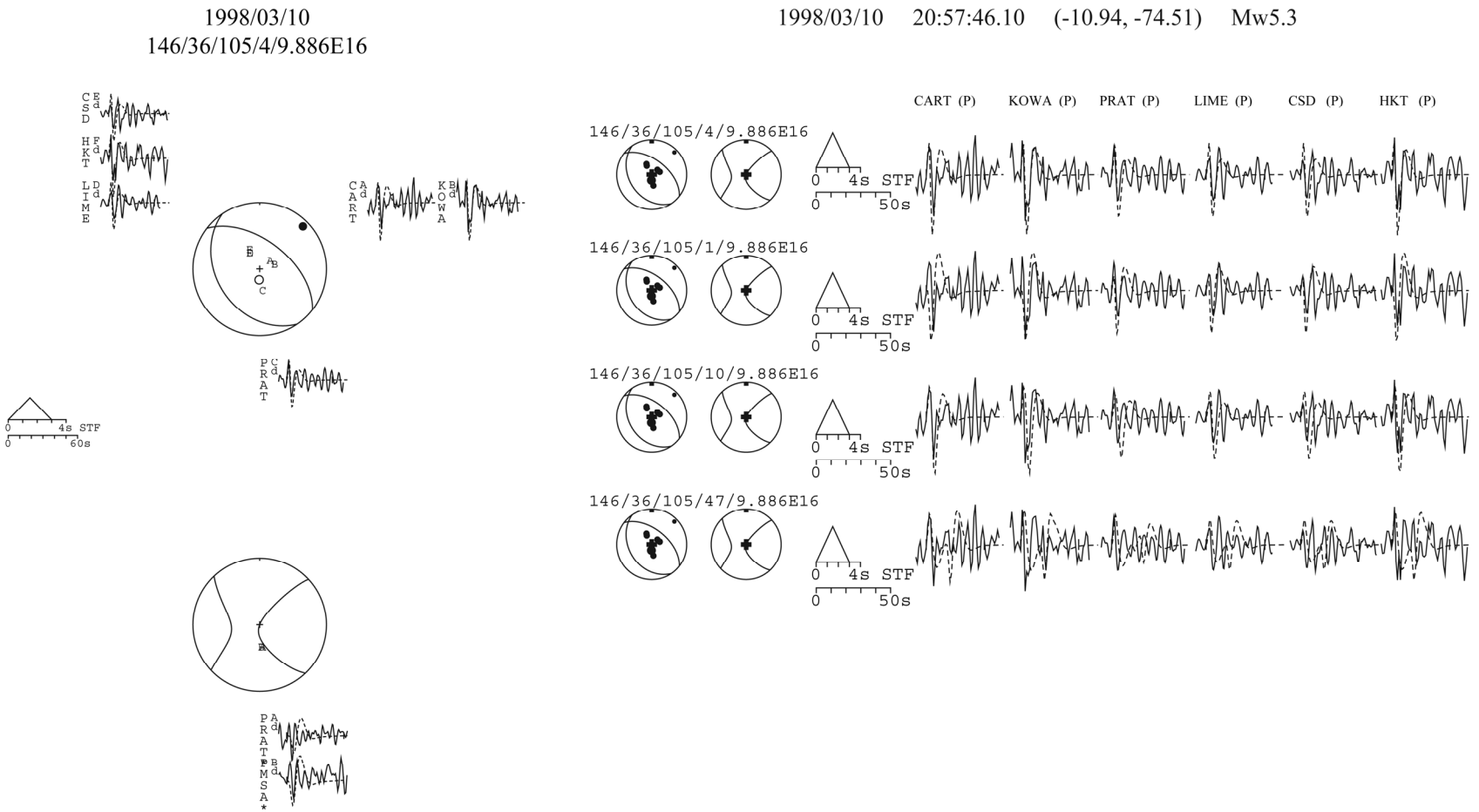

Figure A.13: MT5 waveform inversion solution plot for the 1998/03/10 earthquake. Minimum misfit solution: strike 146°, dip 36°, rake 105°, depth 4 km, and Mw 5.8.

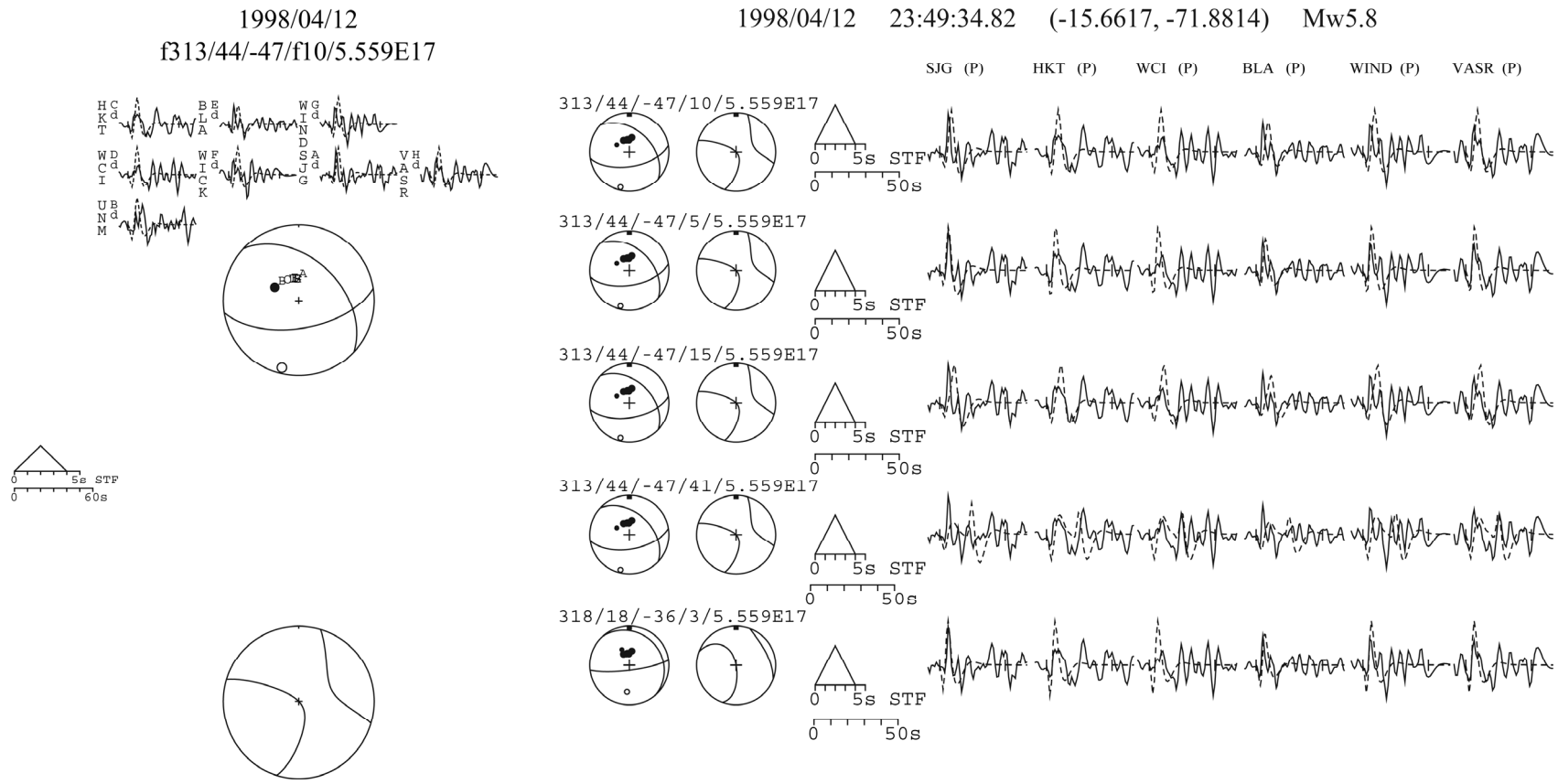

Figure A.14: MT5 waveform inversion solution plot for the 1998/04/12 earthquake. Focal mechanism was held fixed to that reported by the Global CMT catalog and the depth was held fixed by the SHZ analysis depth solution reported in Figure A.13 (10 km).

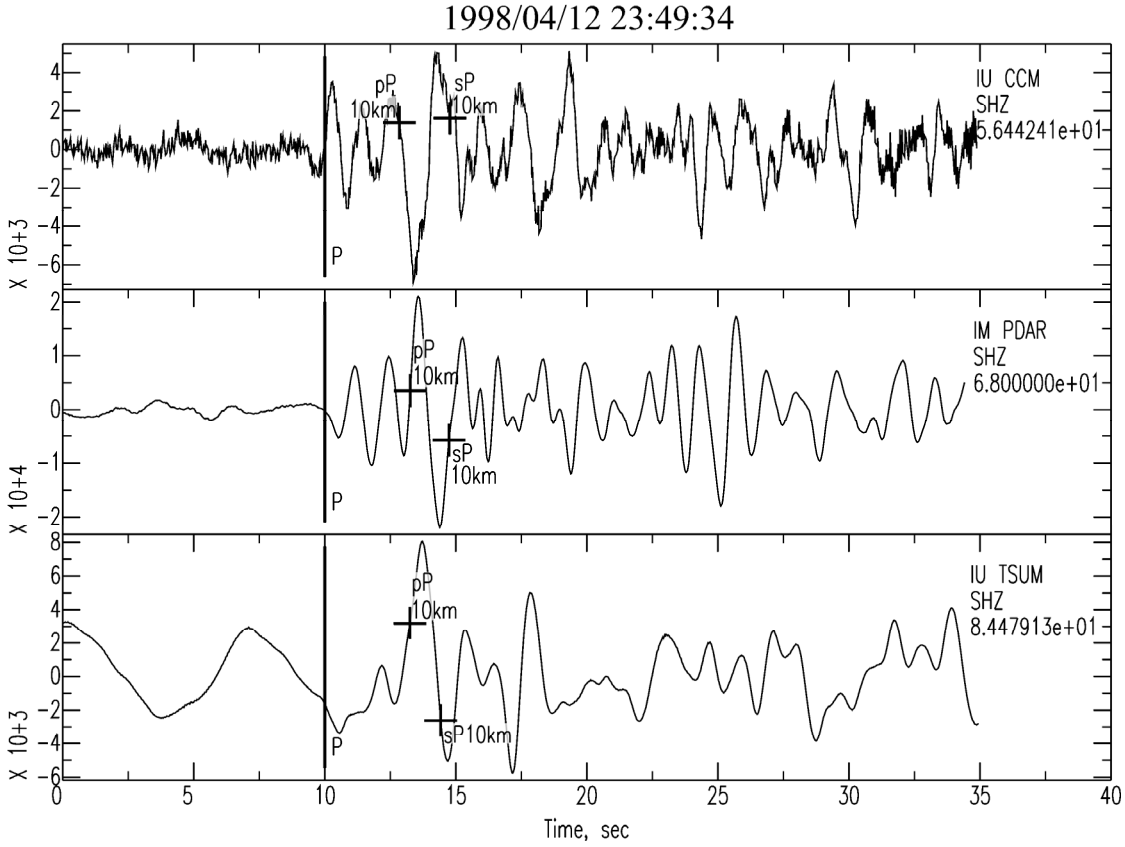

Figure A.15: SHZ analysis plot for the 1998/04/12 earthquake. Event depth was found to be 10 km. IM PDAR waveform is a waveform stack of records recorded by the PDAR seismic array in Wyoming, USA. MT5 waveform inversion solution plot is shown in Figure A.12.

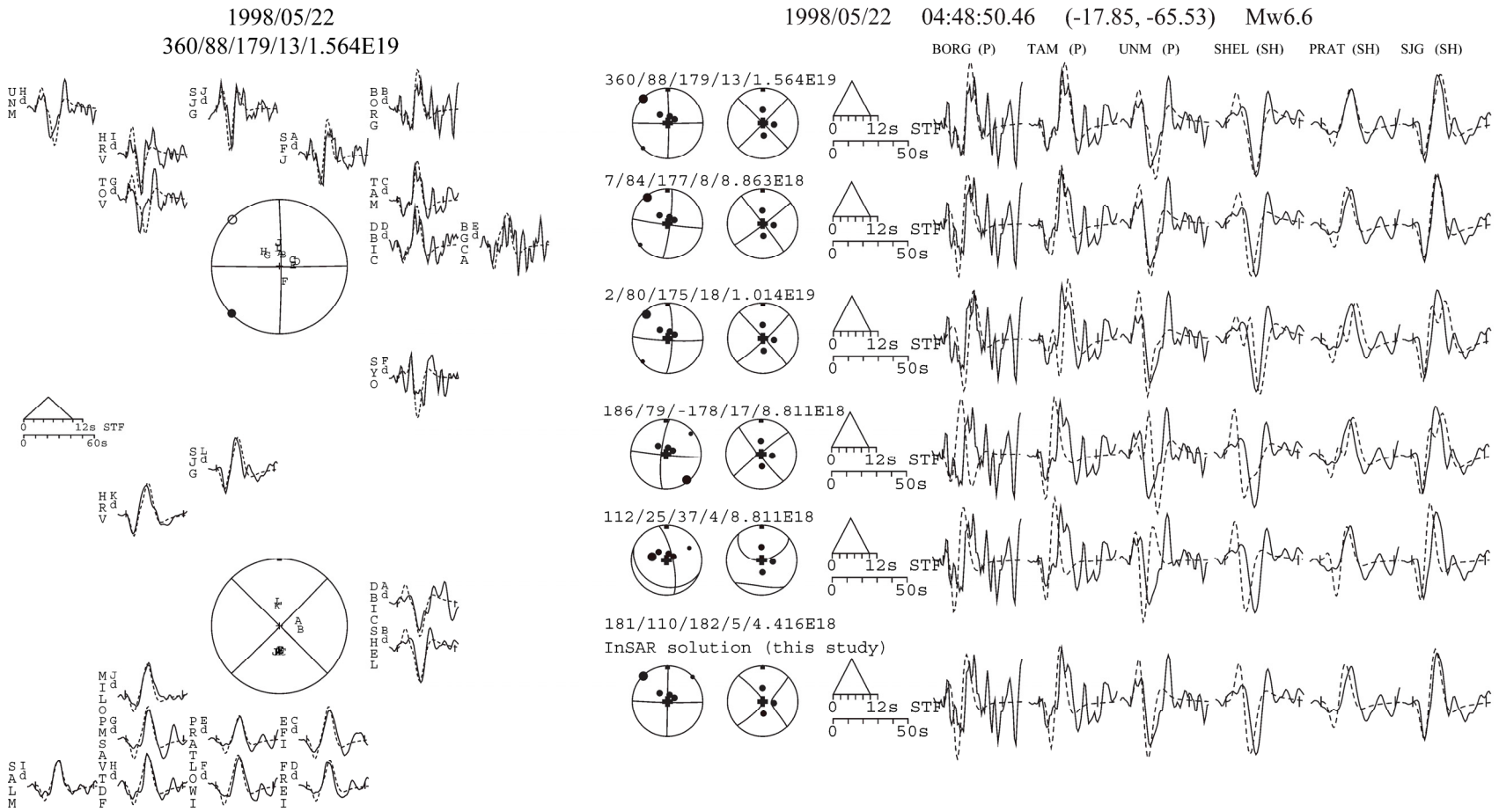

Figure A.16: MT5 waveform inversion solution plot for the 1998/05/22 earthquake. Minimum misfit solution: strike 360°, dip 88°, rake 179°, depth 13 km, and Mw 6.1. This figure is also shown as Figure 2.20.

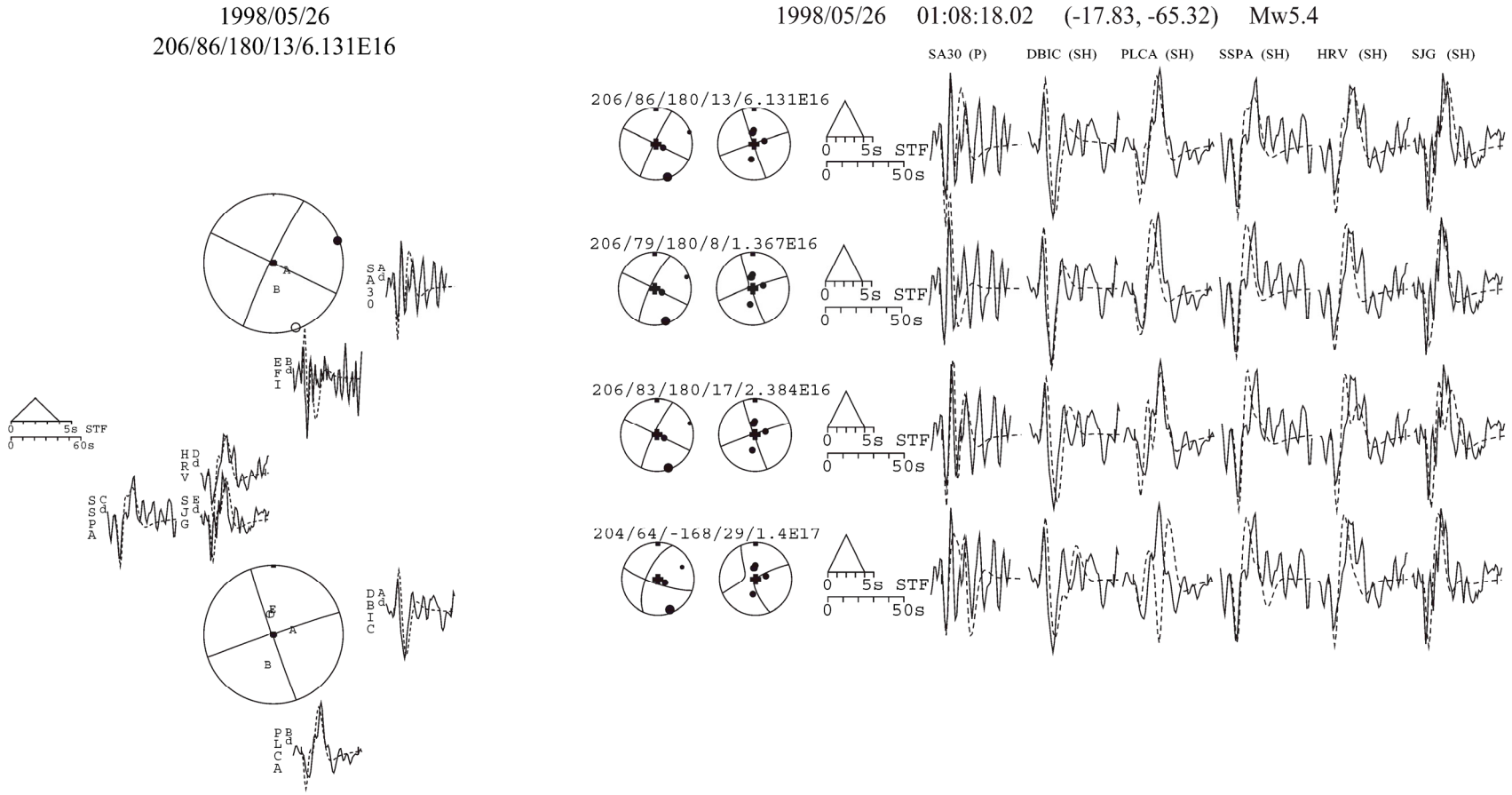

Figure A.17: MT5 waveform inversion solution plot for the 1998/05/26 earthquake. Minimum misfit solution: strike 206°, dip 86°, rake 180°, depth 13 km, and Mw 5.2.

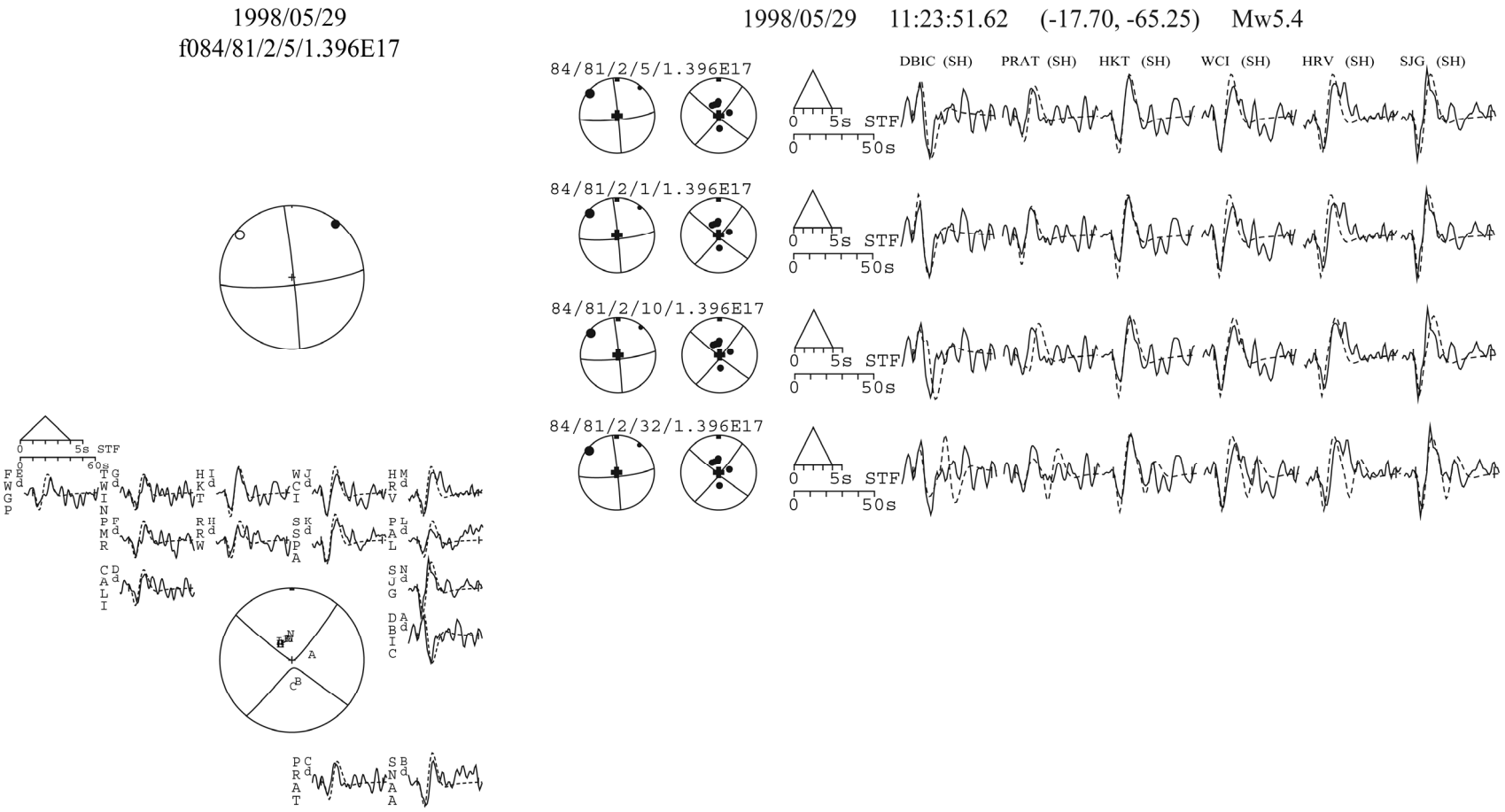

Figure A.18: MT5 waveform inversion solution plot for the 1998/05/29 earthquake. Focal mechanism was held fixed to that reported by the Global CMT catalog. Event depth was found to be 5 km.

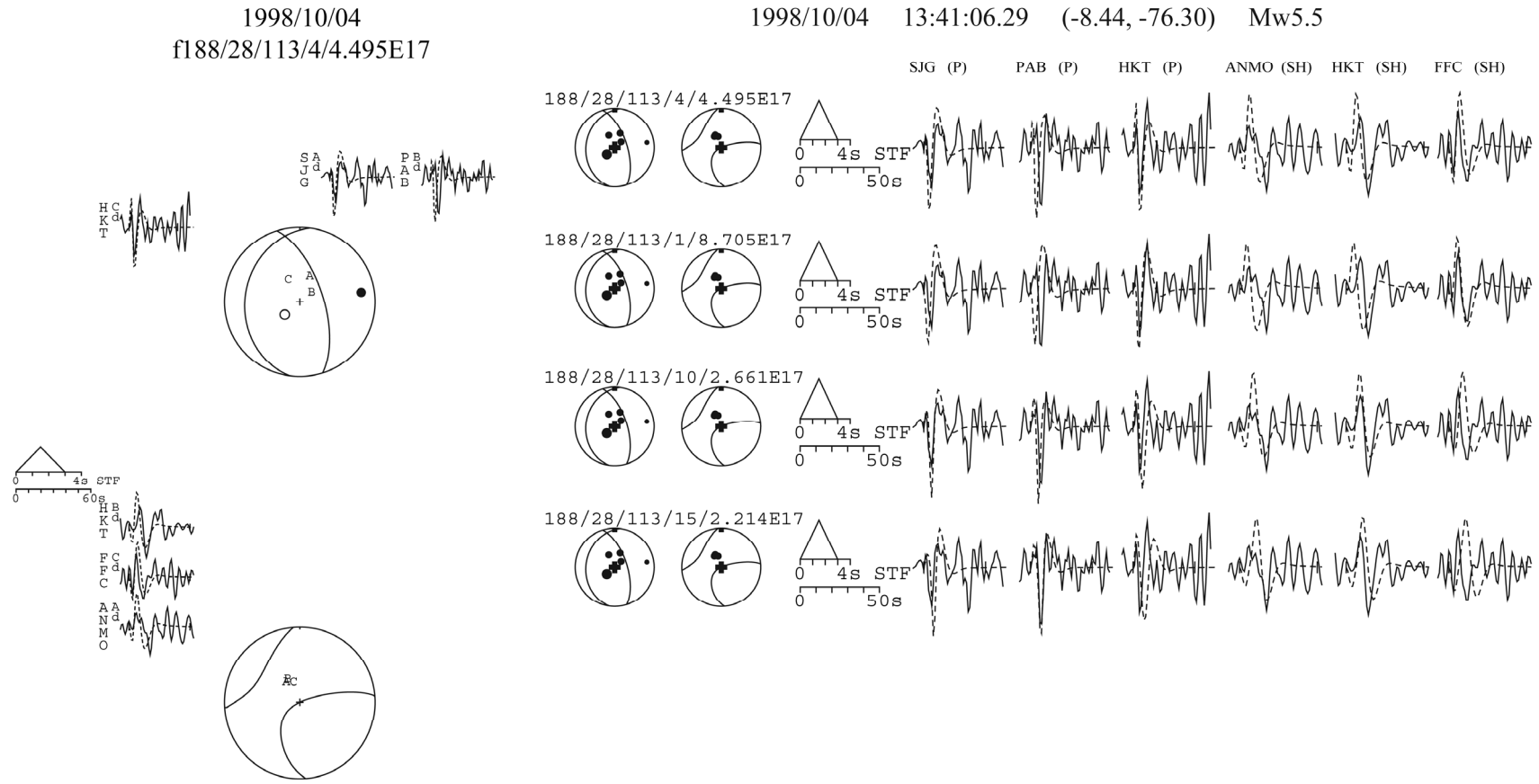

Figure A.19: MT5 waveform inversion solution plot for the 1998/10/04 earthquake. Focal mechanism was held fixed to that reported by the Global CMT catalog. Event depth was found to be 4 km.

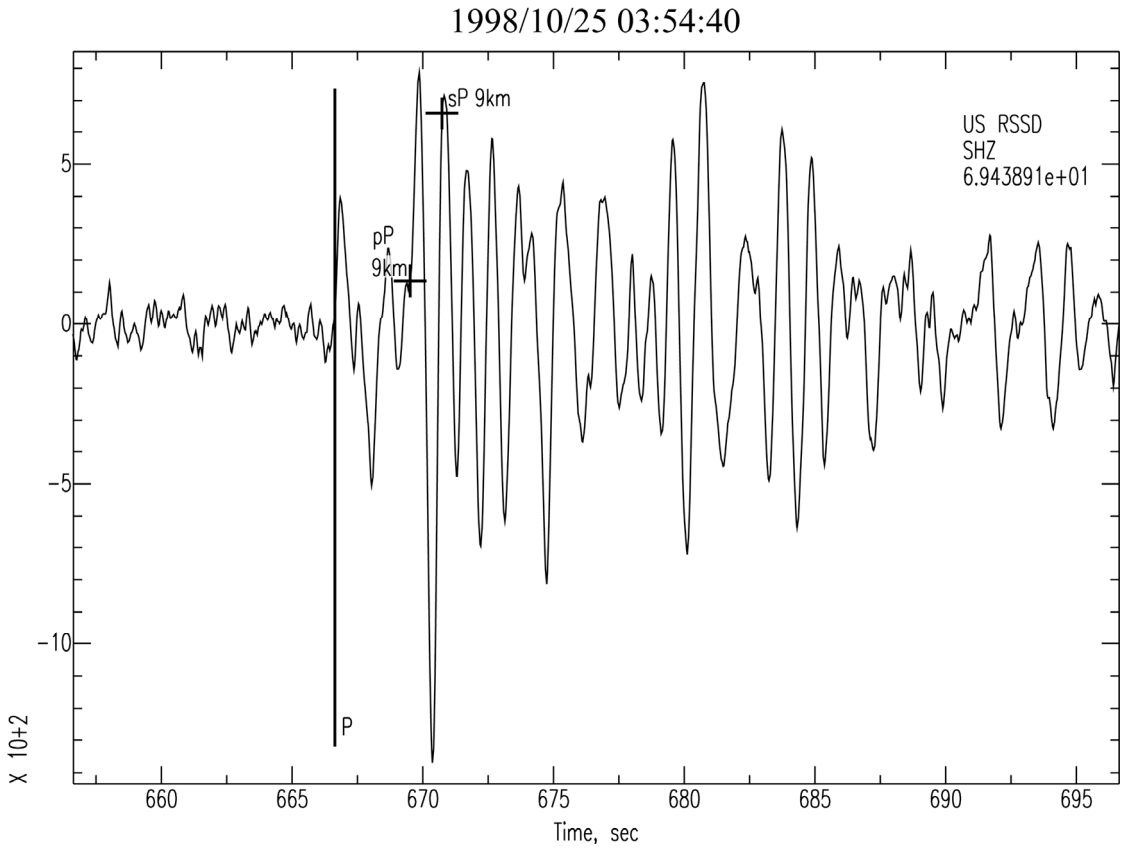

Figure A.20: SHZ analysis plot for the 1998/10/25 earthquake. Event depth was found to be 9 km.

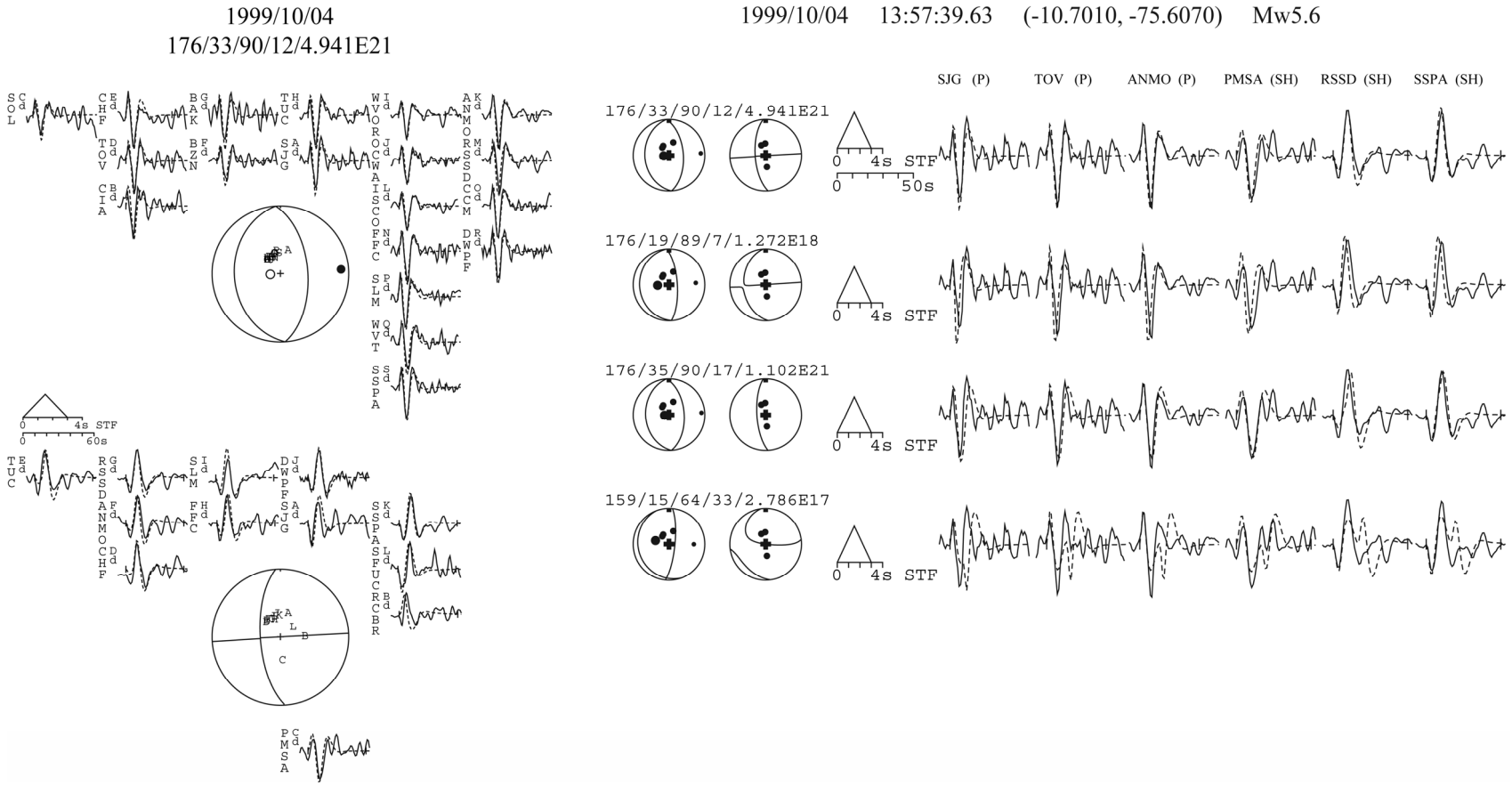

Figure A.21: MT5 waveform inversion solution plot for the 1999/10/04 earthquake. Minimum misfit solution: strike 176°, dip 33°, rake 90°, depth 12 km, and Mw 5.8.

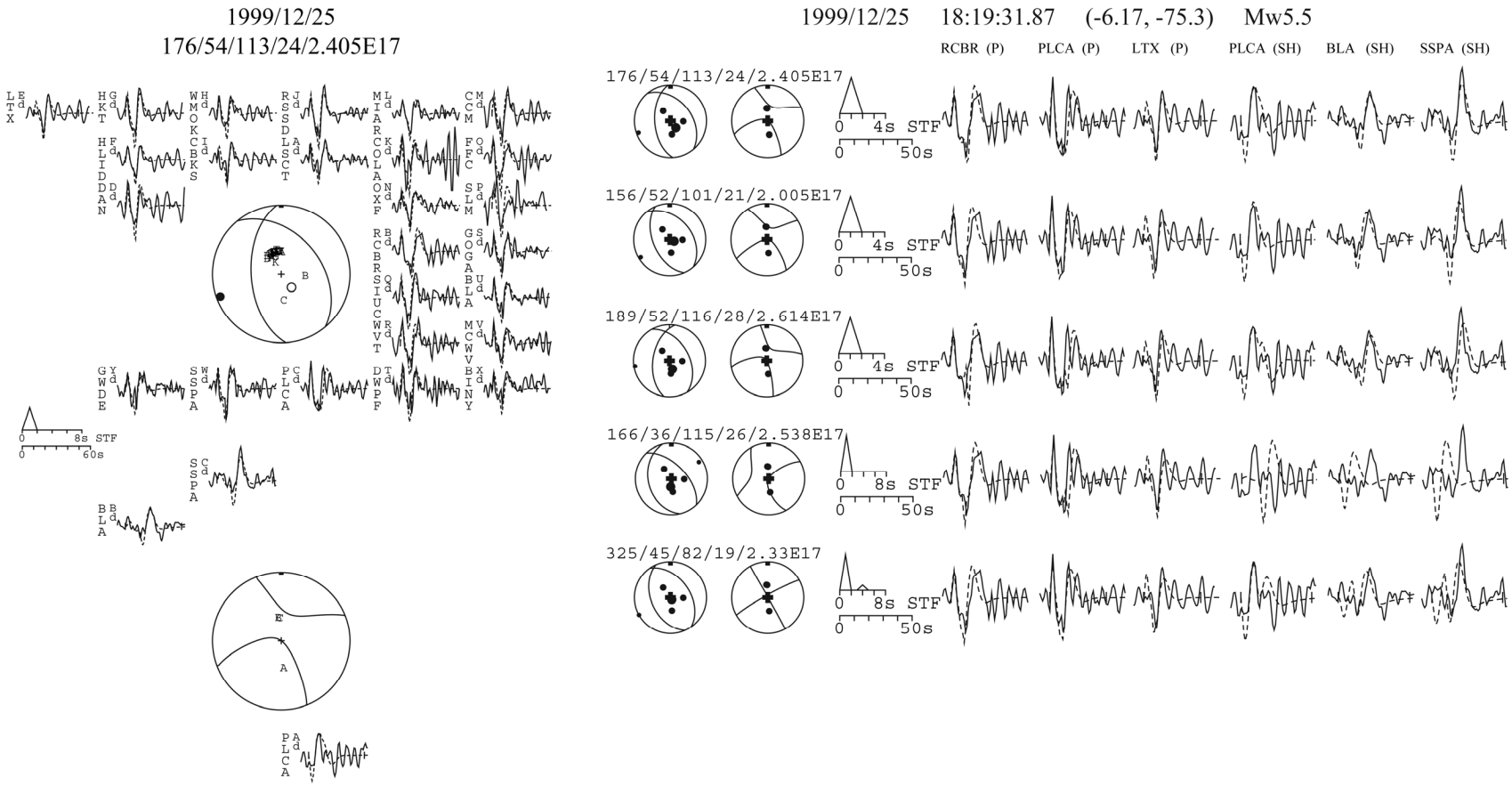

Figure A.22: MT5 waveform inversion solution plot for the 1999/12/25 earthquake. Minimum misfit solution: strike 176°, dip 54°, rake 113°, depth 24 km, and Mw 5.6.

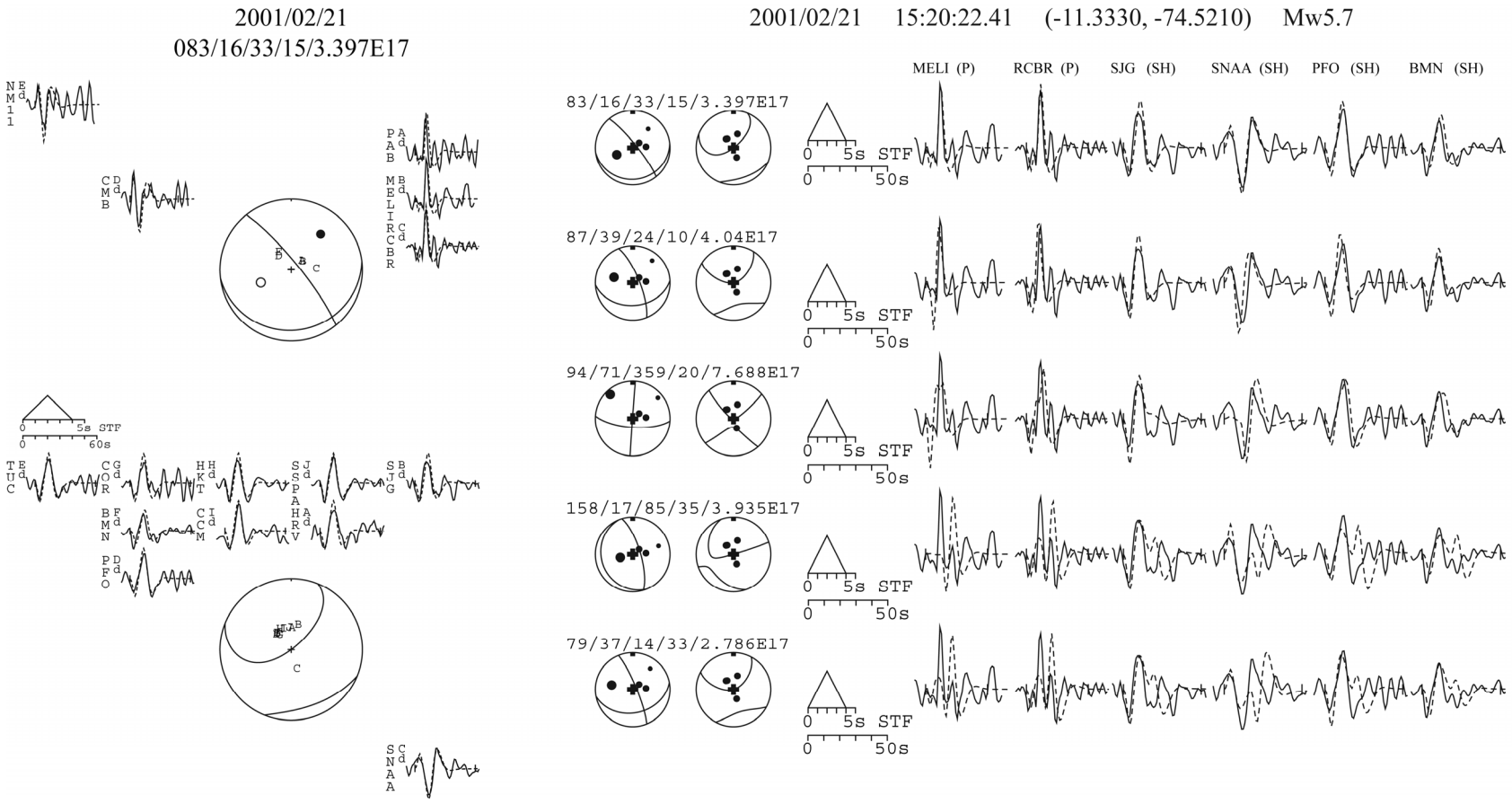

Figure A.23: MT5 waveform inversion solution plot for the 2001/02/21 earthquake. Minimum misfit solution: strike 083°, dip 16°, rake 33°, depth 15 km, and Mw 5.7.

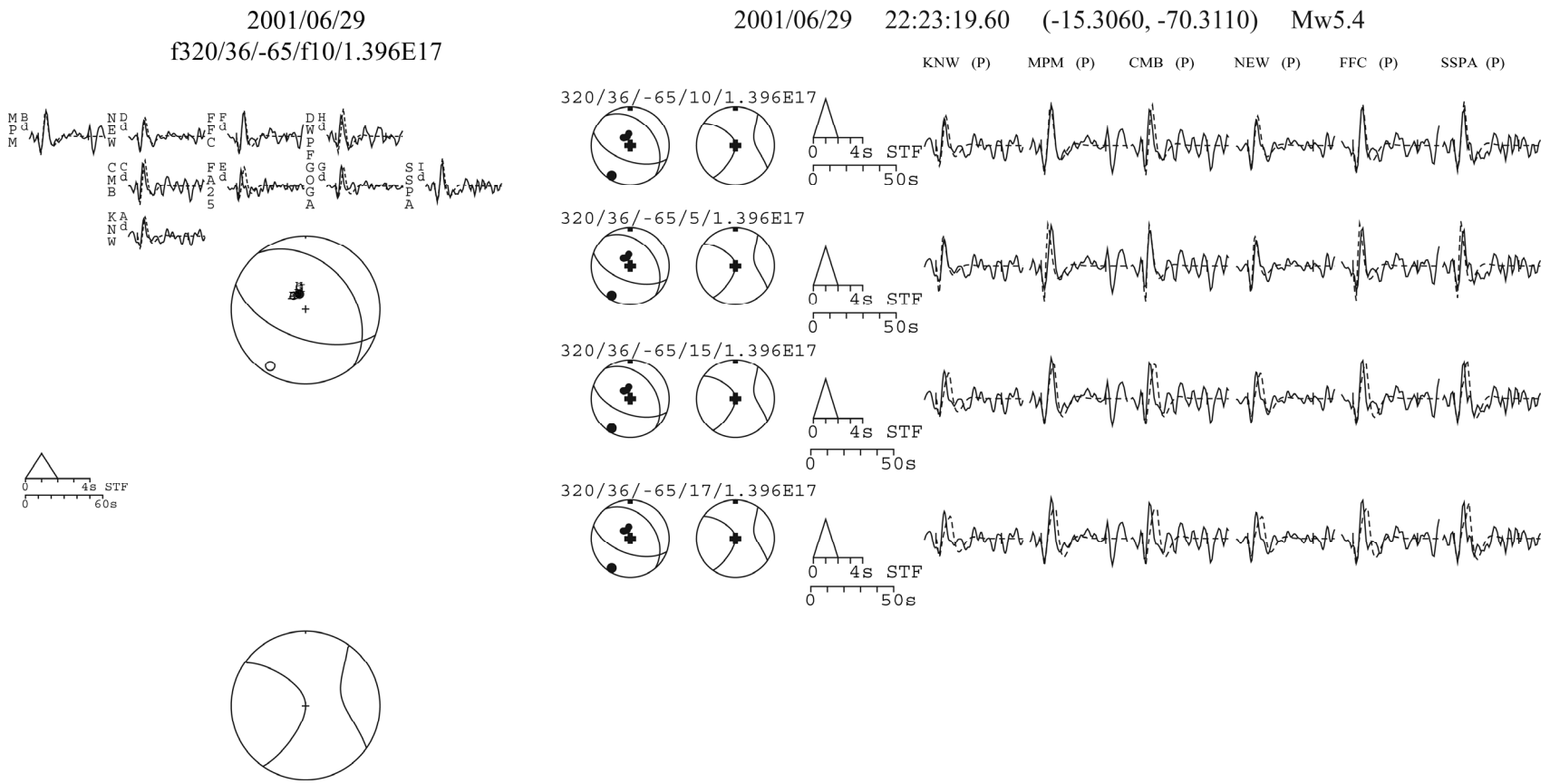

Figure A.24: MT5 waveform inversion solution plot for the 2001/06/29 earthquake. Focal mechanism was held fixed to that reported by the Global CMT catalog and the depth was held fixed by the SHZ analysis depth solution reported in Figure A.23 (10 km).

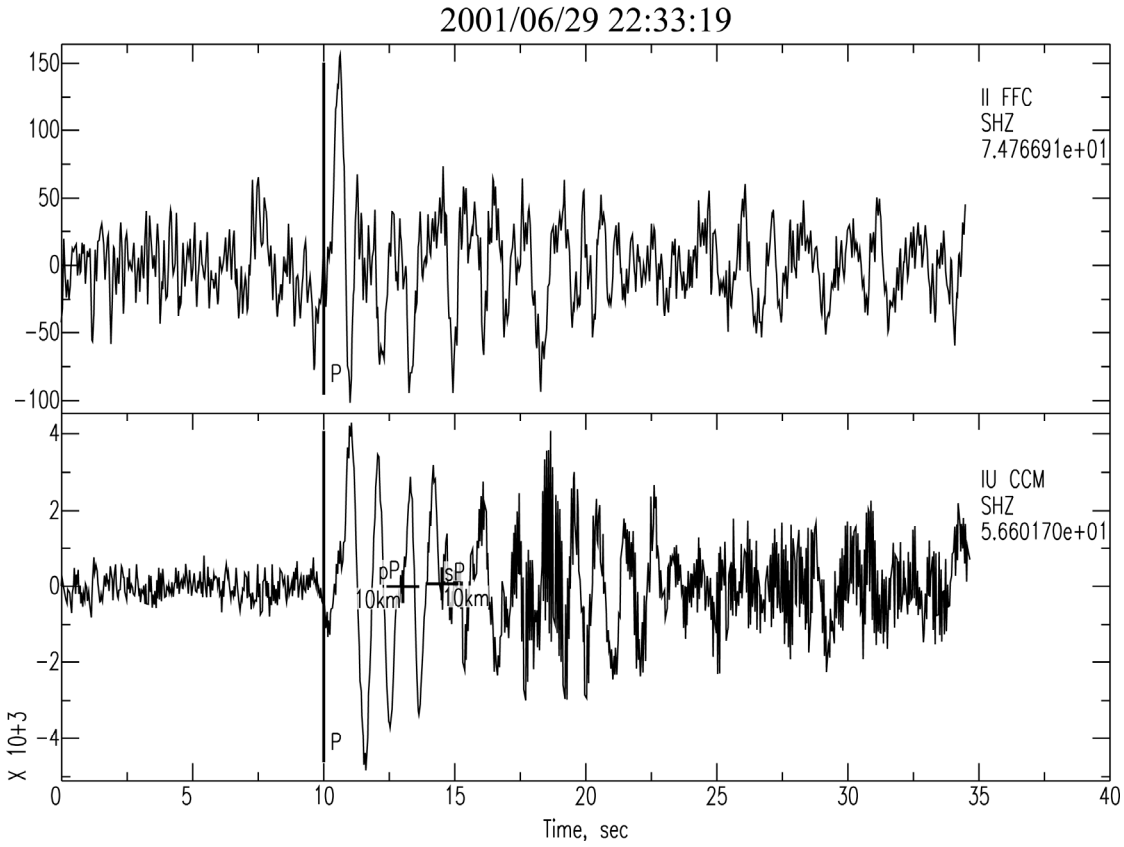

Figure A.25: SHZ analysis plot for the 2001/06/29 earthquake. Event depth was found to be 10 km. MT5 waveform inversion solution plot is shown in Figure A.22.

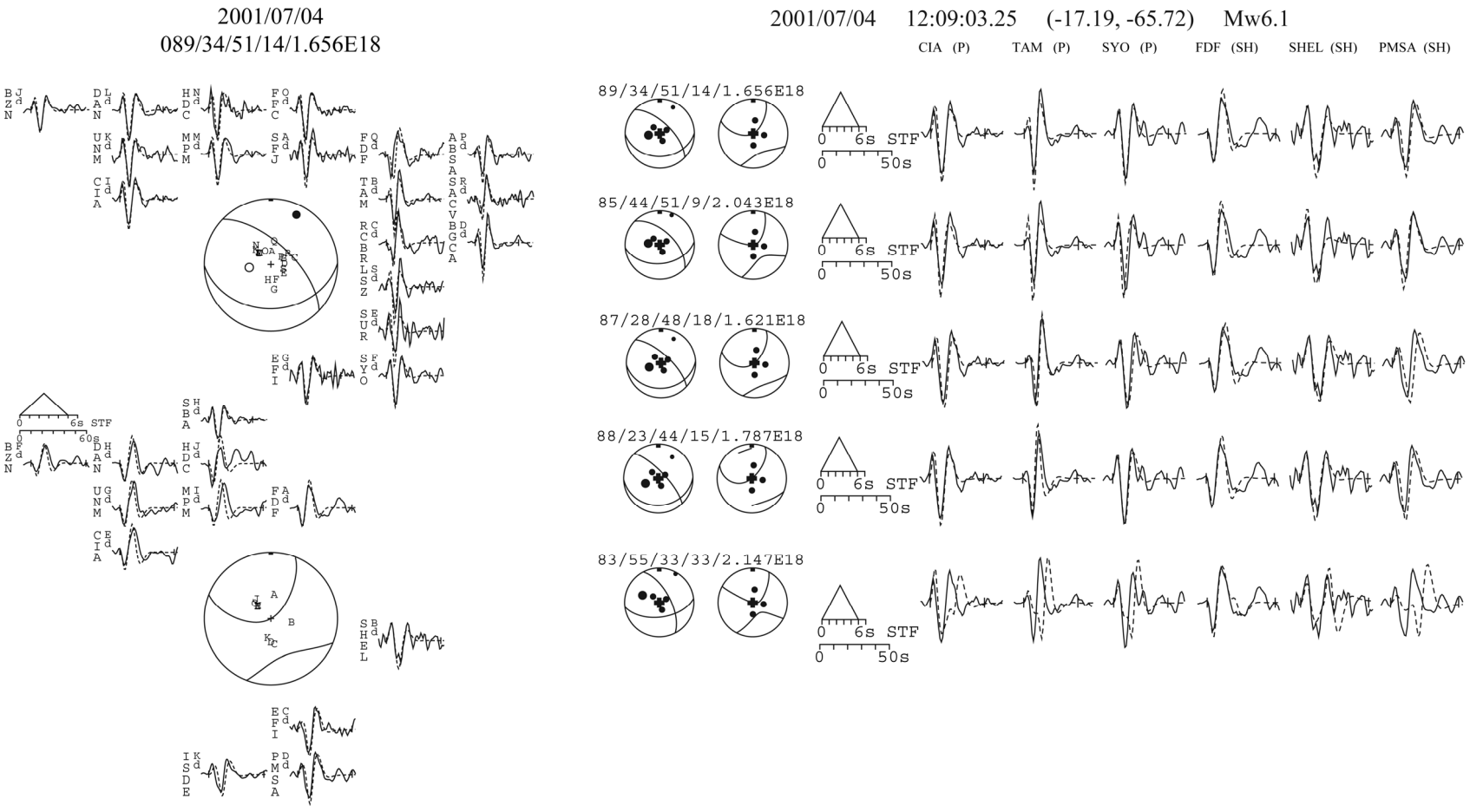

Figure A.26: MT5 waveform inversion solution plot for the 2001/07/04 earthquake. Minimum misfit solution: strike 089°, dip 34°, rake 51°, depth 14 km, and Mw 6.1.

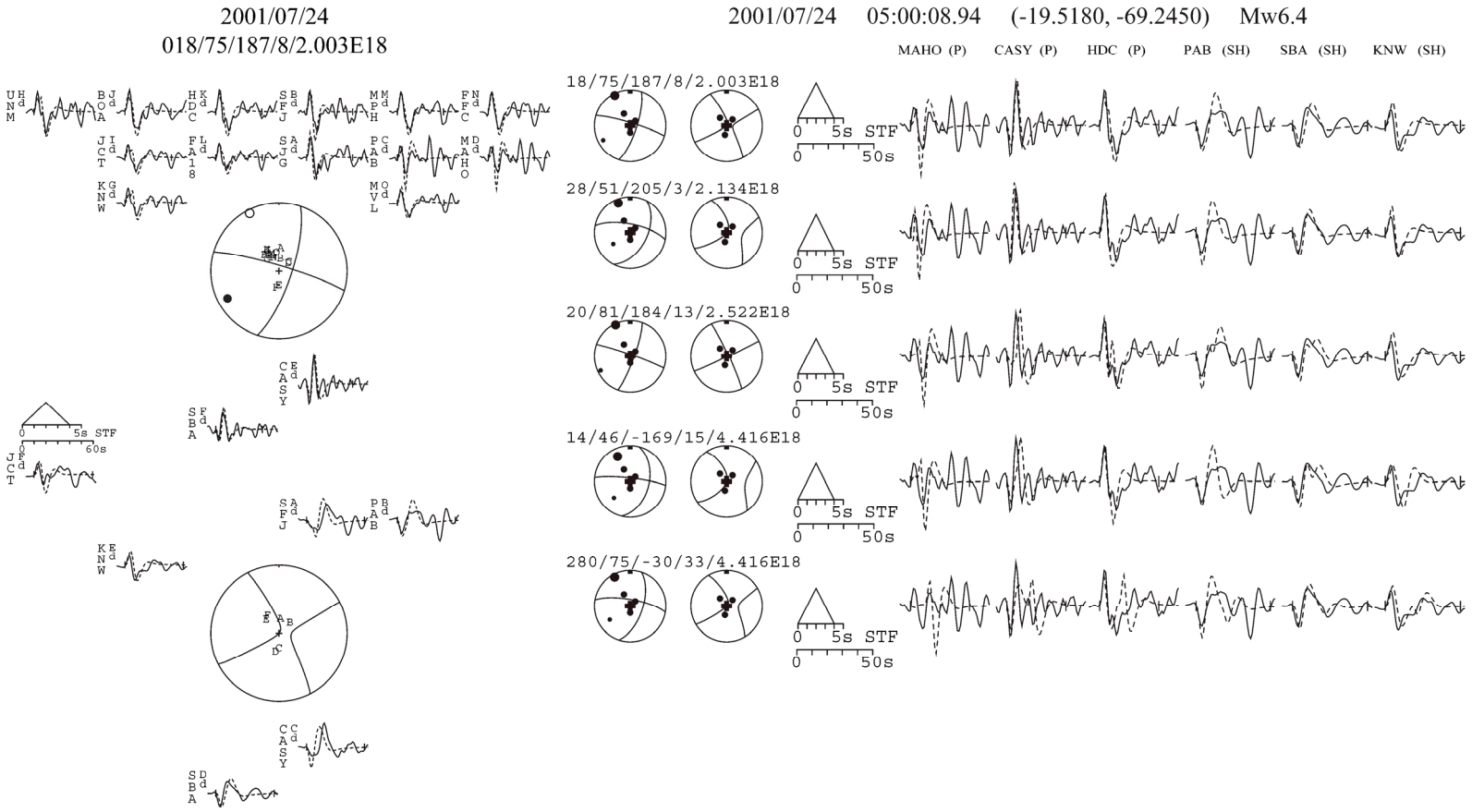

Figure A.27: MT5 waveform inversion solution plot for the 2001/07/24 earthquake. Minimum misfit solution: strike 018°, dip 75°, rake 187°, depth 8 km, and Mw 6.4. The depth determined from waveform inversion analysis is consistent with the depth found from SHZ analysis shown in Figure A.26. This figure is also shown as Figure 2.28.

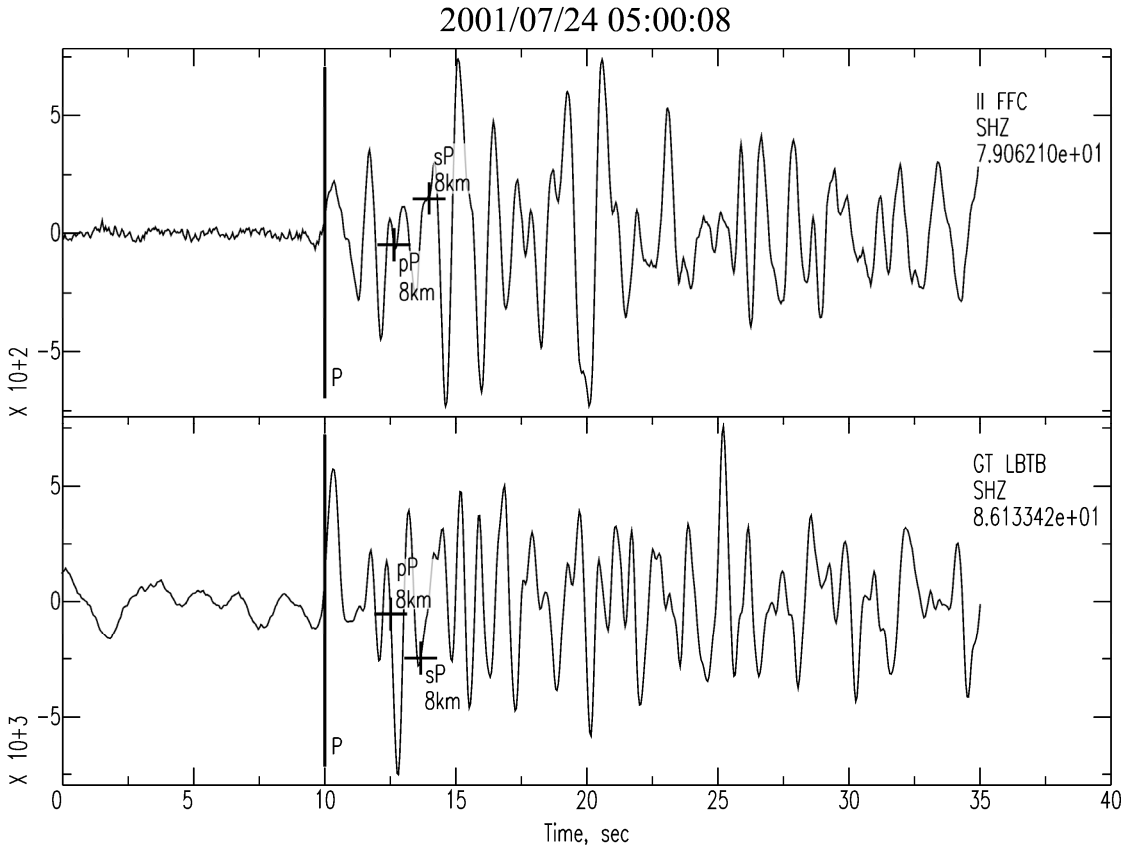

Figure A.28: SHZ analysis plot for the 2001/07/24 earthquake. Event depth was found to be 8 km. MT5 waveform inversion solution plot is shown in Figure A.25.

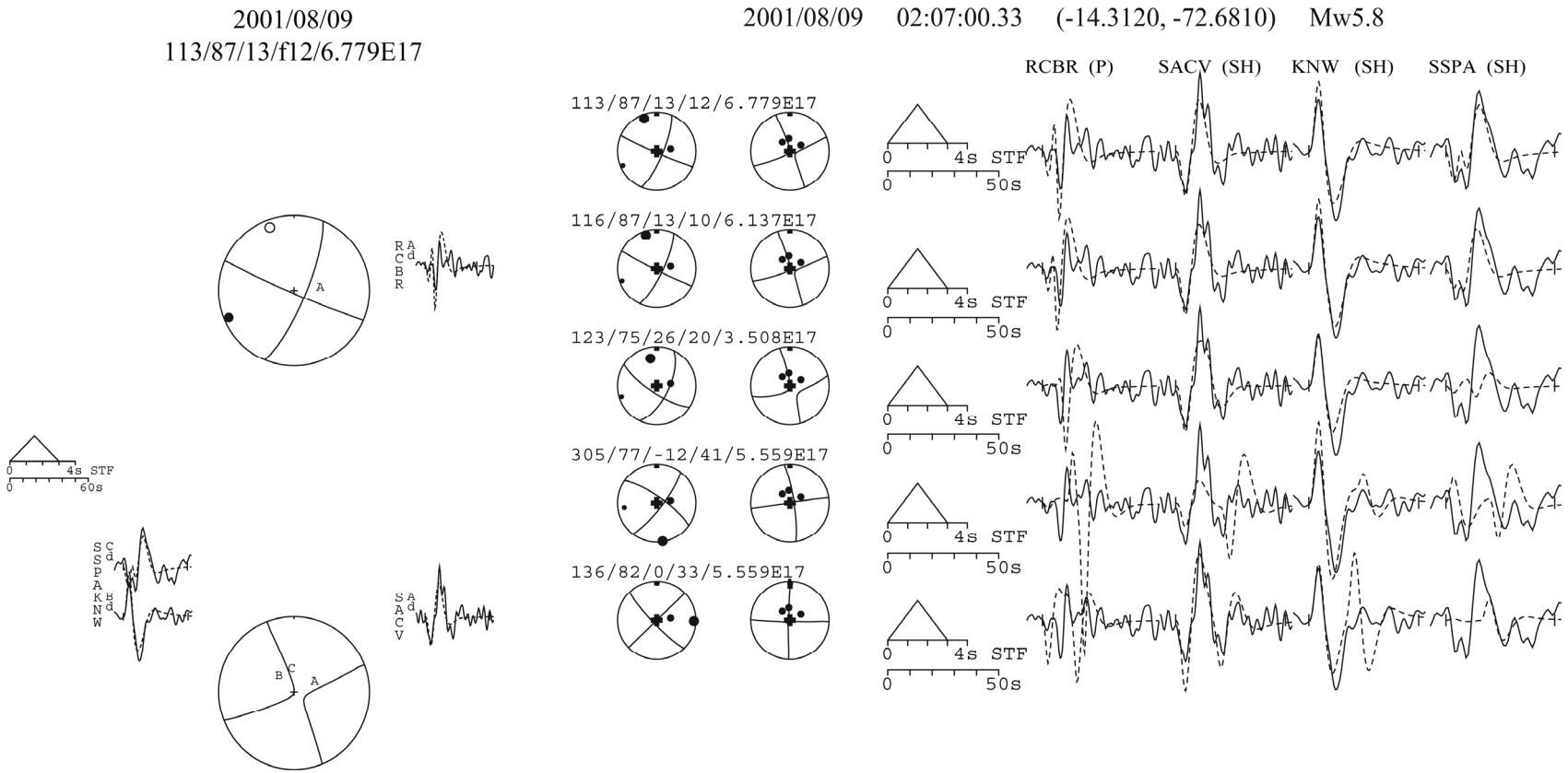

Figure A.29: MT5 waveform inversion solution plot for the 2001/08/09 earthquake. Minimum misfit solution: strike 113°, dip 87°, rake 13°, depth 12 km, and Mw 5.9. Event depth was held fixed by the SHZ analysis depth solution reported in Figure A.28 (12 km).

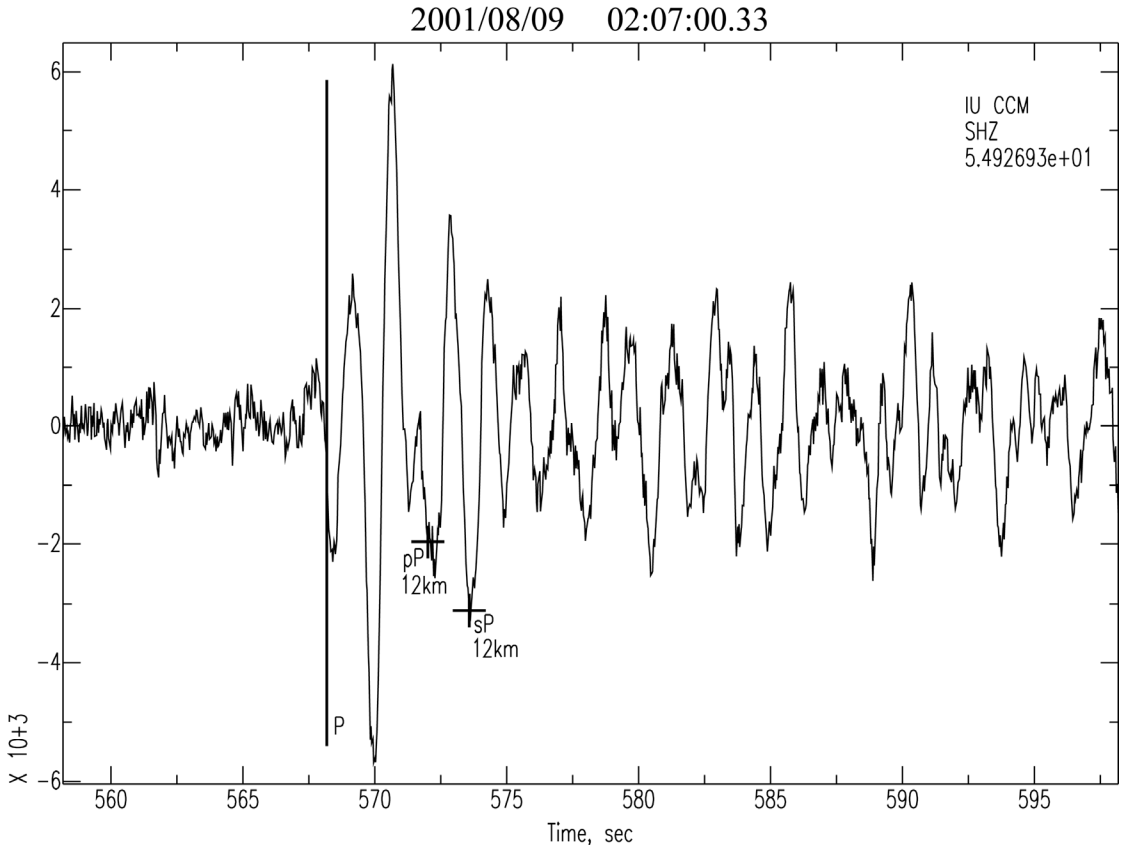

Figure A.30: SHZ analysis plot for the 2001/08/09 earthquake. Event depth was found to be 12 km. MT5 waveform inversion solution plot is shown in Figure A.27.

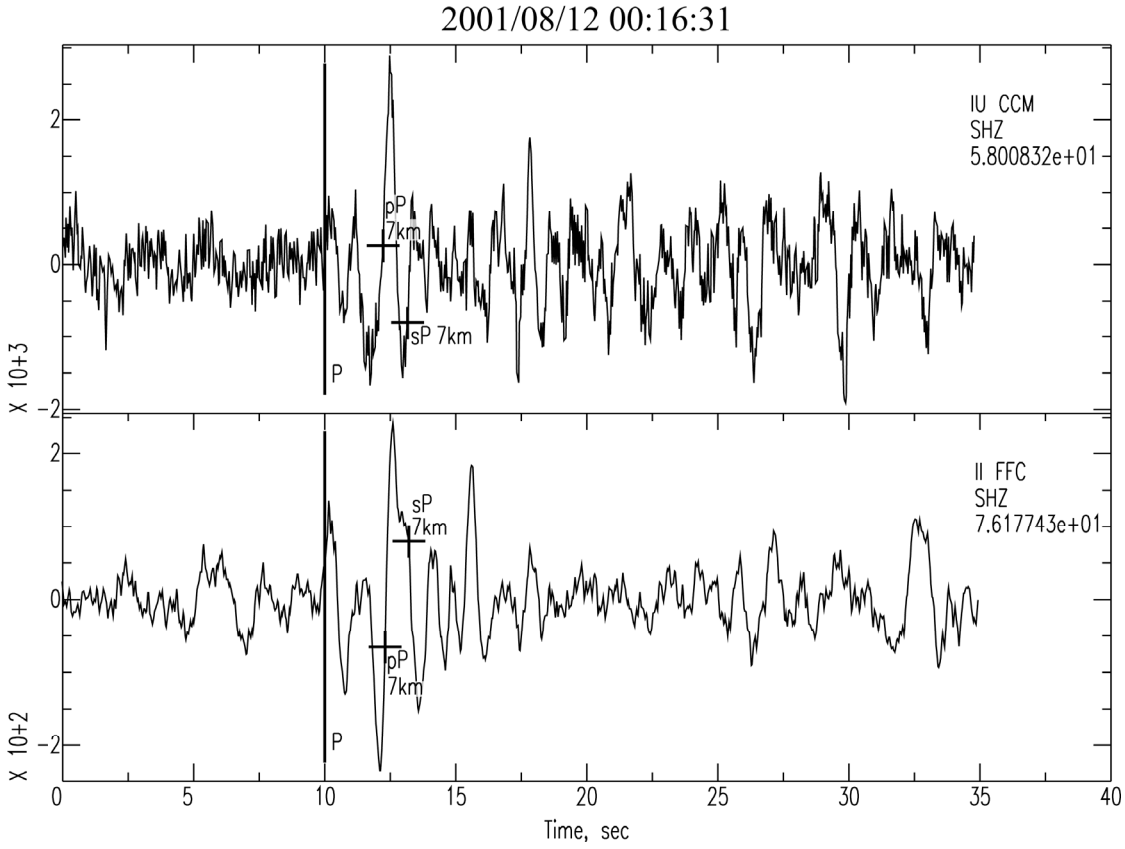

Figure A.31: SHZ analysis plot for the 2001/08/12 earthquake. Event depth was found to be 7 km.

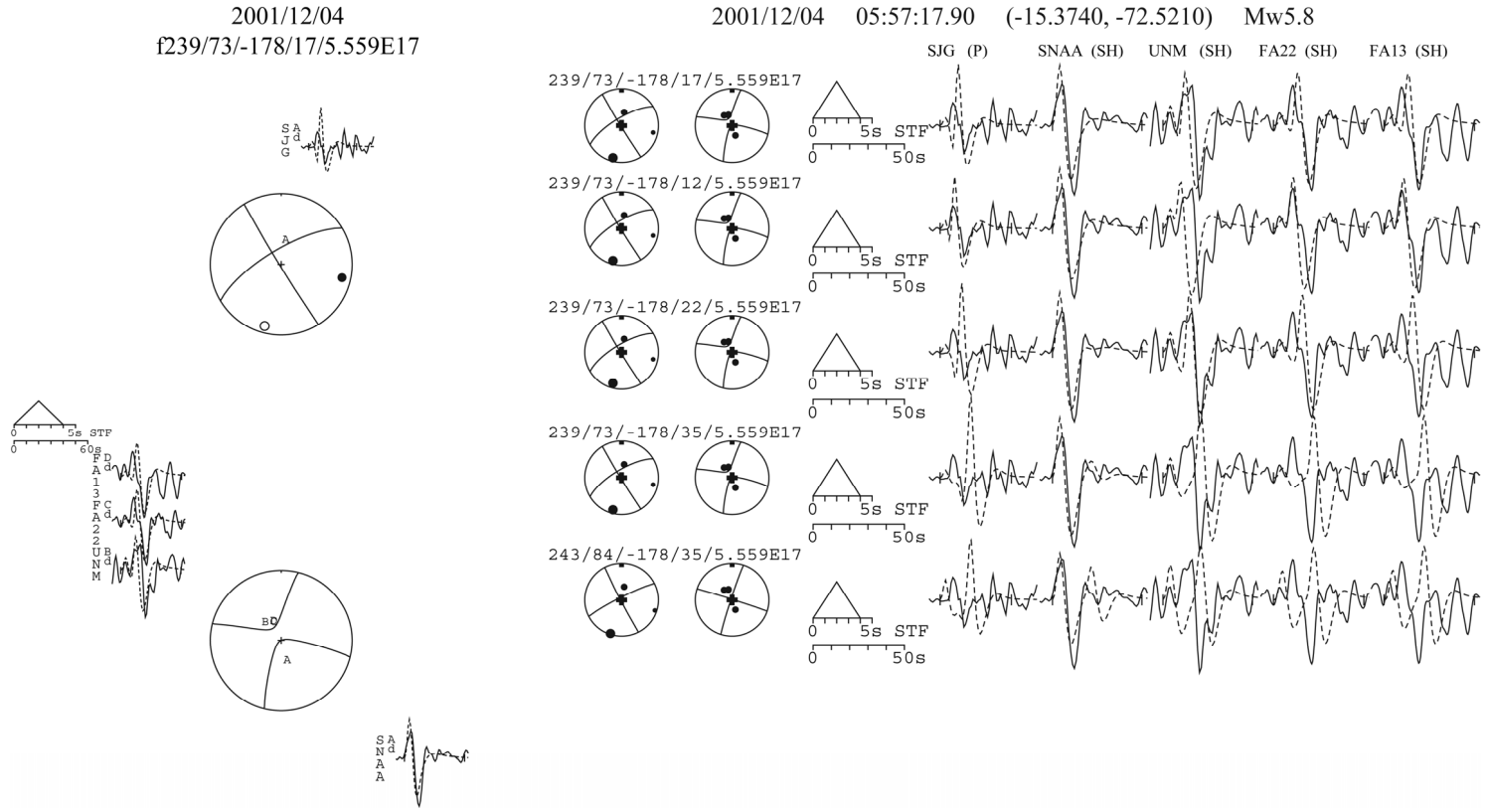

Figure A.32: MT5 waveform inversion solution plot for the 2001/12/04 earthquake. Focal mechanism was held fixed to that reported by the Global CMT catalog and the depth was held fixed by the SHZ analysis depth solution reported in Figure A.31 (17 km).

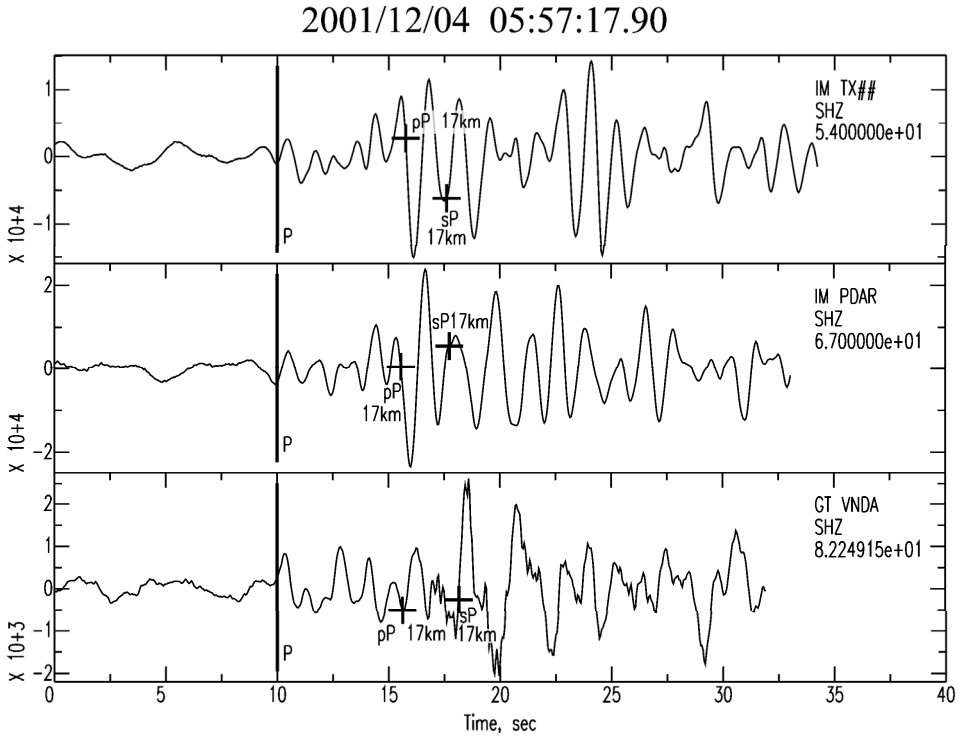

Figure A.33: SHZ analysis plot for the 2001/12/04 earthquake. Event depth was found to be 17 km. MT5 waveform inversion solution plot is shown in Figure A.30. IM TX## waveform is a waveform stack of records reported by the Lajitas Array in Texas, USA. IM PDAR waveform is a waveform stack of records reported by the PDAR seismic array in Wyoming, USA.

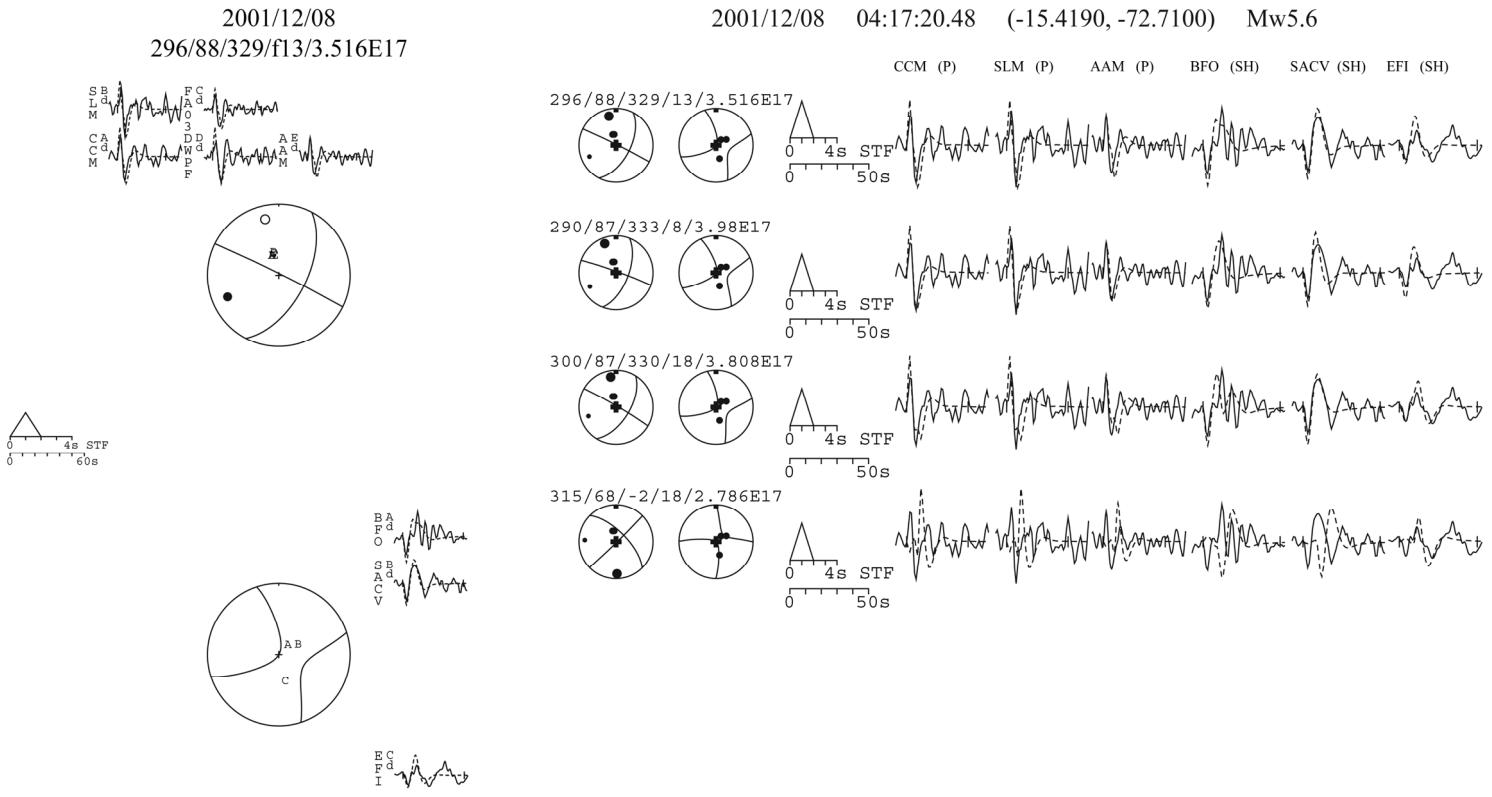

Figure A.34: MT5 waveform inversion solution plot for the 2001/12/08 earthquake. Minimum misfit solution: strike 296°, dip 88°, rake 329°, depth 13 km, and Mw 5.7. Event depth was held fixed by the SHZ analysis depth solution reported in Figure A.33 (13 km).

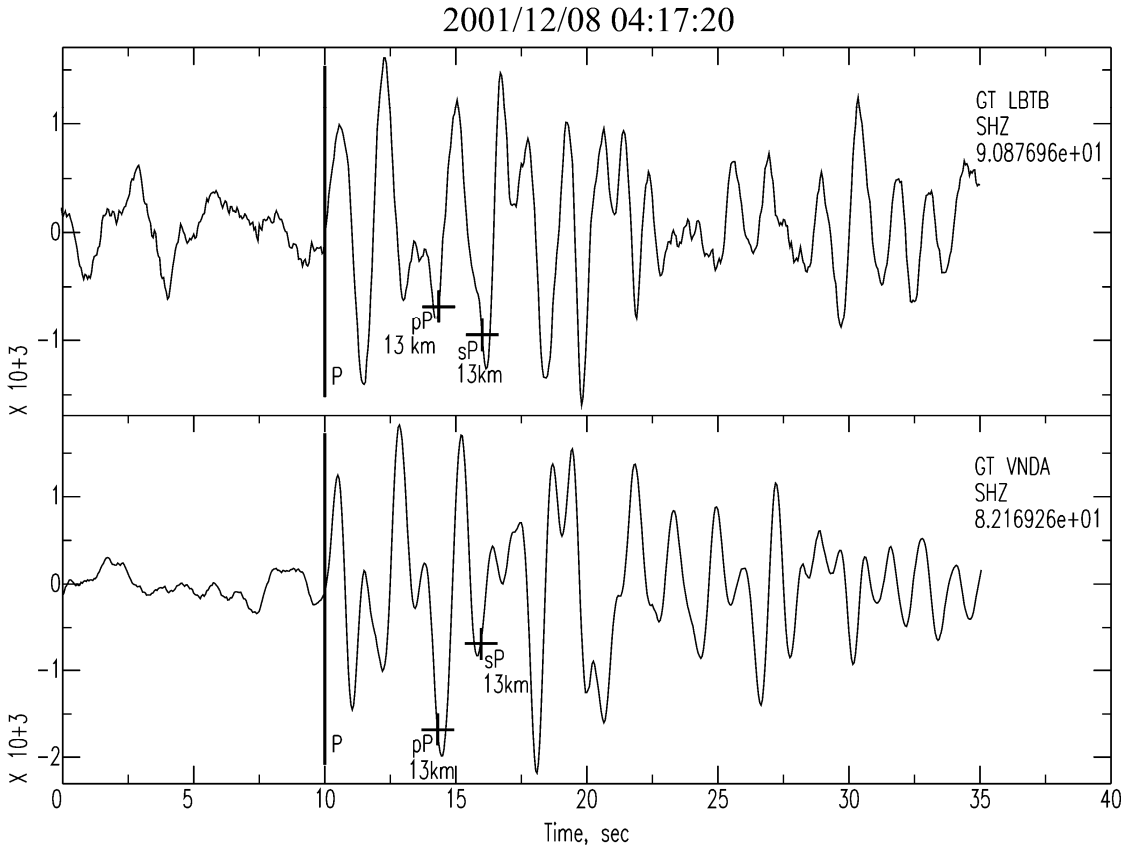

Figure A.35: SHZ analysis plot for the 2001/12/08 earthquake. Event depth was found to be 13 km. MT5 waveform inversion solution plot is shown in Figure A.32.

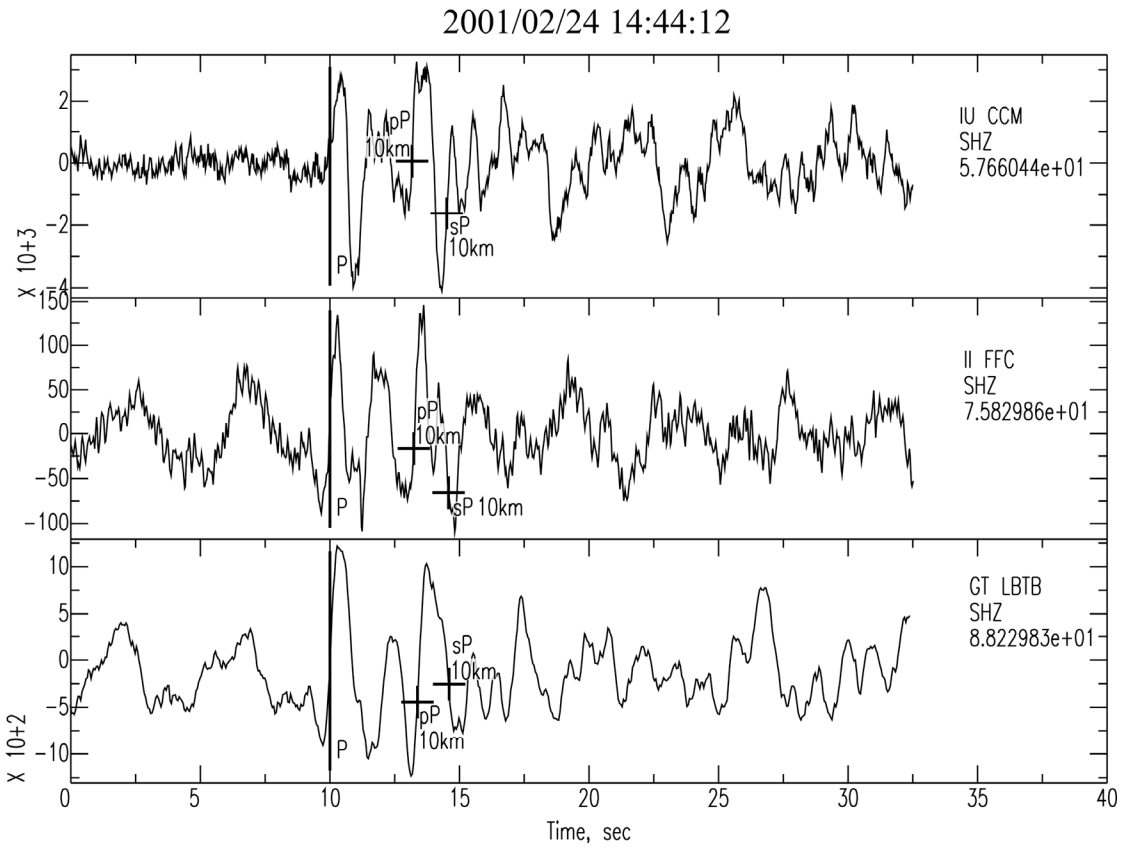

Figure A.36: SHZ analysis plot for the 2001/02/24 earthquake. Event depth was found to be 10 km.

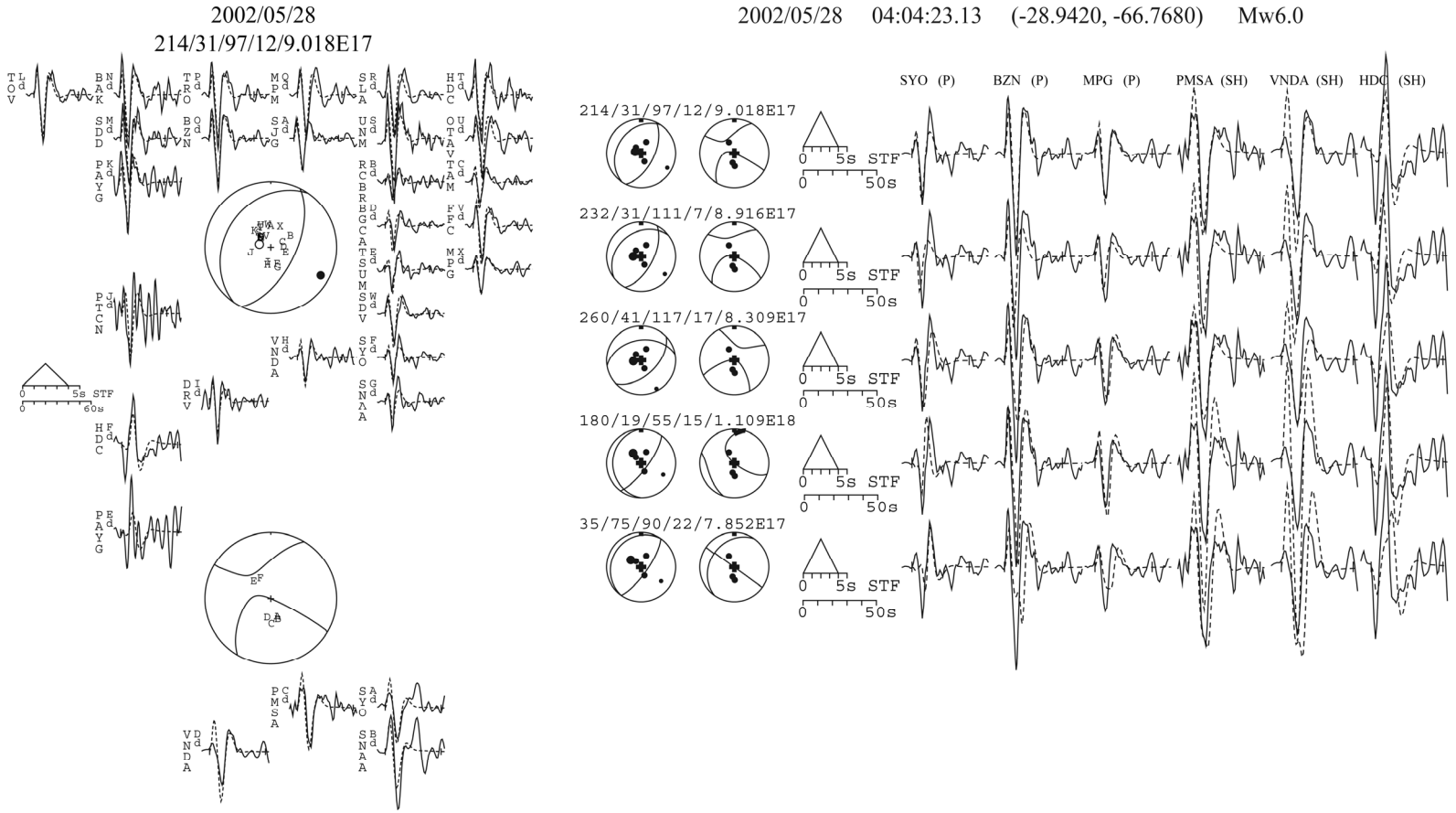

Figure A.37: MT5 waveform inversion solution plot for the 2002/05/28 earthquake. Minimum misfit solution: strike 214°, dip 31°, rake 97°, depth 12 km, and Mw 6.0.

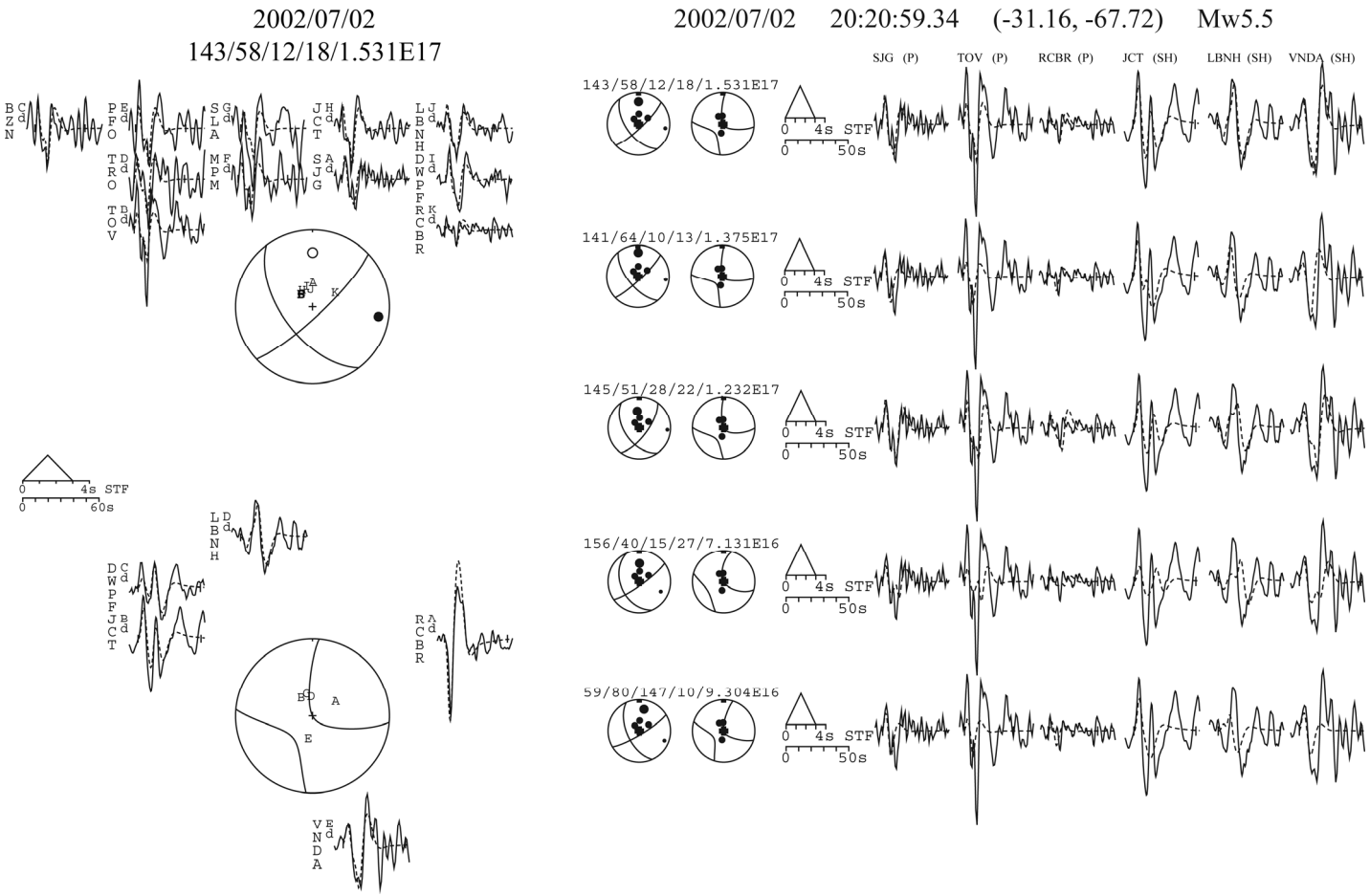

Figure A.38: MT5 waveform inversion solution plot for the 2002/07/02 earthquake. Minimum misfit solution: strike 143°, dip 58°, rake 12°, depth 18 km, and Mw 5.4.

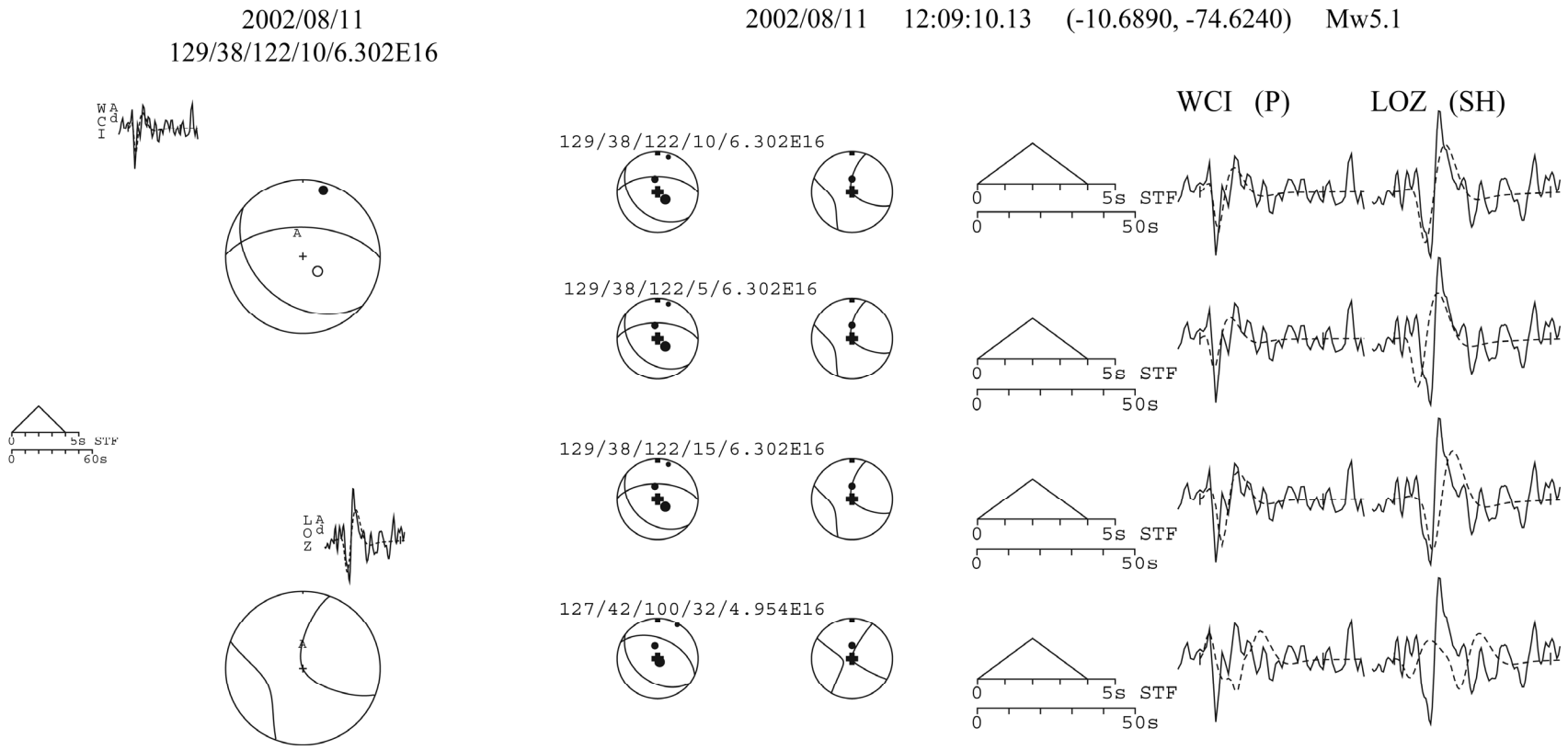

Figure A.39: MT5 waveform inversion solution plot for the 2002/08/11 earthquake. Minimum misfit solution: strike 129°, dip 38°, rake 122°, depth 10 km, and Mw 5.2.

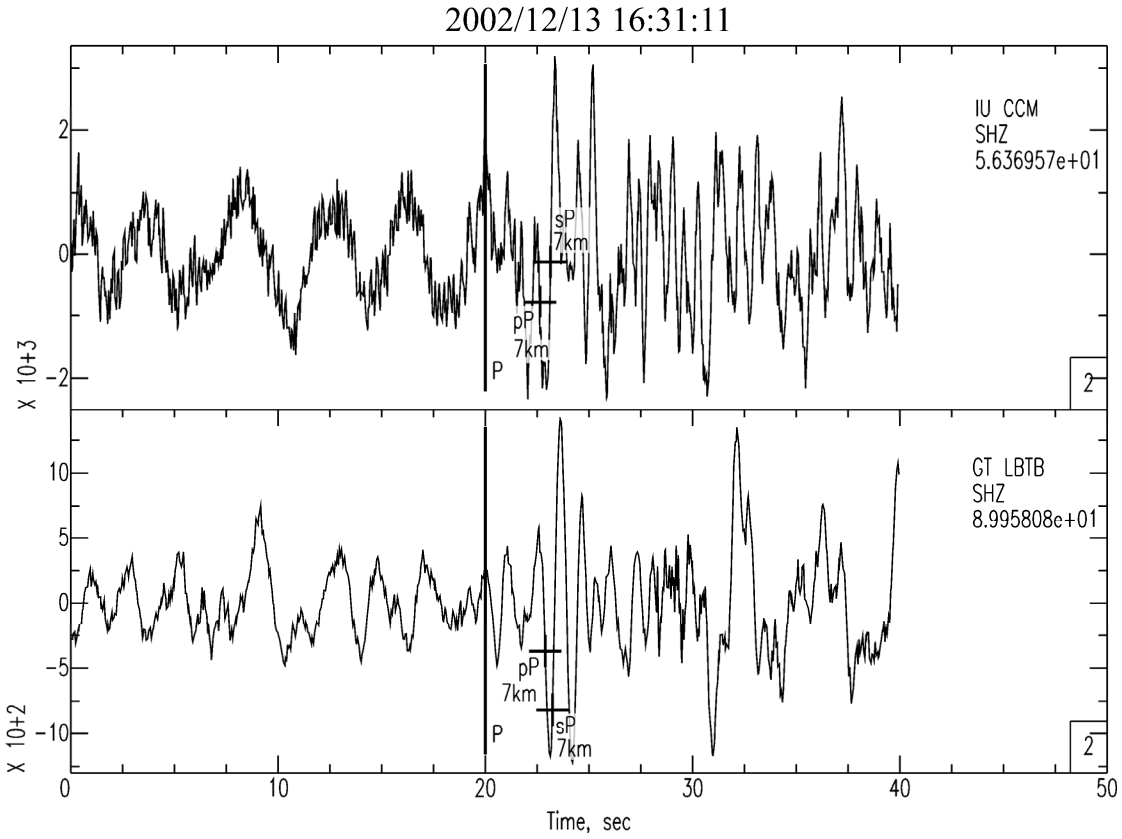

Figure A.40: SHZ analysis plot for the 2002/12/13 earthquake. Event depth was found to be 7 km.

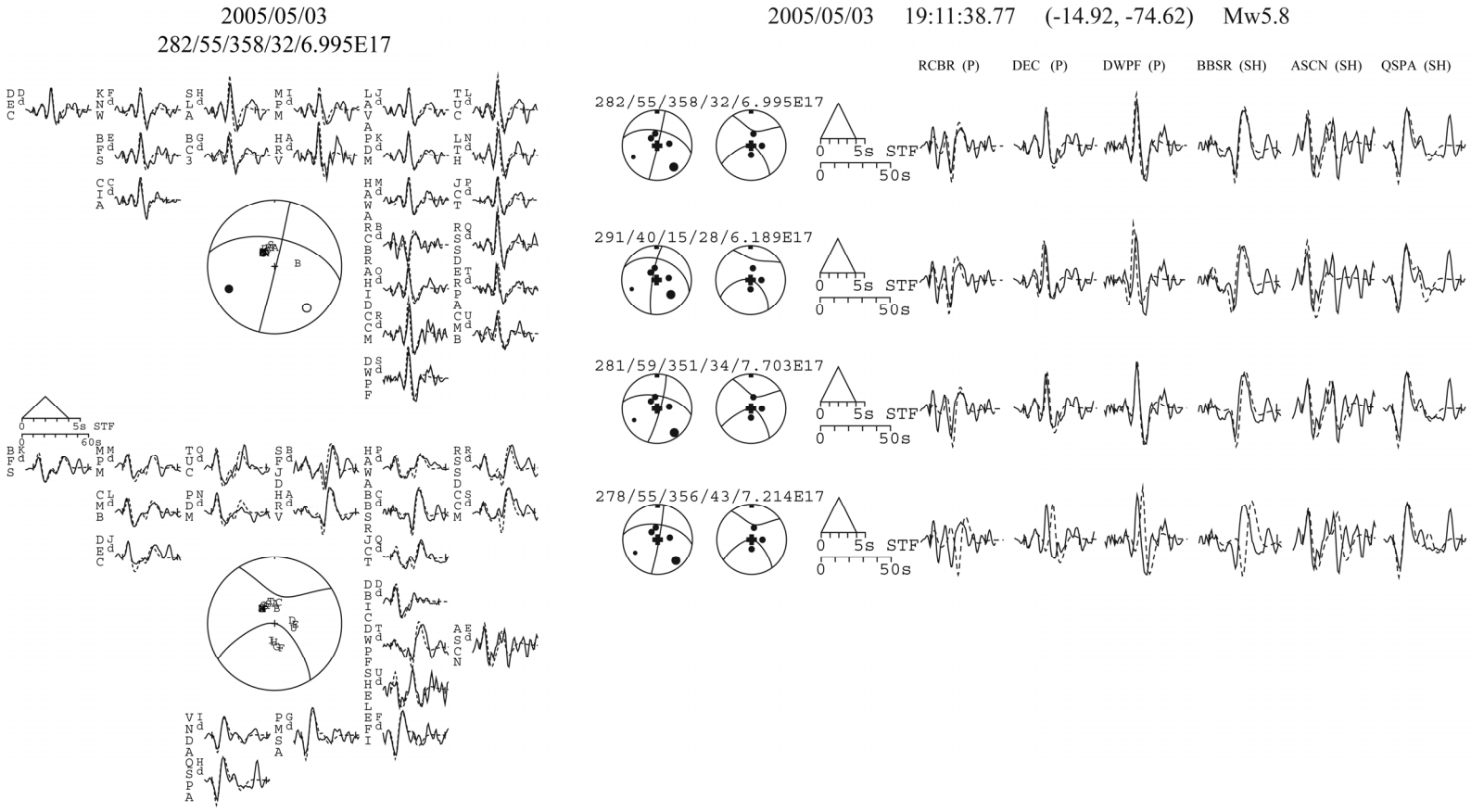

Figure A.41: MT5 waveform inversion solution plot for the 2005/05/03 earthquake. Minimum misfit solution: strike 282°, dip 55°, rake 358°, depth 32 km, and Mw 5.9.

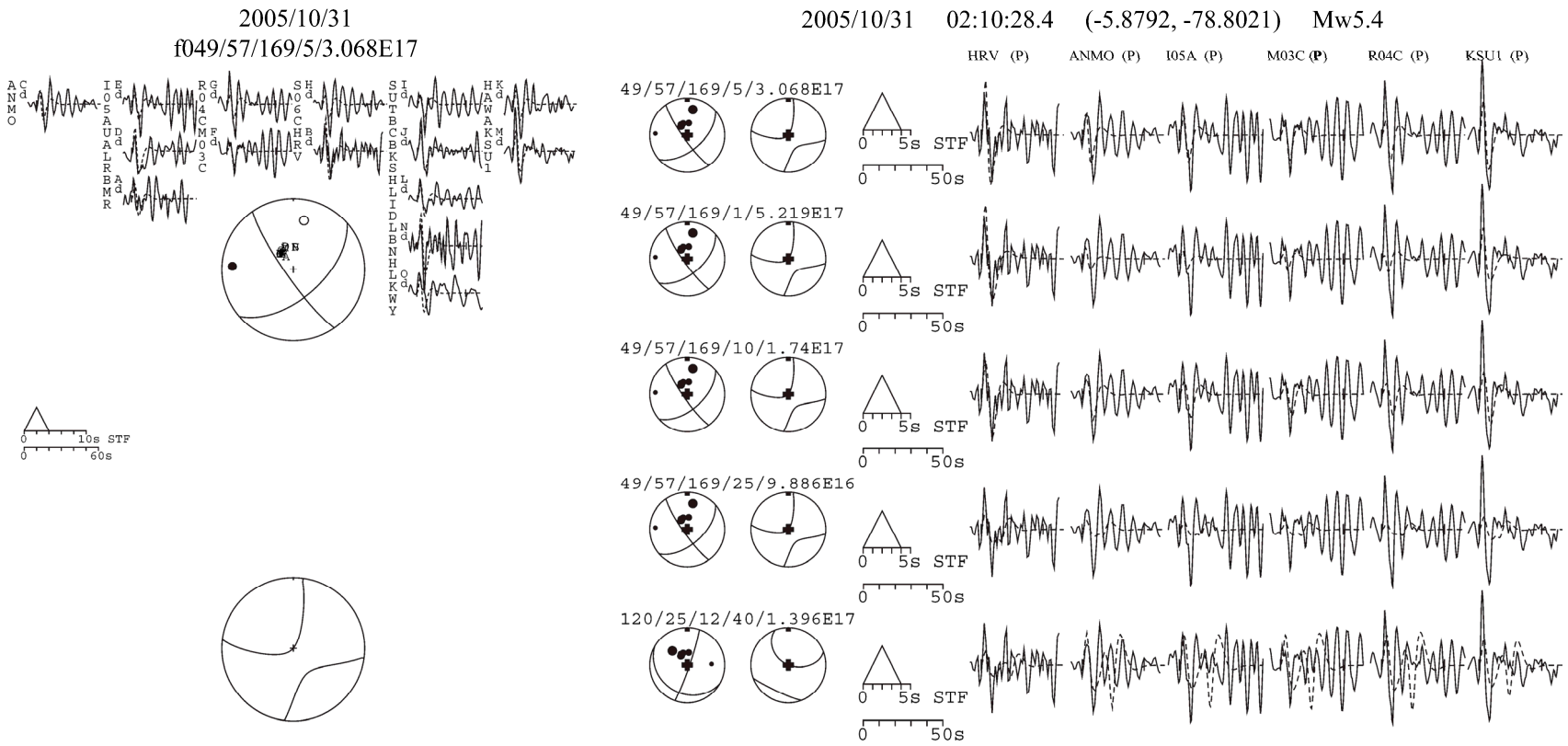

Figure A.42: MT5 waveform inversion solution plot for the 2005/10/31 earthquake. Focal mechanism was held fixed to that reported by the Global CMT catalog. Minimum misfit depth solution: 5 km.

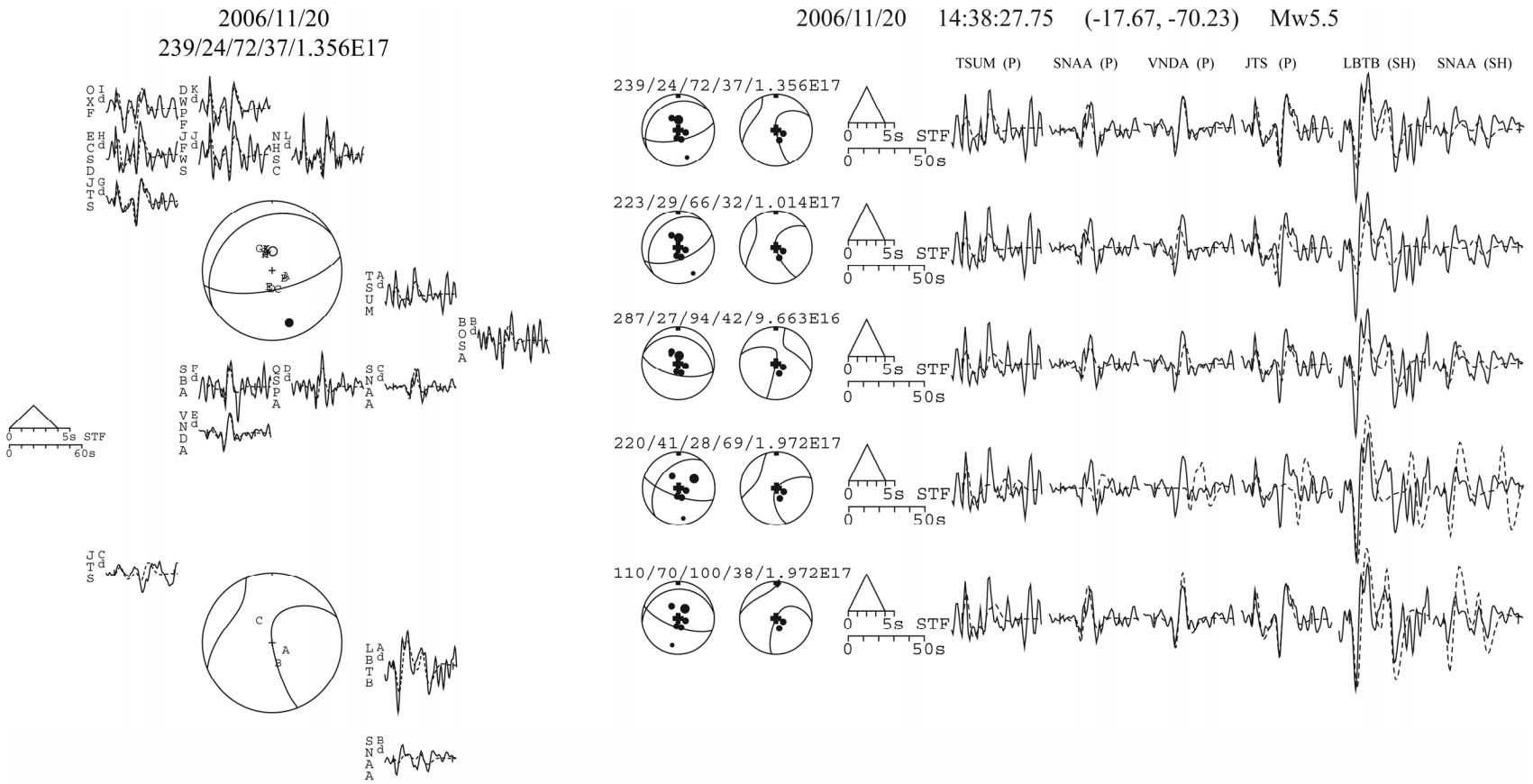

Figure A.43: MT5 waveform inversion solution plot for the 2006/11/20 earthquake. Minimum misfit solution: strike 239°, dip 24°, rake 72°, depth 37 km, and Mw 5.4.

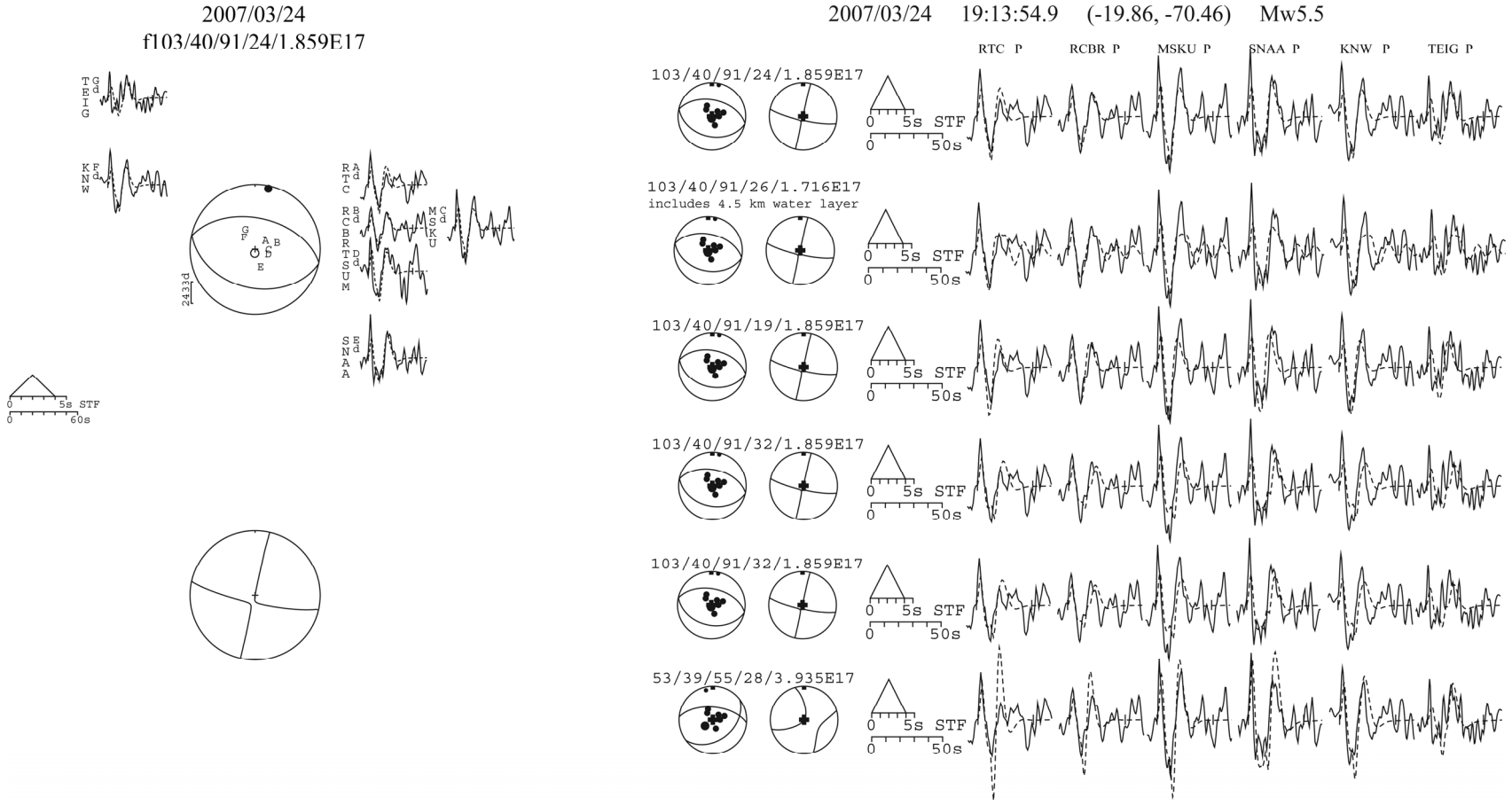

Figure A.44: MT5 waveform inversion solution plot for the 2007/03/24 earthquake. Focal mechanism was held fixed to that reported by the Global CMT catalog. Minimum misfit depth solution: 24 km.

APPENDIX B

EARTHQUAKES IN THE LOWER CONTINENTAL CRUST: T_S AND CRUSTAL THICKNESS

This section reviews the different areas that exhibit earthquakes in the lower continental crust. Each area is described with respect to its regional patterns in T_S and crustal thickness. The seismicity data is limited to earthquakes with depth uncertainties of ± 5 km or better. We consider an area to be experiencing earthquakes in the lower continental crust when T_S reaches to near-Moho depth (i.e., Moho depth minus $T_S \lesssim 10$ km). The areas discussed are summarized in Figure B.1 (Figure 3.2 in the main chapter text) and that figure displays the order in which the areas are discussed in this section with the exception for the Argentine and Peruvian Foreland, which are discussed together. Each section contains a map figure illustrating regional distribution of continental seismicity. Each map contains a topographic base map with earthquake locations shown as colored circles and are color-coded for depth. Yellow events occur in the upper crust, orange events occur in the middle crust, and red events occur in the lower continental crust. Depths intervals of the upper, middle, and lower crust vary between geographic locations depending on crustal thickness. Exact depth intervals are described with the legend of each figure. When focal mechanisms were available, each lower crustal earthquake is accompanied by its best fit focal mechanism solution with dark quadrants indicating compressional motions.

Alpine Foreland and Rhine Graben

Seismicity in the Alpine Foreland (i.e., Molasse Basin, Jura Mountains, etc.) and the Rhine Graben region occur throughout the continental crust, which is contrary to the

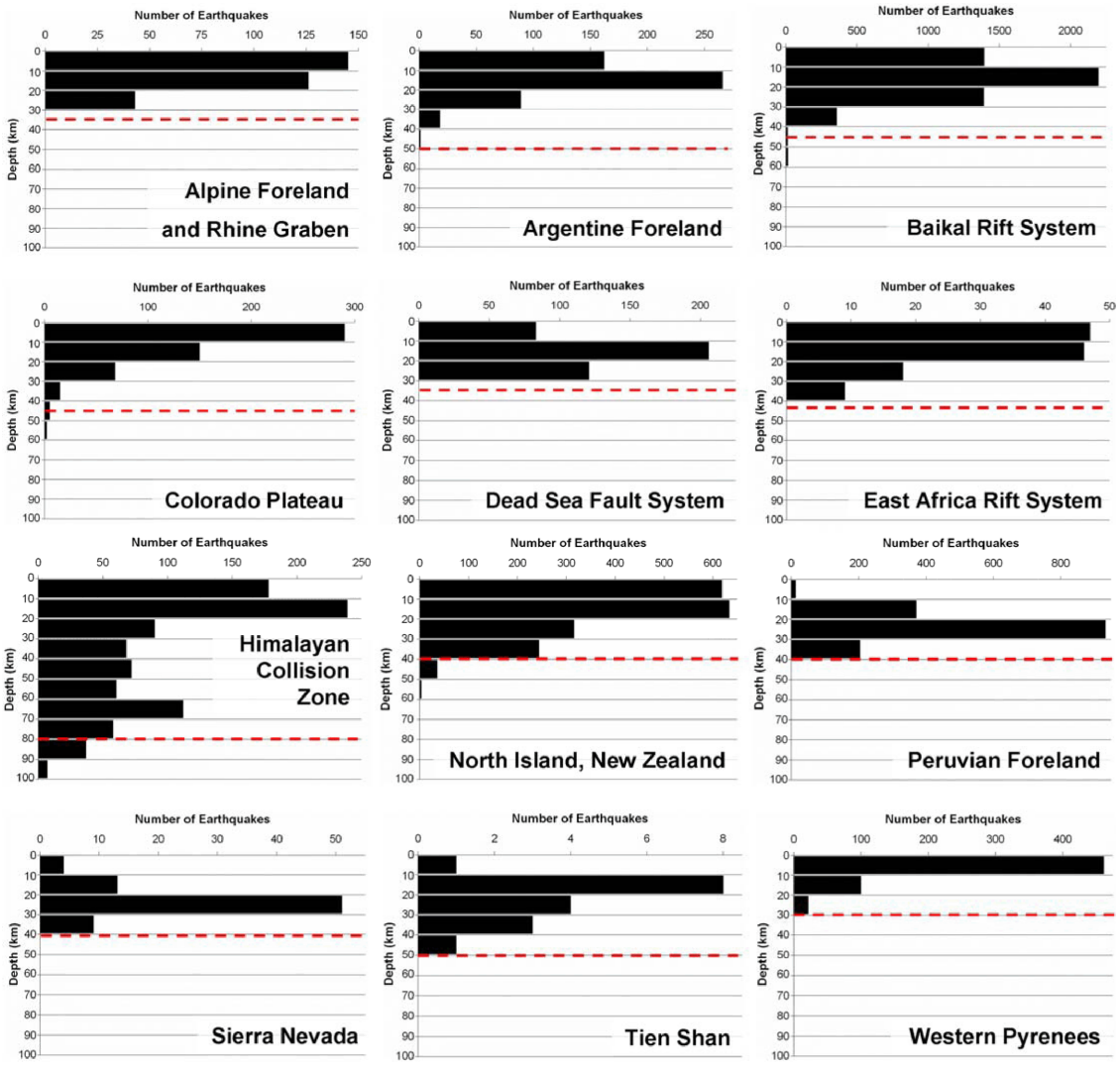

Figure B.1: Earthquake depth histograms for tectonically active continental areas that exhibit a seismic lower crust (Figure 3.2 of main chapter text). Dashed red line indicates approximate Moho depth.

pattern displayed within the Alps proper (Figure B.2). Earthquakes in the Alps are restricted to the upper 20 km of crust, while Moho depths can reach > 50 km (Figure B.3), so the lower crust is aseismic. The cornerstones of seismologic monitoring in these regions are dense permanent seismograph networks operated by French, German, Italian, and Swiss institutes.

The following studies were incorporated into this review to define T_S of the Alps, Alpine Foreland, and Rhine Graben regions, thereby providing the earthquake data for Figure B.2 and the Alpine Foreland and Rhine Graben histogram in Figure B.1. Bonjer et al. [1984] studied earthquakes within the Rhine Graben region utilizing short-period seismographs setup by the French, German, and Swiss. Deichmann [1987], Deichmann and Rybach [1989], and Deichmann et al. [2000] employ the dense short-period network operated by the Swiss Seismological Service (SED, for Schweizerischer Erdbebendienst) plus stations from Germany universities and from a small seismograph array near Basal to constrain event hypocenters in the Alps and Alpine Foreland. Kastrup et al. [2004] compiled an earthquake focal parameter dataset from previously published studies for these regions. The information compiled relied heavily on SED data supplemented with several temporary local networks and stations in neighboring countries. For the south-western Alps, Nicole et al. [2007] constrained event hypocenters using a temporary seismological network deployed from August to December, 1996 supplemented with permanent stations from French and Italian universities.

Moho depths are greatest beneath the Alps (> 50 km) and thin to ~ 25 km beneath the Rhine Graben (Edel et al., 1975; Mueller et al., 1980; Lüschen et al., 1987; Brun et al., 1991). T_S includes the entire continental crust beneath the Alpine Foreland and

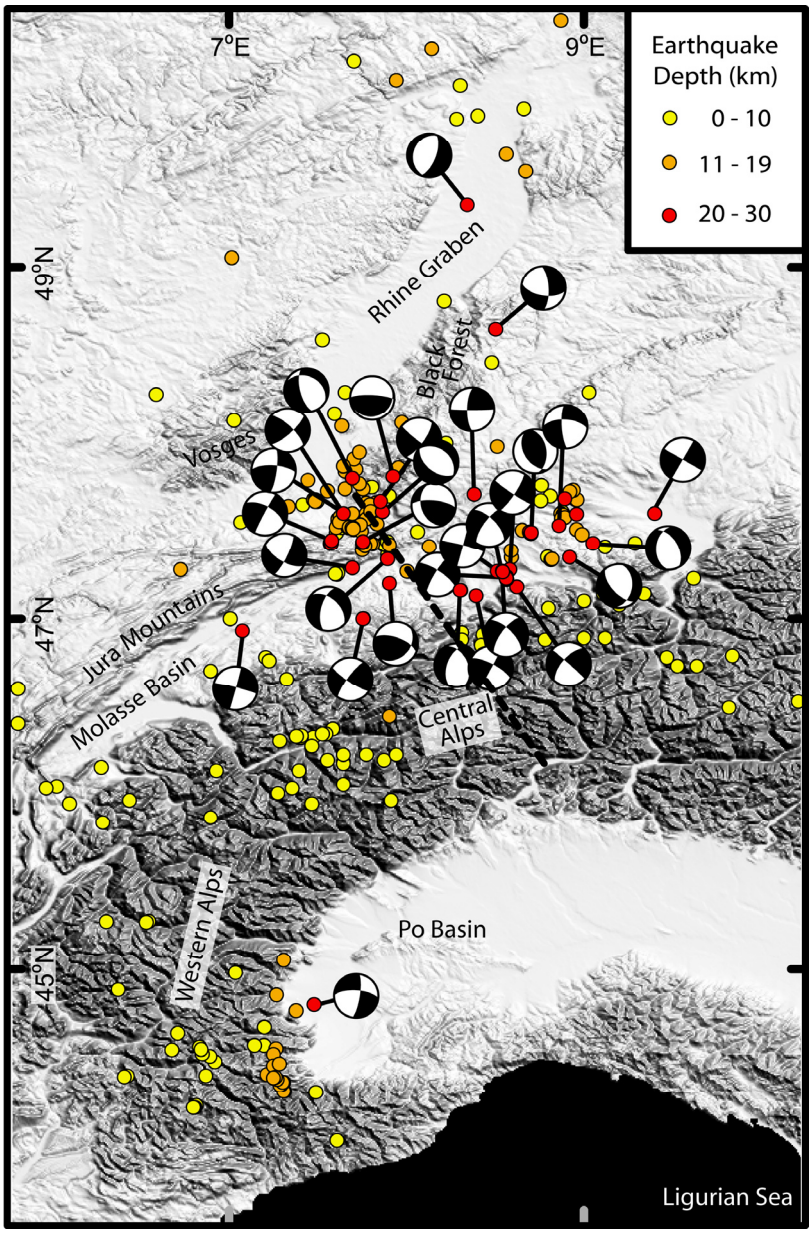

Figure B.2: Crustal earthquakes of the Alps, Alpine Foreland, and Rhine Graben regions. The location of the depth profile in Figure B.3 is represented by the dashed black line. Hypocenter and focal mechanism references: Bonjer et al. [1984], Deichmann [1987], Deichmann and Rybach [1989], Deichmann et al. [2000], Kastrup et al. [2004] and references therein, and Nicole et al. [2007].

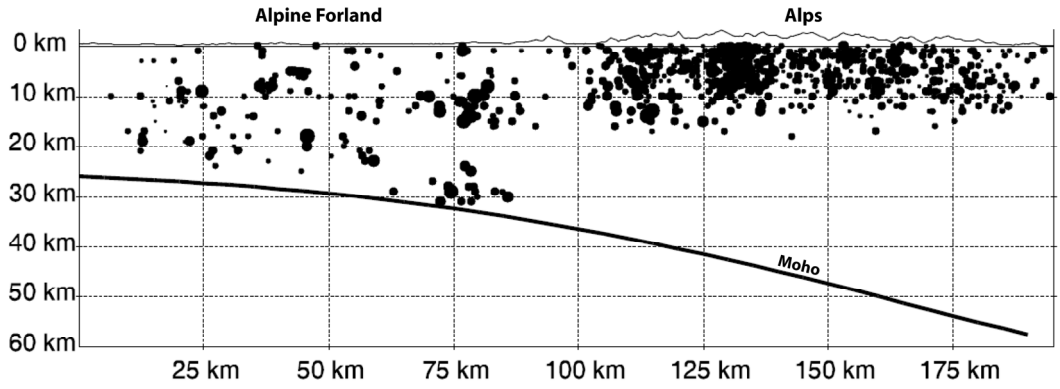

Figure B.3: Earthquake depth profile from Deichmann et al. [2000]. Depth cross-section along a NNW-SSE trending profile, map location shown in Figure B.2. Earthquakes are different than those displayed in Figure B.2, although both datasets reveal the same pattern in T_S. The events were compiled by Deichmann et al. from the Swiss and German seismograph networks between 1975 and 1999.

adjacent Rhine Graben region ($T_S \approx T_c \approx 30$ km, where = T_c thickness of crust), but is restricted to the middle and upper crust (< 20 km) beneath the Alps where $T_c \approx 50$ km, leaving the Alps lower crust aseismic (Figure B.3).

Argentine and Peruvian forelands

The Andes Mountains are located along a convergent plate boundary where the Nazca oceanic plate subducts beneath the South American continental plate. The Andean margin displays major along-strike segmentations involving variations of oceanic subduction angle, foreland structural style, and foreland seismicity [*Barazangi and Isacks*, 1976; *Jordan, et al.*, 1983]. The two most seismically active segments are the forelands of Argentina and Peru. The crust of these regions is seismogenic to nearly Moho depths, the structural style is dominated by reverse faulted basement uplifts, and beneath these regions the Nazca plate subducts at a low angle (~ 10°). Outside of these two foreland regions and into the Altiplano-Puna plateau region, the South American plate exhibits less seismic activity. This different pattern of seismic activity corresponds to where the Nazca plate dips more steeply (~ 30°) and the foreland structural style is described as a thin-skinned fold and thrust belt. Therefore, spatial relationships exist along the Andean foreland that link a seismogenic crust to basement thrusts and low angle subduction.

Argentine foreland – The Sierras Pampeanas are the region of the Argentine Foreland where reverse basement thrusts dominate the structural style (Figure B.4). Numerous studies have described the crustal seismicity in this region. Earthquakes have maximum depths of ~ 45 km and the crust is ~ 50 km thick (Figure B.1 Argentine Foreland). Chinn and Isacks [1983] and Devlin and Isacks [in prep] used teleseismic waveform modeling to constrain event depths through the Central Andes. Kadinsky-

Cade et al. [1985] combined leveling data and seismic observations to study the November 23, 1977, Ms = 7.4 Caucete earthquake in western Argentina, to constrain rupture parameters. The top of the fault rupture was determined to be 17 km below the surface. Smalley and Isacks [1990], Regnier et al. [1992], and Smalley et al. [1993] analyzed data from local seismic networks, the combined footprint of their studies is outlined in Figure B.4. They found two areas of foreland seismicity, one associated with the Sierras Pampeanas basement uplifts, and the other beneath, but not within, the Precordillera thin-skinned fold and thrust belt. Both areas exhibit seismicity to nearly 50 km depth. Assumpçao and Arujo [1993] used teleseismic waveform modeling and analysis of local network data to constrain parameters for two events in the sub-Andean region of northwest Argentina at depths of 18 and 27 km. Alvarado et al. [2005] operated a portable broadband seismic network in the Argentine flat-slab region to study crustal seismicity. They recorded earthquakes throughout the Sierras Pampeanas at middle-to-lower crustal depths. Additionally, Alvarado and Beck [2006] used teleseismic waveform modeling to determine source parameters for two historical earthquakes, the January 15, 1944 event (Mw 7.0) and the June 11, 1952 event (Mw 6.8). Both earthquakes have depth of < 12 km. Earthquake depths reported by these studies were used to construct Figure B.4 and the Argentine Foreland histogram in Figure B.1. Calkins et al. [2006] and McGlashan et al. [2008] provided estimates of Moho depth (~ 50 km) from high frequency receiver functions and teleseismically recorded pmP depth phase precursors, respectively.

Peruvian foreland – Similarly, a large part of the Peruvian foreland exhibits lower crustal seismicity associated with basement thrusts (Figure B.5). Studies describe the crustal seismicity in this region as having maximum event depths of ~ 40 km and a crustal thickness of ~ 40 km (Figure B.1 Peruvian Foreland and Figure B.5). Chinn

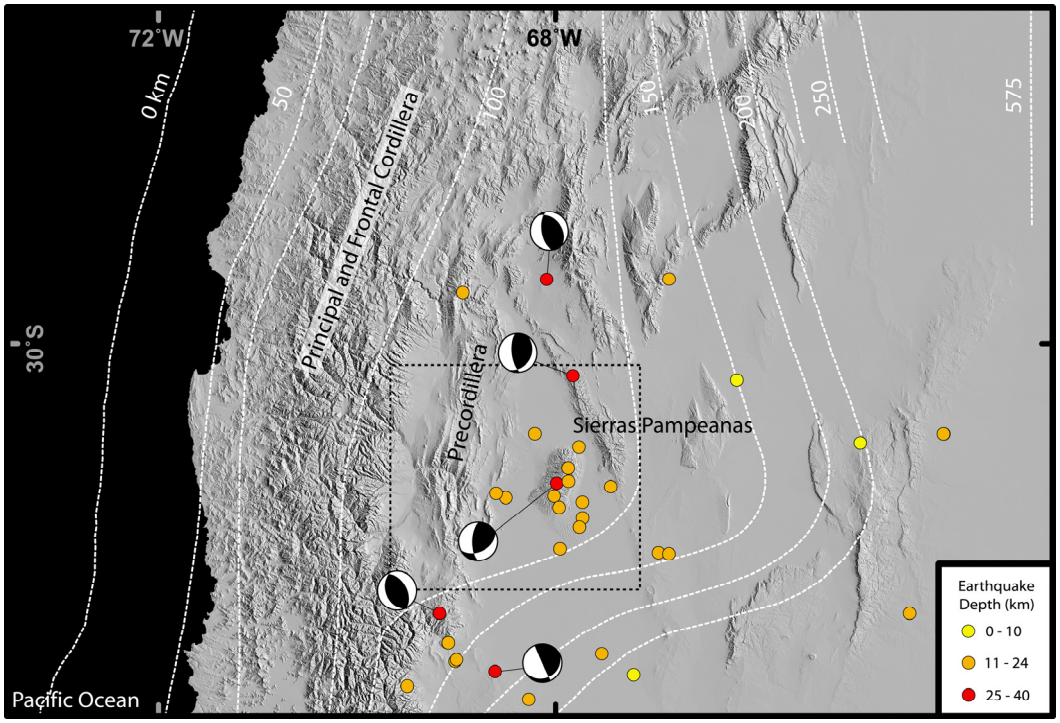

Figure B.4: Crustal earthquakes of the Andean Foreland in Argentina. The combined network footprint from Regnier et al. [1992], Smalley and Isacks [1990], and Smalley et al. [1993] is outlined in the black dashed line. Nazca plate contours are shown as white dashed lines with contour intervals labeled in white text [*Cahill and Isacks*, 1992]. Hypocenter and focal mechanism references: Alvarado et al. [2005], Alvarado and Beck [2006], Assumpçao and Araujo [1993], Chinn and Isacks [1983], Devlin and Isacks [in prep], and Kadinsky-Cade et al. [1985].

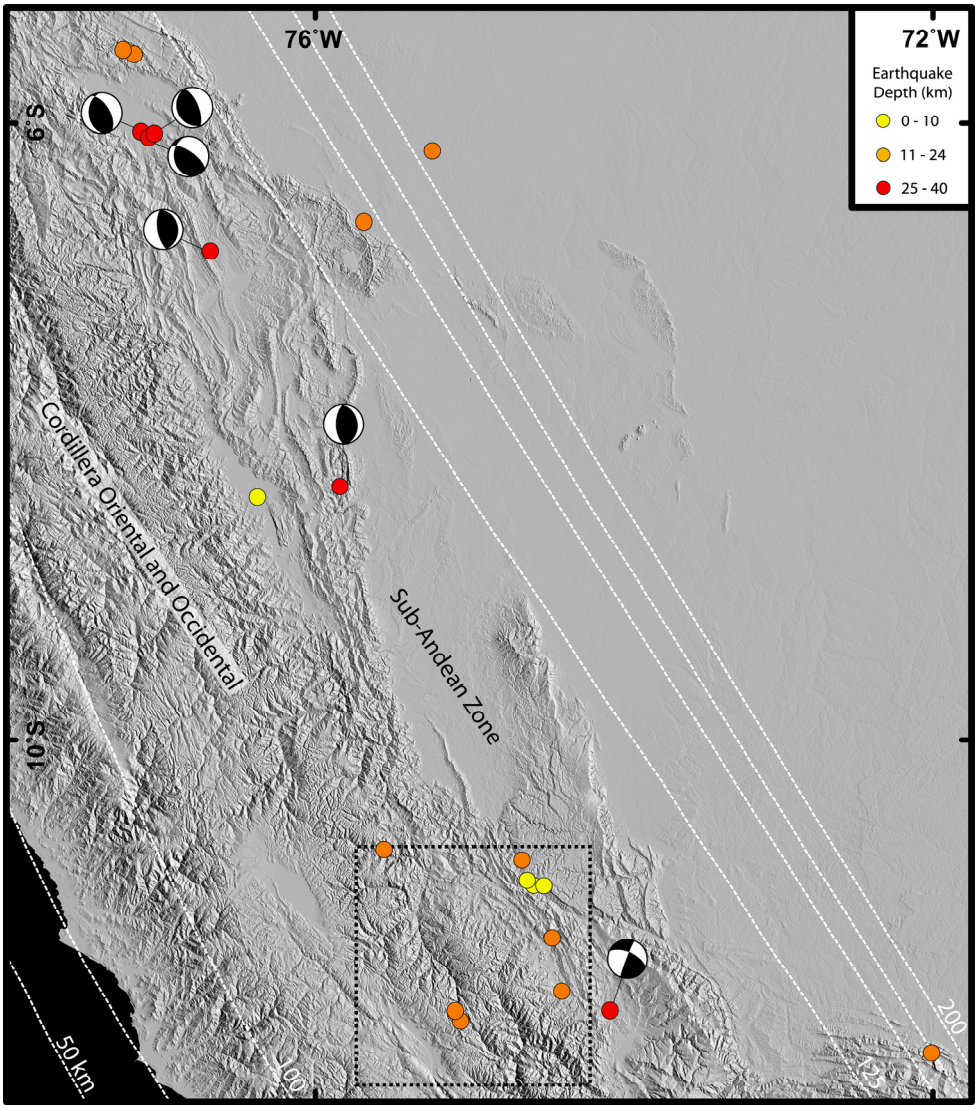

Figure B.5: Crustal earthquakes of the Andean Foreland in Peru. The network footprint from Dorbath et al. [1987] is outlined in the black dashed line. Nazca plate contours are shown as white dashed lines with contour intervals labeled in white text [*Cahill and Isacks*, 1992]. Hypocenter and focal mechanism references: Chinn and Isacks [1983], Devlin and Isacks [in prep], Dorbath et al. [1987], and Suarez et al. [1983].

and Isacks [1983], Suarez et al. [1983], and Devlin and Isacks [in prep] determined event parameters using teleseismic waveform modeling. Dorbath et al. [1987] conducted a local network study in the Andean foothills and located deep crustal earthquakes in the Sub-Andean zone, the northeast extent of their study region. Moho depth (~ 40 km) was constrained via teleseismic receiver functions analysis by James and Snoke [1994].

Baikal Rift System

The Baikal Rift System (BRS) extends over 2500 km from south central Russia into northern Mongolia (Figure B.6) and exhibits limited volcanic activity over it length. Estimates of crustal thicknesses across the Baikal region vary from 35 to 48 km [*Gao, et al.*, 2004; *ten Brink and Taylor*, 2002]. Numerous studies have determined earthquake locations using regional and local seismic networks [*Déverchère, et al.*, 1991; *Déverchère, et al.*, 1993; *Déverchère, et al.*, 2001; *Radziminovich, et al.*, 2003; *Vertlib*, 1981; 1997], while other studies utilized teleseismic waveform modeling [*Bayasgalan, et al.*, 2005; *Bayasgalan and Jackson*, 1999; *Delouis, et al.*, 2002; *Doser*, 1991a; b; *Emmerson, et al.*, 2006]. All studies are consistent with T_S reaching to the Moho and possibly exceeding it (Figure B.1 Baikal Rift System). The majority of earthquakes are restricted to the crust; however there are a few low-magnitude events appearing to occur within the lithospheric mantle [*Emmerson, et al.*, 2006]. Emmerson et al. [2006] conducted a thorough literature review of studies that report deep seismicity in the Baikal region, so we refer readers to that article instead of re-reviewing those studies here

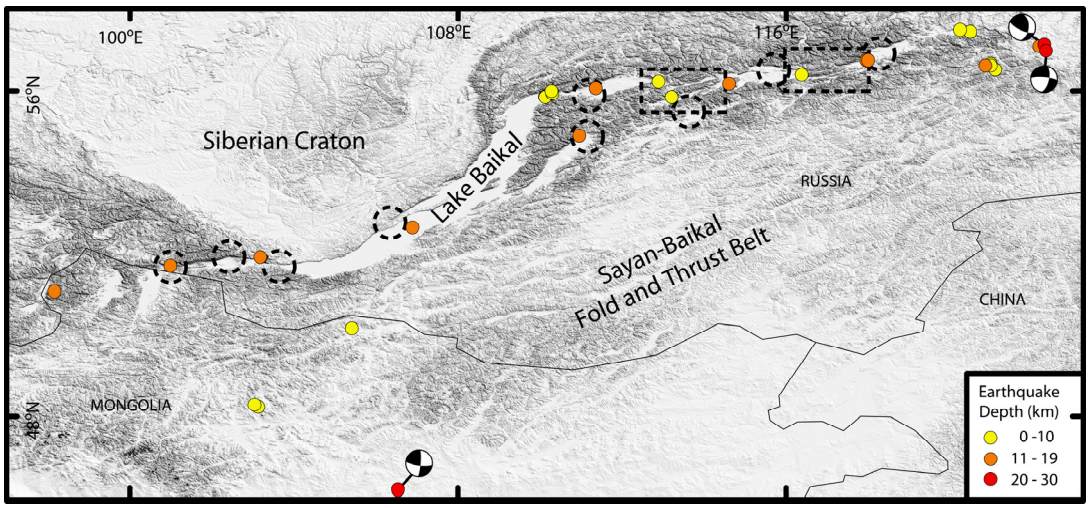

Figure B.6: Crustal earthquakes of the Baikal Rift System. The black dashed polygons show the network footprints where lower crustal earthquakes were reported [*Déverchère, et al.*, 1993; *Déverchère, et al.*, 2001; *Vertlib*, 1981]. Country borders are drawn in thin black lines. Hypocenter and focal mechanism references: Bayasgalan and Jackson [1999], Bayasgalan et al., [2005], Delouis et al. [2002], Doser [1991a; 1991b], Emmerson et al. [2006].

Colorado Plateau

The Colorado Plateau has been characterized as a relatively coherent lithospheric block surrounded on three sides by the extension of the Basin and Range and Rio Grande Rift (Figure B.7). It has been relatively stable during the much of the Phanerozoic, but was epeirogenically uplifted ~ 2 km in the Cenozoic. Geologic evidence attests to a lack of major crustal deformation within the plateau since the end of the Laramide orogeny around 40 Ma ago. Few seismicity investigations have been conducted on the plateau due to the plateau being nearly quiescent. Despite this, two studies have reported accurate depth determinations for plateau earthquakes. Wong et al. [1984] studied two unusually deep earthquakes located within the southeast part of the plateau (triangles and focal mechanisms in Figure B.7). The events occurred in 1976 and 1977 with magnitudes (ML) 4.6 and 4.2, respectively. Their focal depths were found to be 41 and 44 km. Focal depths were constrained using the HYPOELLIPSE location program and were further supported by error analyses, a previous independent study [*Dewey*, 1982], and regional waveform analysis (i.e., *Pn*, *pPn*, and *P*). Wong and Humphrey [1989] used local and regional seismic networks to constrain event hypocenters throughout the plateau. Seismicity with the Canyonlands region in the north-central part for the plateau (Figure B.7 dashed rectangle) was found to reach to ~ 50 km. Crustal thickness estimates from a refraction-reflection survey, receiver functions, and velocity modeling are ~ 45 km [*Gilbert and Sheehan*, 2004; *Jaksha and Evans*, 1984; *Lastowka, et al.*, 2001; *Wilson, et al.*, 2005; *Zandt, et al.*, 1995], which places the 1976 to 1977 events and numerous events from the Wong and Humphrey [1989] study in the lower crust (Figure B.1 Colorado Plateau). In addition, Wong and Humphrey located two events between 50 and 60 km depth, apparently in the lithospheric mantle. However, like in the Baikal Rift region, the

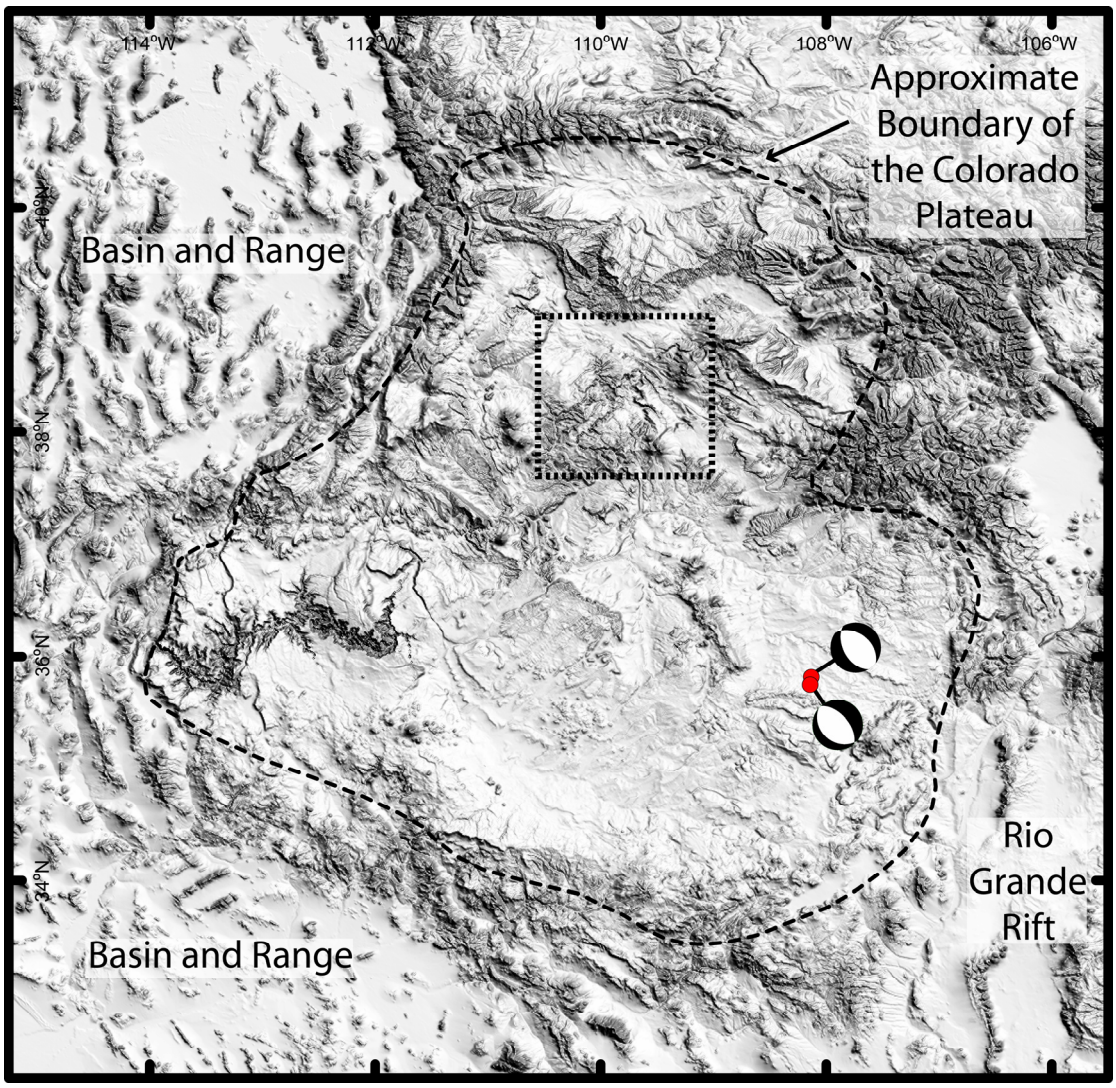

Figure B.7: Crustal earthquakes of the Colorado Plateau. The map footprint of a local network study that recorded lower crustal events (dashed rectangle) [*Wong and Humphrey*, 1989]. The two individual lower crustal event locations are accompanied by their best fit focal mechanism. Event depths are 41 and 44 km. The focal mechanisms are consistent with horizontal extensional stress associated with the nearby Rio Grande Rift system. Hypocenter and focal mechanism reference: [*Wong, et al.*, 1984].

mantle events had small magnitudes (ML < 4.0) and are few in number. Therefore, T_S of the Colorado Plateau reaches to Moho depth and possibly beyond.

Dead Sea Fault System

The Dead Sea Fault System (DSFS) is an intracontinental plate boundary that extends ~ 1000 km from the Red Sea spreading center northward to the collisional zone in southern Turkey. This transform system resulted from the Late Cenozoic breakup of the Arabian-African continent and has accumulated left-lateral slip of ~ 105 km [*Freund, et al.*, 1970; *Quennell*, 1958]. The Dead Sea basin (Figure B.8) is an active pull-apart basin located along the DSFS. Seismic refraction, reflection, and receiver functions have determined crustal thicknesses throughout the region to be ~ 30 to 35 km [*Ginzburg, et al.*, 1981; *Mohsen, et al.*, 2006; *Weber, et al.*, 2004, respectively]. Aldersons et al. [2003] studied the local seismicity of the Dead Sea basin region for the period 1984 to 1997 by relocating 410 events with ML ≤ 3.5 recorded by permanent seismic stations throughout Jordan and Israel. Their finding show more than 40% of the activity occurred below 20 km and $T_S \approx 30$ km. With the maximum Moho depth at 35 km, nearly the entire crust is seismically active, while the upper mantle appears aseismic (Figure B.1 Dead Sea Fault System).

East African Rift System

The East African Rift System (EARS) has experienced tectonism through much of the Cenozoic. The rift valleys of the EARS form two branches, the Eastern Rift extending from Ethiopia into Tanzania and the Western Rift along the border of the Democratic Republic of the Congo with Uganda south to Tanzania and Malawi. The rift branches surround the Archean Tanzania cratonic lithosphere (Figure B.9).

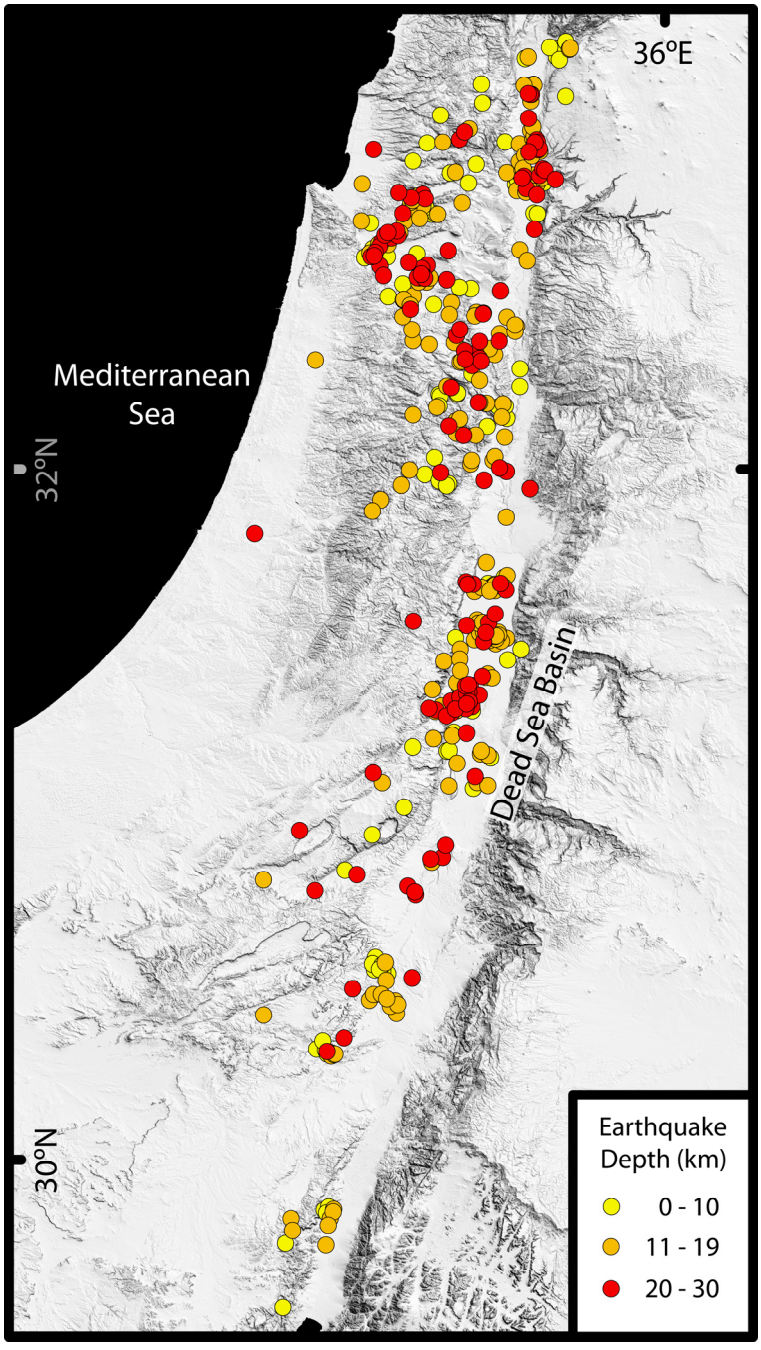

Figure B.8: Crustal earthquakes of the Dead Sea Fault System. Hypocenter reference: [*Aldersons, et al.*, 2003].

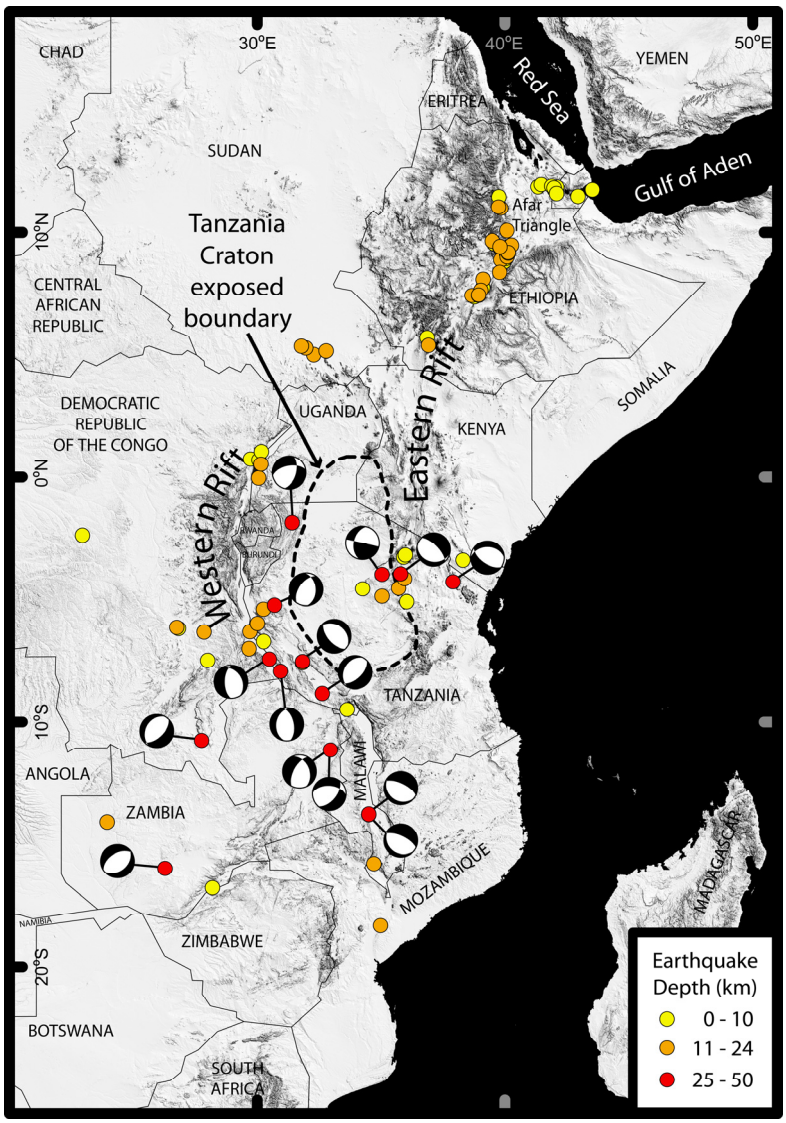

Figure B.9: Lower crustal earthquakes of the East African Rift System. Hypocenter and focal mechanism references: Braunmiller and Nabelek [1990], Brazier et al. [2005], Foster and Jackson [1998], Gaulon et al. [1992], Keir et al. [2006], Nyblade & Langston [1995], Shudofsky [1985], and Wagner & Langston [1988].

Between 1964 and 2000, 15 moderate- to large-magnitude (Mw 4.2 – 6.5) lower crustal earthquakes have occurred in the central and southern EARS (Figure B.9). The regions with seismically active lower crust (the Western Rift and Eastern Rift in Tanzania) experienced the onset of volcanism at ≤ 12 Ma [*Ebinger*, 1989; *George, et al.*, 1998; *Nyblade and Brazier*, 2002 and references therein]. Maximum crustal thickness is ~ 42 km [*Dugda, et al.*, 2005] and T_S is ~ 35 km (Figure B.1 East African Rift System) [*Brazier, et al.*, 2005; *Foster and Jackson*, 1998; *Nyblade and Langston*, 1995; *Shudofsky*, 1985]. Earthquake source parameters were collected from a number of studies, most of which analyzed EARS earthquakes using waveforms recorded at teleseismic distances. One exception is Brazier et al. [2005] who determined event focal parameters using regional and teleseismic recordings. These authors calculated synthetic seismograms to constrain source depth. Foster and Jackson [1998] used teleseismic *P* and *SH* body-waveform inversion. Nyblade and Langston [1995] also performed teleseismic waveform modeling, but supplemented depth determinations using first-motion polarities, *P* and *pP* amplitudes, and determination of *pP–P* and *sP–P* differential travel times, all derived from short-period records. Lastly, Shudofsky [1985] determined source parameters using regional and teleseismic recordings to conduct Rayleigh-wave inversion and body-wave modeling.

Himalayan Collision Zone

The cause of deep seismicity beneath the Himalayas and Tibet has been a topic of much debate since an intermediate depth earthquake was first documented beneath southern Tibet by Chen et al. [1981]. Since then, many studies [*Chen and Kao*, 1996; *de la Torre, et al.*, 2007; *Ekström*, 1987; *Mitra, et al.*, 2005; *Molnar and Chen*, 1983; *Monsalve, et al.*, 2006; *Zhu and Helmberger*, 1996] have reported other deep events throughout southern Tibet and the Himalayas between approximately 85° and 95°E

longitude (Figure B.10). To discuss these earthquakes and others in the surrounding areas, we consider the broad India-Asia collision zone in three regions – the Himalayan collision zone, continental India south of the collision zone, and Tibet north of the collision zone. The Himalayan collision zone is the region where lower crustal earthquakes occur, which roughly corresponds to the area between the Indus-Tsangpo Suture and the Central Indian Plateau. This region includes southern Tibet, the Himalayas, the Ganges Basin, and the Shillong Plateau region (Figure B.10). Moderate- to large-magnitude lower crustal earthquakes occur within the Himalayan collision zone.

Seismicity beneath the Himalayan Collision Zone occurs within the crust from the near-surface to the Moho and possibly to depths within the mantle lid (Figure B.1 Himalayan Collision Zone) [*Baranowski, et al.*, 1984; *Chen and Kao*, 1996; *Chen, et al.*, 1981; *de la Torre, et al.*, 2007; *Ekström*, 1987; *Lyon-Caen and Molnar*, 1989; *Mitra, et al.*, 2005; *Molnar and Chen*, 1983; *Monsalve, et al.*, 2006; *Ni and Barazangi*, 1984; *Zhu and Helmberger*, 1996]. Chen et al. [1981] used *P*, *pP*, and *sP* differential travel times and Rayliegh wave spectral densities to constrain the depth for an intermediate depth earthquake (September 14, 1976; mb 5.4) to ~ 90 km depth. Molnar and Chen [1983] compared synthetic and recorded *P* waveforms for 16 earthquakes beneath the Tibetan plateau, five of which are within the Himalayan Collision Zone. Four events have shallow depth (< 10 km) and one event has a depth of 85 km. Ni and Barazangi [1984] determined depths for 17 earthquakes within the Himalayan collision zone using synthetic *P* waveform modeling and short-period depth phase identification. Depths were determined to be mid-crustal depths, between 9 and 25 km. Baranowski et al. [1984] compared synthetic seismograms with long-period body waves for 9 earthquakes within the Himalayan arc. Focal depths are

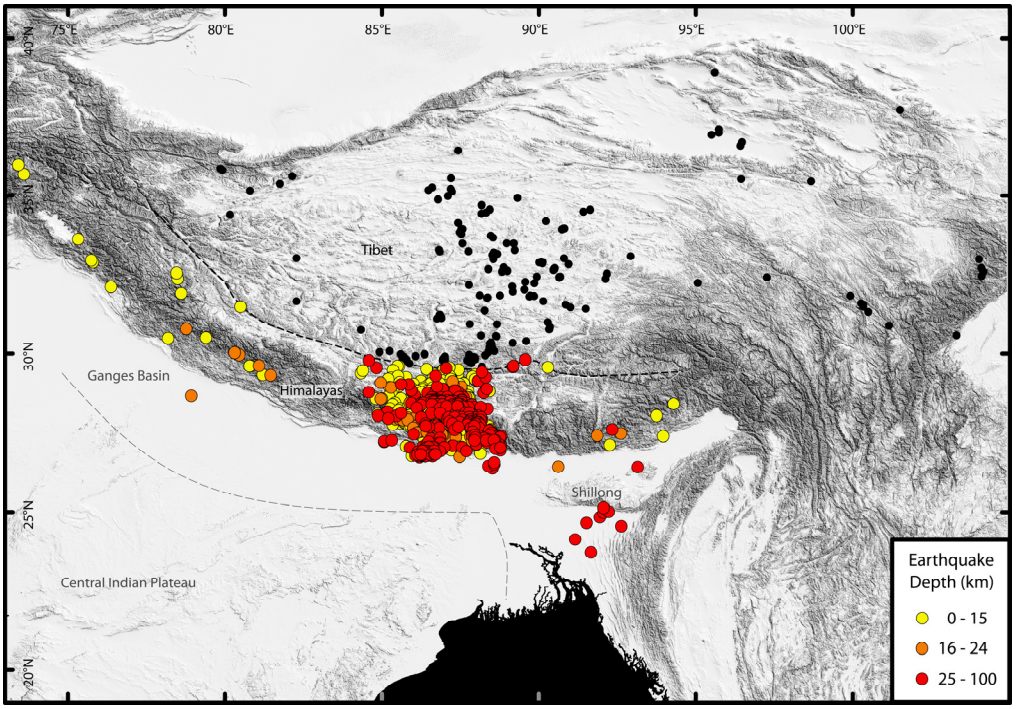

Figure B.10: Earthquakes of the Himalayan Collision Zone. Black circles are Tibetan earthquakes shown in the Figure 3, *Tibet*. Black dashed line is the approximately Indus-Tsangpo Suture and the gray dashed line roughly separates the Ganges Basin and Central Indian Plateau. Hypocenter references: Baranowski et al. [1984]; Chen et al. [1981];Chen & Kao [1996]; de la Torre et al. [2007]; Ekström [1987]; Mitra et al. [2005]; Molnar & Chen [1983]; Molnar & Lyon-Caen [1988]; Monsalve et al. [2006]; Ni & Barazangi [1984]; Zhu & Helmberger [1996].

between 10 and 20 km. Ekström [1987] combined broadband *P* and *SH* body wave analysis and centroid moment tensor inversion to constrain two Himalayan earthquakes both with depths of 44 km. Molnar and Lyon-Caen [1989] synthesized shapes and amplitudes of teleseismic *P* and *SH* waveforms. Depths were determined to be mid-crustal depths, between 7 and 18 km. Zhu and Helmberger [1996] modeled regional broadband waveforms for three intermediate depth earthquakes in the Himalayan collision zone. Depths were 70, 80, and 80 km. Chen and Kao [1996] compared synthetic seismograms with long-period body waves for two earthquakes with epicenters in the Himalayan arc. Event depths were 16 and 51 km. Mitra et al. [2005] used broadband teleseismic data recorded at 8 stations along a north-south profile from Lhasa to south of Shillong plateau to determine receiver functions and crustal velocities. Focal parameters for three events were constrained by analysis of teleseismic *P* and *SH* waveforms using the determined velocity structure. Two events were near the Shillong plateau and one within the Himalayas. Depths were 30, 43, and 37 km, respectively. Monsalve et al. [2006] located earthquake parameters from the HIMNT temporary seismic network. Depths range from the near-surface to 96 km. de la Torre et al. [2007] determined focal mechanisms from moment tension inversion and first motion polarities of the best quality events from the HIMNT. Depths range from 5 to 90 km. Moho depths vary throughout the Himalayan Collision Zone, because India is subducting beneath Tibet. The general pattern is that the Moho is ~ 42 km beneath the Ganges Basin and deepens to ~ 80 km beneath the Indus-Tsangpo Suture [*Mitra, et al.*, 2005; *Schulte-Pelkum, et al.*, 2005; *Shin, et al.*, 2007]. Seismogenic thickness varies along with the deepening Moho, such that $T_S \approx 40$ km beneath the Ganges Basin and increases to $\gtrsim 80$ km depth beneath the Himalayas and southern Tibet.

New Zealand

North Island – The tectonics of North Island, New Zealand (Figure B.11) is dominated by subduction along the Hikurangi Margin and back-arc spreading within the Taupo Volcanic Zone (TVZ). This setting is part of the larger Tonga-Kermadec-Hikurangi subduction and Lau-Havre-Taupo back-arc basin systems, which extend southward into the continental lithosphere of the New Zealand North Island. Rapid ($\gtrsim$ 10 mm/yr) back-arc spreading began ~ 10 Ma in the Lau region and propagated south into Havre around 5 Ma and finally into the Taupo region on the North Island $\lesssim$ 4 Ma [*Parson and Wright*, 1996]. Classic extension occurs in the north and central regions of the island, while mild compression occurs in the central southwest. This transition roughly occurs at Mt. Ruapehu, the southern terminus of the TVZ (Figure B.11 5-point star). A coincident transition occurs in T_S within these regions, where $T_S \approx 20$ km in the north and central regions and is ~ 50 km in the central southwest (Figures B.1 North Island, New Zealand, B.11, and B.12).

Seismogenic thicknesses are determined from two local network studies [*Reyners, et al.*, 2007; *Sherburn and White*, 2005]. Reyners et al. [2007] conducted a six-month dense deployment of portable seismographs across most of the island. They presented three-dimensional tomographic imaging of seismic velocities and seismic attenuation and accurately relocated crustal events. They found the earthquakes form a continuous band along-strike of the TVZ. The events occurred mostly at < 20 km depth beneath the TVZ and deepen to depths of 30 to 50 km southwest of the termination of the volcanic zone (Figure B.12). Sherburn and White [2005] investigated a similar pattern by deploying a dense local seismic network around Mt. Taranaki on the southwest part of the island (Figure B.11 7-point star). That study showed $T_S \approx 20$ km around Mt. Taranaki and thickens to 35 km to the southeast coincident with the deep seismicity

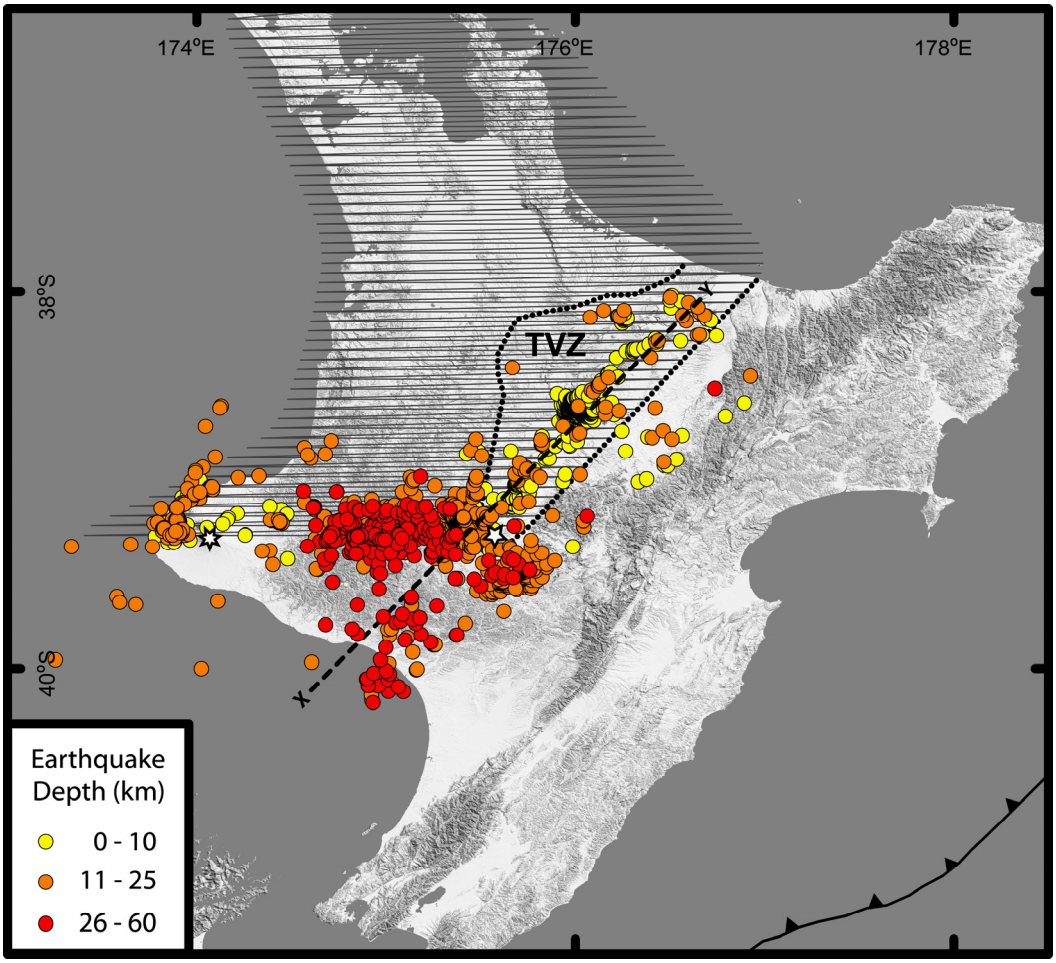

Figure B.11: Crustal earthquakes of the North Island, New Zealand. Dotted black line outlines the Taupo Volcanic Zone (TVZ), the 5-point white star illustrates the position of Mt. Ruapehu, which is considered the southern terminus of the TVZ. The 7-point white star illustrates the position of Mt. Taranaki and the dashed black line labeled XY shows the position of the depth profile in Figure B.12. The gray hachured region represents the zone of thin crust, low *Pn* wave speeds, and low Q [*Stern, et al.*, 2006]. Also shown in the southeast is part of the Hikurangi subduction margin. Hypocenter references: Reyners et al. [2007] and Sherburn and White [2005].

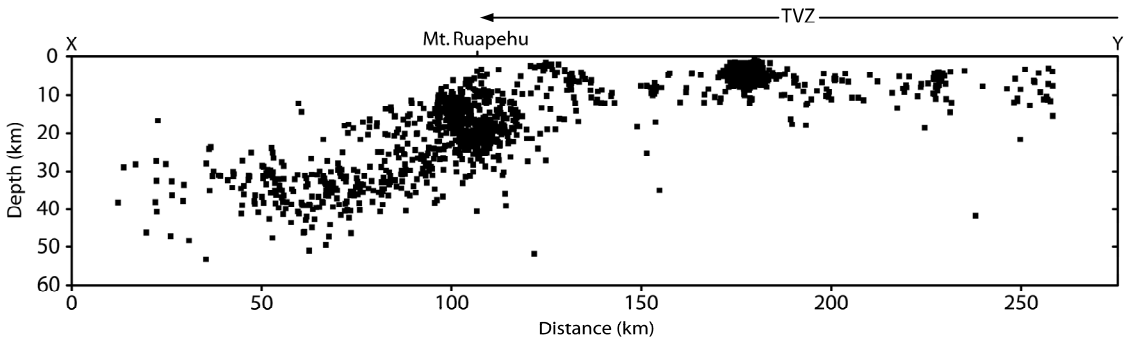

Figure B.12: Earthquake Depth Profile from North Island, New Zealand [modified from *Reyners, et al.*, 2007]. Profile location is shown in Figure B.11 by the black line labeled XY. Individual earthquakes are represented by black squares.

found by Reyners et al. [2007]. Seismic exploration of the crust has also shown two distinct structural domains. In the north and central regions the crust is thin ($T_c \approx 25$ km), *Pn* wave speeds are low, mantle attenuation is high, and gravity anomalies are positive (Figure B.11 hachured region). In the central southwest, crustal thicknesses increase to > 40 km, gravity anomalies are negative, and mantle attenuation is reduced [see *Stern, et al.*, 2006 for review]. These contrasting crustal characteristics suggest that the hachured region in Figure B.11 has experienced more pervasive crustal modification than the areas that exhibit deep crustal earthquakes (i.e., at the boundaries and outside the hachured region). Since maximum $T_S \approx 50$ km and $T_c \gtrsim 40$ km, the possibility of seismicity occurring within the mantle lid exists, however inaccurate constraints on Moho depth limits such an assessment with the current data.

South Island – In this section, we discuss why we contend that what might be interpreted as lower crustal and upper mantle seismicity beneath South Island, New Zealand more probably occur in oceanic lithosphere instead of continental. The Alpine Fault of South Island, New Zealand is considered the transpressional plate boundary between the Australian plate in the west and the Pacific plate in the east. Reyners [1987] and Kohler and Eberhart-Phillips [2003] constrained earthquakes to occur between ~ 30 and 80 km depth within the lower crust and upper mantle east of the Alpine Fault (i.e., within Pacific plate lithosphere). Two active source seismic reflection surveys [*Smith, et al.*, 1995; *Van Avendonk, et al.*, 2004] crossed the region of proposed deep seismicity and imaged a thin (~ 3 – 11 km thick) lower crustal layer with high *P* wave velocities (~ 6.9 – 7.25 km/s). Both studies interpreted this lower crustal layer as oceanic crust with underlying oceanic lithospheric mantle, where a typical thickness for oceanic crust is 6 km [*Turcotte and Schubert*, 2002] and mid to lower crustal velocities are ~ 6.8 – 7.1 km/s [*Lewis*, 1978]. The proposed lower crustal

oceanic layer dips westward continuously from the east beneath the Pacific Ocean to the west just east of the Alpine Fault [*Van Avendonk, et al.*, 2004]. The top of the layer lies at ~ 30 km depth and the bottom reaches to ~ 40 km depth. The base of the oceanic crustal layer is consistent with Moho depth determinations by Kohler and Eberhart-Phillips [2002], which average around ~ 40 km for this region. Most of the upper and middle crust above the proposed oceanic lithosphere is interpreted to consist of the Torlesse greywackes. These sediments are thought to have been deposited on top of Pacific oceanic crust [*Smith, et al.*, 1995] near a trench system [*Adams and Kelley*, 1998]. Therefore, it is likely that lower crustal and upper mantle seismicity beneath the South Island, New Zealand is occurring in oceanic-type lithosphere, which is know to be seismogenic to mantle lid depths. For these reasons, we do not consider deep seismicity beneath South Island, New Zealand to be occurring within continental lithosphere, so we do not incorporate them into our global study of continental lower crustal earthquakes.

Sierra Nevada

The Sierra Nevada Batholith and its foothills separate the relatively thick, stable lithosphere of California's Great Valley from the thin, deformed lithosphere of the Western Basin and Range (Figure B.13). A zone of anomalously deep earthquakes has been identified beneath the Sierra Nevada (Figure B.1 Sierra Nevada). Wong and Savage [1983] were first to observe earthquakes confined to the lower crust at depths between 12 and 38 km beneath the Sierra Nevada. Miller and Mooney [1994] supplemented Wong and Savage's [1983] findings with another local network study that combined accurately located earthquakes with a seismic reflection profile and a new seismic velocity model. Miller and Mooney [1994] found events occurred from the near-surface to ~ 40 km depth, with a peak concentration at ~ 25 km. The ongoing

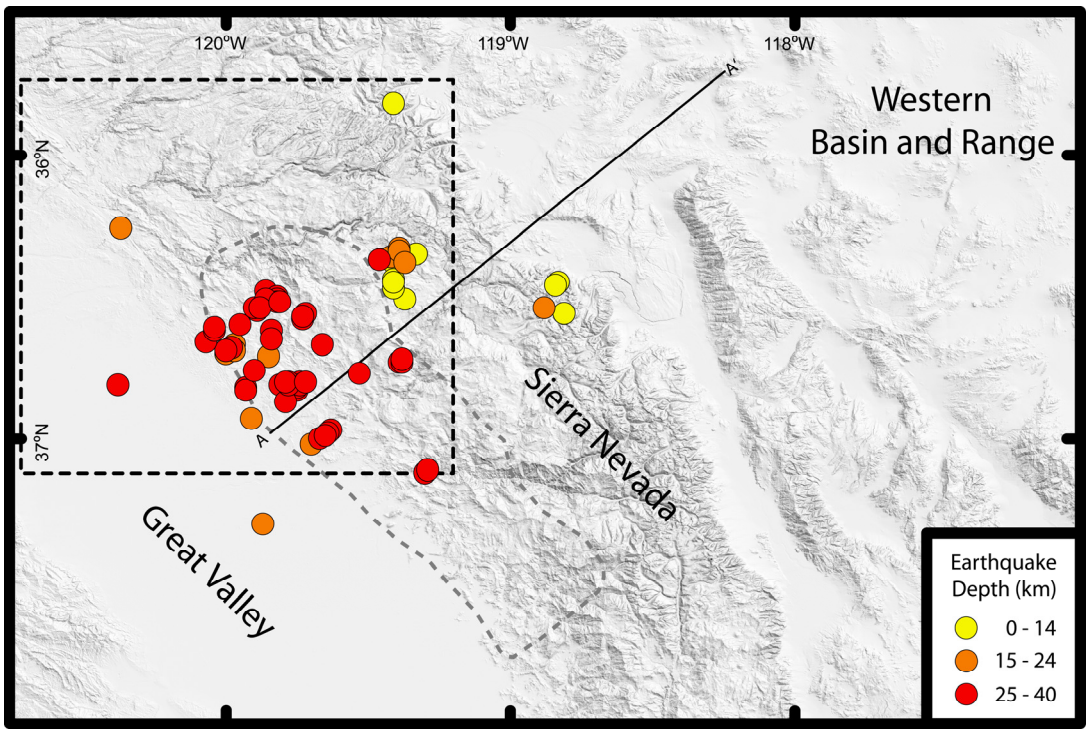

Figure B.13: Crustal earthquakes of the Sierra Nevada. Black dashed line outlines the combined seismic network foot prints from Miller and Mooney [1994] and Wong and Savage [1983]. The gray dashed line outlines the area of seismically imaged foundering lithospheric root [*Gilbert, et al.*, 2007; *Zandt, et al.*, 2004]. The black solid line labeled A-A' is the location of the profile shown in Figure B.14. Hypocenter reference: Gilbert et al. [2007].

Sierra Nevada EarthScope Project (SNEP) FlexArray is focused on understanding lithospheric processes of the Sierra Nevada [*Gilbert, et al.*, 2007]. Gilbert et al. [2007] reported seismicity and receiver function analyses from SNEP and found earthquake depth distributions comparable to those reported by Wong and Savage [1983] and Miller and Mooney [1994] (Figure B.13). The area where the lower crustal earthquakes are occurring coincides with where a compelling case has been made [see *Zandt, et al.*, 2004 for review] for a late Cenozoic delamination event, in which it is hypothesized that a significant portion of lithospheric root is detaching and dropping into the sub-lithospheric mantle (Figure B.13 and B.14). Figure B.13 shows earthquake hypocenters from SNEP [*Gilbert, et al.*, 2007] and the combined seismic network foot prints (black dashed rectangle) from Miller and Mooney [1994] and Wong and Savage [1983]. The gray dashed line outlines the area of seismically imaged foundering lithospheric root [*Gilbert, et al.*, 2007; *Zandt, et al.*, 2004]. Figure B.14 shows an interpreted receiver function profile from Gilbert et al. [2007] that illustrates that lower crustal earthquakes are located above where the delaminating root is proposed to exist. Receiver function analysis does not clearly image a Moho in this location, so the crustal thickness of this area is unknown.

Tien Shan

The active intracontinental mountain belt of the Tien Shan has formed from deformation associated with the collision of India and Eurasia. The Tien Shan is flanked by the relatively aseismic Kazakh Platform to the north and the Tarim Basin to the south (Figure B.15). Crustal thickness estimates from receiver function tomography range from 45 to 70 km, with most of the Tien Shan in the $T_c \approx 50$ km range [*Vinnik, et al.*, 2004]. Seismogenic thickness is characterized by studies conducted at local, regional, and teleseismic distances. Nelson et al. [1987] studied 11

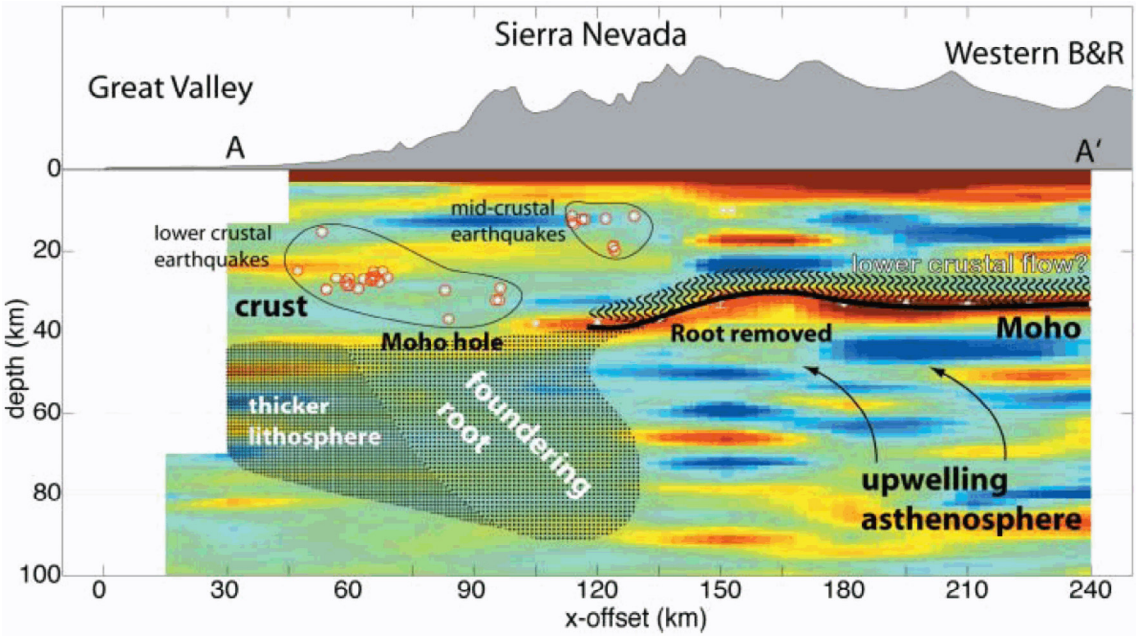

Figure B.14: Interpreted receiver function profile with earthquakes from Gilbert et al. [2007]. Surface topography along this profile is plotted along the top of the cross section. Red colors indicate positive polarity arrivals that correspond to discontinuities where seismic wave speeds increase with depth. Blue colors mark negative polarities and decreasing wave speeds with depth. Earthquakes located near this profile are plotted as white circles with red outlines. See Gilbert et al. [2007] for discussion of the data on which the interpretation is based.

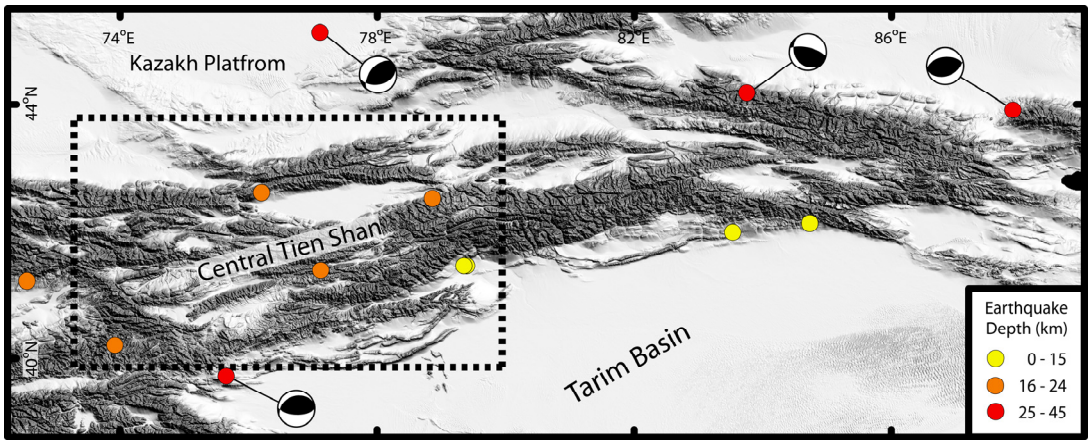

Figure B.15: Crustal earthquakes of the Tien Shan. The network footprint from Xu et al. [2006] is outlined in the black dashed line. Hypocenter and focal mechanism references: Fan et al. [1994], Ghose et al. [1998], and Nelson et al. [1987].

of the largest Tien Shan earthquakes from 1965 to 1982 by modeling *P* and *SH* teleseismic waveforms. Events depths range from 10 to 44 km, with 3 events located in the middle to lower crust (depth > 25 km). Fan et al. [1994] investigated earthquakes throughout a region larger than the Tien Shan, which also included the Hindu Kush-Pamir-Karakorum intracontinental convergence zone located southwest of the Tien Shan. Mantle-depth earthquakes associated with possible subduction beneath the Pamirs obscures assessment of T_S in those areas, however, Fan et al. located one event in the southwest Tien Shan. They used *P* and *SH* modeling and constrained that event depth to 37 km. Ghose et al. [1998] estimated event parameters of moderate-sized earthquakes by matching observed and synthetic seismograms recorded at regional distances. Source depths were found to be between 5 and 31 km. Xu et al. [2006] conducted a local study using broadband seismic networks (Figure B.15 dashed rectangle) and found events depths ranging from the near-surface to 45 km indicating a seismically active lower crust. Therefore, T_S within the Tien Shan is ~ 44 km and $T_c \approx 50$ km (Figure B.1 Tien Shan and Figure B.15).

Western Pyrenees

The Pyrenees result from continent-continent collision between the Iberian and Eurasian plates during the Cretaceous to Early Miocene in a two-stage tectonic event (Figure B.16). In the mid-Cretaceous, extension occurred between the two plates related to the opening of the Bay of Biscay and a following compressional event occurred from the Late Cretaceous to Early Miocene, which explains the crustal shortening associated with the uplift of the east-west striking Pyrenean range.

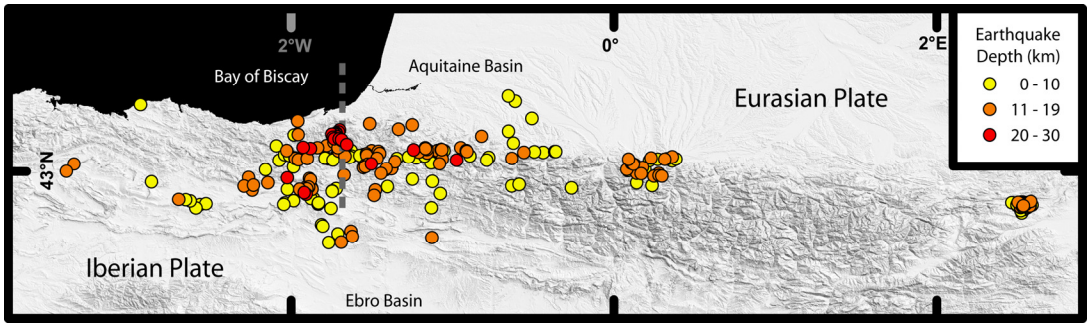

Figure B.16: Crustal earthquakes of the Western Pyrenees. The location of the profile in Figure B.17 is shows as the gray dashed line. Hypocenter references: Pauchet et al. [1999], Rigo et al. [1997], Rigo et al. [2005], and Ruiz et al. [2006].

Seismic reflection and refraction profiles [*Banda, et al.*, 1983; *Choukroune*, 1989; *Daignières, et al.*, 1981; *ECORS Pyrenees team*, 1988; *Pedreira, et al.*, 2003; *Roure, et al.*, 1989; *Suriñach, et al.*, 1993], tomography [*Souriau and Granet*, 1995], and receiver functions [*Díaz, et al.*, 2003] support subduction of the Iberian lithosphere beneath Eurasia and reveal a 10 to 15 km Moho jump beneath the range (Figure B.17). From south to north, the Moho beneath the Ebro Basin on the Iberian plate lies at ~ 31 km depth and increases to 40 km or more beneath the Pyrenees where Iberia subducted beneath Eurasia. North of the range, on the Eurasian plate, crustal thicknesses decrease to ~ 30 km again, such that the Pyrenees are flanked to the north and south by crust that is ~ 30 km thick while the mountains reside above a Moho at $\gtrsim$ 40 km depth (Figure B.17). The seismicity in Figure B.16 (and Figure B.1 Western Pyrenees) is reported by a number of local network studies [*Pauchet, et al.*, 1999; *Rigo, et al.*, 2005; *Rigo, et al.*, 1997; *Ruiz, et al.*, 2006]. Rigo et al. [1997] and Pauchet et al. [1999] analyzed the local magnitude (ML) 5.2 earthquake that occurred 18 February 1996 and associated aftershocks in the eastern Pyrenees. The studies used permanent and temporary network stations and found all events occurred at depths < 15 km. Rigo et al. [2005] studied seismicity of the central Pyrenees with two temporary seismological networks together with permanent network stations during 2000 and 2002. Maximum event depths vary from 10 to 20 km. Ruiz et al. [2006] presented seismic data collected froma temporary network deployed in the western Pyrenees. Their results show a northward dipping belt of seismicity to ~ 30 km depth, where the crust is constrained to be ~ 30 km thick [*Daignières, et al.*, 1981]. Figure B.16 shows the map view of the compiled earthquakes and the location of the profile shown in Figure B.17. Figure B.17 is the cartoon of crustal structure and seismicity compiled by Ruiz et al. [2006], which highlights the occurrence of the Pyrenean lower crustal seismicity.

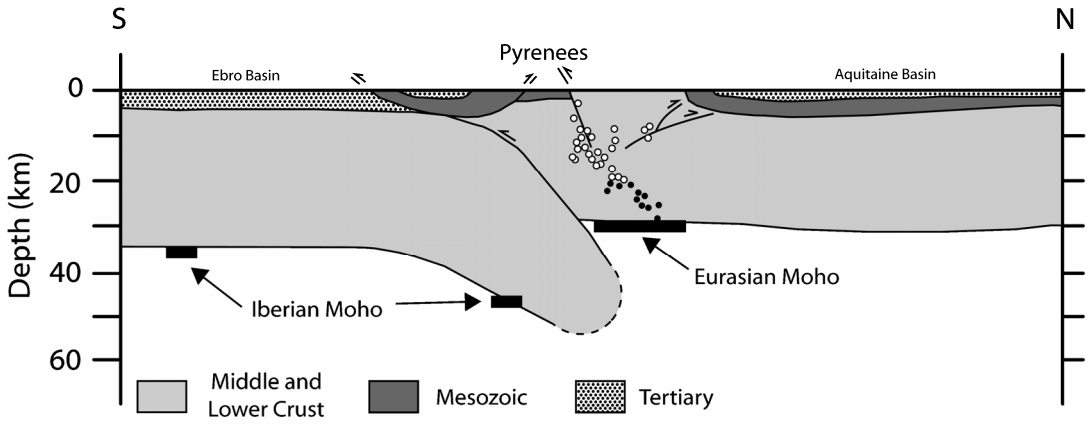

Figure B.17: Crustal structure and seismicity of the Western Pyrenees. Cartoon of crustal structure and seismicity compiled by Ruiz et al. (2006), which highlights the occurrence of Pyrenean lower crustal seismicity (black circles). Constraints on the position of the Moho are marked. Iberian Moho was constrained by Pedreira et al. [2003] and the European Moho by Gallart et al. [1981] and Díaz et al. [2003].

REFERENCES

Adams, C. J., and S. Kelley (1998), Provenance of Permian-Triassic and Ordovician metagraywacke terranes in New Zealand: Evidence from Ar-40/Ar-39 dating of detrital micas, *Geol. Soc. Am. Bull.*, *110* (4), 422-432.

Aldersons, F., et al. (2003), Lower-crustal strength under the Dead Sea basin from local earthquake data and rheological modeling, *Earth Planet. Sci. Lett.*, *214* (1-2), 129-142.

Alvarado, P., and S. Beck (2006), Source characterization of the San Juan (Argentina) crustal earthquakes of 15 January 1944 (Mw 7.0) and 11 June 1952 (Mw 6.8), *Earth Planet. Sci. Lett.*, *243* (3-4), 615–631, doi:10.1016/j.epsl.2006.01.015.

Alvarado, P., et al. (2005), Crustal deformation in the south-central Andes backarc terranes as viewed from regional broadband seismic waveform modeling, *Geophys. J. Int.*, *163* (2), 580–598, doi: 10.1111/j.1365-246X.2005.02759.x.

Assumpçao, M., and M. Araujo (1993), Effect of the Altiplano-Puna Plateau, South America, on the regional intraplate stresses, *Tectonophysics*, *221* (3-4), 475-496.

Banda, E., et al. (1983), Crustal structure beneath Spain from deep seismic sounding experiments, *Phys. Earth Planet. In.*, *31* (4), 277-280.

Baranowski, J., et al. (1984), Focal depths and fault plane solutions of earthquakes and active tectonics of the Himalaya, *J. Geophys. Res.*, *89* (B8), 6918-6928.

Barazangi, M., and B. L. Isacks (1976), Spatial distribution of earthquakes and subduction of the Nazca Plate beneath South America, *Geology*, *4* (11), 686-692.

Bayasgalan, A., et al. (2005), Lithosphere rheology and active tectonics in Mongolia: relations between earthquake source parameters, gravity and GPS measurements, *Geophys. J. Int.*, *163* (3), 1151–1179, doi: 10.1111/j.1365-246X.2005.02764.x.

Bayasgalan, A., and J. A. Jackson (1999), A re-assessment of the faulting in the 1967 Mogod earthquakes in Mongolia, *Geophys. J. Int.*, *138* (3), 784-800, doi:10.1046/j.1365-246x.1999.00907.x.

Bonjer, K. P., et al. (1984), Seismicity and Dynamics of the Upper Rhinegraben, *J. Geophys.-Z. Geophys.*, *55* (1), 1-12.

Braunmiller, J., and J. Nabelek (1990), Rupture Process of the Macquarie Ridge Earthquake of May 23, 1989, *Geophys. Res. Lett.*, *17* (7), 1017-1020.

Brazier, R. A., et al. (2005), Focal mechanisms and the stress regime in NE and SW Tanzania, East Africa, *Geophys. Res. Lett.*, *32* (14), L14315, doi:10.1029/2005GL023156.

Cahill, T. A., and B. L. Isacks (1992), Seismicity and shape of the subducted Nazca Plate, *J. Geophys. Res.*, *97* (B12), 17,503-517,529.

Calkins, J. A., et al. (2006), Crustal images from San Juan, Argentina, obtained using high frequency local event receiver functions, *Geophys. Res. Lett.*, *33* (7), L07309, doi:10.1029/2005GL025516.

Chen, W.-P., and H. Kao (1996), Seismotectonics of Asia: some recent progress, *Bull. Inst. Earth Sci. Acad. Sin.*, *16*, 23-24.

Chen, W.-P., et al. (1981), An intermediate depth earthquake beneath Tibet; source characteristics of the event of September 14, 1976, *J. Geophys. Res.*, *86* (B4), 2863-2876.

Chinn, D. S., and B. L. Isacks (1983), Accurate source depths and focal mechanisms of shallow earthquakes in western South America and in the New Hebrides island arc, *Tectonics*, *2* (6), 529-563.

Choukroune, P. (1989), The ECORS Pyrenean deep seismic profile reflection data and the overall structure of an orogenic belt, *Tectonics*, *8* (1), 23-39.

Daignières, M., et al. (1981), Lateral variation of the crust in the North Pyrenean Zone, *Ann. Geophys.*, *37* (3), 435-456.

de la Torre, T. L., et al. (2007), Earthquake processes of the Himalayan collision zone in eastern Nepal and the southern Tibetan Plateau, *Geophys. J. Int.*, *171* (2), 718-738, doi:10.1111/j.1365-246X.2007.03537.x.

Deichmann, N. (1987), Focal depths of earthquakes in northern Switzerland, *Ann. Geophys.*, *5B* (4), 395-402.

Deichmann, N., et al. (2000), Earthquakes in Switzerland and surrounding regions during 1999, *Eclogae. Geol. Helv.*, *93* (3), 395-406.

Deichmann, N., and L. Rybach (1989), Earthquakes and temperatures in the lower crust below the northern Alpine Foreland of Switzerland, in *Properties and processes of Earth's lower crust*, edited by R. F. Mereu, et al., pp. 197-213, American Geophysical Union.

Delouis, B., et al. (2002), A reappraisal of the 1950 (Mw 6.9) Mondy earthquake, Siberia, and its relationship to the strain pattern at the south-western end of the Baikal rift zone, *Terra Nova*, *14* (6), 491-500, doi:10.1046/j.1365-3121.2002.00445.x.

Déverchère, J., et al. (1991), Evidence for a seismogenic upper mantle and lower crust in the Baikal Rift, *Geophys. Res. Lett.*, *18* (6), 1099-1102.

Déverchère, J., et al. (1993), Seismicity, active faults and stress field of the North Muya region, Baikal Rift; new insights on the rheology of extended continental lithosphere, *J. Geophys. Res.*, *98* (B11), 19,895-819,912.

Déverchère, J., et al. (2001), Depth distribution of earthquakes in the Baikal rift system and its implications for the rheology of the lithosphere, *Geophys. J. Int.*, *146* (3), 714-730.

Devlin, S., and B. L. Isacks (in prep), Crustal Seismicity of the Central Andes.

Dewey, J. W. (1982), Instrumental seismicity of New Mexico, Colorado and southern Wyoming (abstract), *Earthquake Notes*, *53*, 86.

Díaz, J., et al. (2003), Teleseismic imaging of alpine crustal underthrusting beneath N. Iberia, *Geophys. Res. Lett.*, *30* (11), 1554, doi:10.1029/2003GL017073.

Dorbath, C., et al. (1987), On crustal seismicity of the Amazonian foothill of the Central Peruvian Andes, *Geophys. Res. Lett.*, *13* (10), 1023-1026.

Doser, D. I. (1991a), Faulting within the eastern Baikal Rift as characterized by earthquake studies, *Tectonophysics*, *196* (1-2), 109-139.

Doser, D. I. (1991b), Faulting within the western Baikal Rift as characterized by earthquake studies, *Tectonophysics*, *196* (1-2), 87-107.

Dugda, M. T., et al. (2005), Crustal structure in Ethiopia and Kenya from receiver function analysis; implications for rift development in eastern Africa, *J. Geophys. Res.*, *110* (B1), B01303, doi:10.1029/2004JB003065.

Ebinger, C. J. (1989), Tectonic development of the western branch of the East African rift system, *Geol. Soc. Am. Bull.*, *101* (7), 885-903.

ECORS Pyrenees team (1988), The ECORS deep reflection seismic survey across the Pyrenees, *Nature*, *331* (6156), 508-511, doi:10.1038/331508a0.

Ekström, G. A. (1987), A broadband method of earthquake analysis (PhD Thesis), 226 pp.

Emmerson, B., et al. (2006), Seismicity, structure and rheology of the lithosphere in the Lake Baikal region, *Geophys. J. Int.*, *167* (3), 1233-1272, doi:10.1111/j.1365-246X.2006.03075.x.

Fan, G., et al. (1994), Active tectonics of the Pamirs and Karakorum, *J. Geophys. Res.*, *99* (B4), 7131-7160.

Foster, A. N., and J. A. Jackson (1998), Source parameters of large African earthquakes; implications for crustal rheology and regional kinematics, *Geophys. J. Int.*, *134* (2), 422-448.

Freund, R., et al. (1970), The shear along the Dead Sea rift, *Philos. Mag. A*, *267* (1181), 107-130.

Gallart, J., et al. (1981), Crustal structure of the Paleozoic axial zone of the Pyrenees and transition to the North Pyrenean Zone, *Ann. Geophys.*, *37* (3), 457-480.

Gao, S. S., et al. (2004), Significant crustal thinning beneath the Baikal rift zone; new constraints from receiver function analysis, *Geophys. Res. Lett.*, *31* (20), L20610, doi:10.1029/2004GL020813.

Gaulon, R., et al. (1992), Regional Geodynamic Implications of the May July 1990 Earthquake Sequence in Southern Sudan, *Tectonophysics*, *209* (1-4), 87-103, doi:10.1016/0040-1951(92)90012-U.

George, R., et al. (1998), Earliest magmatism in Ethiopia: Evidence for two mantle plumes in one flood basalt province, *Geology*, *26* (10), 923-926.

Ghose, S., et al. (1998), Source parameters of moderate-size earthquakes in the Tien Shan, Central Asia from regional movement tensor inversion, *Geophys. Res. Lett.*, *25* (16), 3181-3184.

Gilbert, H., et al. (2007), Imaging Sierra Nevada Lithospheric Sinking, *Eos Trans. AGU*, *88* (21), 225-236.

Gilbert, H. J., and A. F. Sheehan (2004), Images of crustal variations in the intermountain west, *J. Geophys. Res.*, *109* (B3), doi:10.1029/2003JB002730.

Ginzburg, A., et al. (1981), The structure of the crust and upper mantle in the Dead Sea rift, *Tectonophysics*, *80* (1-4), 109-119, doi:10.1016/0040-1951(81)90144-X.

Jaksha, L. H., and D. H. Evans (1984), Reconnaissance seismic refraction-reflection surveys in northwestern New Mexico, *B. Seismol. Soc. Am.*, *74* (4), 1263-1274.

James, D. E., and J. A. Snoke (1994), Structure and tectonics in the region of flat subduction beneath central Peru; crust and uppermost mantle, *J. Geophys. Res.*, *99* (B4), 6899-6912.

Jordan, T. E., et al. (1983), Andean tectonics related to geometry of subducted Nazca plate, *Geol. Soc. Am. Bull.*, *94*, 341-361.

Kadinsky-Cade, K., et al. (1985), Surface deformation associated with the November 23, 1977, Caucete, Argentina, earthquake sequence, *J. Geophys. Res.*, *90* (B14), 12,691-612,700.

Kastrup, U., et al. (2004), Stress field variations in the Swiss Alps and the northern Alpine Foreland derived from inversion of fault plane solutions, *J. Geophys. Res.*, *109* (B1), B01402, doi:10.1029/2003JB002550.

Keir, D., et al. (2006), Strain accommodation by magmatism and faulting as rifting proceeds to breakup; seismicity of the northern Ethiopian Rift, *J. Geophys. Res.*, *111* (B5), doi:10.1029/2005JB003748.

Kohler, M. D., and D. Eberhart-Phillips (2002), Three-dimensional lithospheric structure below the New Zealand Southern Alps, *Journal of Geophysical Research-Solid Earth*, *107* (B10), 2225, doi:10.1029/2001JB000182.

Kohler, M. D., and D. Eberhart-Phillips (2003), Intermediate-depth earthquakes in a region of continental convergence: South Island, New Zealand, *B. Seismol. Soc. Am.*, *93* (1), 85-93.

Lastowka, L. A., et al. (2001), Seismic evidence for partial lithospheric delamination model of Colorado Plateau uplift, *Geophys. Res. Lett.*, *28* (7), 1319-1322.

Lewis, B. T. R. (1978), Evolution of ocean crust seismic velocities, *Annu. Rev. Earth Pl. Sc.*, *6*, 377-404.

Lyon-Caen, H., and P. Molnar (1989), Constraints on the deep structure and dynamic processes beneath the Alps and adjacent regions from an analysis of gravity anomalies, *Geophys. J. Int.*, *99* (1), 19-32.

McGlashan, N., et al. (2008), Crustal thickness in the Central Andes from teleseismically recorded depth phase percursors, *Geophys. J. Int.*, *in press*.

Miller, K. C., and W. D. Mooney (1994), Crustal structure and composition of the southern Foothills metamorphic belt, Sierra Nevada, California, from seismic data, *J. Geophys. Res.*, *99* (B4), 6865-6880.

Mitra, S., et al. (2005), Crustal structure and earthquake focal depths beneath Northeastern India and southern Tibet, *Geophys. J. Int.*, *160* (1), 227-248.

Mohsen, A., et al. (2006), Thickness of the lithosphere east of the Dead Sea Transform, *Geophys. J. Int.*, *167* (2), 845-852, doi:10.1111/j.1365-246X.2006.03185.x.

Molnar, P., and W.-P. Chen (1983), Focal depths and fault plane solutions of earthquakes under the Tibetan Plateau, *J. Geophys. Res.*, *88* (B2), 1180-1196.

Molnar, P., and H. Lyon-Caen (1988), Some simple physical aspects of the support, structure, and evolution of mountain belts, *Geol. Soc. Am. Spec Pap.*, *218*, 179-207.

Molnar, P., and H. Lyon-Caen (1989), Fault plane solutions of earthquakes and active tectonics of the Tibetan Plateau and its margins, *Geophys. J. Int.*, *99* (1), 123-153.

Monsalve, G., et al. (2006), Seismicity and one-dimensional velocity structure of the Himalayan collision zone: Earthquakes in the crust and upper mantle, *J. Geophys. Res.*, *111* (B10), doi:10.1029/2005JB004062.

Nelson, M. R., et al. (1987), Source Parameters for 11 earthquakes in the Tien Shan, Central Asia, determined by P and SH waveform inversion, *J. Geophys. Res.*, *92* (B12), 12,629-612,648.

Ni, J., and M. Barazangi (1984), Seismotectonics of the Himalayan collision zone; geometry of the underthrusting Indian Plate beneath the Himalaya, *J. Geophys. Res.*, *89* (B2), 1147-1163.

Nicole, B., et al. (2007), Local tomography and focal mechanisms in the south-western Alps: Comparison of methods and tectonic implications, *Tectonophysics*, *432* (1-4), 1-19.

Nyblade, A. A., and R. A. Brazier (2002), Precambrian lithospheric controls on the development of the East African Rift system, *Geology*, *30* (8), 755-758.

Nyblade, A. A., and C. A. Langston (1995), East African earthquakes below 20 km depth and their implications for crustal structure, *Geophys. J. Int.*, *121* (1), 49-62.

Parson, L. M., and I. C. Wright (1996), The Lau-Havre-Taupo back-arc basin: A southward-propagating, multi-stage evolution from rifting to spreading, *Tectonophysics*, *263* (1-4), 1-22.

Pauchet, H., et al. (1999), A detailed analysis of the February 1996 aftershock sequence in the eastern Pyrenees, France, *Geophys. J. Int.*, *137* (1), 107-127.

Pedreira, D., et al. (2003), Seismic evidence of Alpine crustal thickening and wedging from the western Pyrenees to the Cantabrian Mountains (north Iberia), *J. Geophys. Res.*, *108* (B4), 2204, doi:10.1029/2001JB001667.

Quennell, A. M. (1958), The structural and geomorphic evolution of the Dead Sea rift, *Quart. J. Geol. Soc., Lond.*, *114* (453), 1-24.

Radziminovich, N. A., et al. (2003), Earthquake focal depths and crustal strength in the Baikal rift, *Geol. Geofiz.*, *44* (11), 1216-1225.

Regnier, M., et al. (1992), Seismotectonics of Sierra Pie de Palo, a basement block uplift in the Andean foreland of Argentina, *Bull. Seismol. Soc. Am.*, *82* (6), 2549-2571.

Reyners, M. (1987), Subcrustal Earthquakes in the Central South Island, New-Zealand, and the Root of the Southern Alps, *Geology*, *15* (12), 1168-1171.

Reyners, M., et al. (2007), The role of fluids in lower-crustal earthquakes near continental rifts, *Nature*, *446* (7139), 1075-1078.

Rigo, A., et al. (2005), Analysis of the seismicity in the central part of the Pyrenees (France), and tectonic implications, *J. Seismol.*, *9* (2), 211-222.

Rigo, A., et al. (1997), The February 1996 earthquake sequence in the eastern Pyrenees: first results, *J. Seismol.*, *1* (1), 3-14.

Rimando, R. E., and K. Benn (2005), Evolution of faulting and paleo-stress field within the Ottawa Graben, Canada, *J. Geodyn.*, *39* (4), 337-360.

Roure, F., et al. (1989), ECORS deep seismic data and balanced cross sections; geometric constraints on the evolution of the Pyrenees, *Tectonics*, *8* (1), 41-50.

Ruiz, M., et al. (2006), Seismic activity at the western Pyrenean edge, *Tectonophysics*, *412* (3-4), 217-235.

Schulte-Pelkum, V., et al. (2005), Imaging the Indian subcontinent beneath the Himalaya, *Nature*, *435* (7046), 1222-1225.

Sherburn, S., and R. S. White (2005), Crustal seismicity in Taranaki, New Zealand using accurate hypocentres from a dense network, *Geophys. J. Int.*, *162* (2), 494-506, doi:10.1111/j.1365-246X.2005.02667.x.

Shin, Y. H., et al. (2007), Moho undulations beneath Tibet from GRACE-integrated gravity data, *Geophys. J. Int.*, *170* (3), 971-985, doi:10.1111/j.1365-246X.2007.03457.x.

Shudofsky, G. N. (1985), Source mechanisms and focal depths of East African earthquakes using Rayleigh-wave inversion and body-wave modelling, *Geophys. J. Int.*, *83* (3), 563-614.

Smalley, R., Jr., and B. L. Isacks (1990), Seismotectonics of thin- and thick-skinned deformation in the Andean foreland from local network data; evidence for a seismogenic lower crust, *J. Geophys. Res.*, *95* (B8), 12,487-412,498.

Smalley, R., Jr., et al. (1993), Basement seismicity beneath the Andean Precordillera thin-skinned thrust belt and implications for crustal and lithospheric behavior, *Tectonics*, *12* (1), 63-76.

Smith, E. G. C., et al. (1995), A seismic velocity profile across the central South Island, New Zealand, from explosion data, *New Zeal. J. Geol. Geop.*, *38* (4), 565-570.

Souriau, A., and M. Granet (1995), A tomographic study of the lithosphere beneath the Pyrenees from local and teleseismic data, *J. Geophys. Res.*, *100* (B9), 18,117-118,134.

Stern, T. A., et al. (2006), Subduction evolution and mantle dynamics at a continental margin: Central North Island, New Zealand, *Rev. Geophys.*, *44* (RG4002), doi:10.1029/2005RG000171.

Suarez, G., et al. (1983), Seismicity, Fault Plane Solutions, Depth of Faulting, and Active Tectonics of the Andes of Peru, Ecuador, and Southern Colombia, *J. Geophys. Res.*, *88* (B12), 403-428.

Suriñach, E., et al. (1993), Seismic images and evolution of the Iberian crust in the Pyrenees, *Tectonophysics*, *221* (1), 67-80, doi:10.1016/0040-1951(93)90028-I.

ten Brink, U. S., and M. H. Taylor (2002), Crustal structure of central Lake Baikal; insights into intracontinental rifting, *J. Geophys. Res.*, *107* (B7), 2132, doi:10.1029/2001JB000300.

Turcotte, D. L., and G. Schubert (2002), *Geodynamics*, 2 ed., 456 pp., Cambridge University Press, Cambridge.

Van Avendonk, H. J. A., et al. (2004), Continental crust under compression; a seismic refraction study of South Island geophysical transect; I, South Island, New Zealand, *J. Geophys. Res.*, *109, no. B6* (B6), doi: 10.1029/2003jb002790.

Vertlib, M. B. (1981), Determination of focal depths by the composite method for some regions of Pribaikalie, in *Seismic investigations in East Siberia*, edited by V. Rogozhina and M. Nauka, pp. 82-88.

Vertlib, M. B. (1997), Hypocentral field and mechanism of earthquakes in relation to geodynamics of the northeastern Baikal Zone, *Russ. Geol. Geophys.*, *38* (8), 1414-1422.

Vinnik, L. P., et al. (2004), Receiver function tomography of the central Tien Shan, *Earth Planet. Sci. Lett.*, *225* (1-2), 131-146, doi: 10.1016/j.epsl.2004.05.039.

Wagner, G. S., and C. A. Langston (1988), East-African Earthquake Body Wave Inversion with Implications for Continental Structure and Deformation, *Geophys. J. Int.*, *94* (3), 503-518, doi:10.1111/j.1365-246X.1988.tb02271.x.

Weber, M., et al. (2004), The crustal structure of the Dead Sea Transform, *Geophys. J. Int.*, *156* (3), 655-681, doi: 10.1111/j.1365-246X.2004.02143.x.

Wilson, D., et al. (2005), Imaging the seismic structure of the crust and upper mantle beneath the Great Plains, Rio Grande Rift, and Colorado Plateau using receiver functions, *J. Geophys. Res.*, *110* (B5), B05306, doi:10.1029/2004JB003492.

Wong, I. G., et al. (1984), The Crownpoint, New Mexico, earthquakes of 1976 and 1977, *B. Seismol. Soc. Am.*, *74* (6), 2435-2449.

Wong, I. G., and J. R. Humphrey (1989), Contemporary Seismicity, Faulting, and the State of Stress in the Colorado Plateau, *Geol. Soc. Am. Bull.*, *101* (9), 1127-1146.

Wong, I. G., and W. U. Savage (1983), Deep Intraplate Seismicity in the Western Sierra-Nevada, Central California, *B. Seismol. Soc. Am.*, *73* (3), 797-812.

Xu, Y., et al. (2006), Analysis of seismic activity in the crust from earthquake relocation in the central Tien Shan, *B. Seismol. Soc. Am.*, *96* (2), 737-744, doi: 10.1785/0120030220.

Zandt, G., et al. (2004), Active foundering of a continental arc root beneath the southern Sierra Nevada in California, *Nature*, *431* (7004), 41-46, doi: 10.1038/nature02847.

Zandt, G., et al. (1995), Crust and mantle structure across the Basin and Range-Colorado Plateau boundary at 37 degrees N latitude and implications for Cenozoic extensional mechanism, *J. Geophys. Res.*, *100* (B6), 10,529-510,548.

Zhu, L., and D. V. Helmberger (1996), Intermediate depth earthquakes beneath the India-Tibet collision zone, *Geophys. Res. Lett.*, *23* (5), 435-438, doi: 10.1029/96GL00385.

APPENDIX C

PERCENT STRAIN

This section reviews the percent strain calculations that were made to construct Figure 3.6. The reported values result from a variety of data and analyses techniques.

Alpine Region

Alps (~ 58%) – Alpine percent compression of ~ 58% was calculated from Schmid and Kissling's [2000] Figure 7, which shows a kinematic reconstruction of post-collisional (post-35 Ma) shortening in the western Alps. That study combined seismic reflection interpretation, gravity, and geologic mapping data to constrain the reconstruction.

Alpine Foreland (< 15%) – The eastern Jura fold-and-thrust belt is located between the Rhine Graben to the north and the Molasse Basin and Alps to the south. Ustaszewski and Schmid [2006] studied the eastern Jura fold-and-thrust belt by integrating field observations and paleo-stress analysis, subsurface maps based on industry seismic reflection lines, and published geologic maps. They constructed balanced cross sections, which estimated deformation on the order of ~ 4 to 14 % shortening in the last 12 m.y.

Rhine Graben (~ 10%) – Brun et al. [1992] reported the structural analysis results of two deep seismic reflection lines crossing the northern and southern parts of the Rhine Graben. Upper crustal deformation by faulting suggests ~ 10% extension occurred across the graben since 35 Ma.

Andean Foreland – Basement Thrusts (< 10%)

Jordan and Allmendinger [1986] used refraction, seismic reflection, stratigraphic, and drilling data to estimate that the continental basement thrusts of the Sierras Pampeanas in Argentina are associated with ~ 2% east-west shortening, parallel to the plate convergence. Kley et al. [1999] reviewed the along-strike segmentation of the structural styles within Andean foreland including the Sierras Pampeanas and Peruvian basement thrusts and held that basement thrust deformation in the Andean foreland has accommodated < 10% strain in less than 8 Ma [*Ramos, et al.*, 2002].

Baikal Rift System ($\lesssim$ 5%)

Zorin and Cordell [1991] estimated crustal extension across the Baikal Rift System (BRS) from Bouguer gravity anomaly analysis. Amounts of anomalous mass at different lithospheric levels are attributed to a mix of extension, intrusion, uplift, sedimentation, and erosion, from which extension is isolated algebraically. Extension since ~ 30 Ma was on the order of ~ 10 km (i.e., ~ 5% strain). San'kov et al. [2000] combined remote sensing techniques, geologic mapping, and simplified cross section construction to estimate extension of the north BRS. Percent strain calculations of these cross sections yielded < 5%.

Basin and Range ($\gtrsim$ 100%)

Gans [1987] combined previously published strain estimates [*Hamilton and Myers*, 1966; *Stewart*, 1978], geologic maps [*Hintze*, 1983; *Stewart and Carlson*, 1978], and seismic reflection profiles [*Allmendinger, et al.*, 1983; *Gans, et al.*, 1985; *Hauser, et al.*, 1984; *Klemperer, et al.*, 1986; *McCarthy*, 1984] to propose a two-layer model of crustal stretching for the Basin and Range. The model describes an upper crustal layer

accommodating lateral variations in strain (from 15 to 300% extension) via brittle failure and a lower crustal layer more uniformly deforming by ductile flow. Jones et al. [1992] combined geologic, geochemical, and geophysical data across the central Basin and Range and adjacent areas of the western United State. They concluded that abundant data indicate ~ 250 km of extension over a region now about 360 km wide indicating extension of several hundred percent since 16 Ma. Therefore, it is conservative to say that the Basin and Range province has experienced 100% strain.

East African Rift System

Afar Triangle (≥ 100%) – Hayward and Ebinger [1996] quoted > 20 Ma accumulating ≥ 100 % extension in the Afar region from analyzing geologic mapping [*Mohr*, 1972], seismic reflection profiles [*Berckhemer, et al.*, 1975], and magmatic addition calculations [*Barberi, et al.*, 1972].

Eastern Rift (≳ 30%) – The Eastern Rift extends from the Main Ethiopian Rift in the north to the Kenya Rift in the south. Ebinger and Casey [2001] compiled previously published studies to investigate the Main Ethiopian Rift. Percent extension estimates range from ~ 35 to 80% [*Bilham, et al.*, 1999; *Ebinger and Casey*, 2001] based on seismic profiles and geodetic measurements. Further south, Hendrie et al. [1994] employed seismic reflection interpretation and gravity modeling to estimate deformation of the Kenya Rift and found ~ 30% extension across the Turkana region. Extension within the Eastern Rift has propagated from north to south, so the pattern of increased percent strain in the north and less in the south is consistent with the relative timeline of deformation. We chose 30% strain as a lower bound on the amount of deformation the Eastern Rift has sustained in order to be conservative, but extension could be as much as 80%.

Western Rift (< 15 %) – Ebinger [1989] compiled crustal extension estimates for basins throughout the southern East African Rift System. From north to south, the Western Rift basins of Kinu, Nyanza-lac, Marunga, and Karonga have estimated percent extensions of ~ 15, 15, 10, and 5 to 9% respectively. Volcanism began at ~ 12 Ma in the north and at ~ 7 Ma in the south.

North Island, New Zealand

Northeast (≳ 42%) – Nicol et al. [2007] compiled previously published strain profiles into a large dataset to characterize deformation of New Zealand's entire North Island over the last ~ 5 Ma. In the northeast, within the Taupo Volcanic Zone, we extracted profiles #23 and #25 from Nicol et al.'s Figure 3, which resulted in 51 and 42% extension, respectively.

Southwest (~ 5%) – Within the southwest, we calculated percent strain from profile D in Niocl et al.'s [2007] Figure 5, which estimated ~ 5% compression.

Rio Grande Rift (≳ 70%)

Morgan et al. [1986] reviews Cenozoic thermal, mechanical, and tectonic evolution of the Rio Grande Rift. They conclude that two regimes can be interpreted from rocks and structures formed within the last 30 m.y.. Early phase extension involved broad ~30 to 50% extension, while local basin extension may have approached 100%. Late phase deformation resulted in an additional 5 to 20% extension. Percent strain estimates were made by analysis of timing and type of magmatism and deformation, rift basin development, and restored cross sections and palinspastic mapping. The

early and late phase combine to estimate that the Rio Grande Rift broadly experienced as much as 70% strain and in specific localities much more.

Tien Shan (< 35%)

Avouac et al. [1993] estimated crustal shortening across the Tien Shan from a bulk crustal section based on gravity, topography, and assumptions of initial crustal thickness and topography. Estimates of shortening resulting in ~ 34 % strain. Yin et al. [1998] estimates 20 – 30% strain across the southern Tien Shan using geologic mapping and balanced cross section construction. Onset of deformation is thought to be in between 21 and 25 Ma.

Western Pyrenees (~ 33%)

Teixell [1998] used surface geologic and seismic reflection data to constrain a late Cretaceous to Present reconstruction of ~ 80 km of shortening across the western Pyrenees, which is equivalent to ~ 33 % strain for that region.

Zagros (~ 35%)

Percent compression (~ 35%) for the Zagros in the last 30 Ma was calculated and averaged from three restored and balanced cross sections [*Blanc, et al.*, 2003; *Bosold, et al.*, 2005; *McQuarrie*, 2004]. Geologic mapping was used to constrain Blanc et al. [2003] and McQuarrie's [2004] cross sections, while Bosold et al. [2005] combined geologic mapping with seismic reflection data.

REFERENCES

Allmendinger, R. W., et al. (1983), Cenozoic and Mesozoic structure of the eastern Basin and Range province, Utah, from COCORP seismic-reflection data, *11* (9), 532-536.

Avouac, J.-P., et al. (1993), Active thrusting and folding along the northern Tien Shan and late Cenozoic rotation of the Tarim relative to Dzungaria and Kazakhstan, *J. Geophys. Res.*, *98* (B4), 6755-6804.

Barberi, F., et al. (1972), Volcanism in the Afar depression; its tectonic and magmatic significance, *Tectonophysics*, *15* (1-2), 19-29.

Berckhemer, H., et al. (Eds.) (1975), *Deep seismic soundings in the Afar region and on the highland of Ethiopia*, 89-107 pp., Stuttgart.

Bilham, R., et al. (1999), Secular and tidal strain across the main Ethiopian Rift, *Geophys. Res. Lett.*, *26* (18), 2789-2792.

Blanc, E. J. P., et al. (2003), Structural styles in the Zagros Simple Folded Zone, Iran, *J. Geol. Soc. London*, *160* (3), 401-412, 10.1144/0016-764902-110.

Bosold, A., et al. (2005), The structural geology of the high central Zagros revisited (Iran), *Petrol. Geosci.*, *11* (3), 225-238.

Brun, J. P., et al. (1992), Deep Crustal Structure of the Rhine Graben from Dekorp-Ecors Seismic-Reflection Data - a Summary, *Tectonophysics*, *208* (1-3), 139-147.

Ebinger, C. J. (1989), Tectonic development of the western branch of the East African rift system, *Geol. Soc. Am. Bull.*, *101* (7), 885-903.

Ebinger, C. J., and M. Casey (2001), Continental breakup in magmatic provinces: An Ethiopian example, *Geology*, *29* (6), 527-530.

Gans, P. B. (1987), An open-system, two layer crustal stretching model for the eastern Great Basin, *Tectonics*, *6* (1), 1-12.

Gans, P. B., et al. (1985), Tertiary extensional faulting and evolving ductile-brittle transition zones in the northern Snake Range and vicinity; new insights from seismic data, *Geology*, *13* (3), 189-193.

Hamilton, W., and W. B. Myers (1966), Cenozoic tectonics of the western united states, *Rev. Geophys.*, *4* (4), 509-549.

Hauser, E. C., et al. (1984), The COCORP 40 degrees N transect of the North American Cordillera, *Geol. Soc. Am. Abstr. Programs*, *16*, 532 & 626.

Hayward, N. J., and C. J. Ebinger (1996), Variations in the along-axis segmentation of the Afar Rift system, *Tectonics*, *15* (2), 244-257.

Hendrie, D. B., et al. (1994), Cenozoic extension in northern Kenya: a quantitative model of rift basin development in the Turkana region, *Tectonophysics*, *236* (1-4), 409-438.

Hintze, L. F. (1983), Geologic map of Utah, 1:500,000, Utah Geol. and Miner. Surv.

Jones, C. H., et al. (1992), Variations across and along a major continental rift: An interdisciplinary study of the Basin and Range Province, western USA, *Tectonophysics*, *213* (1-2), 57-96.

Jordan, T. E., and R. W. Allmendinger (1986), The Sierras Pampeanas of Argentina; a modern analogue of Rocky Mountain foreland deformation, *Am. J. Sci.*, *286* (10), 737-764.

Klemperer, S. L., et al. (1986), The Moho in the northern Basin and Range Province, Nevada, along the COCORP 40 degrees N seismic-reflection transect, *Geol. Soc. Am. Bull.*, *97* (5), 603-618.

Kley, J., et al. (1999), Along-strike segmentation of the Andean foreland; causes and consequences, *Tectonophysics*, *301* (1-2), 75-94.

McCarthy, J. (1984), Reflection profiles from the Snake Range metamorphic core complex; a window into the mid-crust, in *International symposium on Deep*

structure of the continental crust; results from reflection seismology, edited by M. Barazangi and L. D. Brown, pp. 281-292, American Geophysical Union.

McQuarrie, N. (2004), Crustal scale geometry of the Zagros fold-thrust belt, Iran, *J. Struct. Geol.*, *26* (3), 519-535.

Mohr, P. A. (1972), Surface structure and plate tectonics of Afar in East African Rifts, *J. Geophys. Res.*, *15* (1-2), 3-18.

Morgan, P., et al. (1986), Cenozoic thermal, mechanical, and tectonic evolution of the Rio Grande Rift, *J. Geophys. Res.*, *91* (B6), 6263-6276.

Nicol, A., et al. (2007), Tectonic evolution of the active Hikurangi subduction margin, New Zealand, since the Oligocene, *Tectonics*, *26*, TC4002, doi:10.1029/2006TC002090.

Ramos, V. A., et al. (2002), The Pampean flat-slab of the Central Andes, *J. S. Am. Earth Sci.*, *15* (1), 59-78.

San'kov, V., et al. (2000), Geometry and rate of faulting in the North Baikal Rift, Siberia, *Tectonics*, *19* (4), 707-722.

Schmid, S. M., and E. Kissling (2000), The arc of the Western Alps in the light of geophysical data on deep crustal structure, *Tectonics*, *19* (1), 62-85.

Stewart, J. H. (1978), Basin-range structure in western North America; a review, Geological Society of America (GSA).

Stewart, J. H., and J. E. Carlson (1978), Geologic map of Nevada, U. S. Geological Survey, Reston, VA.

Teixell, A. (1998), Crustal structure and orogenic material budget in the west central Pyrenees, *Tectonics*, *17* (3), 395-406.

Ustaszewski, K., and S. M. Schmid (2006), Control of preexisting faults on geometry and kinematics in the northernmost part of the Jura fold-and-thrust belt, *Tectonics*, *25* (5), TC5003, doi:10.1029/2005TC001915.

Yin, A., et al. (1998), Late Cenozoic tectonic evolution of the southern Chinese Tien Shan, *Tectonics*, *17* (1), 1-27, doi: 10.1029/97TC03140.

Zorin, Y. A., and L. E. Cordell (1991), Crustal extension in the Baikal rift zone, *Tectonophysics*, *198* (1), 117-121.

APPENDIX D

LITHOSPHERIC THICKNESS

This section reviews the estimated lithospheric thicknesses that were compiled to construct Figure 3.7. The reported values result from a variety of data and analyses techniques.

Africa

Afar ($\lesssim$ 50 km), Eastern Rift (~ 60 – 80 km), Tanzanian Craton (~ 100 – 150 km) – Julià et al. [2005] modeled the *S* wave velocity structure beneath Tanzania by jointly inverting receiver functions and surface wave dispersion velocities recorded during a 1994 to 1995 broad-band seismic experiment. They found that the mantle displayed uniformly fast *S* wave velocities (4.5 – 4.7 km/s) to depths of ~ 100 to 150 km over a prominent low-velocity zone. This transition is presumed to be the lithosphere-asthenosphere boundary (LAB). Similarly, Dugda et al. [2007] investigated lithospheric velocity structure by inverting receiver functions and Rayleigh wave group velocities. They studied the lithosphere beneath the Ethiopian Plateau (part of the Eastern Rift) and Afar and found maximum shear wave velocities (~ 4.3 km/s) beneath the plateau extend to ~ 70 to 80 km depth, while maximum mantle shear wave velocities (~ 4.1 – 4.2 km/s) extend to at most ~ 50 km beneath Afar. Therefore, Dugda et al. [2007] propose the Ethiopian Plateau has a ~ 70 to 80 km thick lithosphere and Afar $\lesssim$ 50 km. Simiyu and Keller [1997] integrated gravity survey data and existing seismic refraction results [*KRISP Working Group*, 1987; 1991] and geologic data to model the lithospheric structure beneath the East African Rift System. Simiyu and Keller [1997] found the lithosphere beneath the Eastern Rift in Kenya is $\lesssim$

60 km thick, while the cratonic lithosphere of Tanzania is ~ 120 km thick. Henjes-Kunst and Altherr [1992] estimated lithospheric thicknesses from calculations of pressure and temperature (P–T) paths from crustal and mantle xenoliths throughout the Eastern Rift from northern Kenya south into northern Tanzania. Again, variable thicknesses were found, such that the lithosphere is thin (~ 75 km) in northern Kenya and increases to ~ 115 km and ≳ 145 km in southern Kenya and northern Tanzania, respectively. These estimates are consistent with areas surrounding the Tanzanian Craton having lithospheric thicknesses of ~ 100 to 150 km and those within the Eastern Rift of Ethiopia and northern Kenya being ~ 60 to 80 km. Like Henjes-Kunst and Altherr [1992], Dawson [1994] analyzed xenoliths found in volcanic rocks from the Tanzanian Craton. Those rocks hailed from the Igwisi Hills, a young (possibly Quaternary) example of kimberlite magmatism. Analysis showed the magma formed by small degrees of melting of a carbonate-apatite-bearing peridotite source at depths in excess of 110 km. Furman and Graham [1999] analyzed major and trace elements and Sr – Nd isotopic results for Miocene to Recent mafic lavas from volcanic provinces in Tanzania and Kenya. Variations of isotopic and trace element ratios in the lavas vary systematically with geographic location and are consistent with ~ 100 km melting depth beneath Tanzania and ~ 60 km beneath the Eastern Rift in Kenya. Therefore, estimates of lithospheric thickness from seismic imaging, gravity, and geochemistry are all consistent with thinning of the lithosphere from the south to north within the East African Rift System, such that thicknesses are ~ 100 to 150 km beneath the around the Tanzania Craton, ~ 60 to 80 km beneath the Eastern Rift of Kenya and Ethiopia, and ≲ 50 km beneath Afar.

Congo Craton (~ 250 km)

Ritsema and van Heijst [2000] constructed a seismic model of the upper 400 km of mantle beneath Africa from modeling of Rayleigh wave phase velocities. A prominent feature was a high shear wave velocity structure (as much as 6% higher than in the Preliminary Reference Earth Model (PREM)) beneath the Congo craton that extended to ~ 250 km. Therefore, Ritsema and van Heijst [2000] estimate the thickness of the Congo craton is about 250 km.

Anatolian Plateau (60 km)

Angus et al. [2006] imaged crustal and upper mantle seismic discontinuities beneath eastern Anatolia using receiver functions, specifically *S*-to-*P* converted phases. Several upper mantle converted phases were interpreted as being the signature of the LAB, which indicated that eastern Turkey has an anomalously thin lithosphere, between ~ 60 and 80 km thick. However, other independent seismic measurements beneath the Anatolian Plateau [*Al-Damegh, et al.*, 2004; *Al-Lazki, et al.*, 2004; *Al-Lazki, et al.*, 2003; *Gök, et al.*, 2003; *Maggi and Priestley*, 2005; *Sandvol, et al.*, 2003; *Sandvol and Zor*, 2004] indicate that the uppermost mantle is partially molten and that asthenospheric material is in direct contact with the base of the crust (i.e., there is no mantle lid) (see Barazangi et al. [2006] for review). Hence, lithospheric thickness for this area is likely not much greater than the crustal thickness. Moho depth is, on average, less than 45 km [*Angus, et al.*, 2006; *Zor, et al.*, 2003]. Therefore, our selection of the lithospheric thickness of ~ 60 km is a conservative value.

Andean Foreland – Basement Thrusts (< 125 km)

The lithospheric thickness of 125 km for the Andean Foreland represents the maximum possible thickness of the foreland lithosphere of Peru and Argentina above

Nazca Plate flat subduction. The seismicity of the subducted Nazca Plate locates the subducting lithosphere dipping at an approximate 10° angle from 100 to 125 km depth beneath the cordillera and foreland [*Barazangi and Isacks*, 1976; *Cahill and Isacks*, 1992; *Norabuena, et al.*, 1994; *Pardo, et al.*, 2002; *Smalley and Isacks*, 1990]. Therefore, if the subducted oceanic slab is located at 125 km depth, then the overriding South American (i.e., the foreland) lithosphere in those areas must be less than 125 km thick. Additionally, Whitman et al. [1996] constructed a longitudinal lithospheric cross-section of the Central Andes. Mantle lid thicknesses were inferred from patterns of upper mantle seismic attenuation [*Chinn, et al.*, 1980; *Whitman, et al.*, 1992], such that the Argentine foreland lithosphere was estimated to be ~ 100 km thick.

Baikal Rift System (~ 100 km)

Lithospheric thickness values for the Baikal Rift System (BRS) were estimated from both surface wave tomography and geotherm modeling from P–T estimates from kimberlite xenoliths [*Emmerson, et al.*, 2006]. From geotherm modeling of two kimberlite sites nearest the BRS, Emmerson et al. [2006] calculated the depth of the thermal boundary layer (TBL) [*McKenzie and Bickle*, 1988], the model's transition layer between the thermally convective and conductive mantle (i.e., a LAB layer), as $\lesssim$ 150 km. Emmerson et al. [2006] then compared these estimates to the *Sv* wave speed tomographic model of Priestley and Debayle [2003] and Priestley et al. [2006]. This model uses regional waveforms of the fundamental and first four higher modes to image the upper mantle at depths up to ~ 400 km. The rift is too small to see on the tomography, but the rift's location relative to the seismic imaging places the BRS where the lithosphere transitions between being thick (~ 200 km) and seismically fast (~ 12% higher than in PREM) beneath the Siberian Shield and being thin (< 100 km)

and seismically slow (~ 6% lower than in PREM) beneath the Sayan-Baikal fold-and-thrust belt. This is roughly consistent with the TBL estimate from the geotherm modeling. Thus, we chose the lithospheric thickness of the BRS as ~ 100 km.

Dead Sea Fault System (≲ 80 km)

Mohsen et al. [2006] used *S* receiver function analysis to study the lithosphere across the Dead Sea Fault System (DSFS) using data from a temporary network of 22 broad-band stations operated from 2000 to 2001 as part of the DESERT project. They observed thinning of the lithosphere from west to east across the DSFS, such that the lithosphere thickness ranges from ~ 80 km in the northwest to ~ 67 km in the east. Laske et al. [2008] also used data from the DESERT seismic deployment. They conducted fundamental mode Rayleigh wave analysis at intermediate periods (35 – 150 s) and found a seismically relatively fast mantle lid to a depth of ~ 80 km. Both Mohsen et al. [2006] and Laske et al.'s [2008] finding are consistent with the lithosphere of the DSFS region being ~ 80 km thick.

North America

Great Plains (~ 200 km), Colorado Plateau (≲ 150 km), Rio Grande Rift (≲ 55 km) – Through the LA RISTRA seismic experiment, West et al. [2004] used surface wave phase velocities from 29 earthquakes to map the shear velocity structure to ~ 350 km beneath the southwest United States across the western Great Plains, the Rio Grande Rift, and the eastern Colorado Plateau. Seismically fast mantle was imaged to ~ 200 km beneath the Great Plains and to ~ 120 –150 km depth beneath the Colorado Plateau, presumably indicating the depth limit of the continental lithospheric mantle. Relatively slow mantle velocities were mapped beneath the Rio Grande Rift, such that the lithosphere there is thin, ~ 45 – 55 km. Additionally, part of Zandt et al.'s [1995] *P*

wave receiver function analysis crossed the western Colorado Plateau, where they estimated a lithospheric thickness of ~ 100 km. This calculation is roughly consistent with what West et al. [2004] found for the eastern part of the plateau. Both estimates are $\lesssim$ 150 km.

Southern California ($\lesssim$ 70 km) – Li et al. [2007] analyzed *S* wave receiver functions from sixty-seven broad-band seismic stations throughout the western United States. The data revealed a mantle discontinuity with a velocity reduction downward, which they interpret as the LAB. In the region of Southern California the average depth of the LAB is $\lesssim$ 70 km. Yang and Forsyth [2008] inverted phase and amplitude data of Rayleigh waves (25 to 143 s) for attenuation and shear wave velocities beneath southern California. Their velocity and attenuation model reveals the presence of partial melt over the depth range 70 to 200 km with an approximate linear increase in percent melt from 70 to 120 km depth and a pronounced low velocity zone from ~ 80 km to ~ 200 km.

Basin and Range (~ 60 km) – *P* [*Zandt, et al.*, 1995] and *S* wave [*Li, et al.*, 2007] receiver function analysis are consistent with ~ 60 km thick lithosphere beneath the Basin and Range province.

Siberian Shield ($\gtrsim$ 200 km)

Similar to the Baikal Rift region, lithospheric thickness values for the Siberian Shield were taken from Emmerson et al. [2006]. Please see the Baikal Rift System section above for a description of the analysis techniques. Emmerson et al. [2006] calculated the depth of the Siberian Shield's TBL as ~ 240 km. *Sv* wave speed tomography

correlated well with this estimate and placed the bottom of the seismically fast Siberian mantle lid at ~ 200 km.

Tien Shan (~ 90 – 120 km)

Oreshin et al. [2002] applied *S* receiver function analyses to recordings from thirty-six broad band stations throughout the Tien Shan. They found a high velocity (4.5 km/s) mantle lid to ~ 90 km beneath which the velocity drops to ~ 4.1 km/s. Kumar et al. [2005] also conducted *S* wave receiver function analysis. They studied lithosphere beneath the Tien Shan and the surrounding regions and found the thickness of the lithosphere beneath the Tien Shan varies between ~ 90 to 120 km and increases to 160 km beneath the Tarim Basin. Vinnik et al. [2007] investigated depth dependant azimuthal anisotropy in the mantle by jointly inverting *P* receiver functions and *SKS* wave polarization directions. The results for 10 seismograph stations within the Tien Shan showed a pronounced change in the patterns of azimuthal anisotropy at ~ 100 km depth. Shallower than 100 km anisotropy is relatively weak (~ 3%) and polarization of the fast wave varies laterally in a wide range. Below 100 km depth *S* wave anisotropy is approximately twice as large (~ 5 – 6 %) and the azimuth of the fast wave polarization is aligned with the trend of the mountain belt. Since 100 km depth is roughly consistent with Oreshin et al. [2002] and Kumar et al.'s [2005] estimate for the LAB, Vinnik et al. [2007] have most likely imaged the different patterns of seismic anisotropy in the mantle lithosphere and the underlying asthenosphere.

REFERENCES

Al-Damegh, K., et al. (2004), Regional seismic wave propagation (Lg and Sn) and Pn attenuation in the Arabian Plate and surrounding regions, *Geophys. J. Int.*, *157* (2), 775-795.

Al-Lazki, A. I., et al. (2004), Pn tomographic imaging of mantle lid velocity and anisotropy at the junction of the Arabian, Eurasian and African plates, *Geophys. J. Int.*, *158* (3), 1024-1040.

Al-Lazki, A. I., et al. (2003), Tomographic Pn velocity and anisotropy structure beneath the Anatolian Plateau (eastern Turkey) and the surrounding regions, *The Turkey seismic experiment; the study of a young continent-continent collision*, *30* (24), 8043, doi: 10.1029/2003gl017391.

Angus, D. A., et al. (2006), Lithospheric structure of the Arabian and Eurasian collision zone in eastern Turkey from S-wave receiver functions, *Geophys. J. Int.*, *166* (3), 1335-1346, doi:10.1111/j.1365-246X.2006.03070.x.

Barazangi, M., and B. L. Isacks (1976), Spatial distribution of earthquakes and subduction of the Nazca Plate beneath South America, *Geology*, *4* (11), 686-692.

Barazangi, M., et al. (2006), Structure and tectonic evolution of the Anatolian Plateau in eastern Turkey, *Geol. Soc. Am. Spec Pap.*, *409*, 463-473.

Cahill, T. A., and B. L. Isacks (1992), Seismicity and shape of the subducted Nazca Plate, *J. Geophys. Res.*, *97* (B12), 17,503-517,529.

Chinn, D. S., et al. (1980), High-Frequency Seismic-Wave Propagation in Western South-America Along the Continental-Margin, in the Nazca Plate and across the Altiplano, *Geophys. J. R. Astron. Soc.*, *60* (2), 209-244.

Dawson, J. B. (1994), Quaternary kimberlitic volcanism on the Tanzania Craton, *Contrib. Mineral. Petrol.*, *116* (4), 473-485.

Dugda, M. T., et al. (2007), Thin Lithosphere Beneath the Ethiopian Plateau Revealed by a Joint Inversion of Rayleigh Wave Group Velocities and Receiver Functions, *J. Geophys. Res.*, *112*, B08305, doi:10.1029/2006JB004918.

Emmerson, B., et al. (2006), Seismicity, structure and rheology of the lithosphere in the Lake Baikal region, *Geophys. J. Int.*, *167* (3), 1233-1272, doi:10.1111/j.1365-246X.2006.03075.x.

Furman, T., and D. Graham (1999), Erosion of lithospheric mantle beneath the East African Rift system: geochemical evidence from the Kivu volcanic province, *Lithos*, *48* (1-4), 237-262.

Gök, R., et al. (2003), Sn attenuation in the Anatolian and Iranian Plateau and surrounding regions, *Geophys. Res. Lett.*, *30* (24), 8042, doi: 10.1029/2003gl018020.

Henjes-Kunst, F., and R. Altherr (1992), Metamorphic Petrology of Xenoliths from Kenya and Northern Tanzania and Implications for Geotherms and Lithospheric Structures, *Journal of Petrology*, *33* (5), 1125-1156.

Julià, J., et al. (2005), Evidence for mafic lower crust in Tanzania, East Africa, from joint inversion of receiver functions and Rayleigh wave dispersion velocities, *Geophys. J. Int.*, *162* (2), 555-569.

KRISP Working Group (1987), Structure of the Kenya Rift from Seismic Refraction, *Nature*, *325* (6101), 239-242.

KRISP Working Group (1991), Large-scale variation in lithospheric structure along and across the Kenya rift, *Nature*, *354* (6350), 223-227.

Kumar, P., et al. (2005), The lithosphere-asthenosphere boundary in the Tien Shan-Karakoram region from S receiver functions: Evidence for continental subduction, *Geophys. Res. Lett.*, *32* (L07305), doi:10.1029/2004GL022291.

Laske, G., et al. (2008), Lithosphere structure across the Dead Sea Transform as constrained by Rayleigh waves observed during the DESERT experiment, *Geophys. J. Int.*, *173*, 593–610, doi:10.1111/j.1365-246X.2008.03749.x.

Li, X., et al. (2007), The lithosphere-asthenosphere boundary beneath the western United States, *Phys. Earth Planet. In.*, *170* (2), 700-710, doi:10.1111/j.1365-246X.2007.03428.x.

Maggi, A., and K. Priestley (2005), Surface waveform tomography of the Turkish-Iranian Plateau, *Geophys. J. Int.*, *160* (3), 1068-1080.

McKenzie, D., and M. J. Bickle (1988), The volume and composition of melt generated by extension of the lithosphere, *Journal of Petrology*, *29* (3), 625-679.

Mohsen, A., et al. (2006), Thickness of the lithosphere east of the Dead Sea Transform, *Geophys. J. Int.*, *167* (2), 845-852, doi:10.1111/j.1365-246X.2006.03185.x.

Norabuena, E. O., et al. (1994), Structure of the subducting Nazca Plate beneath Peru, *J. Geophys. Res.*, *99* (5), 9215-9226.

Oreshin, S., et al. (2002), Lithosphere and asthenosphere of the Tien Shan imaged by S receiver functions, *Geophys. Res. Lett.*, *29* (8).

Pardo, M., et al. (2002), Seismotectonic and stress distribution in the central Chile subduction zone, *J. S. Am. Earth Sci.*, *15* (1), 11-22.

Priestley, K., and E. Debayle (2003), Seismic evidence for a moderately thick lithosphere beneath the Siberian Platform, *Geophys. Res. Lett.*, *30* (3).

Priestley, K., et al. (2006), Upper mantle structure of eastern Asia from multimode surface waveform tomography, *Journal of Geophysical Research-Solid Earth*, *111* (B10).

Ritsema, J., and H.-J. van Heijst (2000), New seismic model of the upper mantle beneath Africa, *Geology*, *28* (1), 63-66, doi: 10.1130/0091-7613(2000)0282.3.co;2.

Sandvol, E., et al. (2003), Shear wave splitting in a young continent-continent collision; an example from eastern Turkey, *The Turkey seismic experiment; the study of a young continent-continent collision*, *30* (24), doi: 10.1029/2003gl017390.

Sandvol, E. A., and E. Zor (2004), Upper mantle P and S-wave velocity structure beneath eastern Anatolian Plateau, *Eos Trans. AGU*, *85* (S13B-1056).

Simiyu, S. M., and G. R. Keller (1997), An integrated analysis of lithospheric structure across the East African plateau based on gravity anomalies and recent seismic studies, *Tectonophysics*, *278* (1-4), 291-313, doi:10.1016/S0040-1951(97)00109-1.

Smalley, R., Jr., and B. L. Isacks (1990), Seismotectonics of thin- and thick-skinned deformation in the Andean foreland from local network data; evidence for a seismogenic lower crust, *J. Geophys. Res.*, *95* (B8), 12,487-412,498.

Vinnik, L. P., et al. (2007), Depth localized azimuthal anisotropy from SKS and P receiver functions: The Tien Shan, *Geophys. J. Int.*, *169* (3), 1289-1299, doi:10.1111/j.1365-246X.2007.03394.x.

West, M., et al. (2004), Crust and upper mantle shear wave structure of the Southwest United States; implications for rifting and support for high elevation, *J. Geophys. Res.*, *109* (B3), doi:10.1029/2003JB002575.

Whitman, D., et al. (1992), Attenuation of high-frequency seismic waves beneath the central Andean Plateau, *J. Geophys. Res.*, *97* (B13), 19,929-919,947.

Whitman, D., et al. (1996), Lithospheric structure and along-strike segmentation of the Central Andean Plateau: seismic Q, magmatism, flexure, topography and tectonics, *Tectonophysics*, *259* (1-3), 29-40.

Yang, Y., and D. W. Forsyth (2008), Attenuation in the upper mantle beneath Southern California: Physical state of the lithosphere and asthenosphere, *J. Geophys. Res.*, *113* (B03308), doi:10.1029/2007JB005118.

Zandt, G., et al. (1995), Crust and mantle structure across the Basin and Range-Colorado Plateau boundary at 37 degrees N latitude and implications for Cenozoic extensional mechanism, *J. Geophys. Res.*, *100* (B6), 10,529-510,548.

Zor, E., et al. (2003), The crustal structure of the East Anatolian plateau (Turkey) from receiver functions, *Geophys. Res. Lett.*, *30* (24).